LAPPEENRANTA-LAHTI UNIVERSITY OF TECHNOLOGY LUT

Egor Fadeev

MAGNETOTRANSPORT PROPERTIES OF NANOCOMPOSITES CLOSE TO THE PERCOLATION THRESHOLD

ACTA UNIVERSITATIS LAPPEENRANTAENSIS 1026

LUT
University

Egor Fadeev

MAGNETOTRANSPORT PROPERTIES OF NANOCOMPOSITES CLOSE TO THE PERCOLATION THRESHOLD

Dissertation for the degree of Doctor of Science (Technology) to be presented with due permission for public examination and criticism in the Auditorium 1316 at Lappeenranta-Lahti University of Technology LUT, Lappeenranta, Finland on the 2nd of May, 2022, at noon.

Acta Universitatis
Lappeenrantaensis 1026

Supervisor	Professor Erkki Lähderanta LUT School of Engineering Science Lappeenranta-Lahti University of Technology LUT Finland
Reviewers	Academician Ernest Arushanov Laboratory of Materials for Photovoltaics and Photonics Institute of Applied Physics Republic of Moldova
	PhD Igor S. Dubenko Department of Physics Southern Illinois University USA
Opponent	Professor Arcady Zhukov Department of Polymers and Advanced Materials: Physics, Chemistry and Technology University of the Basque Country (UPV/EHU) Spain

ISBN 978-952-335-817-1
ISBN 978-952-335-818-8 (PDF)
ISSN-L 1456-4491
ISSN 1456-4491

Lappeenranta-Lahti University of Technology LUT
LUT University Press 2022

Abstract

Egor Fadeev
Magnetotransport properties of nanocomposites close to the percolation threshold
Lappeenranta 2022
80 pages
Acta Universitatis Lappeenrantaensis 1026
Diss. Lappeenranta-Lahti University of Technology LUT
ISBN 978-952-335-817-1, ISBN 978-952-335-818-8 (PDF), ISSN-L 1456-4491, ISSN 1456-4491

Magnetic semiconductors and granular metal-insulator systems are the key materials for broadly developing spintronics and for many other fields of solid-state physics. The idea of this work was to investigate magnetotransport and magnetic properties of multilayered ZnO/C magnetic semiconductors and nanogranular metal-insulator composites that were fabricated using an ion-beam sputtering method. The focus of the investigation was on determining conduction mechanisms and finding positive magnetoresistance in both systems, as well as on establishing the role of dispersed magnetic atoms in metal-insulator nanocomposites.

The conduction mechanism of ZnO/C heterostructures changes from the 2D Mott's variable range hopping to the hopping to the nearest neighbors depending on film thickness, the amount of bilayers and temperature. The peculiar low-temperature magnetoresistance behavior was observed for ZnO/C heterostructures – magnetoresistance changes its sign twice in the magnetic field range of 20 T. The three mechanisms were proposed to explain this unusual behavior: the Fermi level shift under the influence of a magnetic field, scattering on the magnetic disorder, and wave function shrinkage due to the effect of magnetic blockade. ZnO/C heterostructures have shown the presence of ferromagnetic ordering in $T \leqslant 120$ K.

The study of metal-insulator nanocomposites has shown that an increase of concentration of dispersed magnetic atoms shifts the metal-insulator transition to lower values, widening the concentration range where temperature dependence of electrical conductivity follows $\rho \propto \ln T$. Low-temperature linear positive magnetoresistance in the range of 10^{-3}–$10^{-2}\%$ T^{-1} was observed for nanocomposites with concentrations close to the percolation threshold. The magnetoresistance results were quantitatively explained by the modified expression based on the Inoue-Meakawa model. The observed magnetoresistance anisotropy of one of the nanocomposites was associated with the formation of the columnar structure at the initial stage of growth of the nanocomposite.

Keywords: Transport properties, magnetic properties, metal-insulator nanocomposites, magnetic semiconductors, magnetoresistance

Acknowledgements

This scientific work and related publications were completed in close collaboration with our colleagues from different Russian universities during 2018–2021. During these years, I have had the privilege to meet and work with a number of inspiring and talented people whose contribution I want to acknowledge here.

First and foremost, I would like to express my deepest gratitude to my supervisor, Professor Erkki Lähderanta, for providing me with the opportunity to conduct the doctoral studies, and for supporting and guiding me throughout the doctoral journey. His management skills and ability to solve problems were invaluable for me.

I am particularly grateful to Professor Alexander Granovsky, without whom this work would not have been finished. His constant willingness to help and answer my questions made my journey much easier. I thank him for organizing the samples, and reading my dissertation text and providing feedback.

My sincere appreciation goes to Mikhail Shakhov for his tolerance and patience when teaching me to operate such a difficult scientific setup, and for trusting and allowing me to utilize it on my own.

I would also like to acknowledge contributions from my closest colleagues in our laboratory: Pavel, Katya, Anton, and Ivan. They not only aided me in scientific matters, but made my studies more relaxing through countless talks, laughter and coffee breaks. In addition, I thank my friends for replenishing my forces by plenty of trips, board games, cozy gatherings, and countless smiles.

Finally, I would like to thank my family for their support, encouragement and faith in me during the whole period of my studies at LUT University – without you I would not even have gone abroad for my master studies.

Egor Fadeev
February 2022
Lappeenranta, Finland

Contents

Abstract

Acknowledgments

Contents

Publications

List of publications

This dissertation is based on the following papers. The rights have been granted by publishers to include the papers in the dissertation.

I. Volochaev, M.N., Granovsky, A.B., Zhilova, O.V., Kalinin, Y.E., Ryl'kov, V.V., Sumets, M.P., Makagonov, V.A., Pankov, S.Y., Sitnikov, A.V., **Fadeev, E.**, Lahderanta, E. and Foshin, V.A. (2020). Transport and magnetic phenomena in ZnO-C thin-film heterostructures. Superlattices and microstructures, 140, p. 106449.

II. **Fadeev, E.A.**, Lähderanta, E., Aronzon, B.A., Mekhiya, A.B., Kalinin, Yu.E., Makagonov, V.A., Pankov, S.Yu., Foshin, V.A. and Granovsky, A.B. (2021). Unconventional magnetoresistance in ZnO/C multilayers at low temperatures. Journal of Magnetism and Magnetic Materials, 535, p. 167963.

III. Rylkov, V.V., Emelyanov, A.V., Nikolaev, S.N., Nikiruy, K.E., Sitnikov, A.V., **Fadeev, E.A.**, Demin, V.A. and Granovsky, A.B. (2020). Transport Properties of Magnetic Nanogranular Composites with Dispersed Ions in an Insulating Matrix. Journal of Experimental and Theoretical Physics, 131(1), pp. 160–176.

IV. Rylkov, V., Sitnikov, A., Nikolaev, S., Emelyanov, A., Chernohlazov, K., Nikiruy, K., Drovosekov, A., Blinov, M., **Fadeev, E.**, Taldenkov, A., Demin, V., Vedeneev, A., Bugaev, A., and Granovsky, A. (2019). Properties of Nanocomposites With Different Concentrations of Magnetic Ions in an Insulating Matrix. IEEE Magnetics Letters, 10, pp. 1–4.

V. **Fadeev, E.A.**, Shakhov, M.A., Lähderanta, E., Taldenkov, A.N., Vasiliev, A.L., Sitnikov, A.V., Rylkov, V.V. and Granovsky, A.B. (2021). High-Field Magnetoresistance of Magnetic Nanocomposites near the Percolation Threshold. Journal of Experimental and Theoretical Physics, 133(6), pp. 771–778.

Author's contribution

I. Planning the experiment and conducting magnetic measurements. Data curation.

II. Planning the experiment and conducting magnetic and magnetotransport measurements. Data curation. Analysis and interpretation of the obtained data. Corresponding author.

III. Literature search and investigation. Reviewing and editing the text.

IV. Planning the experiment and conducting magnetic measurements. Data curation.

V. Planning the experiment and conducting magnetic and magnetotransport measurements. Data curation. Analysis and interpretation of the obtained data. Corresponding author.

Nomenclature

Latin alphabet

a	localization radius
B	magnetic flux density
E_C	Coulomb blockade energy
E_F	Fermi level
G	conductance
$g(E_F)$	density of states at the Fermi level
G_q	conductance quantum
G_t	tunnelling conductance
H	magnetic field strength
h	thickness
H_C	coercive field
k_B	Boltzmann constant
M	magnetization
m	magnetic moment
N_d	concentration of dispersed atoms
T	absolute temperature
T_C	Curie temperature
T_g	growth temperature
x	concentration
x_c	concentration of metal-insulator transition
x_p	concentration of percolation threshold

Greek alphabet

χ	magnetic susceptibility
ϵ	permittivity
μ_B	Bohr magneton
ρ	resistivity
σ	conductivity

Subscripts

max	maximum
min	minimum
sat	saturation

Abbreviations

AFM	antiferromagnetic
AHE	anomalous Hall effect

DM	diamagnetic
DMO	diluted magnetic oxide
DMS	diluted magnetic semiconductor
DOS	density of states
FC	field cooling
FM	ferromagnetic
FW	field warming
HCDA	high concentration of dispersed atoms
LCDA	low concentration of dispersed atoms
LPMR	linear positive magnetoresistance
MI NC	metal-insulator nanocomposite
MIT	metal-insulator transition
MR	magnetoresistance
NC	nanocomposite
PM	paramagnetic
PMFS	pulse magnetic field setup
RT	room temperature
RTFM	room-temperature ferromagnetism
SFM	superferromagnetic
SPM	superparamagnetic
SQUID	superconducting quantum interference device
TM	transition metal
ZFC	zero-field cooled

1 Introduction

Physics of magnetic nanoparticle systems has been an attractive area of research in recent decades due to the potential use of such systems in a variety of fields such as spintronics (Maekawa, 2004; Fujimori et al., 2006), biomedicine (Bogren et al., 2015) and fundamental physics (Dormann et al., 1988).

The study of magnetic nanogranular metal-insulator composites is one of the branches of magnetic nanoparticle systems research. Such composites consist of magnetic nanogranules chaotically distributed in a dielectric matrix. There are two important parameters when considering concentration of nanogranules in such systems: a percolation threshold x_p, which means the appearance of a chain of granules through which current can flow, and a metal-insulator transition x_c, which can be followed by the change of magnetic state. Metal-insulator nanocomposites (MI NC) are of particular interest due to their magnetic, (magneto-)transport, memristive and magnetooptical properties which are promising for practical applications. A variety of effects have been observed when investigating one or another type of magnetic metal-insulator nanocomposites: memristive effect (Rylkov et al., 2018c; Nikiruy et al., 2019); giant magnetoresistance (Milner et al., 1996; Kobayashi et al., 2001); anomalous Hall effect (Pakhomov et al., 1995; Aronzon et al., 1999); magneto-optical Kerr effect (Gan'shina et al., 2004); linear positive magnetoresistance (Gerber et al., 2007; Blinov et al., 2019); quantum size effect (Raquet et al., 2000); etc. Depending on the composition, MI NC can be either in a low or high magnetic state. An increase in the concentration of magnetic nanogranules leads to the change from weak interactions between granules, followed by a manifestation of paramagnetic or superparamagnetic behavior (Neel-Brown model), to strong collective interactions, showing super spin-glass and ferromagnetic behavior. A further increase of the concentration (however, still below percolation threshold) leads to an appearance of a superferromagnetic state (Bedanta and Kleemann, 2008). It has been shown that MI NC can be utilized in high-frequency magnetoelectric devices such as thin-film inductors and noise suppressors, as well as in low magnetic field sensors (Fujimori et al., 2006). Magnetic data recording is another field where MI NC can be used as the core structure of a device. Various memristors, which are used, e.g., to emulate synapses in neuromorphic computing systems, are based on these structures (Nikiruy et al., 2019; Ielmini, 2016; Xia and Yang, 2019). Despite the amount of research on the MI NC, these systems are yet poorly studied and further investigation is required (Bedanta and Kleemann, 2008).

Another class of material that was studied in this present work is diluted magnetic semiconductors (DMS). DMSs are semiconductor alloys doped with magnetic impurities, which are an important branch of modern science and are being extensively developed because they combine both magnetic and semiconductor properties, allowing them to control both charge and spin of electrons. A variety of effects has been observed in DMSs such as control of magnetism by an electric field and current (Ohno et al., 2000), spin-polarized current injection (Schmidt and Molenkamp, 2001), and tunneling anisotropic magnetoresistance in the Coulomb blockade regime (Wunderlich et al., 2006). The properties of DMS make them promising for broadly developing room-temperature spintronics. Quantum well lasers (Bylsma et al., 1985), quantum computing architecture (Loss and DiVincenzo, 1998), and spin light-emitting diodes (Ramsteiner et al., 2008) are a few examples of potential or already existing applications of DMSs. Many classes of DMS materials are known, though the most studied are Mn-doped alloys ($A^{II}_{1-x}Mn_xB^{VI}$, $A^{IV}_{1-x}Mn_xB^{VI}$ and $A^{III}_{1-x}Mn_xB^{VI}$ [Dietl, 2010]). Diluted magnetic oxides (such as ZnO, CoO or TiO) doped with a few percentages of a transition metal are other important materials that show a combination of both magnetic and semiconductor properties (Coey, 2006). ZnO DMOs doped with a transition metal have been of particular interest due to their high Curie temperature, which is the biggest obstacle for developing room-temperature spintronics devices based on DMS/DMO (Liu et al., 2005). However, experimental results of such systems have been inconsistent (Pan et al., 2007). An alternative approach is doping ZnO with non-magnetic carbon – such systems showed room-temperature ferromagnetism (Pan et al., 2007; Ye et al., 2008), though the origin of the magnetism is still unclear.

Thus, the aim of this present work was to investigate the magnetic, transport and magnetotransport properties of nanogranular metal-insulator composites and ZnO/C diluted magnetic oxides. The objectives were:

- To investigate the magnetic, transport and magnetotransport properties of metal-insulator nanocomposites with metallic nanogranules concentrations close to the percolation threshold, and with different materials of metallic and dielectric phases;
- To analyze the role of dispersed atoms in establishing a certain magnetic state or phenomenon and to compare properties of nanocomposites with different concentrations of dispersed atoms;
- To investigate and compare the magnetic, transport and magnetotransport properties of ZnO/C multilayered thin films with different amount of layers and film thickness;
- To determine the conduction mechanism of the ZnO/C multilayered thin films.

2 SQUID magnetometry

There are a variety of methods to detect the magnetic flux of a material: induction, fluxgate, ferromagnetic magnetoresistive, Hall effect magnetic, to name but a few (Ripka, 2021). Among all the existing magnetic flux measurement techniques, Superconducting QUantum Interference Device (SQUID) magnetometry is the most sensitive, with the magnetic field resolution down to 10^{-17} T at low temperatures (Fagaly, 2006). SQUID magnetometers are extremely versatile devices that make them applicable in a variety of areas such as biomedicine, metrology, geophysics, measurements of the magnetic properties of matter, microscopy, nanoscience, astrophysics and non-destructive evaluation (Clarke and Braginski, 2006; Fagaly, 2006). As for laboratory measurements of the magnetic properties of solid state matter, SQUID magnetometers allow the investigation of any kind of materials, from strongly magnetic ferro- and ferrimagents to spin-glasses, multilayers, and weakly magnetic nanostructures. However, like any other techniques, SQUID magnetometry has its own drawbacks, limitations and complications. As an example, the first and most obvious complication one will encounter when working with SQUIDs is the need to maintain a superconductive state, which implies the use of cryogenic liquids and maintaining them in a liquid state throughout the measurement process. The Josephson effect and flux quantization are the basis phenomena of a SQUID magnetometer, but to explain its working principle let us firstly recall the basics of superconductivity.

2.1 Superconductivity

In 1911, Dutch physicist Heike Kamerlingh Onnes discovered the peculiar behavior of resistance of some materials (Hg, Pb, Nb) submerged in liquid helium – resistance dropped to zero. It so happened that there is a critical temperature (T_C) at which transition from normal to superconductive state occurs. Under a superconductive state, a current in a wire will persist for an extremely long time (up to years [Quinn III and Ittner III, 1962]) without losses and heat dissipation. Since the discovery of superconductivity (SC), a variety of different classes of materials have been proven to sustain a SC state below a certain T_C, ranging from almost absolute zero up to almost room temperature (Snider et al., 2020; Keimer et al., 2015).

Another characteristic feature of a superconductor is the so-called Meissner effect (Meissner and Ochsenfeld, 1933). It so happened that SCs are "ideal" diamagnets – they expel any applied magnetic flux. In 1935, the brothers Fritz and Heinz London tried to explain peculiarities of SCs and relate current and magnetic field produced by SCs by developing two equations:

$$\begin{aligned} \frac{dJ_s}{dt} &= \frac{n_s e^2}{m} E, \\ \nabla \times J_s &= -\frac{n_s e^2}{m} B, \end{aligned} \tag{2.1}$$

where J_s is a superconducting current and n_s is a density of superconductive charge carriers (London and London, 1935). The brothers showed that an applied magnetic flux does not penetrate inside SC except for a thin surface layer called London penetration depth (λ_L), which ranges from nano- to micrometers. A magnetic flux applied perpendicularly to a SC ring will induce a so-called "screening" current in the surface layer (λ_L) to produce an opposite magnetic flux. Then, if the applied magnetic flux is turned off, the induced current will persist producing the magnetic flux (Innes and Rhoderick, 1980).

Later, it was discovered that two types of SCs exist: Type-I SC sustains a zero magnetic field inside its interior (except for the thin surface layer) until a critical magnetic field (H_c) is reached, after which SC state disappears (See Fig. 2.1a), and Type-II SC has a so-called "mixed" state between two critical magnetic fields (H_{c1} and H_{c2}) (See Fig. 2.1b). In the "mixed" state (or "vortex" state), some magnetic field lines penetrate the interior of a SC, creating areas of normal state (Rjabinin and Shubnikow, 1935). Below H_{c1} and above H_{c2}, Type-II SCs are in SC and a normal state, respectively (See Fig. 2.1b). It should be noted that a certain critical value of temperature (T_c) and magnetic field are not the only parameters that can break SC state – a critical current density is another parameter that can destroy superconductivity (though it is related to a critical magnetic field). Type-II SCs are usually metal alloys or oxide ceramics, whereas Type-I SCs are commonly single metal elements (Annett et al., 2004).

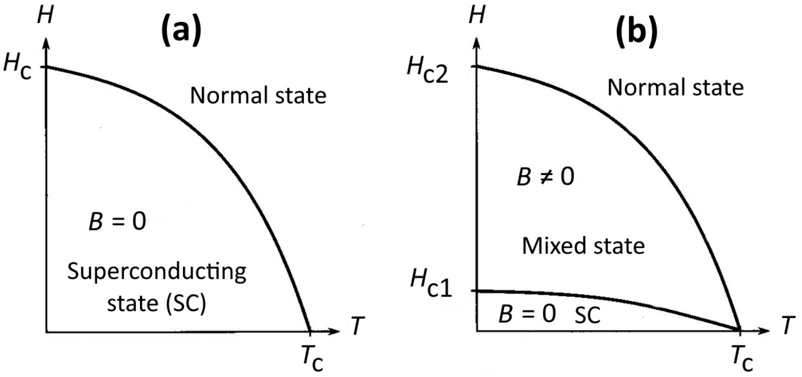

Figure 2.1: Phase diagrams of (a) Type-I and (b) Type-II superconductors.

In 1957, Bardeen-Cooper-Schrieffer developed a theory trying to explain superconductivity (Bardeen et al., 1957). According to the theory, free electrons in a superconductor are bound in pairs (Cooper pairs) caused by phonon interactions, allowing them to travel inside a material without scattering. An average distance between Cooper pairs is called the coherence length ξ. A macroscopic quantum state of the Cooper pairs can be described by a wave function:

$$\Psi(r,t) = |\Psi(r,t)| \exp\{i\phi(r,t)\}, \tag{2.2}$$

where $|\Psi|$ is an amplitude and ϕ is a phase of the wave function (Clarke et al., 2003). The existence of such a quantum state leads to the manifestation of several phenomena such as flux quantization and the Josephson effect (Schwartz, 2013).

2.1.1 Flux quantization

In 1961, it was discovered that a magnetic flux ($\Phi = AB$) cannot be swept continuously – a change of flux values follows a step-like behavior, which implies discrete values of magnetic flux or, in other words, quantization of the flux. One step is a flux quanta ($\Phi_0 = h/(2e) \approx 2.068 \times 10^{-15}$ Wb). If we return to the SC ring, the trapped magnetic field (B) inside the ring will be quantized by a value that depends on an area of the ring. For example, for a ring with A = 1 mm^2, B will be quantized by 2.068×10^{-9} T (Deaver Jr and Fairbank, 1961).

2.1.2 Josephson effect

In 1962, Brian Josephson showed that Cooper pairs can tunnel through a potential barrier of a “normal” insulating junction between two SCs without a voltage drop. Such insulating junctions are called “weak links” or “Josephson junctions”. It should be noted that Cooper pairs can tunnel without voltage drop only if the length of a weak link is less than the coherence length and the current is less than the critical current (I_0) of the weak link (Josephson, 1962). A phase difference between two separated SCs depends on an applied current as

$$I = I_0 \sin \phi_1 - \phi_2 = I_0 \sin \Theta. \tag{2.3}$$

For $I > I_0$, a voltage is developed across a junction, and a phase difference evolve with time following

$$\frac{d\Theta}{dt} = \frac{2\pi V}{\Phi_0} = \frac{2eV}{\hbar}. \tag{2.4}$$

In this case, a SC current oscillates with frequency

$$f = \frac{2eV}{h} = \frac{V}{\Phi_0}. \tag{2.5}$$

However, Josephson junctions have a hysteretic behavior of an $I(V)$ curve – when a current is switched off, a voltage drops to zero only at $I < I_0$. By utilizing a Josephson junction, it is possible to measure a phase difference between two SCs and to precisely track the changes of magnetic flux. As for the geometry of Josephson junctions, there are a variety of options: point contact, Dayem bridge, bicrystal, step edge grain boundary, thin films, etc (Fagaly, 2006).

2.2 SQUID magnetometer

Jaklevic et al. (1964) have shown the effect of quantum interference of two parallel Josephson junctions enclosed in one superconducting ring, where a critical current of such a double junction system is an oscillating function of the magnetic flux applied normally to the ring with a period of oscillation equal to the flux quanta (Φ_0). Since the discovery, this effect has been used as a basis in the development of a variety of SQUID magnetometers. The two main types of SQUID magnetometers are radio frequency (rf) and direct current (dc). The former one is based on a SC ring with only one Josephson junction, which is biased with an alternating current, whereas the latter one utilizes two parallelly arranged Josephson junctions, which are biased with a direct current. Another decisive parameter of a SQUID magnetometer is the critical temperature of a SC ring that defines the usage of either helium (Type-I SC) or nitrogen (Type-II SC) liquid. Obviously, plenty of parameters differ between various SQUID magnetometers, for example, dc SQUIDs produce less amount of white noise compared to rf SQUIDs, however, their electronics is more complex and a fabrication process of two identical Josephson junctions (with nearly identical critical currents) is somewhat challenging (Fagaly, 2006).

2.2.1 Working principle of dc SQUID magnetometer

Since this present work was based on the results of magnetic measurements conducted using a dc SQUID magnetometer, only this type will be discussed in detail. A dc SQUID consists of a superconducting ring of inductance (L) with two resistively shunted Josephson junctions (See Fig. 2.2a). The shunting of the Josephson junctions eliminates the potential hysteresis of an $I(V)$ curve. The system is biased with dc current (I_B). I_0 is a critical current of a Josephson junction. In the absence of external magnetic flux ($\Phi = n\Phi_0$), the bias current is equally divided into two sides of the SC ring and no voltage is induced across the system. If an external magnetic flux is applied to the SC ring, the screening current will be induced in the ring ($J = -\Phi_e/L$). On one side of the ring, the screening current is added to the bias current ($I_{total} = I_B + J > I_0$), whereas on the other side it is subtracted from the bias current ($I_{total} = I_B - J < I_0$) (See Fig. 2.3a). The change of the screening current in the ring induces a direct voltage across the system, which oscillates with a period of Φ_0 (See Fig. 2.2c). By tracking the variation of voltage across the SC ring at a fixed bias current (See Fig. 2.2b), one can determine a change of external magnetic flux. SQUIDs are usually adjusted to operate on the steepest part of a $V(\Phi_e/\Phi_0)$ curve with the best response (Clarke et al., 2003; Clarke, 1996).

Similarly, a maximum SC current (I_m) that can flow through the ring oscillates with Φ_e/Φ_0 (See Fig. 2.3c) since the screening current superimposes itself on the bias current, changing the values of the critical current (I_0). At $J = \Phi_0/2L$ (a half of the flux quantum), the junctions become resistive, the maximum SC current drops by Φ_0/L, and the screening current changes its sign (Fig. 2.3b,c). At $\Phi_e = \Phi_0$, $J = 0$ and $I_m = 2I_0$. Usually, dc SQUIDs are operated at a bias current slightly higher than $2I_0$ to stay in the resistive mode. A more comprehensive description of working principle of dc/rf SQUID magnetometers can be found in Clarke et al. (2003); Gallop and Petley (1976); Clarke et al. (1976).

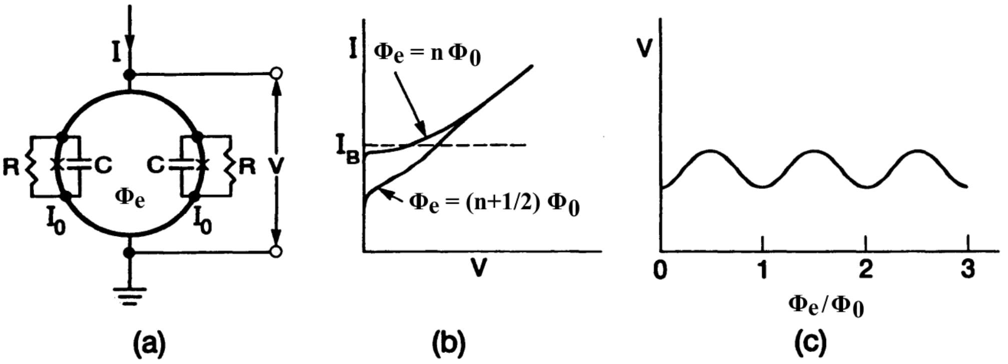

Figure 2.2: A dc SQUID magnetometer: (a) schematic diagram of a SC ring with two Josephson junctions, (b) $I(V)$ characteristics, and (c) $V(\Phi_e/\Phi_0)$ dependence. Adapted from Clarke (1996).

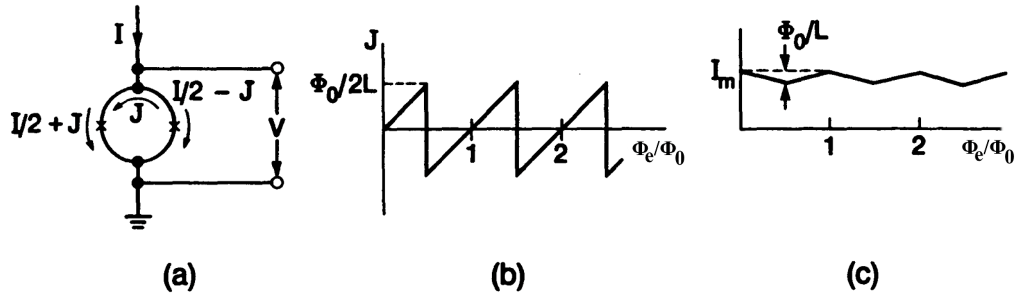

Figure 2.3: A dc SQUID magnetometer: (a) external magnetic flux generates SC current in a SC ring, (b) dependence of SC current on the external magnetic flux, (c) a maximum SC current as a function of external magnetic flux. Adapted from Clarke (1996).

2.2.2 Structure of dc SQUID magnetometer

Up till this point, only a SC ring with two Josephson junctions has been discussed (for brevity, from now on, this will be called a "SQUID ring"), though a whole SQUID setup is more complex and contains various electronics. A block diagram of a typical dc SQUID magnetometer setup is presented in Fig. 2.4. A SQUID ring is located in a cryogenic region and is inductively coupled with feedback, input and modulation coils. The feedback current compensates the changes of magnetic flux in order to keep an output voltage $V(\Phi_e/\Phi_0)$ at a fixed point ("flux-locked regime"). If a change of the magnetic flux is more than $\Phi_0/4$, then the feedback system adjusts the current to keep the signal at the operating point. In this case, feedback current (presented as output voltage) is proportional to the external magnetic flux. Modulation coils generate a sinusoidal flux with an amplitude of $\Phi_0/2$ and a frequency of about 1–500 kHz (Gallop and Petley, 1976; Clarke, 1996). It is important to occasionally tune the SQUID by setting suitable bias and modulation currents to provide a $V(\Phi_e/\Phi_0)$ curve that will support a stable feedback loop and prevent flux jumps.

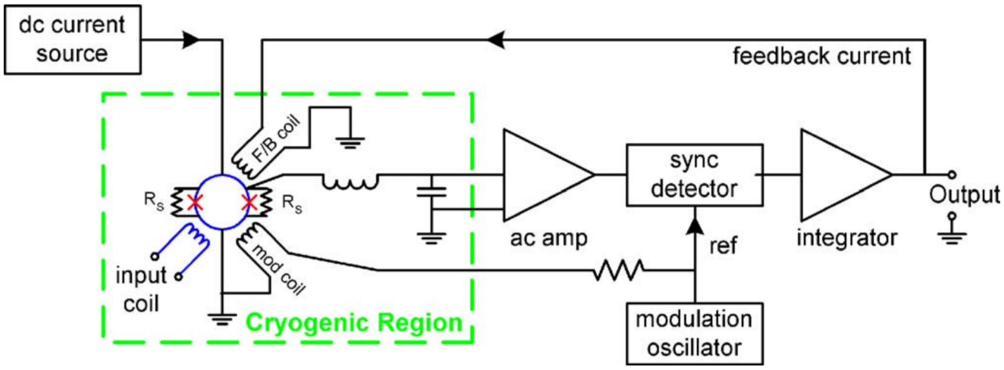

Figure 2.4: Block diagram of a typical dc SQUID magnetometer. Taken from Fagaly (2006).

Since a typical SQUID ring has too small area and inductance to detect the magnetic flux from a sample, a SC system of detection (or “pick-up”) and input coils is used. An input coil is inductively coupled to the SQUID ring and physically connected to a detection coil. Detection coils can be of various configurations, depending on the desired parameters (See Fig. 2.5). The simplest type is a magnetometer that measures magnetic flux using a single loop coil (See Fig. 2.5a). The next type is a gradiometer that measures a gradient of magnetic flux using a multiple loop coil. While magnetometers are suitable for measuring an ambient magnetic field, gradiometers can differentiate the signal of a sample from an ambient magnetic field. In gradiometers, a uniform background magnetic field is suppressed by two parallel and oppositely wound loops (See Fig. 2.5b,d). Another trick that can be used with gradiometers to distinguish a sample signal from a background field is to move a sample up and down inside the coils (See Fig. 2.5d); this is called extraction magnetometry (Sawicki et al., 2011). It should be noted that since detection coils are SC, they detect magnetic flux – not the change of it, hence there is no need to move a sample quickly. The majority of modern SQUIDs utilizes second derivative axial gradiometer detection coils (See Fig. 2.5d) with the output voltage presented as a function of distance that the sample travels up and down, which represents a single longitudinal scan of a dc SQUID magnetometer (See Fig. 2.5e). SQUID electronics then recalculate the output voltage to magnetic moment, m, with a unit of Am^2. By knowing the mass or volume of a sample, it is possible to calculate relative magnetization and susceptibility. Some SQUID magnetometers have transverse detection coils allowing them to perform rotational scans, where the voltage is detected as a function of the sample axis rotational angle.

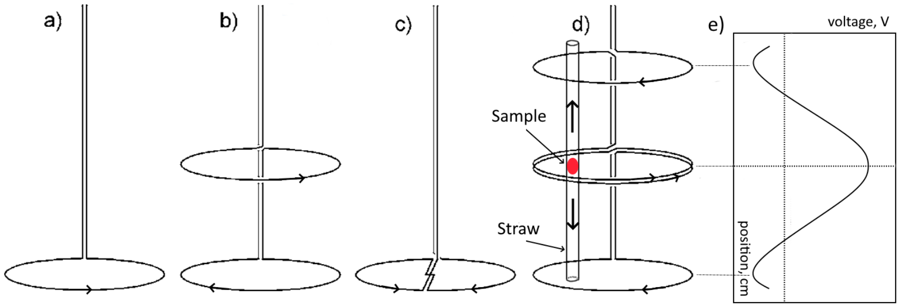

Figure 2.5: Configurations of detection coils: (a) magnetometer, (b) first derivative axial gradiometer, (c) first derivative planar gradiometer, (d) second derivative axial gradiometer with a sample placed inside a straw, which is moved up and down, producing characteristic voltage dependence on the sample position (e). Adapted from Fagaly (2006).

In Fig. 2.6 one can see a schematic diagram of a typical SQUID magnetometer (left) and cross-section of “Cryogenics S700XR” SQUID magnetometer as a concrete example (right). A sample is inserted in a sample tube or in the concrete case of “Cryogenics S700XR” SQUID magnetometer it is called variable temperature insert (VTI). Temperature inside the sample space is controlled by resistive heaters and helium gas flow from the lowest part of the sample space. The helium gas flow is controlled using a set of valves together with a pump (typically an oil free scroll pump). It should be noted that modern SQUIDs that operate using liquid helium can measure the magnetic moment in a temperature ranging from about 1.6 up to 400 K. However, temperatures down to mK and up to 800+ K can be achieved using helium-3 and furnace probe, respectively (Fagaly, 2006). An air-lock system prevents any air sneaking into the system during the removal and insertion of a sample, otherwise nitrogen and oxygen will be immediately crystallized inside the liquid helium causing serious problems. Despite the fact that SQUID cryostats have one or more vacuum layers to prevent heat exchange with the surrounding, still there is constant helium evaporation, hence there is a need for regular liquid helium refills. To solve this issue, some cryostats are equipped with a recondensing system, which utilizes a cryocooler together with a condensing loop immersed in a main liquid helium reservoir (See Fig. 2.6b).

A SQUID ring is typically located inside a niobium can to prevent penetration of any background magnetic fields. A sample is hung to a sample probe and the probe is moved up and down (typically in the range of several centimeters) using a stepper or linear motor. The whole SQUID magnetometer system usually consists of a cryostat, an electronic rack, and a computer with software. An electronic rack contains several units such as gas handling, data acquisition, magnet power supply, filtering, and temperature control. A Mu-metal layer (See Fig. 2.6b) shields the interior of a cryostat from external magnetic fields (Fagaly, 2006; Clarke et al., 2003).

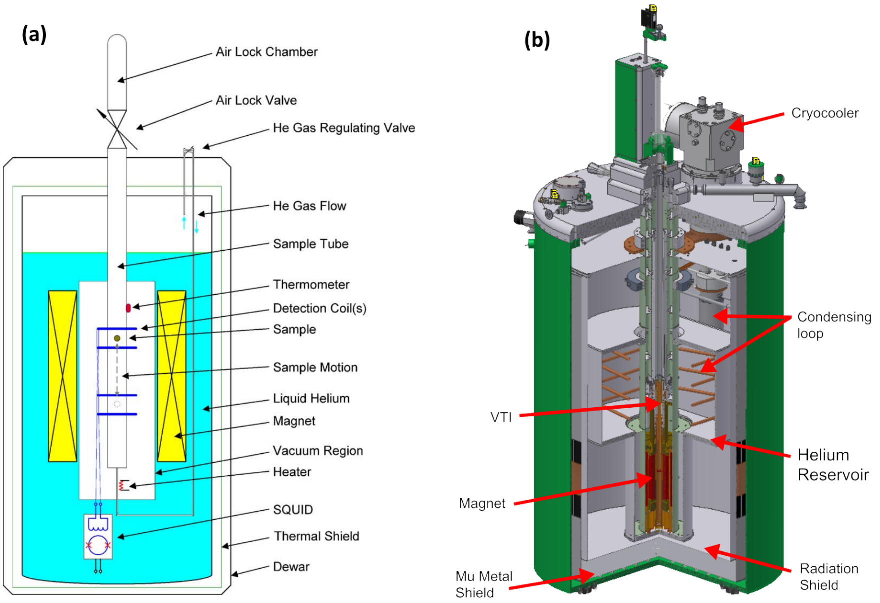

Figure 2.6: (a) Schematic diagram of a typical SQUID magnetometer cryostat. Adopted from Fagaly (2006). (b) Cross section of "Cryogenics S700XR" SQUID magnetometer. VTI stands for variable temperature insert and is basically a sample space. From the manual of "Cryogenics S700XR" SQUID magnetometer.

2.2.3 Magnetic measurement details

There are several sample mounting methods utilized for magnetic measurements using a SQUID magnetometer, though the most popular are straw and copper wire. A sample can be fixed inside a straw using Kapton tape. In the case of powders, a gelatine capsule can be utilized together with straw. For samples that do not fit inside a straw, a copper wire together with Kapton tape of PTFE can be used. Contrary to the big size samples, tiny samples can be glued to a copper wire using superglue. Regardless of the chosen method, it is important to understand that any material to some extent is magnetic and an experimentator should estimate whether the contribution of a sample holder (e.g., capsule, Kapton tape, superglue) is substantial or can be neglected. For example, ferromagnetic (FM) bulk materials will produce such a strong magnetic moment that any paramagnetic/diamagnetic (PM/DM) contribution from a straw or Kapton tape can be easily neglected, whereas the magnetic moment of, for example, carbon-based materials can be comparable to that of the sample holders. One should also consider demagnetization fields, which depend on the shape of a sample, when processing raw data. As for sample limitations, basically any solid state sample can be measured, with the only constraint being its size. Except for an obviously limited diameter of a sample space, the big size of a sample can mean too strong a magnetic moment which may exceed the SQUID's maximum value of the magnetic moment it can detect. Moreover, too strong a magnetic moment may cause the detachment of a sample from a sample holder and harm to a system. Commonly, samples are not bigger than $\approx$ 6–8 mm in one of the dimensions used with SQUIDs. The precise centering of a sample inside a detection coil is another crucial factor that determines the true value of the magnetic moment. Sawicki et al. (2011) have provided a comprehensive list of possible artifacts and pitfalls one may encounter when working with a SQUID magnetometer. It should be noted that a “Cryogenic S700XR” rf/dc SQUID magnetometer was used in the present research. This model allows magnetic measurements in the temperature range of 1.6–400 K and in a magnetic field up to 7 T.

3 Transport and magnetotransport measurement techniques

3.1 Resistivity measurement techniques

In physics, the transport properties of a material are one of the core parameters because they tell us about the nature of chemical bonding and the electronic structure of a material. Based on the resistivity values, we classify materials as metals, semiconductors, or insulators, and knowing resistivity values, one can estimate the charge carrier density and mobility of them, type of conductivity, lifetime of charge carriers, etc. The resistivity of a material depends on temperature, doping level, various environmental parameters, magnetic field, mechanical stresses, etc.

There are various methods of measuring the transport and magnetotransport properties of a material, though the most common are two-/four-probe, four-point probe (Valdes, 1954), Van der Pauw (Philips' Gloeilampenfabrieken, 1958), and the Montgomery method (Montgomery, 1971). When choosing a measurement method, one should consider the following sample parameters: dimensions and dimensionality, degree of resistivity, chemical composition, homogeneity, surface roughness, etc. Nowadays, some of the aforementioned methods are so advanced that one can measure the transport properties of even nanoobjects (Ru et al., 2010).

3.1.1 Two-probe method

This method is suitable for a sample with high resistivity. A sample is connected to a power supply and resistivity is calculated from the voltage drop, current, and dimensions of the sample:

$$\rho = \frac{VA}{IL}, \tag{3.1}$$

where V is the voltage, A is the cross sectional area, I is the current, L is the length between the probes (See Fig. 3.1a). In this method, one pair of connectors (probes) acts as both the source and voltage probes.

3.1.2 Four-probe method

For low resistive samples, one may prefer a slightly different variant of the two-probe method, with two additional probes, which are voltage probes (See Fig. 3.1b). The working principle and equation for resistivity are the same (See Eq. 3.1), the only difference is that the length is now measured between the voltage probes, not the source probes. It also should be noted that if the voltage probes are finite size contacts, then the distance between the two probes is measured not from the edges, but from the center of them. The advantage of this method over the two-probe method is that the resistivity of source connectors and wires is not added to the sample resistance, hence, one can measure low

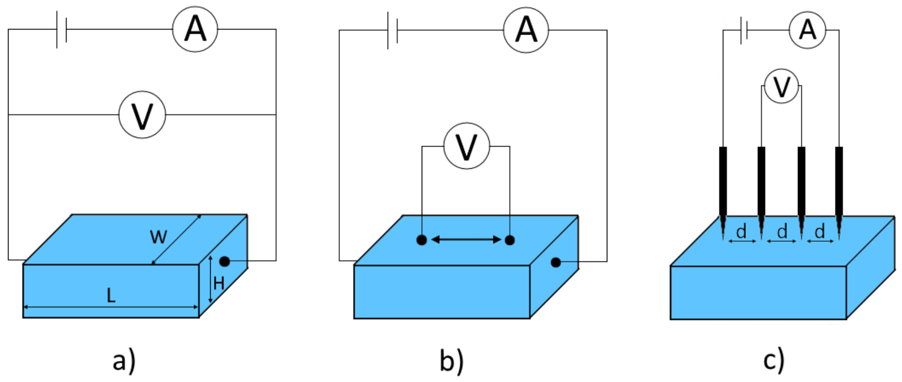

Figure 3.1: Resistivity measurement methods: (a) two-probe, (b) four-probe, (c) four-point probe.

resistive materials with higher accuracy. Note that there are some requirements for this method such as the absence of sample surface leakage, the size of voltage probe contacts and their geometrical arrangement, and the homogeneous resistivity along the sample. By adding a second pair of voltage probes and aligning them parallelly to each other, one can measure the Hall voltage under an applied magnetic field normal to the current plane.

3.1.3 Four-point probe method

This technique utilizes four collinear point probes, equally separated by distance, d (Valdes, 1954). The working principle is the same – the current is applied via outer source probes and the voltage is measured via the inner voltage probes. Commonly, probes are needle-like shaped with a sharp hemispherical tip, making this method applicable for extremely small samples. However, a resistivity calculation based on resistance values obtained using this method is somewhat challenging. Depending on the geometry and position of the probes, the dimensionality and dimensions of the sample, the current paths are different and hence the ρ/R ratio. For 2D infinite thin films or coatings, resistivity can be calculated as follows (Miccoli et al., 2015):

$$\rho = \frac{V}{I}\frac{\pi t}{\ln 2}, \tag{3.2}$$

where t is the thickness of a film; whereas for a 3D semi-infinite sample, this is

$$\rho = \frac{2\pi d V}{I}. \tag{3.3}$$

For a finite-size sample, a correction factor should be taken into account that depends on the dimensions of the sample, position of the probes, and the length between them (Miccoli et al., 2015). As an example, the resistivity of semiconductor wafers is measured using this method.

Another variation of the four-point probe method is the Van der Pauw method (Miccoli et al., 2015). In contrast to the former method, the probe arrangement of the latter is around the perimeter of the sample, allowing measurement of the average resistivity of the sample and of the Hall voltage.

3.2 Pulse magnetic field setup

Magnetotransport measurements in strong magnetic fields have been an important branch of experimental science in recent decades due to the discovery of a variety of phenomena such as the Hall effect, anomalous or quantum Hall effects (Nagaosa et al., 2010; Cage et al., 2012), giant magnetoresistance (Tsymbal and Pettifor, 2001), Shubnikov-de Haas oscillations (Lifshits and Kosevich, 1958), and weak localization effect (Hikami et al., 1980).

To measure (magneto-)transport properties and to observe and analyze related effects in a wide range of materials, a pulse magnetic field setup (PMFS) has been designed, constructed, tested and optimized by M.A. Shakhov, Ioffe Physical-Technical Institute (hardware) and M.O. Safontchik, Ioffe Physical-Technical Institute (software). Semiconductors, semimetals, superconductors, heterostructures, fullerenes and magnetic semiconductors are the few examples of materials that can be measured using this setup. A variety of scientific articles has been published based on the PMFS measurement data (Guc et al., 2017; Lähderanta et al., 2016, 2019, 2018; Hajdeu-Chicarosh et al., 2018).

3.2.1 Structure of the setup

The measurement technique of this setup is based on the four-probe method with one pair of current probes and two pairs of voltage probes. The setup consists of a solenoid, a capacitor bank with a thyristor discharge circuit, a cryostat with a sample holder, a vacuum management apparatus with two pumps, and electronics. The schematic diagram of the PMFS is presented in Fig. 3.2. The electronics are controlled using programs developed using "LabVIEW" software. A pulsed magnetic field is generated by discharging the capacitor bank through a multiturn normal state solenoid. There is a possibility to switch the polarity of the magnetic field. The sample space can be sealed and pumped to reach lower than cryogenic liquid (nitrogen or helium) temperatures. The cryostat is filled with liquid nitrogen to cool the solenoid after each pulse shot. During pulses, output signals (e.g., voltage between voltage probes) are measured and converted through four independent measurement channels of an analog-to-digital converter (ADC, 16 bit) with a conversion time of about 1 μs, and then the signals are recorded to a 4×256 kB cache memory.

The measurement data from the PMFS is obtained in the form of separate pulses or, in other words, shots ($U(B)$) at a specific temperature, maximum value of a magnetic field, and a polarity of both magnetic field and current. To measure the full dependence of resistance on a magnetic field (let us say up to 20 T), an operator should make several pulses with a gradual increase of a maximum value of a magnetic field (e.g., B_{max} = 0.5, 1, 2, 5, 10, 20 T). Magnetoresistance and/or Hall voltage curves are then obtained by combining multiple pulses with different magnetic field amplitudes and polarities. There is also a possibility to measure thermoresistive curves ($R(T)$). A list of the main technical parameters of the PMFS is presented below:

- Temperature range: 1.6–310 K using liquid helium and 50–310 K using liquid nitrogen.
- Magnetic field: up to 45 T.
- Pulse duration: $\approx$ 12 ms.
- Current source (constant or pulsed): 1 μA – 200 mA.
- Sensitivity limited noise: $\approx$ 5 μV.
- Cooling time of the solenoid after, e.g., a 30 T pulse: $\approx$ 30 minutes.
- Volume of the sample space in the form of a partial cylinder: $\approx$ 0.15 cm^3.

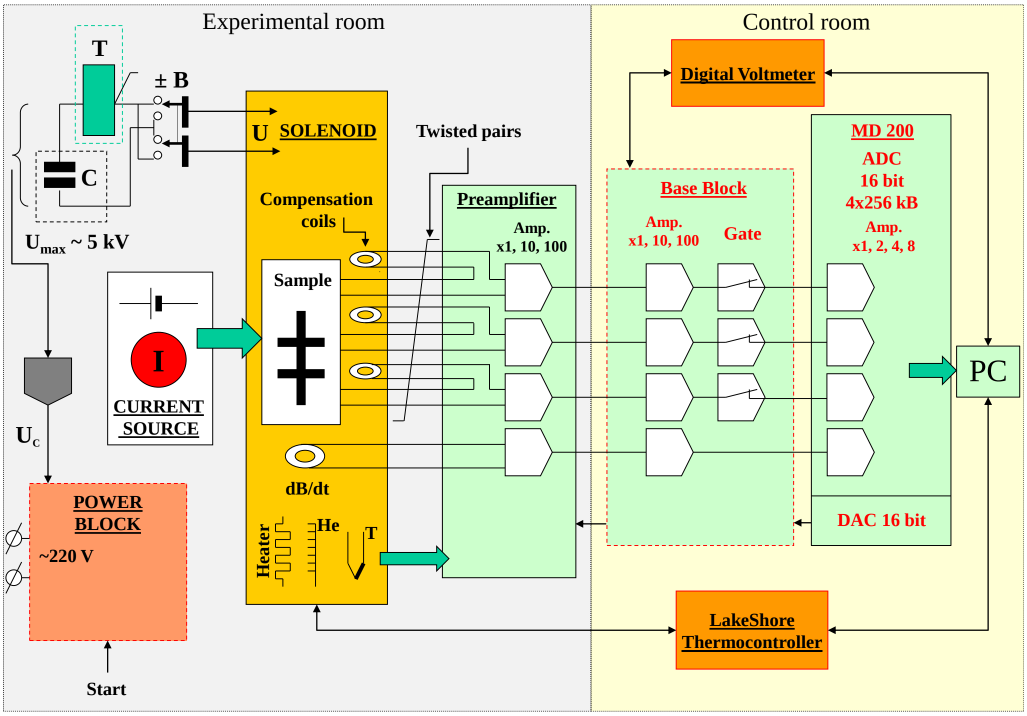

Figure 3.2: Schematic diagram of the pulse magnetic field setup.

The Capacitor bank, thyristors, cryostat, sample holder with preamplifier, vacuum management system, pumps, and all other related components are located in a separate experimental room, which has a Faraday cage shielding. The door to the experimental room is equipped with a limit switch (which shuts off a high voltage) to prevent the entrance of an operator during the capacitors charging or pulsing. All the electronics (thermocontroller, current source, digital multimeters, high voltage block, base block, PC) are located in the adjacent control room. Furthermore, all electrical systems are grounded and high voltage circuits have a galvanic isolation.

3.2.2 Sample preparation and insertion

Samples of different configurations can be measured using the PMFS such as 2D thin films on a substrate or 3D samples of various geometries. However, there are two limitations for the sample when considering measurements using the PMFS: dimensions and resistance. The resistance of the sample should be in the range of 0.01 Ω – 100 kΩ. The possible dimension configurations of the sample are (mm): 5.3×1, 4.4×1.5, 4×1.7, 2.9×2, etc. The minimum size of the sample is limited by the necessity to attach or solder six finite-size contacts: one pair of current contacts and two pairs of voltage contacts. Schematic diagrams of contact arrangement for 2D and 3D samples are presented in Fig. 3.3. The current is supplied using contacts 1-2. The longitudinal resistivity of the sample is recorded using contacts 3-5/4-6, and the transverse Hall voltage is measured using 3-4/5-6.

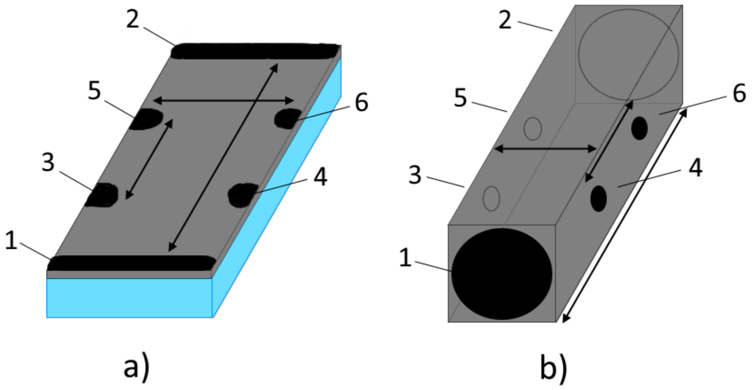

Figure 3.3: Visualization of contact arrangement for (a) 2D and (b) 3D sample. The black strips and dots are the contacts. Contacts 1-2 are the current contacts, while others are the voltage contacts.

Typically, sample contacts are made out of either indium or tin-lead solder, though one should not be restricted to only these. Indium contacts are attached to the sample using so-called cold soldering, which means that indium is smeared and rubbed on a sample surface until it is firmly stuck to it, whereas tin-lead contacts are soldered using a heat soldering. Following this, copper wires are either attached or soldered to the contacts. The core diameter of the copper wires that are typically used is either 0.03 or 0.06 mm, depending on the resistance of the sample. Three twisted pairs of the copper wires are intertwined together for a reduction of a electromagnetic interference. The sample with the connected wires is then placed in a sample holder and fixed in the desired orientation using molten wax. The sample holder is a long tube that goes all the way down to the level of the solenoid. A lower part of the sample holder (where the sample is located) consists of two thermometers, a compensation coil, a detection coil to measure the value of the magnetic field, a coil heater, and a liquid helium level gauge. The sample space is made by cutting part of the sample holder tube. A thermal shielding is installed above the sample space. A preamplifier is connected to an upper part of the sample holder (which is located in a room-temperature region) and is required for switching and preamplification of input signals and rough/fine manual compensation of electromagnetic interference generated by the magnetic field pulse (dB/dt).

The opportunity to rotate a sample inside the sample holder allows measurements of anisotropy of magnetotransport properties. A sample plane can be oriented parallel (in-plane) or perpendicular (out-of-plane) to a magnetic field, B. In the in-plane orientation, the sample can be oriented so that a current direction is parallel or perpendicular to the magnetic field B. In total, three orientations of a sample relative to a magnetic field typically are utilized, and as previously mentioned, an operator can also manually switch the polarity of a magnetic field and current. Since the sample space is made in the form of a partial cylinder with a length of 1.2 cm, a 0.35 cm radius and a 0.25 cm height, the in-plane (in contrast to out-of-plane) orientation allows the measurement of a bigger sample. It should be noted that the Hall effect measurements are possible only in the out-of-plane orientation, when a magnetic field is oriented normal to a current flow direction and a sample plane.

3.2.3 Sample temperature control

The temperature of the sample is monitored using two thermometers that are positioned in close proximity to the sample: a Cernox® thin-film resistance temperature detector and a differential thermometer. Data from the thermometers are then read by a "LakeShore 332" thermocontroller. The thermocontroller also controls the temperature of the sample using a heating element that consists of two coils wound around the sample holder above and below the sample. The thermocontroller's proportional-integral-derivative (PID) parameters can be adjusted automatically or manually. The temperature of the sample is also controlled by changing the degree of vacuum (by means of a rotary pump, "Edwards Vacuum RV5") inside the vacuum layer of the cryostat. There is also a possibility to pour either liquid nitrogen or helium into the sample holder to reach cryogenic temperatures. Moreover, when the sample space is filled with liquid nitrogen, an operator can lower the temperature of the liquid nitrogen (and, hence, of the sample) down to $\approx$ 50 K by means of vacuum vapor pumping (using the second rotary pump of the same model). During the vacuum vapor pumping, an operator has the possibility to maintain an intermediate temperature (between 50 and 77 K) for some time (until liquid nitrogen is evaporated) using a manostat and a set of valves. The same vacuum vapor pumping method is valid for the case of liquid helium poured inside the sample holder. With liquid helium, temperatures down to $\approx$ 1.6 K can be achieved, as well as some intermediate temperatures. An operator should be able to find and maintain a balanced interplay between cooling from the cryogenic liquids and heating from the coil heater. It should be noted that during the vacuum vapor pumping, apart from the two thermometers next to the sample, there is also a vacuum gauge installed in the vacuum management system to measure the pressure of the cryogenic liquid vapors, the measurement values of which can be used to calculate the temperature of the cryogenic liquids and hence of the sample.

3.2.4 Current source

An autonomous current source with high output impedance was designed especially for PMFS. Pulsed or constant current in the range of 1 μA – 200 mA can be set to work in either “+” or “–” polarity. Pulse duration parameters are programmable.

3.2.5 Solenoid

The pulse solenoid is a handmade multiturn coil wound with flat copper wire encapsulated with an epoxy compound. A uni-directional glass banding tape was used for outer banding of the solenoid. To prevent destruction of the solenoid due to huge heat dissipation and thermal shocks during pulses, the solenoid is constantly cooled with liquid nitrogen. After each pulse, there is a cooling period when it is prohibited to shoot the next pulse, and the cooling period time depends on the maximum magnitude of a magnetic field of the previous pulse. For example, after 30 T pulse, an operator should wait $\approx$ 30 minutes. It should be noted that short-time pulses from a normal state magnet allow investigation of time dependencies and relaxation effects that, in principle, is not possible with superconducting magnets. The main technical parameters of the solenoid are listed below:

- capacitance: 6 mF,
- maximum voltage: $\approx$ 5 kV,
- inner diameter: 1.2 cm,
- inductance: 2.377 mH,
- coil resistance: = 0.08305 Ω,
- maximum current: $\approx$ 6.5 kA,
- axial non-linearity at 5 mm from the center of the solenoid: –0.37%,
- radial non-linearity at 7 mm from the center of the solenoid: 0.09%.

Charging of the capacitor bank and its voltage monitoring is done using the high voltage block located in the control room. Two digital multimeters are installed in the high voltage block to show the voltage values in two independent sections of the capacitor bank.

3.2.6 Software

All the programs were written using the “LabVIEW” software. The main program (See Fig. 3.4) shows the results of all the recorded pulses from a chosen folder (a separate folder for each measurement temperature) from one of the three measurement channels and for specific configurations of the current and magnetic field polarities. All the pulses ($U(B)$) with different values of a maximum magnetic field are displayed in one common graph (See Fig. 3.4). Each pulse consists of two curves that are induced by the increase and decrease of the magnetic field (over $\approx$ 12 ms time period), and then they are programmably added to each other creating a single curve of $U(B)$ dependence (See Fig. 3.5b). However, the presence of a magnetic hysteresis or(and) sample heating due to eddy currents can cause divergence of the $U(B)$ curve when adding two parts of it. In order to differentiate the longitudinal resistance or the Hall voltage, which are presented in the different quadrants of the $U(B)$ dependence, from the total signal, magnetoresistance measurements are conducted in both polarities of the magnetic field (See Fig. 3.5c).

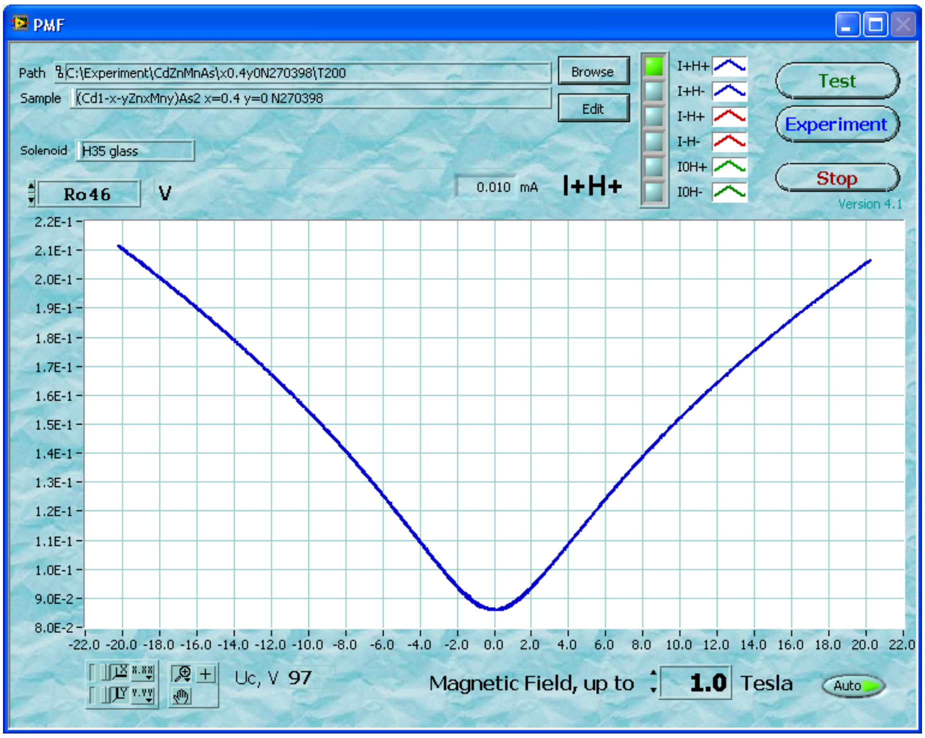

Path C:\Experiment\CdZnMnAs\x0.4y0N270398\T200
Sample (Cd1-x-yZnxMny)As2 x=0.4 y=0 N270398
Solenoid H35 glass
Ro46 V
0.010 mA
Uc, V 97
Magnetic Field, up to 1.0 Tesla

Figure 3.4: The main program of the PMFS, where one can see the magnetic field dependence of voltage between contacts 4 and 6 at a specific temperature. Note the presence of data for both magnetic field polarities. Even though the curve appears continuous, in reality it consists of several separate pulses with different values of the maximum magnetic field.

In the sample parameters editor (“Edit” button) an operator specifies:

- Name of the sample, its description, and any other comments.
- Dimensions of the sample, such as length between current contacts, width of the sample and height of the current path (which in most cases is the thickness of the sample).
- Distances between the center of the probe contacts along (contacts 3-5/4-6) and across (3-4/5-6) the current direction (See Fig. 3.3).
- Configuration of the three measurement channels. A typical configuration is two longitudinal resistivity, meaning $\rho(B)$ (contacts 3-5 and 4-6) and one Hall voltage (either 3-4 or 5-6), though other configurations are used as well. In case of a loss of a voltage probe, e.g., due to mechanical and/or thermal shocks, an operator can change the configurations of the measurement channels. It is also possible to conduct measurements between sidelong contacts (3-6/4-5).

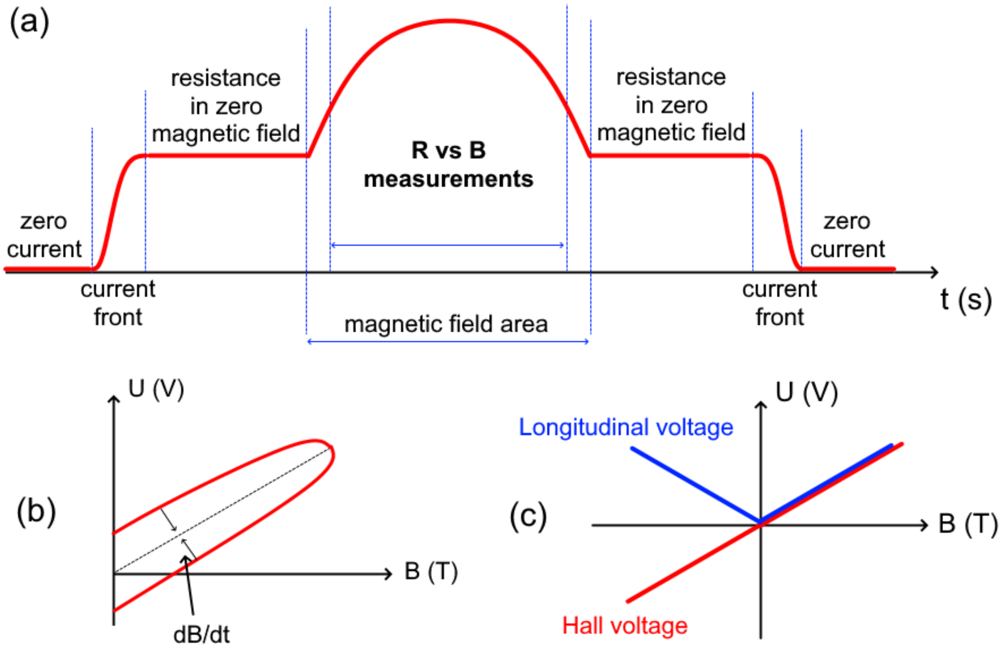

Figure 3.5: (a) A simplified cyclogram of pulsed magnetoresistance measurements; (b) An ideal magnetic field dependence of voltage. The dB/dt correction function converge $B\uparrow$ and $B\downarrow$ curves leading to one curve (the black dashed line); (c) Difference between longitudinal resistance and Hall voltage.

In the test window (See Fig. 3.6), before shooting, an operator can adjust the level of amplification of the voltage measurement channels, which is the sum of preamplification (×1/10/100), base amplification (×1/10/100), and ADC amplification (×1/2/4/8). The same “test” window (See Fig. 3.6) appears after each pulse and one can preview the raw data of a pulse from all four channels. The first channel shows the magnetic field derivative, while the other three are the measurement channels, which are set in the sample parameter editor. Depending on the channel, one can see the cyclogram of either voltage, current or magnetic field, with the time range being ≈ 12 ms. A typical cyclogram consists of several physical switching points (See Fig. 3.5a), and the pulsed current and magnetic field are switched on/off at different times. It should be noted that the pulsed current is not switched on/off in a steplike behavior, rather it has a front period that takes several milliseconds. When the current has reached its value, prior to switching on the magnetic field, resistance values in the zero magnetic field are recorded. The actual resistance versus magnetic field measurements take about 12 milliseconds. Note that Fig. 3.5 depicts a simplified version of the actual cyclogram, meaning some steps, such as compensation fronts, are omitted for simplicity. The time ranges of different steps of the cyclogram can be adjusted manually. As the maximum amplitude of cyclogram voltage is 10 volts, an operator should find a balance between an applied current and an amplification level before shooting a pulse so that the obtained cyclogram will not exceed 10 volts in an amplitude.

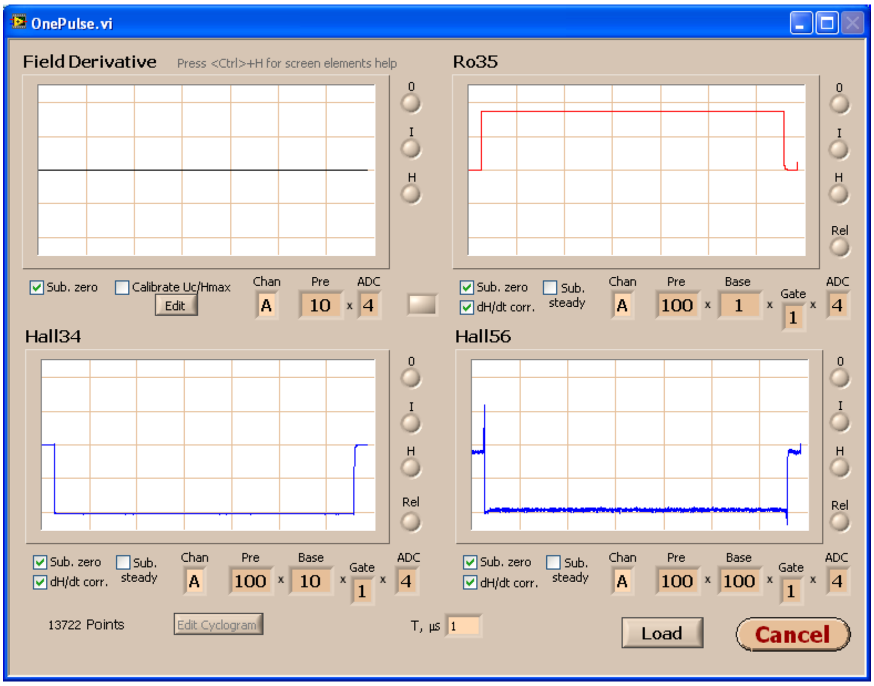

Field Derivative: ☑ Sub. zero ☐ Calibrate Uc/Hmax Chan A Pre 10 x ADC 4

Ro35: ☑ Sub. zero ☑ dH/dt corr. ☐ Sub. steady Chan A Pre 100 x Base 1 x Gate 1 x ADC 4

Hall34: ☑ Sub. zero ☑ dH/dt corr. ☐ Sub. steady Chan A Pre 100 x Base 10 x Gate 1 x ADC 4

Hall56: ☑ Sub. zero ☑ dH/dt corr. ☐ Sub. steady Chan A Pre 100 x Base 100 x Gate 1 x ADC 4

13722 Points

T, µs 1

Figure 3.6: The test window that shows signals from four channels. No magnetic field is applied yet, only a pulsed current. “Ro” means longitudinal resistivity measurement, while “Hall” means the Hall voltage measurements. There is also an “S” option, which means sidelong resistivity measurements (not shown here). The vertical axis is voltage (for “field derivative” channel it is magnetic field), and the horizontal axis is time.

Prior to pressing the “Experiment” button (See Fig. 3.4), which starts the capacitor bank charging, an operator sets a desired value of the maximum magnetic field in the main window. Voltage values (U_c) required to charge the capacitor bank for a certain value of a magnetic field are automatically taken from a file with the calculated $U_c(B_{max})$ dependence. When the capacitor bank is charged, either the program automatically shoots a pulse or an operator does it manually.

Three supplementary programs are used during measurements. The first program visualizes the liquid helium level in the sample holder in the range of 0 to 1. The liquid helium level is gauged by means of a resistance measurement of the SC wire immersed in liquid helium. The second program is used for monitoring various parameters such as capacitors’ voltage, temperatures from two sample thermometers, DAC voltage, helium level gauge voltage, the temperature of the cryogenic liquid calculated based on the pressure values measured using the vacuum gauge. To read all these parameters, a multimeter “Keithley 2100” is used, which allows the measurement of up to 8 independent channels. The third program visualizes the sample temperature from the two thermometers (located in close proximity to a sample).

Processing of raw data from pulses includes the smoothing of curves using regression splines or local polynomial algorithms, and averaging data values over the increase and decrease of a magnetic field, and over polarity of the magnetic field. Physical parameters are also recalculated based on the geometrical parameters of a sample. Processed data is then combined in one final curve using a program that allows the smoothing of curves, the elimination of separate pulses with the different values of the maximum magnetic field, a change of a number of data points on the curve, and a change from linear to logarithmic scale. Hall data can be automatically recalculated from the Hall voltage to the Hall coefficient. Pulses with oscillations (e.g., Shubnikov-de-Haas oscillations) are processed in a separate program that allows signal smoothing (elimination of high-frequency noise), detrending, differentiation, the signal’s peaks search, etc.

Apart from magnetotransport measurements, the dependence of resistivity on the temperature can be measured using the PMFS. To measure the thermoresistive curves, the current source is switched to the constant current mode. When changing from pulse to constant current mode, one should be cautious not to burn the copper wires that connect the sample to the sample holder. The PMFS allow resistance measurements as a function of temperature in three independent channels. An operator can adjust the measurement rate (seconds), relay wait (ms) and the preamplification for each channel. The rate of temperature change can be controlled using the thermocontroller and the cooling from the cryogenic liquids. Output data files contain resistance values from all three channels, and by knowing the geometrical parameters of a sample, one can calculate resistivity values.

Transport and magnetotransport properties of the studied materials in the current dissertation were investigated using the PMFS. These materials include nanogranular metal-insulator composites, namely Co-SiO_2, CoNbTa-SiO_2, Co-$LiNbO_3$, CoFeB-Al_2O_3, CoNbTa-Al_2O_3, CoFeB-$LiNbO_3$, CoFeB-SiO_2, and diluted magnetic semiconductors, namely multilayered ZnO/C thin films. The investigation of the (magneto-)transport properties of the ZnO/C thin films showed unconventional behavior of magnetoresistance at low temperatures. Linear positive magnetoresistance at different temperatures was observed for some of the listed above metal-insulator nanocomposites.

4 Magnetotransport and magnetic properties of ZnO/C heterostructures

As mentioned in the Introduction, the study of dilute magnetic semiconductors (DMS) is one of the prominent areas of material physics science due to the combination of both magnetic and semiconductor properties in these materials. Such a combination would provide an additional way to control conductivity, allowing influence not only on charge carriers but also on their spin, which would give new possibilities in semiconductor technologies. An ideal for practical applications DMS should meet the following major criteria: high Curie temperature ($T_C >$ RT), high magnetic moment, manifestation of anomalous Hall effect, high charge carriers mobility, a possibility to choose between N- and P-doping, and a long spin diffusion length (Coey, 2006). The investigation of diluted magnetic semiconductors have been occurring for several decades leading to the appearance of various classes, though no material has been yet found to meet all the criteria. The biggest problem of most DMSs is low Curie temperature, which usually does not exceed 200 K. As an example, one of the most popular DMSs is GaAs doped with Mn and its Curie temperature is limited to about 180 K (Coey and Chambers, 2008). It is of great importance to develop room-temperature operating spintronics devices for practical and economical reasons, which prompts further study of DMSs (Coey and Chambers, 2008).

A subcategory of DMSs that pursues the same goals is dilute magnetic oxides (DMO). The first DMO was a thin film of TiO_2 doped with 7 at.% of cobalt resulting in a Curie point of 400 K and a magnetic moment of $0.32\mu_B$ per Co^{2+} ion (Matsumoto et al., 2001). Dilute magnetic oxides in the form of thin films and nanoparticles, which consist of semiconducting oxides (e.g., ZnO, TiO_2, SnO_2, CeO_2) doped with a few percentages (typically not higher than 10%) of 3d transition metals (TM) (e.g., V, Co, Fe, Mn, Ni, Cr), have shown high-temperature ferromagnetism (up to 900 K). Coey and Chambers (2008) have presented a comprehensive list of TM-doped diluted magnetic oxides with the main parameters such as a doping percentage, magnetic moment, bandgap, and a Curie temperature. Even though DMOs show high Curie temperatures, most of the other requirements are not met, and moreover, there are still disputes about the nature of the ferromagnetism (Matsumoto et al., 2001). When reporting magnetism in DMOs doped with TM, an author should be cautious due to some technical challenges that can distort the true values of the magnetic parameters of a material. These challenges include an appearance of clusters and secondary phases during a fabrication process, possible contamination, and measurement artefacts (Coey, 2006). As for the magnetic measurements of any DMOs doped with non-magnetic cations, an operator should take into account the possibility of contaminating a sample with magnetic particles, which will greatly affect the obtained data and may lead to the publication of spurious results. Precautions should be taken when using SQUID/VSM magnetometers for magnetic measurements ($m(H, T)$), for example, the elimination of any magnetic instruments throughout the sample handling process such as metallic tweezers and sample holders, and markers, which typically contain magnetic impurities.

ZnO (together with GaN) has been predicted to be one of the most prominent candidates for high-temperature FM in DMOs (Dietl, 2010). Indeed, many ZnO-based compounds doped with TM have shown FM/AFM behavior (Liu et al., 2005). ZnO has a direct bandgap of $E_g \approx 3.3$ eV and exciton binding energy of 60 meV at RT; its crystal structure is either hexagonal (wurtzite) or cubic zinc-blende; and conductivity is typically N-type due to electrons originating from defects. As for the advantages of ZnO (for example, over GaN), it has simple growth technology that reduces the cost of a device based on this semiconductor, and a possibility to fabricate good quality single crystals (Özgür et al., 2005). It has been shown that a large number of vacancy defects in undoped ZnO nanostructures can induce d^0 magnetism (Qi et al., 2017). Undoped thin films of hafnium dioxide have also shown the presence of magnetism (Venkatesan et al., 2004a).

Shortly after the start of doping ZnO with TMs, researchers have discovered that not only TMs can induce magnetism in ZnO – reports started appearing claiming the manifestation of weak RT ferromagnetism in ZnO doped with non-magnetic ions such as copper, carbon or scandium (Buchholz et al., 2005; Pan et al., 2007; Venkatesan et al., 2004b). This discovery has prompted researchers to experiment with different diamagnetic or paramagnetic dopants. As for the carbon dopant, its choice is partly dictated by the manifestation of magnetism in carbon-based systems, with intrinsic defects being one of the proposed explanations of the observed magnetism (Rode et al., 2004; Lehtinen et al., 2004). It has been shown that thin films of ZnO-C deposited by a pulsed-laser deposition technique have $T_C > 400$ K and magnetic moment of (1.5–3)μ_B per carbon with P-type conductivity (Pan et al., 2007). As for the origin of magnetism in ZnO-C systems, there are still disputes and there is no clear understanding of why magnetism appears, hence further investigation of this system is required to shed light on this problem. However, it is undoubtedly true that magnetism of oxides doped with non-magnetic ions depends on structural defects, a fabrication method and a type of conductivity. Currently, there are two main concepts regarding the origin of room-temperature ferromagnetism (RTFM) in ZnO-C. The first concept is based on a hole-mediated p-p coupling interaction near the Fermi level. Carbon atoms reside in oxygen sites of ZnO and introduce holes, thus allowing p-p coupling interaction between the carbon atoms and the holes. A sufficient amount of holes can mediate the spin alignment of carbon atoms, leading to ferromagnetic coupling interaction between them (Wang et al., 2009; Pan et al., 2007). This process is similar to p-d exchange interaction in TM-doped DMS/DMOs (Liu et al., 2005). The second concept is based on the defect-induced d^0 ferromagnetism detected in several pristine oxides such as Cu_2O, SnO_2 and MgO (Liao et al., 2009; Araujo et al., 2010; Hong et al., 2008). Even though quite often ferromagnetism of DMOs can be explained by the described above contaminants, secondary phases and measurements artefacts, these are not general explanations of ferromagnetism in DMOs (Coey, 2005). It seems that oxygen vacancies are somehow responsible for the appearance of the magnetic ordering in DMOs, and annealing in oxygen for several hours significantly reduces the magnetic moment of the DMOs, which supports the idea (Hong et al., 2006). The nature of the defect-induced d^0 ferromagnetism is still unclear, though there are several theories. One of the most prominent theories implies that defects, i.e., delocalized electrons from oxygen vacancies, form an impurity band, and if a density of states is sufficient enough, then the Stoner criterion is fulfilled ($D(E_F)I > 1$), and ferromagnetism appears (Coey, 2019). Other popular theories are discussed in papers by Coey (2005, 2019).

The dependence of magnetic parameters on structural defects and fabrication methods, as well as the absence of a clear explanation of the magnetism in the DMOs have motivated a further study. This chapter summarizes the research results of **Publication 1** and **2** by describing the magnetic and magnetotransport properties of ZnO/C thin-film heterostructures fabricated using an ion-beam sputtering process.

4.1 Sample fabrication and measurement details

In this present study, an ion-beam sputtering technique was used to fabricate $(\text{ZnO/C})_{25}$ and $(\text{ZnO/C})_{81}$ multilayered thin films. The numbers "25" and "81" indicate the number of bilayers sputtered on a substrate. Knowing the thickness of the whole film and the number of bilayers, one can easily calculate the thickness of one bilayer. The targets of ZnO and C were sputtered layer-by-layer onto (100)Si or pyroceramics substrate in an argon atmosphere with a purity of 99.998% and at a pressure of 7×10^{-4} torr. During the whole sputtering process, which lasted 3h 12min for $(\text{ZnO/C})_{25}$ and 5h 50min for $(\text{ZnO/C})_{81}$, the surface temperature did not deviate from the room temperature by more than 2 °C. To implement the layer-by-layer sputtering process, a substrate holder was rotated from one target to another at a rotational speed of 0.13 rpm and 0.23 rpm for $(\text{ZnO/C})_{25}$ and $(\text{ZnO/C})_{81}$, respectively. A V-shaped screen, which was located between the targets and the substrate holder, was used to vary the thickness of the carbon interlayer. In total, 150 thin films were fabricated with the film thickness (h) varied from 35 to 169 nm, which was measured using an optical interferometer "MII-4". A more detailed description of the fabrication process can be found in **Publication 1**.

A focused ion beam system ("Hitachi FB2100") was used to prepare cross-sectional lamellae of the fabricated thin films. To investigate elemental composition, a scanning electron microscope ("Oxford INCA Energy 250" with an energy dispersive X-ray add-on device "JEOL JSM-6380LV") was used. An X-ray diffraction method ("Bruker D2 Phaser diffractometer", λCuKα1 = 1.54 Å) and a transmission electron microscope ("Hitachi HT7700", V = 100 kV [W source]) were used to investigate the structure of the samples. Measurements of electrical resistivity were conducted using a digital multimeter "B7-78/1" (two-probe method) and the PMFS (four-probe method). Magnetoresistance curves (MR = $(R_B - R_0)/R_0 \times 100\%$) in a magnetic field ($B$) up to 25 T were obtained using the PMFS. During the magnetoresistance measurements, an applied direct current in the range of 4 μA – 100 μA was used depending on the sample. Seebeck effect measurements (thermopower) were done using a differential method with errors not exceeding 3%, where cold and hot ends were made out of silver with a purity of 99.99%. "Cryogenic S700XR" SQUID magnetometer was used to conduct in-plane magnetic measurements ($m(B, T)$). During the magnetic measurements, the samples were fixed in a straw using

Kapton tape.

4.2 Results and discussion

The X-ray diffraction (XRD) spectra indicate that carbon and zinc oxide layers are amorphous and crystalline (hexagonal, with P63mc space group [Zhilova et al., 2017]), respectively (See Fig. 4.1c). The XRD pattern of $(ZnO/C)_{81}$ thin film indicates a texture with $\langle 001 \rangle$ axis perpendicular to a substrate. However, the small-angle XRD spectra of the $(ZnO/C)_{81}$ films do not show any diffraction peaks (See Fig. 4.1a), indicating an island structure, not a multilayered structure. Since ZnO and C phases are mixed, and $(ZnO/C)_{81}$ is basically a composite with blurred interfaces, we can consider a thickness of the whole film, but not of an individual bilayer ZnO/C. As opposed to the $(ZnO/C)_{81}$ films, the small-angle XRD spectra of $(ZnO/C)_{25}$ films show the presence of diffraction peaks, suggesting the existence of a multilayered structure (See Fig. 4.1b).

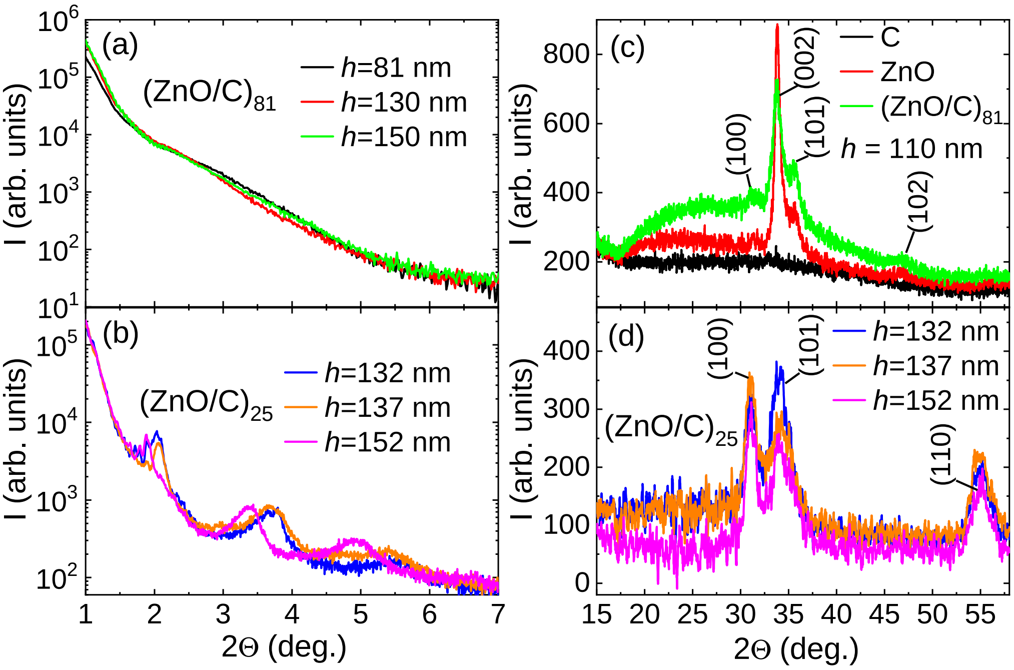

Figure 4.1: (a, b) Small-angle XRD spectra of $(ZnO/C)_{81}$ and $(ZnO/C)_{25}$ films. (c, d) XRD spectra of C, ZnO, $(ZnO/C)_{81}$ and $(ZnO/C)_{25}$ films.

The structure of the studied films was also investigated using TEM microscopy. As can be seen in Fig. 4.2, TEM micrographs verify the nanocrystalline randomly-distributed composite structure of $(ZnO/C)_{81}$ films and the nanocrystalline multilayered structure of $(ZnO/C)_{25}$ films. Electron diffraction patterns show phases of hexagonal ZnO (See inserts of Fig. 4.2).

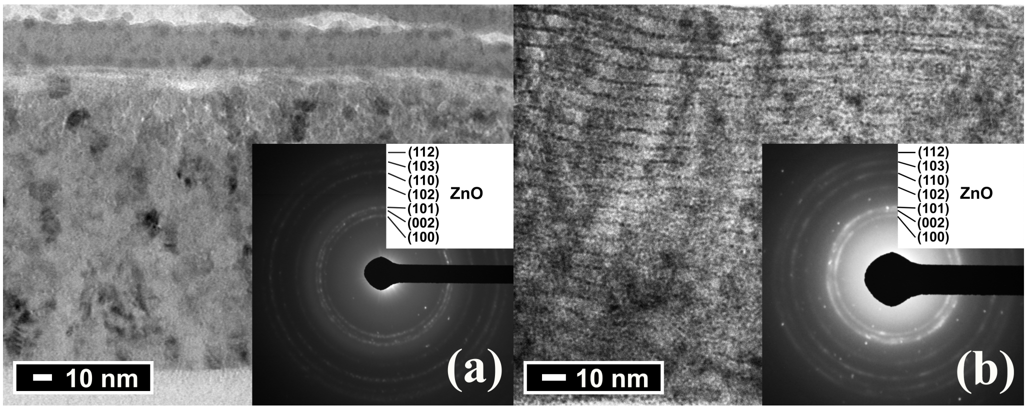

Figure 4.2: TEM images of the obtained cross-sections of samples: (a) $(ZnO/C)_{81}$ with h = 157 nm and (b) $(ZnO/C)_{25}$ with h = 135 nm. The inserts show electron diffraction patterns.

As shown in Fig. 4.3a, the resistivity of $(ZnO/C)_{81}$ films rises with the film thickness decrease. Moreover, the resistivity difference between the $(ZnO/C)_{81}$ samples and undoped ZnO depends on the thickness of the films – at low thicknesses, the resistivity of the $(ZnO/C)_{81}$ films is less by more than two orders of magnitude. This can be explained by an increased number of interfaces and grain boundaries that can act as charge transport channels in wide bandgap semiconductors (Lashkova et al., 2016). In comparison to the $(ZnO/C)_{81}$ films, the resistivity behavior of the $(ZnO/C)_{25}$ films changes only quantitatively (See Fig. 4.3c). In the thickness range of 130–140 nm of the $(ZnO/C)_{25}$ samples, ZnO layers are alternated with the carbon island interlayers, reducing the resistivity of the films with the thickness increase (See Fig. 4.3c). The carbon islands enlarge and start to overlap each other, increasing the concentration of the dangling bonds at the interfaces, and hence reducing the electrical resistivity. Moreover, randomly distributed charges generate a chaotic potential. All of these indicate that strong localization conditions occur at the interfaces with the presence of carbon islands for the $(ZnO/C)_{25}$ samples with h = 130–140 nm (Lashkova et al., 2016). The $(ZnO/C)_{25}$ films with $h > 140$ nm consist of a layered structure of crystalline ZnO and amorphous C, where carbon layers, together with their interfaces, act as conductive channels. With the thickness increase of the $(ZnO/C)_{25}$ films, a transition from strong to weak localization occurs, which changes the conduction mechanism (Nistor et al., 2018). A similar behavior was observed in the multilayered structure $(SnO_2/In_2O_3)_{69}$ (Zhilova et al., 2019). The negative sign of thermoelectric power of $(ZnO/C)_{81}$, $(ZnO/C)_{25}$ and undoped ZnO indicates N-type conductivity (See Fig. 4.3b,d).

The charge transport mechanism was investigated using temperature dependencies of resistivity (thermoresistive curves). As can be seen from Fig. 4.4a,b, the electrical resistivity of all the studied samples increases with a temperature decrease. The same thermoresis-

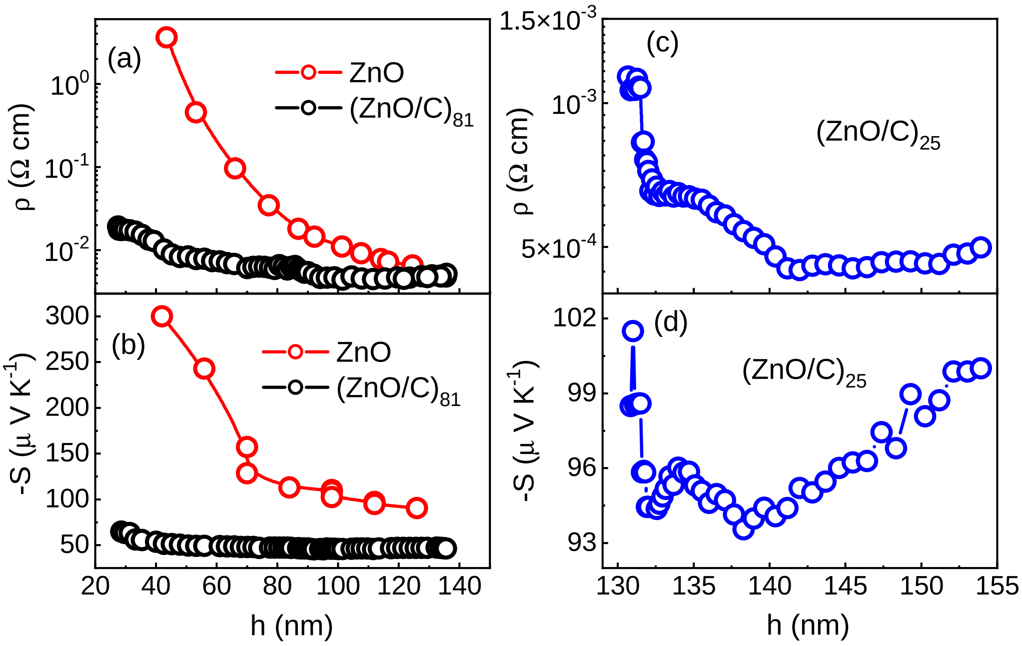

Figure 4.3: Dependencies of room-temperature resistivity on a thickness of the ZnO, $(ZnO/C)_{81}$ (a) and $(ZnO/C)_{25}$ (c) films. Dependencies of room-temperature thermopower on a thickness of the ZnO, $(ZnO/C)_{81}$ (b) and $(ZnO/C)_{25}$ (d) films.

tive curves but in the $\ln \rho/\rho_0 - T^{-1/3}$ coordinates, in the temperature range of 77–170 K, are presented in Fig. 4.4c,d. The linear behavior of the thermoresistive curves in these coordinates suggests a variable range hopping (VRH) mechanism over the localized states in a narrow energy band near the Fermi level (Mott and Davis, 2012). Based on this mechanism, resistivity of 2D systems follows

$$\rho = \rho_0 \exp\left\{ \left(\frac{T_m}{T} \right)^{1/3} \right\}, T_m = \frac{\beta}{k_B g(E_F) a^2}, \tag{4.1}$$

where k_B is the Boltzmann constant, $g(E_F)$ is a density of states at the Fermi level, and a is a localization radius (Mott and Davis, 2012). This is the so-called 2D Mott's VRH mechanism. Using a slope of the curves in Fig. 4.4c,d, one can calculate the value of characteristic temperature (T_m) for different thicknesses of the films. The calculated values of T_m are presented in Table 4.1. The localization radius is taken as the zinc ionic radius, $a \sim 0.8$ Å. The density of states at the Fermi level is then calculated using Eq. 4.1, the values of which are also presented in Table 4.1.

The high-temperature (T = 200–300 K) thermoresistive behavior is described well by a hopping conductivity to the nearest neighbors, the so-called NNH polaron model (Jaime et al., 1996). Based on this mechanism, Arrhenius-type temperature dependence of resis-

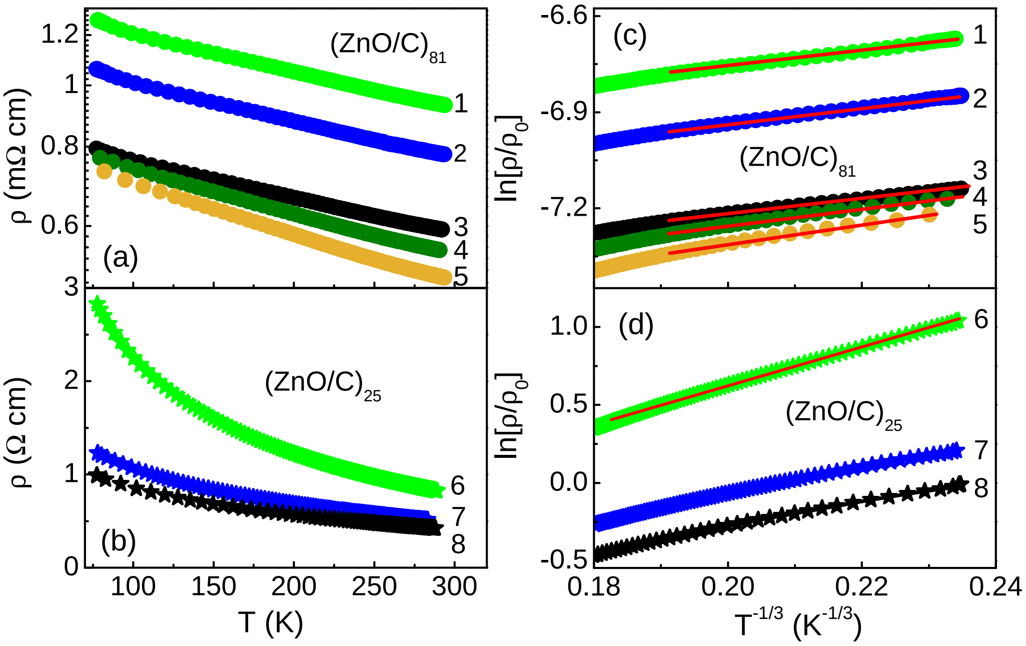

Figure 4.4: Temperature dependencies of electrical resistivity of (ZnO/C)$_{81}$ (a) and (ZnO/C)$_{25}$ (b) films. The same curves, but in the $\ln \rho/\rho_0 - T^{-1/3}$ coordinates, are presented in (c, d). The numbers on the graphs represents various thicknesses (nm): 1–35, 2–45, 3–70, 4–98, 5–129, 6–150, 7–157, 8–169. Red solid lines are linear fits.

Table 4.1: The calculated values of the characteristic temperature (T_m), the DOS at the Fermi level ($g(E_F)_{2D}$) and the hopping activation energy (W_h) as a function of the (ZnO/C)$_{81}$ film thickness.

h (nm)	T_m (K)	$g(E_F)_{2D}$ (eV^{-1}cm^{-2})	W_h (meV)
35	16.77	3.2×10^{17}	6.8
45	16	3.4×10^{17}	6.8
70	11.85	4.6×10^{17}	6.6
98	20.79	2.6×10^{17}	7.6
129	30.66	1.8×10^{17}	8.9

tivity follows

$$\rho = \rho_0 \exp\left(\frac{-W_h}{k_B T}\right), \tag{4.2}$$

where W_h is a hopping activation energy (Mott and Davis, 2012). As shown in Fig. 4.5a, the thermoresistive curves of the (ZnO/C)$_{81}$ films are linear in the $\ln \rho/\rho_0 - 1000/T$ coordinates. The calculated values of a hopping activation energy of the (ZnO/C)$_{81}$ films with different thicknesses are presented in Table 4.1. The thermoresistive curves of the

$(ZnO/C)_{25}$ samples with $h > 150$ nm are linear in the $\rho - \ln T$ coordinates (See Fig. 4.5b), which is typical for weak electron localization in 2D/3D systems (Nistor et al., 2018). Similar behavior of thermoresistance at T = 80–300 K was observed for Ga-doped ZnO films (h = 100–400 nm) fabricated by a radio frequency magnetron sputtering process (Li et al., 2013). The observed resistance of these films with h = 100 and 200 nm decreased with the temperature increase, and the behavior was explained by the weak charge localization. The thermoresistive curve of the film with h = 400 nm has shown the change of resistivity at T = 160 K, with the weak localization effect observed at $T <$ 160 K. Thus, the thermoresistive behavior of $(ZnO/C)_{25}$ samples with $h > 150$ nm can be associated with the weak charge localization effect.

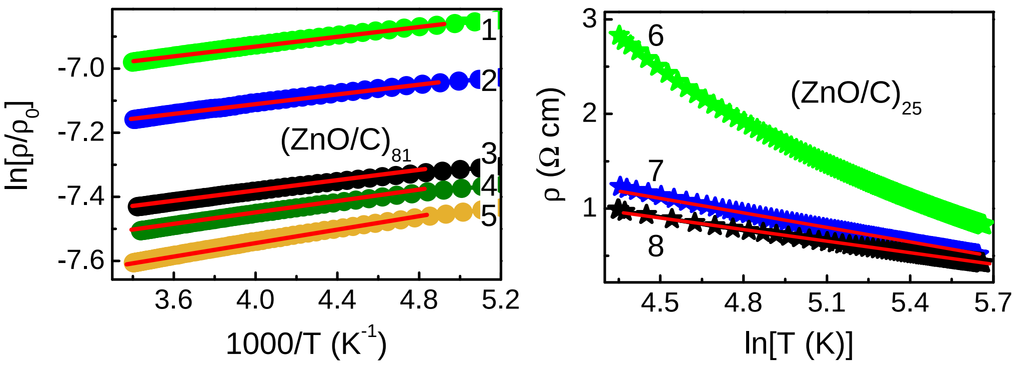

Figure 4.5: (a) Temperature dependencies of electrical resistivity in the coordinates of $\ln \rho/\rho_0 - 1000/T$ of the $(ZnO/C)_{81}$ films with thicknesses (nm): 1–35, 2–45, 3–70, 4–98, 5–129. Red linear lines are theoretically fitted using Eq. 4.2. (b) Temperature dependencies of electrical resistivity in the coordinates of $\rho - \ln T$ of the $(ZnO/C)_{25}$ films with thicknesses (nm): 6–150, 7–157, 8–169. Red solid lines are linear fits.

Two samples of the $(ZnO/C)_{25}$ series with h = 146 and 153 nm were separately investigated using the PMFS and the SQUID magnetometer (**Publication 2**). The thermoresistive curves were measured in the temperature range of 15–300 K, while the in-plane and out-of-plane magnetoresistance curves in a magnetic field (B) up to 25 T were recorded at different temperatures, ranging from 15 to 300 K.

The thermoresistive curves of both $(ZnO/C)_{25}$ samples with h = 146 and 153 nm are well described by the 2D Mott's VRH at $T \lesssim 100$ K (See Fig. 4.6b). This agrees with the results of **Publication 1** and indicates low conductivity of carbon at low temperatures and a high concentration of interface defects, leading to an increased charge carrier concentration when compared to individual ZnO and C. It should be noted that by using the term interfaces this not only means interfaces themselves but also adjacent carbon layers since the thickness of the carbon layers is less than 1 nm (See Fig. 4.2b). The density of states of the studied samples can be calculated using Eq. 4.1. The localization radius, a, is taken as the Bohr radius, meaning $a = (4\pi\hbar^2\epsilon\epsilon_0)/(m_{eff}e^2)$, where for ZnO, ϵ = 7.8 and electron effective mass $m_{eff} = 0.24m_e$ (Meyer et al., 2004), therefore a = 1.73 nm.

For a rectangular shape of DOS, β = 13.8 (Shklovskii and Efros, 2013). A characteristic temperature was estimated from the slopes of the curves in Fig. 4.6b: T_m = 1405 and 779 K for h = 153 and 146 nm, respectively. The calculated values of DOS are $g(E_F)$ = 3.7×10^{15} and 6.9×10^{15} eV^{-1}cm^{-2} for h = 153 and 146 nm, respectively, which is around two orders of magnitude smaller than that of the composite samples (ZnO/C)$_{81}$ (with randomly distributed ZnO and C). The difference in the values of DOS is attributed to the differences in microstructure and the thickness of the samples (ZnO/C)$_{25}$ and (ZnO/C)$_{81}$. Moreover, for the samples (ZnO/C)$_{25}$, the localization radius was estimated as for ZnO, whereas for the samples (ZnO/C)$_{81}$, it was taken as the Zn ion radius.

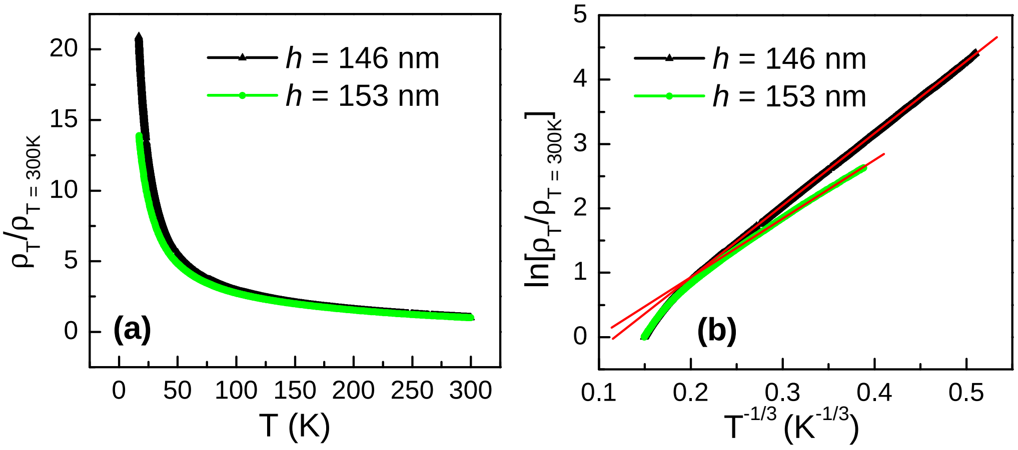

Figure 4.6: Temperature dependencies of normalized electrical resistivity of the (ZnO/C)$_{25}$ films with h = 146 and 153 nm in the coordinates of (a) $\rho/\rho_{300K} - T$ and (b) $\ln \rho/\rho_{300K} - T^{-1/3}$. The red solid lines are linear fits.

Both the out-of-plane and in-plane magnetoresistance of the (ZnO/C)$_{25}$ sample with h = 153 nm shows unexpected behavior at T = 15–20 K: it is negative in low magnetic fields, positive in moderate fields, and negative again in high fields (See Fig. 4.7). At higher temperatures (50 K $\leqslant T \leqslant$ 65 K), a change of the magnetoresistance sign takes place only once from negative, which goes up to ~3–8 T, to positive, which persists up to the maximum measured magnetic field. At $T \geqslant$ 80 K, magnetoresistance is negative throughout the magnetic field range, increases with the field increase, and does not show signatures of saturation. A value of the magnetic field B_{min}, which corresponds to a trough value of negative MR at low-moderate magnetic fields, increases with the temperature increase (T = 15–65 K). The observed positive MR can be explained by the Efros-Shklowskii mechanism, which can be described as a shrinkage of the electron wave functions in the magnetic field. According to this mechanism, positive MR increases following

$$\rho(B) = \rho_0 \exp(constB^n), \tag{4.3}$$

where n is determined by a dimensionality of a sample and by a magnetic field strength (Shklovskii and Efros, 2013). This dependence is associated with the stretching of s-like states in the presence of a magnetic field, leading to a reduction of the wavefunction tails overlap, hampering the hopping of charge carriers between sites. However, it is obvious that this mechanism cannot be responsible for the whole MR behavior of the sample with h = 153 nm.

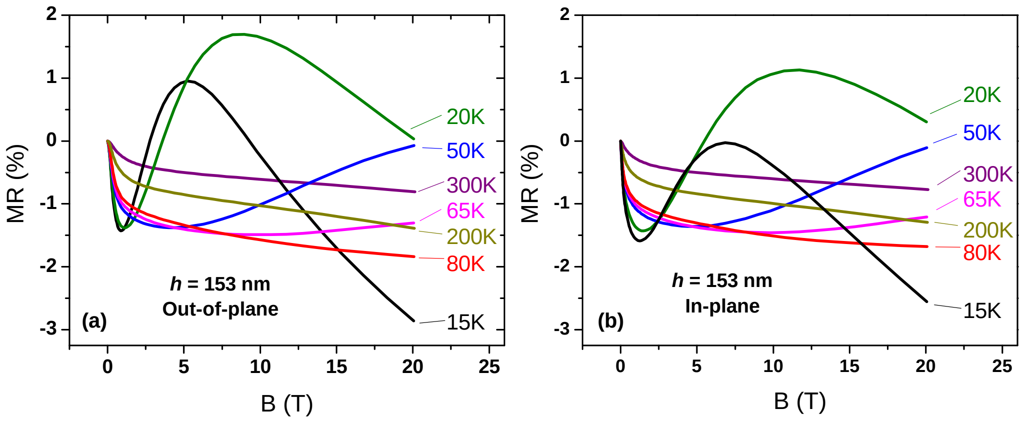

Figure 4.7: Out-of-plane (a) and in-plane (b) magnetoresistance curves of (ZnO/C)$_{25}$ film with h = 153 nm measured at various temperatures.

The MR behavior of the sample with h = 146 nm (See Fig. 4.8) is similar to that with h = 153; however, there are two distinctive features that should be noted. First, the value of negative MR in $B \lesssim$ 1.5 T is the same for both sample orientations, whereas in stronger magnetic fields, this value is higher for the out-of-plane orientation. Secondly, the value of the magnetic field B_{max}, which corresponds to a peak value of positive MR, is higher at T = 20 K than at 15 K and is similar for both orientations.

Based on the results of the MR measurements, it would be reasonable to suggest the existence of two processes responsible for the negative MR and one process for the positive MR. It should be noted that the positive MR weakens with the temperature increase, and at low temperatures it does not exponentially increase with the field as in the case of the Efros-Shklowskii mechanism but rather saturates. Four possible processes can be responsible for the negative MR in low magnetic fields (up to $\sim$1.5 T). The first is the quantum interference, which is a consequence of the weak localization effect (Raikh et al., 1992). This process is characterized by the out-of-plane MR being considerably weaker than the in-plane MR; however, as shown in Fig. 4.8, this is not the case neither in low nor high magnetic fields (Raikh et al., 1992). The second process is the hopping of nonzero orbital momentum states, which is characterized by negative and linear in low magnetic fields MR (Alexandrov et al., 2012), though low-field MR curves of the studied samples are not linear (See Fig. 4.8). The third process is the scattering on the magnetic disorder, which is characterized by a strong magnetization and MR saturation. The results of the magnetic measurements of the (ZnO/C)$_{25}$ samples with h = 146 nm revealed the presence of apparent hysteresis loops at $T \leqslant$ 120 K with an intrinsic coercivity ranging from $\approx$ 310 G at 5 K to $\approx$ 30 G at 120 K (See Fig. 4.9a). As for the temperature dependence of

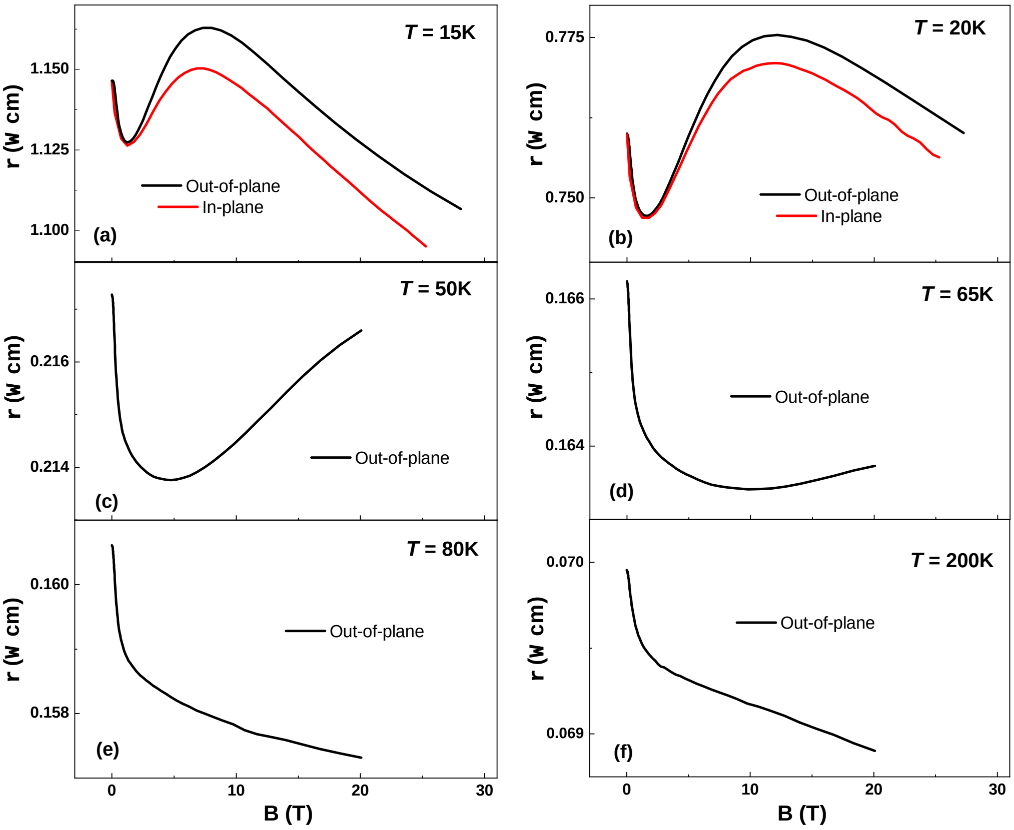

Figure 4.8: Magnetoresistance curves of (ZnO/C)$_{25}$ film with h = 146 nm measured at various temperatures.

magnetization, the zero-field cooled (ZFC) curve drops at low temperatures reaching its trough at $T \approx 20$ K, then starts to rise up to the maximum value at $T \approx 50$ K, and then gradually decreases with the temperature increase up to RT (See Fig. 4.9b). The results of the magnetic measurements indicate the existence of ferromagnetic ordering in the (ZnO/C)$_{25}$ film with h = 146 nm. In this case, an applied magnetic field should diminish moment disorientation, contributing to negative MR. Moreover, in the case of substantial magnetization, B_{max} should depend on a field orientation due to demagnetization fields; however, this dependence is not observed (See Fig. 4.8) and magnetization is relatively weak (See Fig. 4.9). Both the absence of the tendency to MR saturation, even in magnetic fields higher than the saturation field ($B_{sat} \sim 0.1$ T, not shown on the graph) and the weak magnetization, show that this process is definitely not a major process responsible for the low-field negative MR.

The fourth process is an increase of the density of states due to the Fermi level shift under an applied magnetic field. An applied magnetic field reduces the spread of the energy levels, causing narrowing of the impurity band (induced by defects at the interfaces), and as a result, the tail of the DOS becomes steeper (Raikh et al., 1992). The Fermi level is located in the tail of the DOS (according to the Mott's law), though, following from the conservation law of the total number of electrons, under an applied magnetic field the Fermi level is shifted toward the centre of the impurity band by Δg (Raikh et al., 1992):

$$\frac{\Delta\rho}{\rho} = -1/3\frac{\Delta g}{g}. \tag{4.4}$$

Following from Eq. 4.4, MR should be negative and should not depend on temperature. As Fig. 4.10a illustrates, MR remains temperature-independent in $B \lesssim 0.3$ T up to 80 K; however, in $B \gtrsim 0.3$ T, MR curves diverge. This divergence can be caused by an activation of the positive MR. To conclude, the low-field negative MR is mainly determined by the increase of the DOS due to the Fermi level shift under an applied magnetic field.

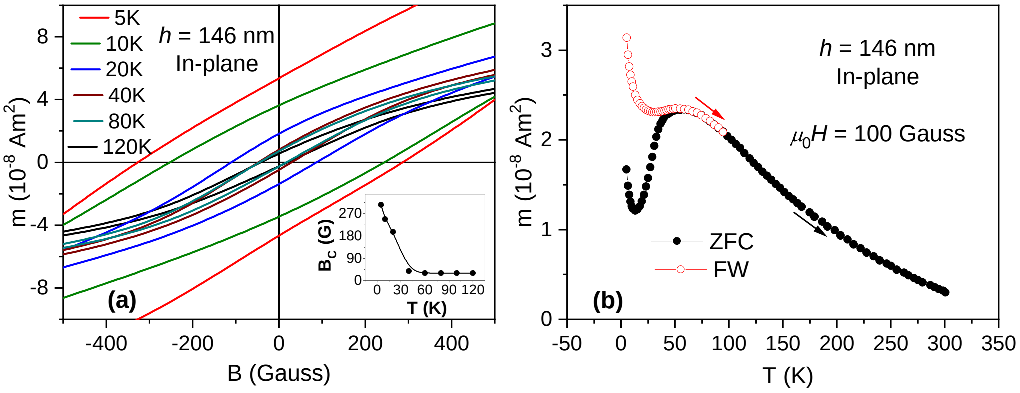

Figure 4.9: Magnetic properties of the (ZnO/C)$_{25}$ film with h = 146 nm. (a) Hysteresis loops measured at T = 5–120 K. The insert shows temperature dependence of intrinsic coercivity. (b) Zero-field cooled (ZFC) and field warming (FW) curves measured in B = 100 G. Note the absence of a field cooling (FC) curve.

The positive MR activates only at low temperatures, leading to the appearance of the trough (B_{min}) and the peak (B_{max}) of MR curves (See Fig. 4.8). In low magnetic fields, the Efros-Shklowskii mechanism is compensated by negative contribution; however, in higher fields, MR increases exponentially following $\rho(B) = \rho_0 \exp\big(constB^{1/3}\big)$ and induces positive contribution to MR (See Fig. 4.10b). It should be noted that MR curves are linear in the $\ln \rho/\rho_0 - B^{1/3}$ coordinates in the relatively narrow range of the magnetic field. Moreover, in-plane MR is weaker than out-of-plane MR, which agrees with the mechanism proposed in Raikh et al. (1992). The exponential growth of MR ceases in higher magnetic fields, as predicted by the Efros-Shklowskii mechanism. Such behavior can be explained by the effect of a magnetic blockade, when a magnetic field polarizes spin of a charge carrier, making it energetically unfavourable for the charge carrier to hop to another spin-polarized state. Such an effect was used to explain MR in granular magnetic films (Inoue and Maekawa, 1996) and in amorphous semiconductors, considering the processes of spin-flip (Movaghar and Schweitzer, 1978) and interatomic electron-electron interaction (Kurobe and Kamimura, 1983). Even though the presence of magnetic moment intensifies the effect, magnetically ordered systems are not the only systems to manifest the effect of the magnetic blockade. In the studied samples, both the magnetic moment and charge carriers are produced by dangling bonds (one electron per a dangling bond) at the interfaces. The hopping of electrons happens only from occupied to empty states and some of the transitions are prohibited by the Pauli principle, which was not taken into account in the Efros-Shklowskii mechanism and hence diminishes the positive contribution to MR. This idea is justified by the calculated MR in the paper Kurobe and Kamimura (1983), where positive contribution weakens in high magnetic fields reaching a peak. For the studied sample, the ferromagnetic ordering at low temperatures enhances the effect of the magnetic blockade because spin polarization decreases the number of sites between which hopping is possible.

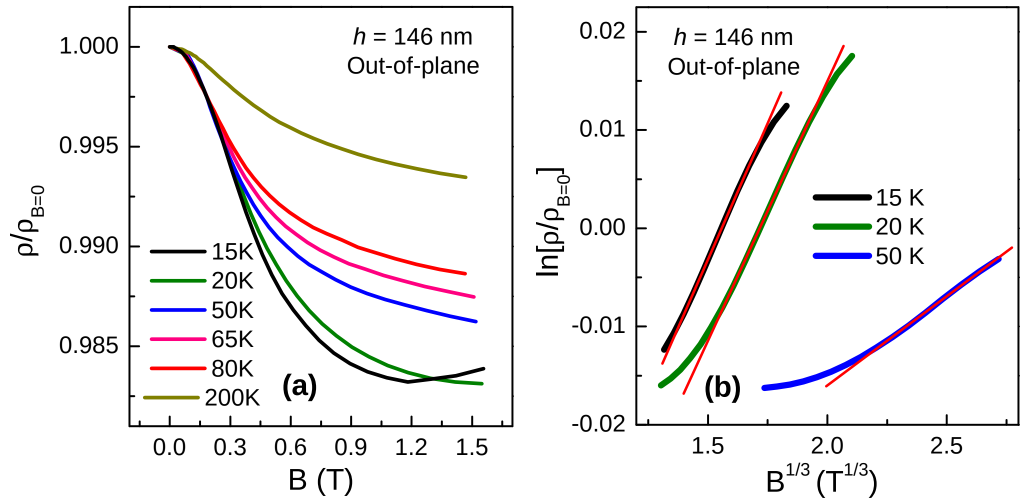

Figure 4.10: Magnetic field dependencies of normalized electrical resistivity of the (ZnO/C)$_{25}$ film with h = 146 nm in the coordinates of $\rho/\rho_{B=0} - B$ (a) and $\ln \rho/\rho_{B=0} - B^{1/3}$ (b). Red solid lines are linear fits.

As for the origin of the magnetic ordering in the (ZnO/C)$_{25}$ sample with h = 146, we can rule out the previously described hole-mediated p-p coupling interaction near the Fermi level due to the absence of P-type conductivity of the studied samples, which agrees with the results of the paper Park et al. (2010). The defect-induced d^0 magnetism can be responsible for the observed magnetic ordering since the studied multilayered structures contain a large amount of interfaces and island structures that produce a high concentration of defects.

5 Magnetotransport and magnetic properties of metal-insulator nanocomposites

This chapter summarises the research results of **Publications 3**, **4** and **5** by describing the magnetic and (magneto-)transport properties of metal-insulator nanocomposites (MI NC) fabricated using an ion-beam sputtering process, focusing on the investigation of the effects of dispersed magnetic ions in an insulating matrix of MI NCs, and on the search of positive magnetoresistance in them.

Magnetic nanogranular metal-insulator composites are systems that consist of nanogranular metallic phases chaotically embedded in a dielectric matrix. These systems are promising due to their potential application in spintronics, magnetic data recording, and high-frequency magnetoelectronic devices (Sullivan, 2009; Fujimori et al., 2006). Thin films of metal-insulator nanocomposite material have shown a combination of large resistance and induced magnetic anisotropy, and large spin-dependent tunnelling magnetoresistance (Ohnuma et al., 1996; Fujimori et al., 1995). Other prominent effects observed in MI NCs are a giant anomalous Hall effect, an enhanced magnetooptical Kerr effect, a memristive effect, and linear positive magnetoresistance (Rylkov et al., 2018c; Aronzon et al., 1999; Gan'shina et al., 2004; Gerber et al., 2007; Blinov et al., 2019).

Metal-insulator nanocomposite systems are utilised to study the quantum size effect and percolation phenomenon, as well as the (magneto-)transport, (magneto-)optical and high-frequency properties of interacting magnetic nanogranules. The magnetic properties of MI NCs depend on the chemical composition of metallic granules and dielectric matrices, their concentrations, and the size and shape of the metallic granules. The MI NCs can show paramagnetic (PM), ferromagnetic (FM), superferromagnetic (SFM), superparamagentic (SPM) or spin-glass magnetic behavior (Bedanta and Kleemann, 2008).

Two critical concentrations of the metallic phase are considered when studying MI NCs. The first is a metal-insulator transition (x_c) that is usually followed by a change of magnetic state, and the second is a percolation threshold (x_p) that is achieved when nanogranules form a continuous chain through the whole sample that acts as an electric current conductor.

Commonly, magnetic properties of nanocomposites are dictated by dipole-dipole interaction between granules. However, it has been shown that apart from metallic granules, nanocomposites can contain singular and/or small clusters of magnetic ions dispersed in a dielectric matrix that can greatly affect magnetic parameters of nanocomposites (Rylkov et al., 2017). Such dispersed magnetic ions can induce FM exchange interaction between granules leading to the observed SFM ordering at concentrations below a percolation threshold (x_p) (Rylkov et al., 2017; Timopheev et al., 2012). Under these conditions, nanocomposites are magnetically percolated while being unpercolated physically. There is no clear understanding of the role of the dispersed magnetic ions in the formation of SFM ordering (Timopheev et al., 2012), which prompts the further study of systems with different compositions and concentrations of metallic phases and dielectric matrices. Therefore, it is necessary to investigate how dispersed magnetic ions affect the properties of MI NCs and to compare the magnetic and (magneto-)transport properties of samples with low and high concentrations of dispersed magnetic ions.

The high-field linear positive MR (LPMR) up to 10^{-1}% T^{-1}, which was observed in ferromagnetic materials, composites and manganites (Gerber et al. (2007); Blinov et al. (2019), and references therein), has induced significant interest because it could not be explained by the known mechanisms of MR. The observed LPMR is isotropic and does not saturate in magnetic fields up to 60 T (Gerber et al., 2007). Commonly, the MR of ferromagnetic materials is negative due to the suppression of magnetic disorder by an applied magnetic field, and anisotropic in magnetic fields lower than a saturation one due to spin-orbit interaction (SOI). However, anisotropic MR in nanocomposites is suppressed due to the size effect and is not observed in the vicinity of a percolation threshold (Blinov et al., 2019). Gerber et al. (2007) associate the observed LPMR with the influence of the Zeeman effect on the quantum corrections to electrical conductivity, which are induced by electron-electron interaction, though this concept cannot explain the magnitude of the observed LPRM effect (10^{-1}% T^{-1}). Moreover, the authors could not explain why the quantum corrections to conductivity exist up to 200 K. Blinov et al. (2019) have observed LPMR in CoNbTa-Al_2O_3 and CoFeB-SiO_2 NCs and associated it with a change of a tunnel barrier height in the case of spin-polarised tunnelling under the influence of the Zeeman effect. Based on the Inoue-Meakawa model of tunneling MR in granular films (Rylkov et al., 2017), authors of the paper Blinov et al. (2019) have developed an equation that allowed them to explain qualitatively the LPMR results. However, it should be noted that the Inoue-Maekawa model is valid only for granular films with $x < x_c$, where electrical resistivity follows $\ln \rho \propto T^{-1/2}$. Therefore, the origin of LPMR in different systems is still an open question and further investigation is required to determine whether LPMR has the same physical nature in different systems. Moreover, it is necessary to modify the LPMR expression for nanocomposites with $x_c < x < x_p$, with strong tunnel coupling between granules, where electrical resistivity follows $\rho \propto \ln T$.

5.1 Sample fabrication and measurement details

In the present study, metal-insulator nanocomposites were fabricated by ion-beam sputtering of components' targets on a glass-ceramic substrate. The choice of the ion-beam sputtering process is dictated by its advantages over other types of fabrication processes: low growth temperature, the possibility of sputtering both conducting and insulating materials, good adhesion properties, and relatively high growth rate ($\approx$ 0.25 nm/s) (Rylkov et al., 2018a). Another crucial advantage of an ion-beam sputtering process is that it allows the growth of complex alloys while maintaining an accurate percentage of sputtering materials.

The sputtering process was conducted in an argon atmosphere of a pressure $P \approx$ 3–8 $\times 10^{-4}$ torr. The targets with size of 280 × 80 mm^2 consisted of either Co, $Co_{84}Nb_{14}Ta_2$ or $Co_{40}Fe_{40}B_{20}$ metallic alloys. 14 oxide strips (80 × 10 mm^2) of either Al_2O_3, $LiNbO_3$ or SiO_2 were fixed on the metallic part of the target with the gradually changing distance between the strips along the target length. Such configuration allowed fabrication of nanocomposites with the continuous variation of a metallic phase ($dx \approx$ 0.5–2 at.%) in the wide concentration range (x = 6–60 at.%) during a single sputtering cycle. Depending on the sample, the thickness of the nanocomposite films varied from about 1 to 3 microns. A list of the studied nanocomposites is presented in Table 5.1.

Table 5.1: List of the studied (metal)$_x$(insulator)$_{100-x}$ nanocomposites.

	Co	$Co_{84}Nb_{14}Ta_2$	$Co_{40}Fe_{40}B_{20}$
SiO_2	✓	✓	✓
$LiNbO_3$	✓		✓
Al_2O_3		✓	✓

Depending on the sample, the growth temperature (T_g) varied from room temperature up to 90 °C. The elevated growth temperatures (70–90 °C) were used to decrease the concentration of dispersed metallic atoms in the nanocomposite films.

The cross-sectional lamellae of the studied nanocomposites were prepared using a focused ion beam (FIB) Ga^+ system in a scanning electron microscope "Helios NanoLab^{TM} 600i" (Thermo Fisher Scientific, USA).

Two transmission and scanning transmission electron microscopes (TEM / STEM) were used for the structural studies of the samples: 1) "Tecnai Osiris" (Thermo Fisher Scientific, USA) operating at U = 200 kV equipped with an energy dispersive X-ray spectrometer (EDXS) "Super-X" (Bruker, USA), and a high-angle annular dark-field detector (HAADF) (Fischione, USA); 2) "TITAN 80–300" (FEI, USA) operating at U = 300 kV, equipped with a Cs-probe corrector, HAADF (Fischione, USA), and an EDX microanalysis spectrometer (EDAX, USA).

A scanning electron microscope "Oxford INCA Energy 250" with an energy dispersive X-ray add-on device "JEOL JSM-6380LV" was used to investigate the elemental composition of the samples.

In order to measure the (magneto-)transport properties of the nanocomposites in a planar geometry, the samples were prepared using a photolithography method. The resulting geometry of the samples resembles a double-cross shape with the conduction channel of length l = 4 mm and width w = 1.2 mm, and with a distance between voltage probes l_{vp} = 1.4 mm.

The PMFS (four-probe method) was used to measure the temperature dependencies of resistance, and the magnetoresistance curves (MR = $(R_B - R_0)/R_0 \times 100\%$) in a pulsed magnetic field (B) up to 20 T.

The magnetic properties of the nanocomposite films ($m(H, T)$) were measured using SQUID magnetometers "Cryogenic S700XR" and "Quantum Design MPMS-XL7".

A special setup, consisting of a vacuum insert with a superconducting solenoid (with magnetic field up to 1.5 T) immersed in liquid helium, was used to measure electrical conductivity in the temperature range of 10–300 K.

5.2 Electrical conductivity regimes of metal-insulator nanocomposite materials

Depending on the concentration of the metallic phase, conductivity of MI NC materials in the close vicinity to a metal-insulator transition (MIT or x_c) can be described by two regimes. The first regime is observed when $x \leqslant x_c$, and conductivity is described by the so-called "T$^{1/2}$" law (Beloborodov et al., 2007):

$$\ln \rho \propto \left(\frac{T_0}{T} \right)^{1/2}. \tag{5.1}$$

In this regime, an average tunnelling conductance between adjacent granules (G_t) is less than the conductance quantum ($G_q = 2e^2/h$):

$$g = \frac{G_t}{G_q} < 1. \tag{5.2}$$

The second regime activates when $x_c \leqslant x \leqslant x_p$ and $G_t/G_q \gg 1$. In this regime, strong tunnel coupling between granules appears and conductivity is described by the so-called "$\ln T$" law (Lähderanta et al., 2016; Beloborodov et al., 2007):

$$\rho \propto \ln T. \tag{5.3}$$

A logarithmic temperature dependence of conductivity ("$\ln T$" law) of the two-dimensional nanogranular structures with "metallic" concentrations can be explained by the weak localization effects. However, there have been reports where thick films at high temperatures demonstrate logarithmic temperature dependencies of conductivity that cannot be explained by the weak localization effects (Rylkov et al., 2017, 2018b,c; Blinov et al., 2019). It has been shown that such logarithmic dependencies can be induced by renormalizing the Coulomb interaction (Efetov and Tschersich, 2003; Beloborodov et al., 2007). Under these conditions, the electrical conductivity of nanocomposite films with concentrations of metal granules below a percolation threshold ($g \geqslant 1$) and with an ordered distribution of granules follows

$$\sigma(T) = \sigma_0 \left(1 - \frac{1}{2\pi D g} \ln \frac{g E_C}{k_B T}\right), \tag{5.4}$$

where D is the dimensionality of a system, σ_0 is the conductivity at high temperatures when the effect of Coulomb interaction can be neglected (Beloborodov et al., 2007), k_B is the Boltzman constant, and $g = G_t/G_q$. The Coulomb blockade energy (E_C) follows

$$E_C = \frac{e^2 s}{\epsilon a^2 (1/2 + s/a)}, \tag{5.5}$$

where s is the tunnel gap width or, in other words, the distance between granules, a is the diameter of a granule, and ϵ is the permittivity of the matrix (Abeles et al., 1975). The temperature coefficient of resistivity ($\alpha = d\rho/dT$) in the "metallic" region ($x_c \leqslant x \leqslant x_p$) is negative, though its sign can change to positive above a percolation threshold (Bartov et al., 2014). The change of the α sign can be used as a method to estimate the value of a percolation threshold. Moreover, the temperature dependencies of resistivity of MI NCs do not follow the logarithmic law above a percolation threshold that can also be used to verify a value of x_p. It should be noted that Eq. 5.4 is valid only in the energy range of $g\delta \ll k_B T \ll E_C$, where δ is energy spacing between quantized levels of an isolated granule.

The theory proposed by Efetov and Tschersich (2003) and Beloborodov et al. (2007) can also be utilized for nanocomposites with a disordered arrangement of granules and with the presence of dispersed metallic granules in between the granules since its main parameter is tunnelling conductance. Recent studies of MI NCs have demonstrated that dispersed metallic ions enhance FM exchange interaction, and hence the tunnel coupling between granules, leading to a shift of a MIT to lower values (Rylkov et al., 2019, 2018b,c). The shift of a MIT widens the "metallic" concentration range ($dx = x_p - x_c$) in which Eq. 5.4 is valid, which was observed for the following MI NCs: (CoFeB)$_x$(LiNbO$_3$)$_{100-x}$ (Rylkov et al., 2018c,b), (CoFeB)$_x$(Al$_2$O$_3$)$_{100-x}$ (Rylkov et al., 2017, 2018b; Mikhailovskii et al., 2016), (CoFeB)$_x$(SiO$_2$)$_{100-x}$ and (CoNbTa)$_x$(Al$_2$O$_3$)$_{100-x}$ (Blinov et al., 2019). As illustrated in Fig. 5.1, the temperature dependencies of conductivity of the (CoFeB)$_x$(Al$_2$O$_3$)$_{100-x}$ NCs follow the logarithmic law at $T \approx$ 10–300 K and in the concentration range of 49–56 at.%. The estimated values of the critical concentrations for these MI NCs are: $x_c \approx$ 47 at.% and $x_p \sim$ 56–59 at.%, meaning $dx = x_p - x_c \approx$ 9–12 at.%, whereas granular Ni-SiO$_2$ films without dispersed metallic ions have $dx = x_p - x_c \approx$ 1 at.% (Bartov et al., 2014).

According to the curves in Fig. 5.2, the (CoFeB)$_x$(LiNbO$_3$)$_{100-x}$ NCs demonstrate $dx = x_p - x_c \approx$ 8 at.%. Moreover, for these nanocomposites, the temperature range where the conductivity follows the logarithmic law is shifted to $T \approx$ 10–220 K. The shift of the temperature range can be induced by suppression of the Coulomb blockade effect due to the enlargement of granules (due to their elongation) and the high permittivity of LiNbO$_3$ (ϵ up to 10^4 [Mitsuyu and Wasa, 1981]) (Beloborodov et al., 2007).

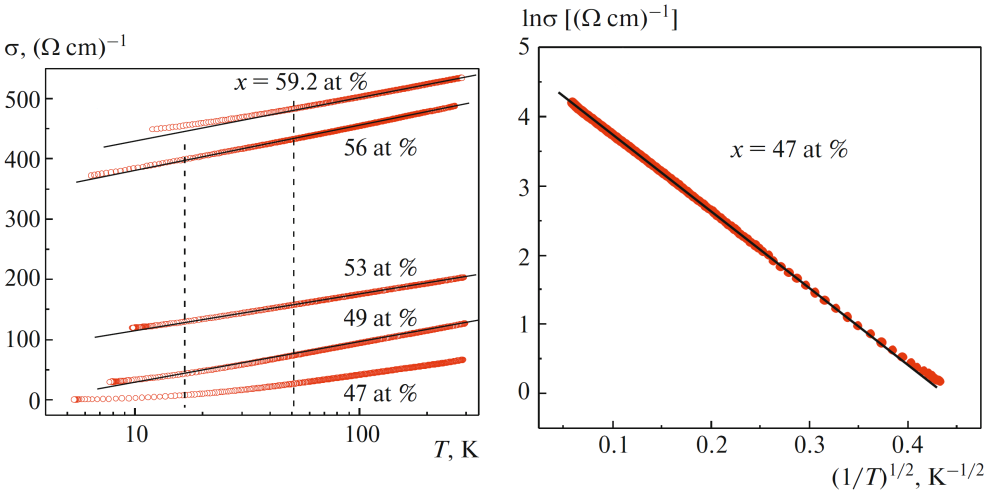

Figure 5.1: Temperature dependencies of conductivity of $(CoFeB)_x(Al_2O_3)_{100-x}$ nanocomposites at various concentrations of metallic phase (x = 47–59.2 at.%) represented in the coordinates of (left) "$\ln T$" and (right) "$T^{1/2}$" laws. The black solid lines are linear fits. Taken from Rylkov et al. (2017).

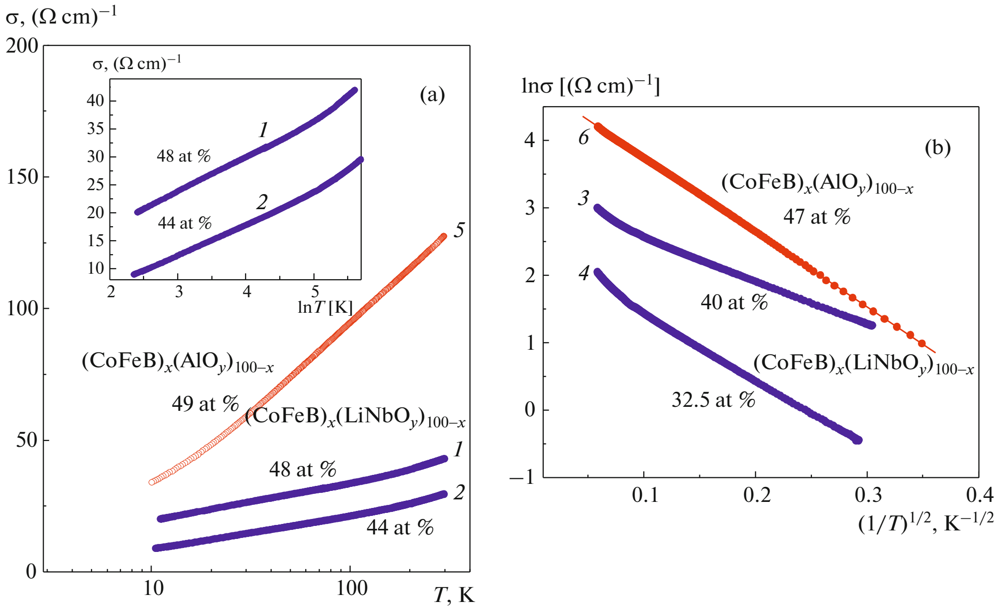

Figure 5.2: Temperature dependencies of conductivity of $(CoFeB)_x(Al_2O_3)_{100-x}$ (red curves) and $(CoFeB)_x(LiNbO_3)_{100-x}$ (blue curves) NCs with different concentrations of metallic phase in the coordinates of (a) "$\ln T$" and (b) "$T^{1/2}$" laws. The insert shows the same curves but on different scales. Taken from Rylkov et al. (2018c).

5.3 Comparison of magnetic and transport properties of metal-insulator nanocomposites with low and high concentration of dispersed atoms

This subchapter describes the results of the comparative investigation of the magnetic and transport properties of $(Co_{40}Fe_{40}B_{20})_x(LiNbO_3)_{100-x}$ NCs with low (LCDA) and high (HCDA) concentrations of dispersed magnetic atoms (Fe, Co).

Rylkov et al. (2018c,b) have shown that the low-temperature magnetization of MI NCs has both PM and FM components, and for some NCs contribution of the PM component is almost three times more than that of the FM component. It has been determined that such strong PM contribution originates from dispersed Fe^{2+} and Co^{2+} ions. At this point, it should be noted that the value x of the studied NCs include concentrations of both metallic granules and dispersed ions. The concentration of dispersed ions (N_d) depends on a nanocomposite growth temperature (Rylkov et al., 2018c,b). For instance, $(CoFeB)_x(LiNbO_3)_{100-x}$ nanocomposite fabricated at a low growth temperature ($T_g \leqslant 40$ °C) has $N_d \approx 10^{22}$ cm^{-3} (HCDA), whereas at $T_g \approx 80$ °C, $N_d \lessapprox 10^{21}$ cm^{-3} (LCDA). The increase of the growth temperature leads to the enlargement of metallic granules from ~2.5 up to ~3.5 nm. As can be seen in the magnetization curves in Fig. 5.3, the lower the growth temperature, the higher the M_{PM}/M_{FM} ratio, which is caused by the increase of the concentration of dispersed ions. The M_{PM} and M_{FM} components originate from dispersed ions and metallic alloy granules, respectively. Calculations of the average magnetic moment of dispersed ions, their concentrations (N_d), and M_{PM}/M_{FM} ratios were done by analyzing the temperature dependence of magnetization at $T < 10$ K, where the PM component is most pronounced. Two $M(H)$ curves measured at different temperatures give the change of magnetization $\Delta M(H, T_1, T_2) = M(H, T_1) - M(H, T_2)$, which is then fitted by the difference of Brillouin's functions $\Delta B_J(H, T_1, T_2) = B_J(H, T_1) - B_J(H, T_2)$ (calculation details can be found in Rylkov et al. (2018b)). The resulting values of the magnetic moment per PM ion were in the range of 5.1–5.8μ_B, whereas the magnetic moments of Fe^{3+}, Fe^{2+} and Co^{2+} ions are 5.9, 5.4 and 4.8μ_B (Kittel et al., 1996), respectively, which are similar values to those calculated.

It should be noted that in the temperature range of 10–200 K, conductivity of both nanocomposites with LCDA and HCDA follow the "$\ln T$" law in the concentration range of $x_c \leqslant x \leqslant x_p$ and "$T^{1/2}$" law in $x < x_c$. However, the MIT value ($x_c \approx 48$ at.%) of NCs with LCDA is larger by about 5 at.% compared to NCs with HCDA ($x_c \approx 43$ at.%) (See Fig. 5.4). The high concentration of the dispersed atoms enhances intergranular coupling leading to the decrease of the MIT value. Moreover, the presence of HCDA lowers the tunnel barrier height, facilitating electron hopping transport in the vicinity of percolation threshold, resulting in the presence of high-field positive MR in NCs with HCDA (Blinov et al., 2019).

It has been observed that dispersed magnetic ions facilitate SFM ordering in MI NCs (Bedanta et al., 2007; Timopheev et al., 2012). $(CoFeB)_x(LiNbO_3)_{100-x}$ NCs with concen-

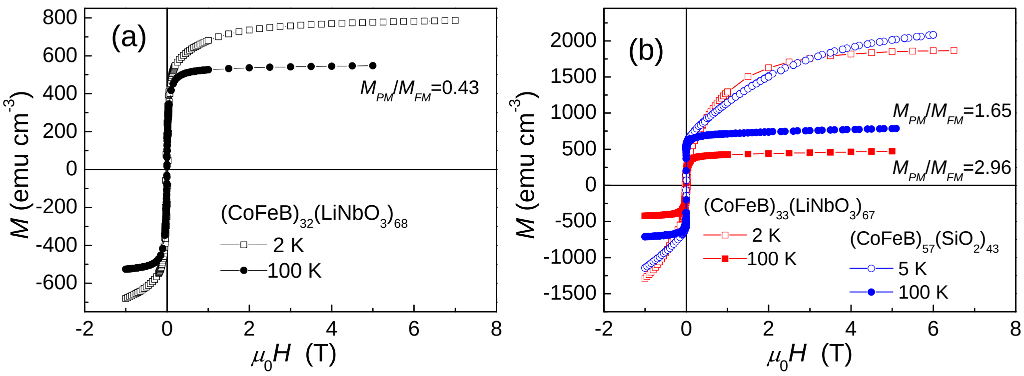

Figure 5.3: Magnetic field dependencies of volume magnetization of (a) (CoFeB)$_{32}$(LiNbO$_3$)$_{68}$ NC grown at $T_g \approx 75$ °C with $N_d \approx 3.2 \times 10^{21}$ cm^{-3}, (b) (CoFeB)$_{33}$(LiNbO$_3$)$_{67}$ and (CoFeB)$_{57}$(SiO$_2$)$_{43}$ NCs grown at $T_g \approx 40$ °C with $N_d \approx 3.1 \times 10^{22}$ and 3.2×10^{22} cm^{-3}, respectively.

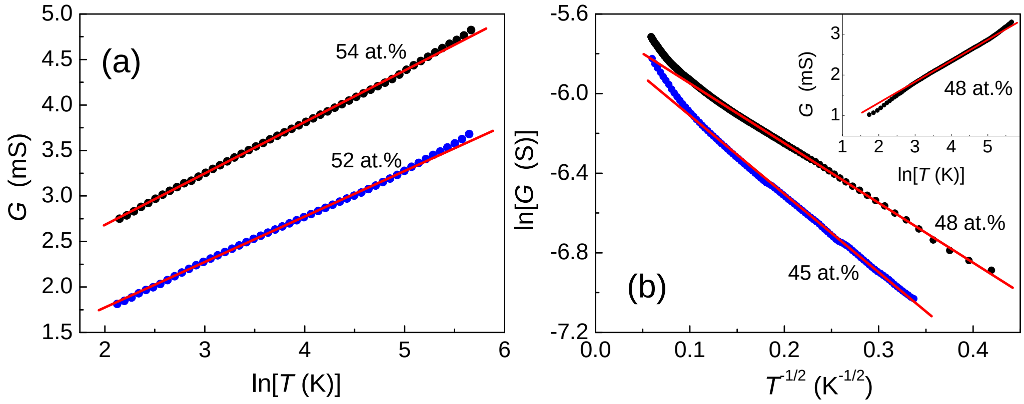

Figure 5.4: Temperature dependencies of conductance of CoFeB-LiNbO$_3$ nanocomposites with LCDA ($T_g \approx 75$ °C) at various metallic concentrations (x = 45–54 at.%) represented in the coordinates of (a) "$T^{1/2}$" and (b) "$\ln T$" laws. The red solid lines are linear fits.

trations far below percolation threshold have shown magnetic coercivity (See Fig. 5.5), which is a signature of SFM ordering. The anomaly in the temperature dependence of coercivity of the NC with HCDA, namely the minimum at $T \approx 50$ K (See the green curve in Fig. 5.5), can be attributed to the influence of the surface magnetic anisotropy of granules (Rylkov et al., 2019). The temperature dependencies of coercivity of LCDA NCs with $x \leqslant 42$ at.% are well described by the Neel-Brown law for noninteracting granules with the blocking temperature of about 25 K (See Fig. 5.5). The absence of intergranular interactions in the LCDA NCs is also confirmed by angular dependencies of the FMR linewidth (See **Publication 4**).

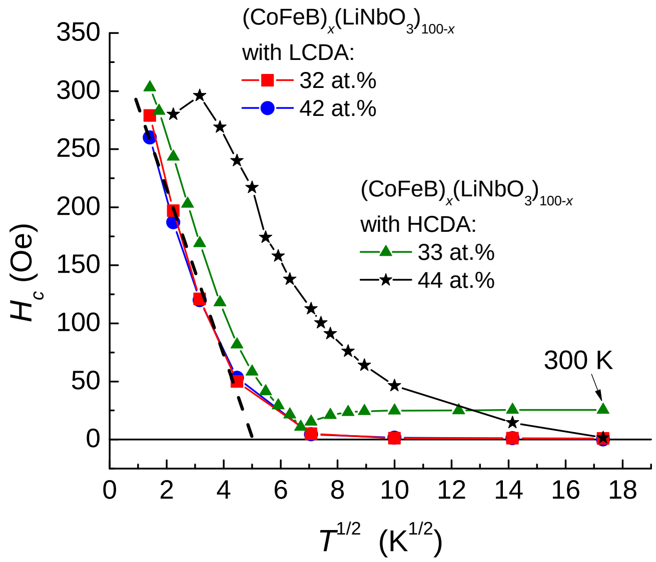

Figure 5.5: Temperature dependencies of the coercive field of LCDA ($T_g \approx 75$ °C) and HCDA ($T_g \approx 40$ °C) (CoFeB)$_x$(LiNbO$_3$)$_{100-x}$ NCs with $x < x_p$ in the coordinates of $H_C - T^{1/2}$. The dashed black line is a linear fit.

5.4 High-field linear positive magnetoresistance of magnetic nanocomposites near the percolation threshold

This subchapter describes the results of the magnetic and (magneto-)transport study of Co-SiO_2, Co-$LiNbO_3$, CoNbTa-SiO_2 magnetic nanocomposites fabricated at the elevated growth temperature of 80 °C. The out-of-plane MR was measured in magnetic fields up to 20 T in the temperature range T = 4.2–300 K, while the in-plane and out-of-plane magnetic hysteresis loops in magnetic fields up to 7 T were recorded at various temperatures (T = 2–300 K). The thermoresistive curves were measured in T = 50–300 K.

In order to calculate the LPMR values of the samples in the $x \leqslant x_c$ regime, Blinov et al. (2019) derived an equation in the framework of the Inoue-Maekawa model. This equation is based on the influence of the Zeeman effect on a tunnel barrier height, and at low temperatures can be written as

$$\frac{\Delta\rho(H)}{\rho(0)} = \frac{\rho(H) - \rho(H=0)}{\rho(H=0)} = \xi \frac{\mu_B H}{U - E_F(0)} \sqrt{\frac{\lambda C}{k_B T}}, \tag{5.6}$$

where k_B is the Boltzmann constant, μ_B is the Bohr magneton, $C = sE_C$, and ξ is a parameter characterising a shift of the Fermi level (which is equal to spin polarisation, P). The Fermi level depends on a magnetic field as

$$E_F(H) = E_F(0) - \xi\mu_B H. \tag{5.7}$$

The parameter λ characterises the wave function decay of a tunnelling electron in a barrier with a height of $[U - E_F(0)]$ and can be written as follows

$$\lambda = \sqrt{\frac{2m}{\hbar^2}(U - E_F(0))}, \qquad \lambda(H) = \sqrt{\frac{2m}{\hbar^2}(U - E_F(0) + \xi\mu_B H)}. \tag{5.8}$$

Following from Eq. 5.6, LPMR should increase with the temperature decrease as $T^{-1/2}$. The results of the MR measurements of $(Co_{40}Fe_{40}B_{20})_x(SiO_2)_{100-x}$ and $(Co_{84}Nb_{14}Ta_2)_x(Al_2O_3)_{100-x}$ nanocomposites in the paper by Blinov et al. (2019) show that in $H < H_{sat}$, MR is negative, whereas in $H > H_{sat}$, LPMR appears and increases with the temperature decrease reaching its maximum value of about 0.005–0.009% T^{-1} (See Fig. 5.6 and [Blinov et al., 2019]). These experimental values are similar to the results of calculations using Eq. 5.6 (Blinov et al., 2019). As shown in Fig. 5.6, the LPMR is stronger for nanocomposites with a lower potential barrier, i.e., for the $(Co_{84}Nb_{14}Ta_2)_x(Al_2O_3)_{100-x}$ sample, thus, it would be reasonable to expect higher values of LPMR in MI NCs with a high concentration of dispersed ions in intergranular gaps. The Co-SiO_2, CoNbTa-SiO_2 and Co-$LiNbO_3$ MI NCs were fabricated at $T_g \approx$ 80 °C to check this hypothesis. The concentration of dispersed ions (N_d) in these NCs was about 10^{21} cm^{-3}.

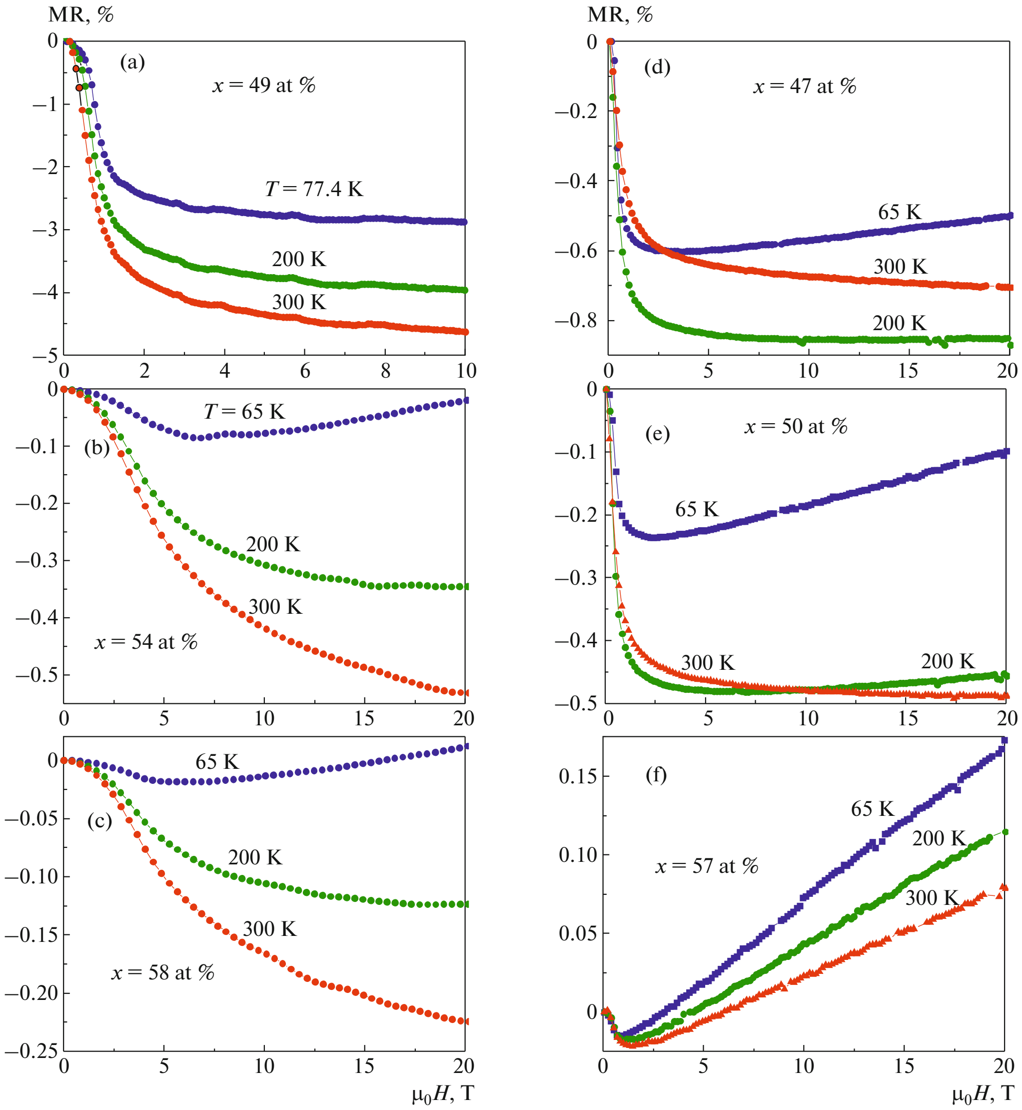

Figure 5.6: Out-of-plane MR curves of $(CoFeB)_x(SiO_2)_{100-x}$ (left column) and $(CoNbTa)_x(Al_2O_3)_{100-x}$ (right column) NCs measured at different temperatures. Taken from Blinov et al. (2019).

The results of the magnetic measurements of the Co-SiO_2, CoNbTa-SiO_2 and Co-$LiNbO_3$ NCs in the form of hysteresis loops are presented in Fig. 5.7. As can be seen from Fig. 5.7, the in-plane and out-of-plane hysteresis loops converge in $H \approx$ 2–3 kOe and $H \approx$ 10 kOe, respectively. The room-temperature magnetization saturates in $H \approx$ 3–15 kOe depending on the orientation, whereas at low temperatures magnetization continues to grow in higher magnetic fields. The absence of magnetization saturation at low temperatures indicates the presence of superparamagnetic particles and magnetic ions (Rylkov et al., 2017).

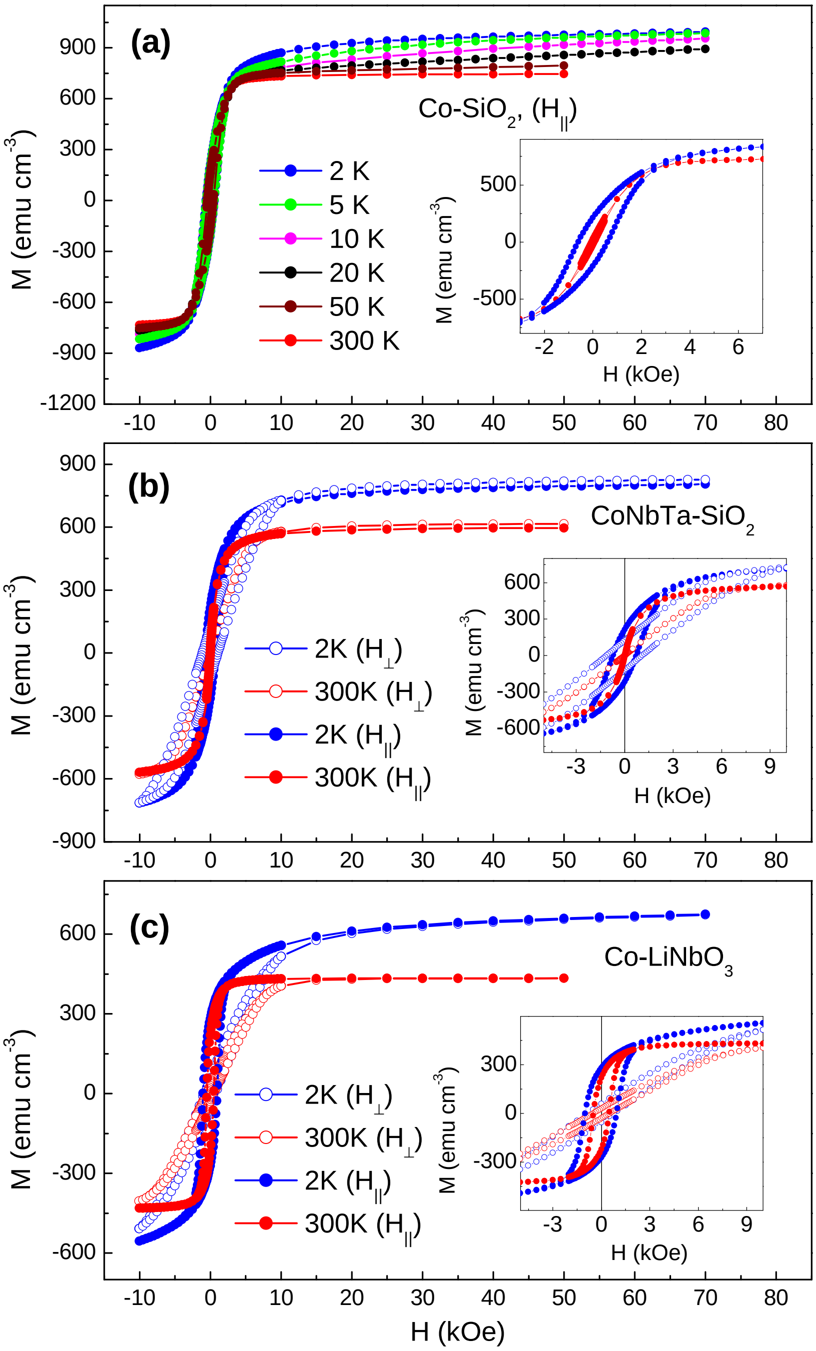

Figure 5.7: Magnetic hysteresis loops of (a) Co-SiO_2, (b) CoNbTa-SiO_2 and (c) Co-$LiNbO_3$ nanocomposites measured in different orientations and temperatures. The same curves, but on different scales, are presented in the inserts.

The out-of-plane MR curves of the studied samples are presented in Fig. 5.8 and 5.9. In $H < H_{sat}$, MR is negative and its value rises sharply with the magnetic field increase. In $H > H_{sat}$, the value of negative MR continues to grow gradually, which is a characteristic behavior of the tunnelling MR with the presence of superparamagnetic particles (Rylkov et al., 2017). The LPMR of the Co-SiO$_2$ (x = 65 at.%) and CoNbTa-SiO$_2$ (x = 58.5 at.%) samples was observed only at T = 4.2 K and in $H > H_{sat}$, and this was 0.03 and 0.06% T^{-1}, respectively. These values are similar to those obtained in the papers (Gerber et al., 2007; Blinov et al., 2019). Due to the high resistance of the Co-LiNbO$_3$ (x = 49 at.%) nanocomposite at $T < 50$ K, which was above the limitations of the PMFS, the MR was measured only at T = 50–300 K. However, as apparent in Fig. 5.9, the LPMR of the Co-LiNbO$_3$ (x = 49 at.%) was detected even at T = 50 and 120 K and this was in the order of 10^{-3}% T^{-1}.

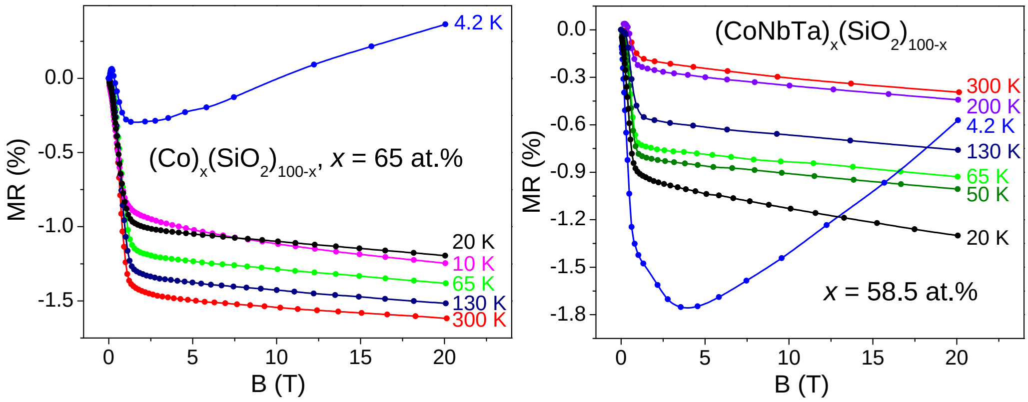

Figure 5.8: Out-of-plane MR curves of the Co-SiO$_2$ and CoNbTa-SiO$_2$ nanocomposites measured at T = 4.2–300 K.

The temperature dependencies of electrical resistivity of the Co-SiO$_2$ (x = 65 at.%) and CoNbTa-SiO$_2$ (x = 58.5 at.%) NCs follow the “$\ln T$” law (See Fig. 5.10, 5.11). Therefore, in order to calculate the LPMR values of these NCs using the expression (Eq. 5.6) developed in the work by Blinov et al. (2019), it was necessary to modify the expression for the “metallic” region from the MIT ($x_c \leqslant x \leqslant x_p$) because Eq. 5.6 is valid only for NCs with concentrations below the MIT ($x < x_c$).

In the $x_c \leqslant x \leqslant x_p$ regime, conductance follows

$$G(H) \propto (1 + P^2 m^2) \exp\{-2\lambda(H)s\}, \tag{5.9}$$

where m is a relative magnetization (Inoue and Maekawa, 1996). Then, one can derive an equation for LPMR in this regime in $H > H_{sat}$ using Eq. 5.4, 5.7–5.9:

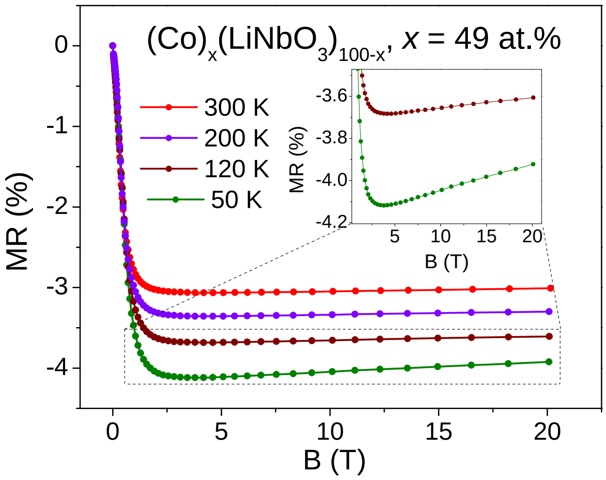

Figure 5.9: Out-of-plane MR curves of the Co-LiNbO$_3$ nanocomposite measured at T = 50–300 K.

$$\frac{\Delta\rho(H)}{\rho(0)} = \xi \frac{\mu_B H}{U - E_F(0)} \frac{\lambda s}{2\pi D g} \left[\ln \frac{g E_C}{k_B T} - 1 \right]. \tag{5.10}$$

It should be noted that both Eq. 5.6 and 5.10 yield the same order of magnitude of LPMR but different temperature dependencies.

For $a \approx 3$ nm, $s \approx 1$ nm, D = 3, and $\epsilon \approx 3.75$ (for SiO$_2$), the Coulomb blockade energy $E_C \approx 51.5$ meV. Then for $[U - E_F(0)]$ = 1.0 eV and g = 1.0, at T = 4.2 K, $\Delta\rho(H)/\rho(0) \approx$ 0.01% T^{-1}. In the $x_c \leqslant x \leqslant x_p$ regime, this is the maximum value of LPMR since we assumed that ξ = 1.0 (100% spin polarisation). The decrease of the barrier height down to $[U - E_F(0)]$ = 0.1 eV leads to the increase of the LPMR value by 3.3 times, whereas at $[U - E_F(0)]$ = 0.1 eV and g = 10, $\Delta\rho(H)/\rho(0) \approx 0.1\%$ T^{-1}. The LPMR results of CoFeB-SiO$_2$ and CoNbTa-Al$_2$O$_3$ nanocomposites in the work by Blinov et al. (2019) that were measured at T = 65 K follow the "$\ln T$" law and their values are in the range of $\Delta\rho(H)/\rho(0) \approx 10^{-3}$–$10^{-4}\%$ T^{-1}. These values are in agreement with the calculated values using Eq. 5.10. It should be noted that the LPMR mechanism proposed in the paper Gerber et al. (2007) cannot explain the LPMR results of the paper by Blinov et al. (2019) since the signatures of quantum corrections for these nanocomposites were not observed. The detailed investigations of each of the three newly fabricated systems (Co-SiO$_2$, CoNbTa-SiO$_2$ and Co-LiNbO$_3$) are presented below. The temperature dependencies of resistivity were measured for Co-SiO$_2$ (x = 53 and 65 at.%), CoNbTa-SiO$_2$ (x = 51 and 58.5 at.%) and Co-LiNbO$_3$ (x = 49 at.%), and are presented in the coordinates of the "$\ln T$" and "T$^{1/2}$" laws in Fig. 5.10–5.12.

5.4.1 $(\mathrm{Co})_x(\mathrm{SiO}_2)_{100-x}$

Among the two studied concentrations of the Co-SiO$_2$ nanocomposites, LPRM of about 0.03% T^{-1} was observed only for x = 65 at.% and only at T = 4.2 K (See Fig. 5.8). As seen in Fig. 5.10, the thermoresistive curve of the Co-SiO$_2$ (x = 65 at.%) nanocomposite is linear in the wider temperature range in coordinates of the "$\ln T$" law, and for this concentration, at D = 3, $g \approx 1$. However, for the considered model, $2D$ is equal to a number of adjacent granules between which tunnelling is possible, i.e., for disordered case $D < 3$, hence, $g > 1$, and it is possible to utilise Eq. 5.10, which correctly describes the obtained data.

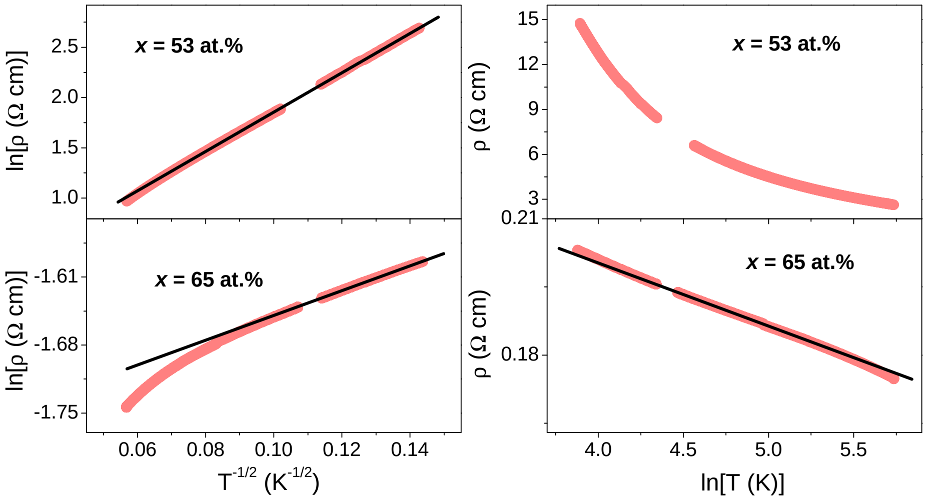

Figure 5.10: Temperature dependencies of resistivity of Co-SiO$_2$ (x = 53 and 65 at.%) nanocomposites in the coordinates of $\ln\rho - T^{-1/2}$ (left column) and $\rho - \ln T$ (right column). The black solid lines are linear fits.

It should be noted that the value of the negative MR of Co-SiO$_2$ (x = 65 at.%) sample is higher at T = 300 K than at lower temperatures. This can be explained by the presence of aggregates and granules, which can be formed at concentrations close to an MIT. Apart from the tunnelling MR, this may also induce negative MR caused by the suppression of magnetic disorder in granules and aggregates, which can be of a similar magnitude as the negative tunnelling MR and rise with a temperature increase due to an increase of spin fluctuations. The images from electron microscopy confirm the presence of such aggregates. Moreover, metallic phase concentrations of the Co-SiO$_2$ NCs in the vicinity of the percolation threshold are higher than those of the other studied nanocomposites, which means higher possibilities for the formation of aggregates. Moreover, the effect of the magnetic blockade, which induces positive MR, can diminish total negative MR at low temperatures (Inoue and Maekawa, 1996).

5.4.2 $(CoNbTa)_x(SiO_2)_{100-x}$

The LPMR up to 0.06% T^{-1} was observed only for CoNbTa-SiO_2 NC with x = 58.5 at.% (See Fig. 5.8) and the thermoresistive behavior of this sample is described well by the "$\ln T$" law (See Fig. 5.11). The increase of the LPMR value in comparison to the previous sample can be explained by a change of the tunnel barrier height and spin polarization, induced by a change in the concentration of ions dispersed in the dielectric matrix, and by the variation of the composition of ferromagnetic granules. The LPMR value of this sample was the highest among all the studied nanocomposites.

As illustrated in Fig. 5.8, the LPMR of both Co-SiO_2 (x = 65 at.%) and CoNbTa-SiO_2 (x = 58.5 at.%) nanocomposites is absent already at T = 10 K. However, following from Eq. 5.6 and 5.10, a strong temperature dependence should not be observed. This discrepancy can be explained by a high sensitivity of LPMR values to a concentration of dispersed magnetic and nonmagnetic ions in a tunnel gap. On the one hand, such ions can decrease a tunnel barrier height, but on the other hand, by changing the permittivity of a matrix, their presence can reduce the Coulomb blockade energy and also lead to an absence of magnetic and MR saturation in high magnetic fields. Moreover, the growth temperature (80 °C) of the studied nanocomposites is higher than of those in the work by Blinov et al. (2019), which implies different microstructures and hence magnetic properties. For example, as previously mentioned, magnetization of Co-SiO_2 nanocomposites continues to grow after reaching its saturation value (See Fig. 5.7), indicating an increase of negative tunnelling contribution to MR that makes positive contribution indistinguishable. To summarise, the absence of LPRM at $T > 4.2$ K is caused by the strong competitive negative MR caused by the presence of superparamagnetic granules and dispersed ions.

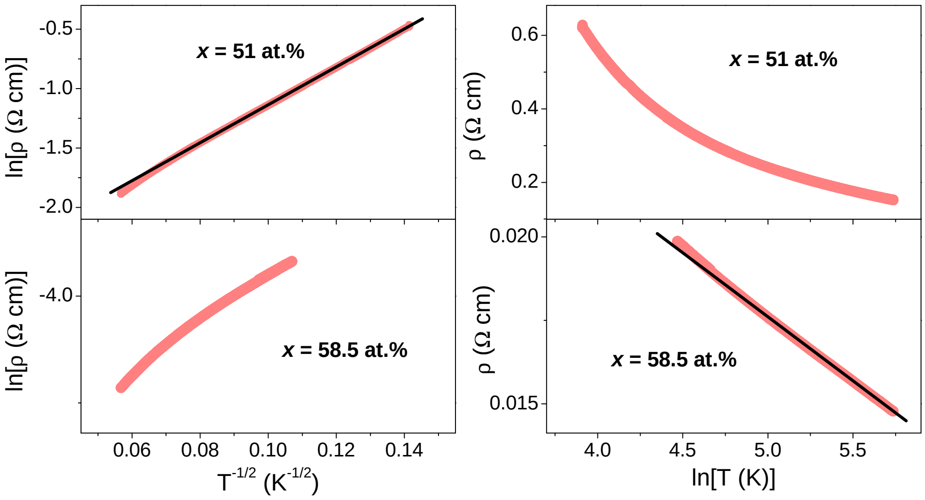

Figure 5.11: Temperature dependencies of resistivity of CoNbTa-SiO_2 (x = 51 and 58.5 at.%) nanocomposites in the coordinates of $\ln \rho - T^{-1/2}$ (left column) and $\rho - \ln T$ (right column). The black solid lines are linear fits.

5.4.3 $(\mathrm{Co})_x(\mathrm{LiNbO}_3)_{100-x}$

The LPMR of Co-LiNbO$_3$ (x = 49 at.%) nanocomposite at T = 50–120 K is in the order of 10^{-3}% T^{-1} (See Fig. 5.9), though the thermoresistive curves of this sample follow neither "$T^{1/2}$" nor "$\ln T$" laws (See Fig. 5.12). The LPMR values of this nanocomposite are comparable to those of the CoFeB-SiO$_2$ and CoNbTa-Al$_2$O$_3$ nanocomposites from the paper by Blinov et al. (2019). However, the MR of the Co-LiNbO$_3$ sample is anisotropic. As Fig. 5.13 shows, the MR of the Co-LiNbO$_3$ NC is different depending on an orientation of the film plane and current direction relative to an applied magnetic field (B). The in-plane MR is larger when B is perpendicular to the current direction rather than parallel. Moreover, when B is parallel to the current direction, the in-plane and out-of-plane MR are different. Such anisotropy was not observed in the other studied films, nor in the results of the paper by Gerber et al. (2007), and can be associated with the microstructure properties of the Co-LiNbO$_3$ film.

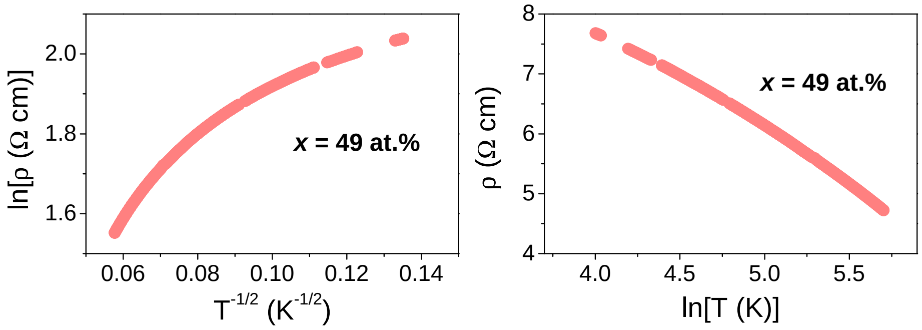

Figure 5.12: Temperature dependence of resistivity of Co-LiNbO$_3$ (x = 49 at.%) nanocomposite in the coordinates of $\ln \rho - T^{-1/2}$ (left) and $\rho - \ln T$ (right).

The results of TEM / STEM studies of the Co-LiNbO$_3$ film (x = 49 at.%) revealed the presence of the columnar formation near the interface between the film and the substrate (See Fig. 5.14B). This formation consists of cobalt granules elongated in the direction of film growth up to ~20–25 nm, where they start to bend. A lateral size of these Co granules in the direction of the film plane is ~5–8 nm. Above the columnar formation, the film consists of spherical nanocrystalline Co nanoparticles with the size of ~5–30 nm, randomly distributed in the amorphous matrix (See Fig. 5.14). The results of the TEM studies together with EDXS mapping (not shown here) confirm that crystalline nanoparticles consist of Co, and amorphous matrix of LiNbO$_3$. It should be noted that the Co nanogranules contain defects such as twins and stacking faults. A possible formation of an equilibrium phase of LiCoO$_2$ can explain the growth anisotropy of the film, causing unexpected nucleation behavior.

As for the ferromagnetic properties of the Co-LiNbO$_3$ film, strong tunnel coupling between large granules in the upper part of the film is excluded due to the wide gaps between the granules (~5 nm) (See Fig. 5.14). The hopping mechanism along the localized defects of the amorphous matrix determines the conductivity of the upper part of the film, and is

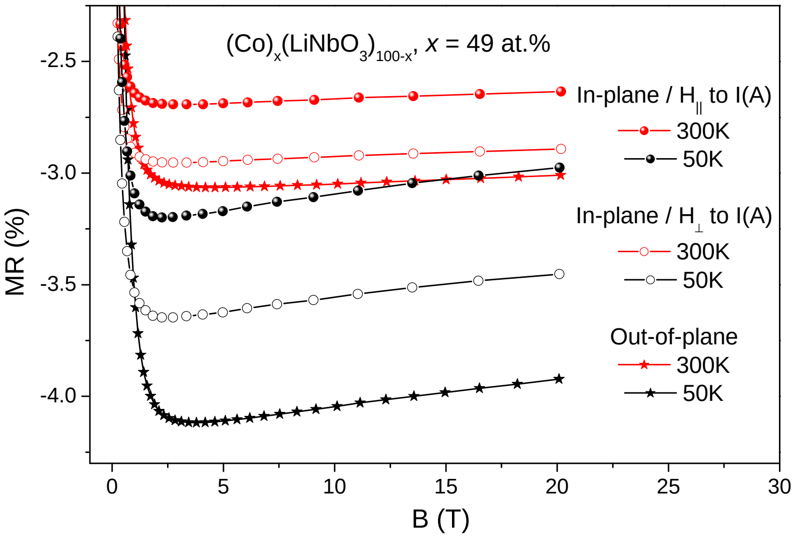

Figure 5.13: Magnetoresistance of the Co-LiNbO$_3$ nanocomposite (x = 49 at.%) at T = 50 and 300 K and at different orientations of a magnetic field (B) relative to the sample plane and current direction.

commonly described by the "$T^{1/4}$" Mott's law. Conductivity of the lower part with the elongated granules can be similar or even higher than the conductivity of the upper part, and is determined by the so-called "oblique tunnelling" with the subsequent transport of electrons along the chains of elongated granules (Beloborodov et al., 2007). Therefore, the conductivity of the film does not follow either "$T^{1/2}$" or "$\ln T$" laws. It should be noted that the high value of permittivity of LiNbO$_3$ (Mitsuyu and Wasa, 1981) decreases the Coulomb blockade energy and, hence, the possible value of LPMR during tunnelling between the granules in the lower part of the film.

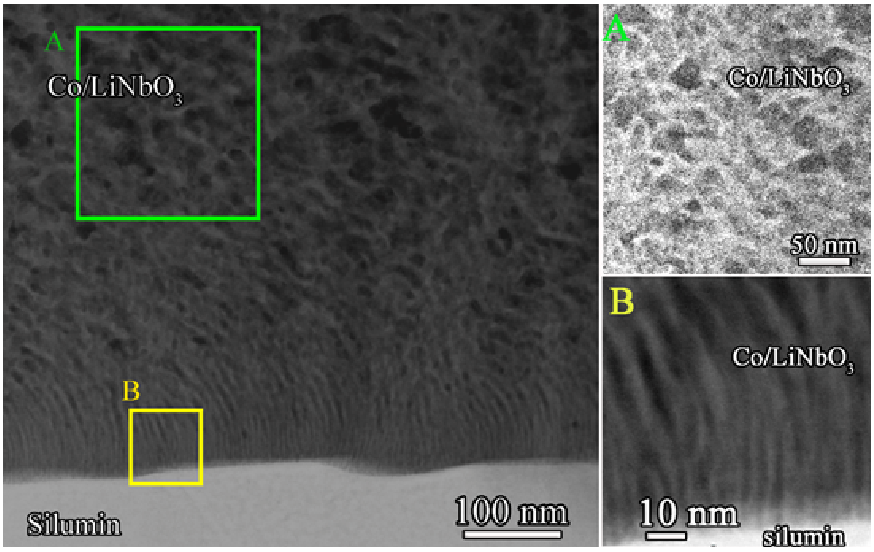

Figure 5.14: A bright-field STEM image of the cross-section of Co-LiNbO$_3$ film (x = 49 at.%) on the glass-ceramic substrate (left side). The top right image (A) shows a dark-field TEM image obtained using hollow cone illumination mode with the objective aperture set in the diffuse background area. Such a mode leads to the bright contrast of the amorphous layer in between the crystalline Co particles. The bottom right image (B) shows a bright-field STEM image of the interface area. The elongated grains forming from the interface up to ∼20–25 nm are clearly visible.

6 Conclusions

The $(ZnO/C)_{25}$ and $(ZnO/C)_{81}$ thin films were fabricated using a layer-by-layer ion-beam sputtering method. The XRD analysis showed the multilayered structure of the $(ZnO/C)_{25}$ films, which consist of crystalline ZnO and amorphous C layers. The $(ZnO/C)_{81}$ films have an island nanocomposite structure, where the nanocrystalline ZnO and amorphous phases of carbon are randomly distributed. Both the $(ZnO/C)_{25}$ and $(ZnO/C)_{81}$ films have N-type conductivity, and their electrical resistivity is 1–3 orders of magnitude lower than those of the undoped ZnO films. The ferromagnetic ordering of the $(ZnO/C)_{25}$ films was observed at $T \leqslant 120$ K with intrinsic coercivity ranging from 30 to 310 G. The calculated values of DOS of the $(ZnO/C)_{25}$ samples are smaller by two orders of magnitude than of the $(ZnO/C)_{81}$, which is associated mainly with different microstructures and thicknesses of the films.

The results of the transport measurements showed that the conduction mechanism of the composite $(ZnO/C)_{81}$ samples with an island structure changes from the variable range hopping in a narrow energy band near the Fermi level (2D Mott's VRH) to the hopping to the nearest neighbors throughout the measured temperature range. The $(ZnO/C)_{25}$ samples show the transition from strong to weak charge localization at h = 150 nm. The additional low-temperature transport measurements of the $(ZnO/C)_{25}$ samples with h = 146 and 153 nm have demonstrated the 2D Mott's variable range hopping mechanism at $T \lesssim 100$ K.

The magnetotransport measurements (up to 20 T) revealed the peculiar low-temperature magnetoresistance behavior of the $(ZnO/C)_{25}$ films with h = 146 and 153 nm. The MR at $T \leqslant 20$ K is negative in low magnetic fields, positive in moderate fields, and again negative in high magnetic fields. Three mechanisms were proposed to explain this unconventional behaviour: the Fermi level shift under the influence of a magnetic field, scattering on the magnetic disorder, and wave function shrinkage due to the effect of the magnetic blockade. The weak local magnetism, which is presumably induced by the defects at the interfaces, strengthens the magnetic blockade effect, causing the suppression of positive MR.

The magnetic, transport and magnetotransport properties of nanogranular metal-insulator composites, fabricated using an ion-beam sputtering process, have been studied. The conduction regimes of nanocomposites below and above a metal-insulator transition have been discussed. The comparative investigation of magnetic and magnetotransport properties of nanocomposites $(CoFeB)_x(LiNbO_3)_{100-x}$ with low ($\lessapprox 10^{21}$ cm^{-3}) and high ($\approx 10^{22}$ cm^{-3}) concentrations of dispersed magnetic ions (Fe, Co) in the dielectric matrix and with total concentrations of metallic phase below the percolation threshold ($x_p \approx$ 50–55 at.%) have been conducted. It has been shown that the increase of the dispersed ions concentration up to $\approx 10^{22}$ cm^{-3} leads to the shift of the metal-insulator transition from 48 to 43 at.%, widening the "metallic" concentration range ($x_c \leqslant x \leqslant x_p$) with strong tunnel coupling between granules, where electrical resistivity follows $\rho \propto \ln T$.

Moreover, magnetic coercivity of nanocomposites with $x < x_c$ (down to 33 at.%) has been observed. The magnetic coercivity is attributed to the presence of dispersed ions that favours superferromagnetic ordering.

Magnetotransport measurements of $(Co)_x(SiO_2)_{100-x}$ (x = 65 at.%) and $(CoNbTa)_x(SiO_2)_{100-x}$ (x = 65 at.%) nanocomposites with concentrations close to the percolation threshold revealed the presence of linear positive magnetoresistance (LPMR) – at T = 4.2 K and in $H > H_{sat}$ this was 0.03 and 0.06% T^{-1}, respectively. Temperature dependencies of resistivity of the nanocomposites that have shown the LPMR follow the logarithmic law ($\rho \propto \ln T$), indicating a strong tunnel coupling between granules. It should be noted that LPMR was observed along with negative MR that is associated with spin-dependent tunnelling. The developed expression based on the influence of the Zeeman effect on the tunnel barrier height in the spin-dependent tunnelling qualitatively explains the results. The MR of $(Co)_x(LiNbO_3)_{100-x}$ (x = 49 at.%) nanocomposite is anisotropic, and the LPMR at T = 50 K is about 10^{-3}% T^{-1}, which is associated with the formation of the columnar structure at the initial stage of growth of this film.

References

Abeles, B., Sheng, P., Coutts, M., and Arie, Y. (1975). Structural and electrical properties of granular metal films. *Advances in Physics*, 24(3), pp. 407–461.

Alexandrov, A.S., Dediu, V.A., and Kabanov, V.V. (2012). Hopping magnetotransport via nonzero orbital momentum states and organic magnetoresistance. *Physical review letters*, 108(18), p. 186601.

Annett, J.F. et al. (2004). *Superconductivity, superfluids and condensates*, vol. 5. Oxford University Press.

Araujo, C.M., et al. (2010). Room temperature ferromagnetism in pristine MgO thin films. *Applied physics letters*, 96(23), p. 232505.

Aronzon, B., et al. (1999). Anomalous Hall effect in granular Fe/SiO_2 films in the tunneling-conduction regime. *Journal of Experimental and Theoretical Physics Letters*, 70(2), pp. 90–96.

Bardeen, J., Cooper, L.N., and Schrieffer, J.R. (1957). Theory of superconductivity. *Physical review*, 108(5), p. 1175.

Bartov, D., Segal, A., Karpovski, M., and Gerber, A. (2014). Absence of the ordinary and extraordinary Hall effects scaling in granular ferromagnets at metal-insulator transition. *Physical Review B*, 90(14), p. 144423.

Bedanta, S., et al. (2007). Overcoming the dipolar disorder in dense CoFe nanoparticle ensembles: Superferromagnetism. *Physical Review Letters*, 98(17), p. 176601.

Bedanta, S. and Kleemann, W. (2008). Supermagnetism. *Journal of Physics D: Applied Physics*, 42(1), p. 013001.

Beloborodov, I., Lopatin, A., Vinokur, V., and Efetov, K.B. (2007). Granular electronic systems. *Reviews of Modern Physics*, 79(2), p. 469.

Blinov, M., et al. (2019). Magnetoresistance of $(Co_{40}Fe_{40}B_{20})_x(SiO_2)_{100-x}$ and $(Co_{84}Nb_{14}Ta_2)_x(Al_2O_3)_{100-x}$ nanocomposites below the percolation threshold in pulsed magnetic fields. *Journal of Magnetism and Magnetic Materials*, 469, pp. 155–160.

Bogren, S., et al. (2015). Classification of magnetic nanoparticle systems–synthesis, standardization and analysis methods in the nanomag project. *International journal of molecular sciences*, 16(9), pp. 20308–20325.

Buchholz, D., Chang, R., Song, J.Y., and Ketterson, J.B. (2005). Room-temperature ferromagnetism in Cu-doped ZnO thin films. *Applied Physics Letters*, 87(8), p. 082504.

Bylsma, R., et al. (1985). Stimulated emission and laser oscillations in ZnSe-$Zn_{1-x}Mn_xSe$ multiple quantum wells at $\sim$453 nm. *Applied physics letters*, 47(10), pp. 1039–1041.

Cage, M.E., et al. (2012). *The quantum Hall effect*. Springer Science & Business Media.

Clarke, J. (1996). SQUID fundamentals. In: *SQUID sensors: fundamentals, fabrication and applications*, pp. 1–62. Springer.

Clarke, J. and Braginski, A.I. (2006). *The SQUID handbook: Applications of SQUIDs and SQUID systems*. John Wiley & Sons.

Clarke, J., Clarke, J., and Braginski, A.I. (2003). *The SQUID Handbook: Fundamentals and Technology of SQUIDs and SQUID Systems*, vol. 1. Wiley-Vch.

Clarke, J., Goubau, W.M., and Ketchen, M.B. (1976). Tunnel junction dc SQUID: fabrication, operation, and performance. *Journal of Low Temperature Physics*, 25(1), pp. 99–144.

Coey, J. (2005). d^0 ferromagnetism. *Solid State Sciences*, 7(6), pp. 660–667.

Coey, J. (2006). Dilute magnetic oxides. *Current Opinion in Solid State and Materials Science*, 10(2), pp. 83–92.

Coey, J. (2019). Magnetism in d^0 oxides. *Nature materials*, 18(7), pp. 652–656.

Coey, J. and Chambers, S. (2008). Oxide dilute magnetic semiconductors–fact or fiction? *MRS bulletin*, 33(11), pp. 1053–1058.

Deaver Jr, B.S. and Fairbank, W.M. (1961). Experimental evidence for quantized flux in superconducting cylinders. *Physical Review Letters*, 7(2), p. 43.

Dietl, T. (2010). A ten-year perspective on dilute magnetic semiconductors and oxides. *Nature materials*, 9(12), pp. 965–974.

Dormann, J., Bessais, L., and Fiorani, D. (1988). A dynamic study of small interacting particles: superparamagnetic model and spin-glass laws. *Journal of Physics C: Solid State Physics*, 21(10), p. 2015.

Efetov, K.B. and Tschersich, A. (2003). Coulomb effects in granular materials at not very low temperatures. *Physical Review B*, 67(17), p. 174205.

Fagaly, R. (2006). Superconducting quantum interference device instruments and applications. *Review of scientific instruments*, 77(10), p. 101101.

Fujimori, H., Mitani, S., and Ohnuma, S. (1995). Tunnel-type GMR in metal-nonmetal granular alloy thin films. *Materials Science and Engineering: B*, 31(1-2), pp. 219–223.

Fujimori, H., Ohnuma, S., Kobayashi, N., and Masumoto, T. (2006). Spintronics in metal–insulator nanogranular magnetic thin films. *Journal of magnetism and magnetic materials*, 304(1), pp. 32–35.

Gallop, J. and Petley, B. (1976). SQUIDs and their applications. *Journal of Physics E: Scientific Instruments*, 9(6), p. 417.

Gan'shina, E., et al. (2004). Evolution of the optical and magnetooptical properties of amorphous metal-insulator nanocomposites. *Journal of Experimental and Theoretical Physics*, 98(5), pp. 1027–1036.

Gerber, A., et al. (2007). Linear positive magnetoresistance and quantum interference in ferromagnetic metals. *Physical review letters*, 99(2), p. 027201.

Guc, M., et al. (2017). Mechanisms of charge transfer and electronic properties of Cu_2ZnGeS_4 from investigations of the high-field magnetotransport. *Scientific reports*, 7(1), pp. 1–13.

Hajdeu-Chicarosh, E., et al. (2018). High-field magnetotransport in Cu_2ZnGeS_4 single crystals. *Solar Energy*, 172, pp. 184–190.

Hikami, S., Larkin, A.I., and Nagaoka, Y. (1980). Spin-orbit interaction and magnetoresistance in the two dimensional random system. *Progress of Theoretical Physics*, 63(2), pp. 707–710.

Hong, N.H., Poirot, N., and Sakai, J. (2008). Ferromagnetism observed in pristine SnO_2 thin films. *Physical Review B*, 77(3), p. 033205.

Hong, N.H., Sakai, J., Poirot, N., and Brizé, V. (2006). Room-temperature ferromagnetism observed in undoped semiconducting and insulating oxide thin films. *Physical Review B*, 73(13), p. 132404.

Ielmini, D. (2016). Resistive switching memories based on metal oxides: mechanisms, reliability and scaling. *Semiconductor Science and Technology*, 31(6), p. 063002.

Innes, A.R. and Rhoderick, E. (1980). *Introduction to superconductivity*. Pergamon Press.

Inoue, J. and Maekawa, S. (1996). Theory of tunneling magnetoresistance in granular magnetic films. *Physical Review B*, 53(18), p. R11927.

Jaime, M., et al. (1996). High-temperature thermopower in $La_{2/3}Ca_{1/3}MnO_3$ films: Evidence for polaronic transport. *Physical Review B*, 54(17), p. 11914.

Jaklevic, R., Lambe, J., Silver, A., and Mercereau, J. (1964). Quantum interference effects in Josephson tunneling. *Physical Review Letters*, 12(7), p. 159.

Josephson, B.D. (1962). Possible new effects in superconductive tunnelling. *Physics letters*, 1(7), pp. 251–253.

Keimer, B., et al. (2015). From quantum matter to high-temperature superconductivity in copper oxides. *Nature*, 518(7538), pp. 179–186.

Kittel, C., McEuen, P., and McEuen, P. (1996). *Introduction to solid state physics*, vol. 8. Wiley New York.

Kobayashi, N., Ohnuma, S., Masumoto, T., and Fujimori, H. (2001). (Fe–Co)–(Mg-fluoride) insulating nanogranular system with enhanced tunnel-type giant magnetoresistance. *Journal of Applied Physics*, 90(8), pp. 4159–4162.

Kurobe, A. and Kamimura, H. (1983). Theory of magnetoresistance in amorphous semiconductors. *Journal of Non-Crystalline Solids*, 59, pp. 41–44.

Lähderanta, E., et al. (2016). Influence of scattering and interference effects on the low-temperature magnetotransport of Cu_2ZnSnS_4 single crystals. *Journal of Applied Physics*, 120(3), p. 035704.

Lähderanta, E., et al. (2018). High-field hopping magnetotransport in kesterites. *Journal of Magnetism and Magnetic Materials*, 459, pp. 246–251.

Lähderanta, E., et al. (2019). Low-temperature quantum magnetotransport of graphene on SiC (0 0 0 1) in pulsed magnetic fields up to 30 T. *Journal of Physics: Condensed Matter*, 32(11), p. 115704.

Lashkova, N., et al. (2016). Synthesis of ZnO-based nanostructures for heterostructure photovoltaic cells. *Semiconductors*, 50(9), pp. 1254–1260.

Lehtinen, P., et al. (2004). Structure and magnetic properties of adatoms on carbon nanotubes. *Physical Review B*, 69(15), p. 155422.

Li, Y., Huang, Q., and Bi, X. (2013). The change of electrical transport characterizations in Ga doped ZnO films with various thicknesses. *Journal of Applied Physics*, 113(5), p. 053702.

Liao, L., et al. (2009). P-type electrical, photoconductive, and anomalous ferromagnetic properties of Cu_2O nanowires. *Applied Physics Letters*, 94(11), p. 113106.

Lifshits, E. and Kosevich, A. (1958). Theory of the Shubnikov-de Haas effect. *Journal of Physics and Chemistry of Solids*, 4(1-2), pp. 1–10.

Liu, C., Yun, F., and Morkoc, H. (2005). Ferromagnetism of ZnO and GaN: a review. *Journal of Materials Science: Materials in Electronics*, 16(9), pp. 555–597.

London, F. and London, H. (1935). The electromagnetic equations of the supraconductor. *Proceedings of the Royal Society of London. Series A-Mathematical and Physical Sciences*, 149(866), pp. 71–88.

Loss, D. and DiVincenzo, D.P. (1998). Quantum computation with quantum dots. *Physical Review A*, 57(1), p. 120.

Maekawa, S. (2004). Spin-dependent transport in magnetic nanostructures. *Journal of Magnetism and Magnetic Materials*, 272, pp. E1459–E1463.

Matsumoto, Y., et al. (2001). Room-temperature ferromagnetism in transparent transition metal-doped titanium dioxide. *Science*, 291(5505), pp. 854–856.

Meissner, W. and Ochsenfeld, R. (1933). Ein neuer effekt bei eintritt der supraleitfähigkeit. *Naturwissenschaften*, 21(44), pp. 787–788.

Meyer, B.K., et al. (2004). Bound exciton and donor–acceptor pair recombinations in ZnO. *physica status solidi (b)*, 241(2), pp. 231–260.

Miccoli, I., Edler, F., Pfnür, H., and Tegenkamp, C. (2015). The 100th anniversary of the four-point probe technique: the role of probe geometries in isotropic and anisotropic systems. *Journal of Physics: Condensed Matter*, 27(22), p. 223201.

Mikhailovskii, Y.O., et al. (2016). Logarithmic temperature dependence of electrical resistivity of $(Co_{41}Fe_{39}B_{20})_x(Al–O)_{100-x}$ nanocomposites. *Physics of the Solid State*, 58(3), pp. 444–446.

Milner, A., et al. (1996). Spin-dependent electronic transport in granular ferromagnets. *Physical review letters*, 76(3), p. 475.

Mitsuyu, T. and Wasa, K. (1981). High dielectric constant films of amorphous $LiNbO_3$ prepared by sputtering deposition. *Japanese Journal of Applied Physics*, 20(1), p. L48.

Montgomery, H. (1971). Method for measuring electrical resistivity of anisotropic materials. *Journal of applied physics*, 42(7), pp. 2971–2975.

Mott, N.F. and Davis, E.A. (2012). *Electronic processes in non-crystalline materials*. Oxford university press.

Movaghar, B. and Schweitzer, L. (1978). A model for the anomalous magnetoresistance in amorphous semiconductors. *Journal of Physics C: Solid State Physics*, 11(1), p. 125.

Nagaosa, N., et al. (2010). Anomalous hall effect. *Reviews of modern physics*, 82(2), p. 1539.

Nikiruy, K., et al. (2019). Adaptive properties of spiking neuromorphic networks with synapses based on memristive elements. *Technical Physics Letters*, 45(4), pp. 386–390.

Nistor, M., Gherendi, F., and Perrière, J. (2018). Degenerate and non-degenerate In_2O_3 thin films by pulsed electron beam deposition. *Materials Science in Semiconductor Processing*, 88, pp. 45–50.

Ohno, H., et al. (2000). Electric-field control of ferromagnetism. *Nature*, 408(6815), pp. 944–946.

Ohnuma, S., Fujimori, H., Mitani, S., and Masumoto, T. (1996). High-frequency magnetic properties in metal–nonmetal granular films. *Journal of Applied Physics*, 79(8), pp. 5130–5135.

Özgür, Ü., et al. (2005). A comprehensive review of ZnO materials and devices. *Journal of applied physics*, 98(4), p. 11.

Pakhomov, A., Yan, X., and Zhao, B. (1995). Giant Hall effect in percolating ferromagnetic granular metal-insulator films. *Applied physics letters*, 67(23), pp. 3497–3499.

Pan, H., et al. (2007). Room-temperature ferromagnetism in carbon-doped ZnO. *Physical review letters*, 99(12), p. 127201.

Park, J.W., et al. (2010). The role of carbon doping in ZnO. *Journal of the Korean Physical Society*, 57(6), pp. 1482–1485.

Philips'Gloeilampenfabrieken, O. (1958). A method of measuring specific resistivity and Hall effect of discs of arbitrary shape. *Philips Res. Rep*, 13(1), pp. 1–9.

Qi, B., Ólafsson, S., and Gíslason, H. (2017). Vacancy defect-induced d^0 ferromagnetism in undoped ZnO nanostructures: Controversial origin and challenges. *Progress in Materials Science*, 90, pp. 45–74.

Quinn III, D. and Ittner III, W. (1962). Resistance in a Superconductor. *Journal of Applied Physics*, 33(2), pp. 748–749.

Raikh, M., et al. (1992). Mechanisms of magnetoresistance in variable-range-hopping transport for two-dimensional electron systems. *Physical Review B*, 45(11), p. 6015.

Ramsteiner, M., et al. (2008). $Co_2FeSi/GaAs/(Al,Ga)As$ spin light-emitting diodes: Competition between spin injection and ultrafast spin alignment. *Physical Review B*, 78(12), p. 121303.

Raquet, B., et al. (2000). Quantum size effect transition in percolating nanocomposite films. *Physical Review B*, 62(24), p. 17144.

Ripka, P. (2021). *Magnetic sensors and magnetometers*. Artech house.

Rjabinin, J. and Shubnikow, L. (1935). Magnetic properties and critical currents of supraconducting alloys. *Nature*, 135(3415), pp. 581–582.

Rode, A.V., et al. (2004). Unconventional magnetism in all-carbon nanofoam. *Physical Review B*, 70(5), p. 054407.

Ru, C., et al. (2010). Automated four-point probe measurement of nanowires inside a scanning electron microscope. *IEEE Transactions on Nanotechnology*, 10(4), pp. 674–681.

Rylkov, V.V., et al. (2018a). Magnetic Metal-Nonstoichiometric Oxide Nanocomposites: Structure, Transport, and Memristive Properties. In: *Novel Magnetic Nanostructures*, pp. 427–464. Elsevier.

Rylkov, V., et al. (2017). Tunneling anomalous Hall effect in nanogranular CoFe-B-Al-O films near the metal-insulator transition. *Physical Review B*, 95(14), p. 144202.

Rylkov, V., et al. (2018b). Properties of granular $(CoFeB)_x(Al_2O_3)_{100-x}$ and $(CoFeB)_x(LiNbO_3)_{100-x}$ nanocomposites: Manifestation of superferromagnetic ordering effects. *Journal of Magnetism and Magnetic Materials*, 459, pp. 197–201.

Rylkov, V., et al. (2018c). Transport, Magnetic, and Memristive Properties of a Nanogranular $(CoFeB)_x(LiNbO_y)_{100-x}$ Composite Material. *Journal of Experimental & Theoretical Physics*, 126(3).

Rylkov, V., et al. (2019). Unusual behavior of the coercive field in a $(CoFeB)_x(LiNbO_y)_{100-x}$ nanocomposite with a high content of magnetic ions in an insulating matrix. *Journal of Experimental and Theoretical Physics*, 128(1), pp. 115–124.

Sawicki, M., Stefanowicz, W., and Ney, A. (2011). Sensitive SQUID magnetometry for studying nanomagnetism. *Semiconductor Science and Technology*, 26(6), p. 064006.

Schmidt, G. and Molenkamp, L.W. (2001). Dilute magnetic semiconductors in spin-polarized electronics. *Journal of Applied Physics*, 89(11), pp. 7443–7447.

Schwartz, B. (2013). *Superconductor applications: SQUIDs and machines*, vol. 21. Springer Science & Business Media.

Shklovskii, B.I. and Efros, A.L. (2013). *Electronic properties of doped semiconductors*, vol. 45. Springer Science & Business Media.

Snider, E., et al. (2020). Room-temperature superconductivity in a carbonaceous sulfur hydride. *Nature*, 586(7829), pp. 373–377.

Sullivan, C.R. (2009). Integrating magnetics for on-chip power: Challenges and opportunities. In: *2009 IEEE Custom Integrated Circuits Conference*, pp. 291–298.

Timopheev, A., et al. (2012). Superferromagnetism and coercivity in $Co\text{-}Al_2O_3$ granular films with perpendicular anisotropy. *Journal of Applied Physics*, 111(12), p. 123915.

Tsymbal, E.Y. and Pettifor, D.G. (2001). Perspectives of giant magnetoresistance. *Solid state physics*, 56, pp. 113–237.

Valdes, L.B. (1954). Resistivity measurements on germanium for transistors. *Proceedings of the IRE*, 42(2), pp. 420–427.

Venkatesan, M., Fitzgerald, C., and Coey, J. (2004a). Unexpected magnetism in a dielectric oxide. *Nature*, 430(7000), pp. 630–630.

Venkatesan, M., Fitzgerald, C., Lunney, J., and Coey, J. (2004b). Anisotropic ferromagnetism in substituted zinc oxide. *Physical review letters*, 93(17), p. 177206.

Wang, X., et al. (2009). Ferromagnetism in carbon-doped ZnO films from first-principle study. *Physics Letters A*, 373(34), pp. 3091–3096.

Wunderlich, J., et al. (2006). Coulomb blockade anisotropic magnetoresistance effect in a (Ga,Mn)As single-electron transistor. *Physical review letters*, 97(7), p. 077201.

Xia, Q. and Yang, J.J. (2019). Memristive crossbar arrays for brain-inspired computing. *Nature materials*, 18(4), pp. 309–323.

Ye, X., et al. (2008). The effect of nitrogen incorporation on the magnetic properties of carbon-doped ZnO. *Journal of Physics D: Applied Physics*, 41(15), p. 155005.

Zhilova, O., et al. (2017). The structure and the gas sensitive properties of the thin films of zinc oxide. In: *AIP Conference Proceedings*, vol. 1886, 1, p. 020054.

Zhilova, O., et al. (2019). Structure and electrophysical properties of thin-film SnO_2–In_2O_3 heterostructures. *Journal of Materials Science: Materials in Electronics*, 30(13), pp. 11859–11867.

Publication I

Volochaev, M.N., Granovsky, A.B., Zhilova, O.V., Kalinin, Y.E., Ryl'kov, V.V., Sumets, M.P., Makagonov, V.A., Pankov, S.Y., Sitnikov, A.V., Fadeev, E., Lahderanta, E., and Foshin, V.A.

Transport and magnetic phenomena in ZnO-C thin-film heterostructures

Reprinted with permission from
Superlattices and Microstructures
Vol. 140, p. 106449, 2020.

Superlattices and Microstructures 140 (2020) 106449

Contents lists available at ScienceDirect

Superlattices and Microstructures

journal homepage: www.elsevier.com/locate/superlattices

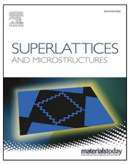

Transport and magnetic phenomena in ZnO-C thin-film heterostructures

M.N. Volochaev [a], A.B. Granovsky [b], O.V. Zhilova [c], Yu.E. Kalinin [c], V.V. Ryl'kov [d], M. P. Sumets [e,*], V.A. Makagonov [c], S. Yu Pankov [c], A.V. Sitnikov [c], E. Fadeev [f], E. Lahderanta [f], V.A. Foshin [c]

[a] Kirensky Institute of Physics, Krasnoyarsk, 660036, Russia
[b] Lomonosov Moscow State University, Moscow, 119991, Russia
[c] Voronezh State Technical University, Voronezh, 394026, Russia
[d] National Research Centre "Kurchatov Institute", Moscow, 123182, Russia
[e] Voronezh State University, Voronezh, 394003, Russia
[f] Lappeenranta-Lahti University of Technology, Lappeenranta FI, 53851, Finland

ARTICLE INFO

Keywords:
Zinc oxide
Amorphous carbon
Multi-layered structures
Composites
Hopping conductivity
Weak localization
Magnetoresistance

ABSTRACT

ZnO- and C-based heterostructures were fabricated by the layer-by-layer deposition technique using the ion-beam sputtering process. Structure, electrical and magnetic properties of fabricated heterostructures are discussed. The two-phase (ZnO and C) films are evolved into a multilayer structure, consisting of amorphous carbon and crystalline ZnO layers when the bilayer thickness increases. When carbon is added to ZnO, its electrical resistivity reduces. The conduction mechanism changes from the variable-range hopping in a narrow energy band to the nearest neighbors hopping in ZnO–C films with a thickness of $h < 150$ nm. The temperature dependence of conductivity changes from the Arrhenius-like to logarithmic law, indicating that the strong charge localization turns into a weak one when the film thickness is about 150 nm. The negative magnetoresistance of up to 1%was detected at 77 K. The film ferromagnetism at the temperature of 10 K was not found.

1. Introduction

The diluted magnetic semiconductors (DMS) are great of interest due to a wide range of their applications like spintronics which base on spin-dependent transport [1,2]. Primarily, DMS are fabricated through the doping of semiconductors by transition metals (TM). As predicted, ZnO and GaN are the ideal candidates for DMS at room temperatures [1]. Even though that ferromagnetism is observed in ZnO-based systems, doped by TM and even without doping in dielectric oxides [3], the reported experimental results are controversial and the origin of ferromagnetism is not clear. Hypothetically, the TM doping produces clusters of the secondary phases, making properties of DMS worse. Thus, the new alternative doping elements like carbon have been investigated actively. Many researchers reported that ZnO, doped by non-magnetic C, manifests the room-temperature ferromagnetism (RTFM) [4,5]. Nevertheless, the physical nature of this phenomenon is still discussing.

Nowadays, there are two explanations of RTFM in the ZnO–C system. The first explanation implies that the hole-mediated exchange

---

* Corresponding author.
E-mail address: maxsumets@gmail.com (M.P. Sumets).

https://doi.org/10.1016/j.spmi.2020.106449
Received 11 November 2019; Received in revised form 5 February 2020; Accepted 17 February 2020

interaction exist in ZnO:C. This interaction occurs between 2p-localized spins of C atoms, residing in O- atomic positions of ZnO (p-p exchange interaction). This model postulates that ZnO:C is a p-type semiconductor contrary to the theoretical models predicting an n-type conductivity of C-doped ZnO films, and manifesting the RTFM [6,7]. Besides, the majority of carbon atoms are in the intersite or Zn positions or forming the graphite-like clusters [5,8]. Thus, the role of carbon in the ferromagnetic ordering of ZnO is still unclear.

The second approach is based on the defect-induced ferromagnetism [1,2]. The ferromagnetic ordering (d^0 -ferromagnetism) as a common effect, supporting this model and originated from RTFM, was detected in pure undoped oxides such as TiO_2, In_2O_3, SnO_2, Cu_2O и MgO [9–13]. According to the density functional theory (DFT), ferromagnetism in ZnO does not stem from the non-paired 2p-states of O atoms neighboring the zinc vacancies (V_{Zn}) and causing the spin polarization in the valence band (V_B) [14]. The strong exchange interaction between 2p orbitals O and high effective masses of carriers near the top of V_B satisfy the Stoner criteria for the occurrence of spontaneous ferromagnetism. This effect cannot be attained easily by doping with the acceptor impurities residing in the O sites in ZnO [15,16]. As emphasized in the works [17–19], oxygen vacancies (V_O) or intersite Zn atoms in the ZnO low-dimension systems like thin films, nanoparticles, and nanowires can trigger the RTFM. Thus, it is still unclear what role the oxygen and zinc vacancies, as well as surface defects, play in the occurrence of d^0-ferromagnetism. Besides, the grain boundaries and interfaces affect the charge transport in oxide semiconductors greatly [20]. The most prominentlythis effect is observed in thin films where the film-substrate interface and film surface influence the charge transport. Consequently, the magnetic properties and transport phenomena in the doped ZnO are interdependent.

From this point of view, the nanostructured ZnO with various types of Zn/O interfaces (ordered and disordered) poses an interest in the study of magnetic ordering and electrical properties of the Zn–O system. It is undoubtedly true that the fabrication technique and conditions dictate the structure and properties of thin films.

Being an effective deposition technique, an ion-beam sputtering method has not utilized for the fabrication of single- and multi-layered ZnO-C heterostructures. Taking into account that the film structure and properties depend on the fabrication method greatly, this paper aims to investigate the structure, charge transport and magnetic properties of ZnO- and C-based multilayer systems, fabricated by the ion-beam sputtering method.

2. Materials and method

Multilayer ZnO–C thin films were fabricated by layer-by-layer ion-beam sputtering of the ZnO and C ceramic targets in an argon atmosphere with a purity of 99.998% at a pressure of 7×10^{-4} Torr as described in Ref. [21]. The targets were fixed and differently positioned in a vacuum chamber on the water-cooled 280×80 mm^2 copper bases. The substrates were located offset from the target erosion zone during the ion-beam sputtering to eliminate the plasma effect on a growing film. A massive aluminum bar served as a substrate holder getting off heat released under the film growth process. The surface temperature was controlled by five thermocouples positioned uniformly along the surface. During the deposition lasting for 3 h 12min and 5 h 50min for the $(ZnO/C)_{25}$ and $(ZnO/C)_{81}$ films respectively, the temperature did not deviate from room temperature more than by 2°. To carry out the layer-by-layer deposition at room temperature, the substrates were moved from one sputtering position to another one, by rotating the substrate holder around a sputtering chamber axis. The silicon wafers (100)Si and pyroceramics were used to investigate the structure and electrical properties respectively. A V-shaped screen was installed between the target and the substrate holder to vary the C- interlayer thickness during a single deposition process. The rotational speed was equal to 0.13 rpm and 0.23 rpm for $(ZnO/C)_{25}$ and $(ZnO/C)_{81}$ films respectively. The numbers 25 and 81 mean the number of passes through the deposition stages, where ZnO and C were sequentially deposited onto a substrate. As demonstrated further, the rotation speed is critical to the film structure. In total 150 samples were fabricated.

To estimate the thickness of each layer in a multilayer structure, a preliminary deposition of single-phase ZnO and C films was performed with the pre-selected process parameters. The thickness of the obtained films was measured using the optical interferometer (MII-4). Knowing the number of revolutions of a carousel, it is possible to calculate the thickness of a monolayer-film, deposited when the substrate passes once the area of material deposition. It is worth noting, that the monolayer thickness estimated by this method, does not account for the possible island growth (i.e. this is the effective thickness provided that this film is continuous).

The number of the substrate holder revolutions determines the number of bilayers in a multilayer heterostructure. According to the method described above, 25 and 81 equivalent bilayers were deposited for each sample at the rotational speed of 0.13 rpm and 0.23 rpm respectively. The total thickness of the multilayers ranged from 40 to 160 nm.

The study of elemental composition was conducted using scanning electron microscopy (SEM, Oxford INCA Energy 250 with an energy dispersive X-ray add-on device on a JEOL JSM-6380 L V). The structure was investigated by X-ray diffraction methods (XRD, Bruker D2 Phaser diffractometer, $\lambda_{CuK\alpha1} = 1.54$ Å) with the DIFFRAC.EVA 3.0 software and the ICDD PDF Release 2012 database. The transmission electron microscopy (TEM) patterns were obtained by a Hitachi HT7700 microscope with an accelerating voltage of 100 kV (W source). The cross-sections of about 40–50 nm thick were made using a single-beam system (a focused ion beam system FIB, Hitachi FB2100). The electrical resistivity of the studied films was measured by the two-probe method using a B7-78/1 universal digital multimeter with errors not exceeding 2%. The thermopower was investigated by the differential method with errors not exceeding 3%. Silver (99.99% of purity) was used as a material for the cold and hot probes.

The Hall measurements were conducted by the Van der Pauw method (ECOPIA HMS-5500) at room temperature and the magnetic field of 0.55 T with the measuring current ranged from 0.1 to 2.0 mA.

The field dependence of magnetization was measured using a SQUID magnetometer (Cryogenic S700X) in the range of ±5 T at a temperature of 10 K. The samples were located vertically in the magnetometer, with their long axis oriented to the field.

3. Results and discussion

The analysis of XRD spectra (Fig. 1a) of thin films deposited onto a rotating substrate revealed that thin carbon films are amorphous [22], whereas a single-phase ZnO sample has the hexagonal crystal structure with the P63mc space group [23]. The multilayer films $(ZnO/C)_{81}$ manifest a texture with the <001>axis perpendicular to the substrate.

The small-angle XRD pattern of the $(ZnO/C)_{81}$ system (Fig. 2a) does not manifest any diffraction maxima, suggesting that an island structure, rather than a multilayer film, is formed in each layer. Consequently, it can be assumed that the zinc oxide nanocrystallites and the amorphous carbon phase are coexisted in $(ZnO/C)_{81}$ films. Thus, despite the layer-by-layer deposition of ZnO and C, the $(ZnO/C)_{81}$ system is a composite with the blurred interlayer interfaces. Therefore, the total film thickness, rather than an equivalent bilayer thickness, has to be used to describe these samples.

As follows from the XRD patterns (Fig. 1b), the $(ZnO/C)_{25}$ system contains the ZnO crystalline phase. The small-angle XRD patterns (Fig. 2b) contain the diffraction peaks, attributed to the formation of a layered structure. The period of the multilayer structure d was calculated through the Bragg formula:

$$n\lambda = 2d \sin \theta \tag{1}$$

here, θ is the Bragg angle, n is the diffraction maximum order (in our case $n = 1$), and λ is the X-ray wavelength.

The obtained values of d for the $(ZnO/C)_{25}$ multilayer heterostructures are in good agreement with those obtained through the optical interferometry.

Fig. 3 shows the TEM micrographs of the studied $(ZnO/C)_{81}$ and $(ZnO/C)_{25}$ films, demonstrating the nanocrystalline structure of the studied samples. Besides, the electron diffraction patterns (see insets in Fig. 3a and b) reveal the phases of hexagonal crystalline ZnO. As mentioned above, analyzing the small-angle XRD patterns, the layered structure is formed for all thin $(ZnO/C)_{25}$ films (Fig. 3b), whereas the $(ZnO/C)_{81}$ system is a randomly distributed composite (Fig. 3a).

Fig. 4a shows the electrical resistivity as a function of thickness for the studied ZnO and $(ZnO/C)_{81}$ samples. As seen from Fig. 4, the electrical resistivity of thin $(ZnO/C)_{81}$ films two orders of magnitude lower than that for a pure ZnO. The reason is that $(ZnO/C)_{81}$ films have a higher number of interfaces and grain boundaries (being the charge transport channels in wide-gap semiconductors [24]) compared to ZnO. The sign of thermopower (Fig. 4b) indicates that both $(ZnO/C)_{81}$ and ZnO films are the n-type semiconductors.

The electrical resistivity and thermopower of $(ZnO/C)_{81}$ layered structure decrease from $1.7 \cdot 10^{-2}$ Ω cm to $4.9 \cdot 10^{-3}$ Ω cm and from 65 μV/K to 47 μV/K when the film thickness rises from 30 nm to 130 nm respectively.

As regards the $(ZnO/C)_{25}$ multilayer structure, it demonstrates a threefold decrease in the electrical resistivity with the thickness

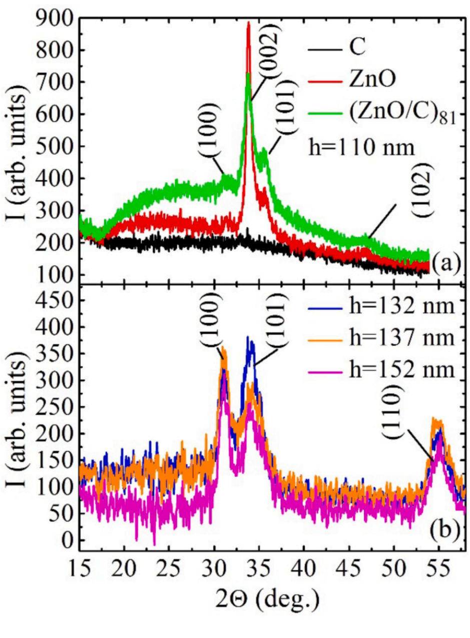

Fig. 1. XRD patterns of C, ZnO, and $(ZnO/C)_{81}$ thin films with the thickness of $h = 110$ nm (a) and $(ZnO/C)_{25}$ (b) with the thickness of 132 nm, 137 nm, and 152 nm.

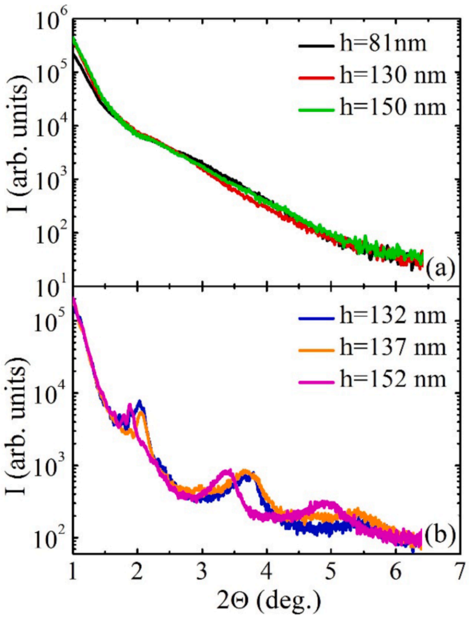

Fig. 2. Small-angle XRD pattern of $(ZnO/C)_{81}$ (a) and $(ZnO/C)_{25}$ (b) thin films.

(see Fig. 5a). The negative sign of thermopower indicates that electrons are the major charge carriers (Fig. 5b). The electrical resistivity of $(ZnO/C)_{25}$ increases with the amount of ZnO in it.

The Hall measurements at room temperature also confirm that the addition of carbon in ZnO does not change its conductivity type. The charge carrier concentration is a weak linear function of the film thickness for $(ZnO/C)_{81}$ and decreases from $5{\cdot}10^{20}$ to $8{\cdot}10^{20}$ cm^{-3} when the thickness rises from 30 nm to 130 nm respectively. Fig. 6 demonstrates how the charge mobility μ depends on the film thickness. A broad maximum with the magnitude of 2 cm^2 V^{-1} s^{-1}, corresponding to the thickness of ~80 nm, is observed on the $\mu(h)$ curve shown in Fig. 6. An increase in the carrier mobility with the thickness d up to 80 nm can be attributed to the classical size effect at the thin film boundaries. The μ declines with $h > 80$ nm, due to the scattering processes at the ZnO/C interfaces.

For the $(ZnO/C)_{25}$ films the carrier concentration and mobility decrease from $3.2{\cdot}10^{20}$ cm^{-3} to $1.6{\cdot}10^{20}$ cm^{-3} and from 1.4 cm^{2}V^{-1}·s^{-1} to 2.8 cm^{2}V^{-1}·s^{-1} respectively when the film thickness rises from 130 nm to 155 nm. The "apparent" decrease in mobility occurs due to electronic states existing at the layer interfaces in the $(ZnO/C)_{25}$ films and influencing the charge transport. When the thickness and number of ZnO and C layers increase their structure remains the same. Consequently, the number of carriers taking part in the charge transport does not change when the amount of material not contributing to the conductivity rises. As a result, the "apparent" decrease in charge concentration occurs. An increase in mobility of the $(ZnO/C)_{25}$ films stems from the classical size effect at the boundaries.

The temperature dependence of electrical resistivity ρ(T) was studied at the temperatures ranged from 80 to 300 K (Fig. 7), to determine the charge transport mechanisms in the samples $(ZnO/C)_{81}$ and $(ZnO/C)_{25}$. As seen from Fig. 7, the electrical resistivity decreases with temperature over the entire temperatures range.

The magnetoresistance (MR) as a function of the magnetic field strength for as-grown layered $(ZnO/C)_{25}$ heterostructures are shown in Fig. 8. The magnitude of MR was determined as$MR = (R_H - R_0)/R_0$, where R_H and R_0 are the resistance, measured in an external magnetic field and without a magnetic field respectively. It follows from Fig. 8 that the electrical resistance declines with the magnetic field strength. For the $(ZnO/C)_{81}$ heterostructures, no change in the electrical resistance was detected under an applied magnetic field of up to 1 T.

The magnetization measurements (see Fig. 9) did not reveal the ferromagnetic ordering at the temperature of 10 K since no hysteresis was detected. This fact rules out the presence of the room temperature magnetism in the studied samples.

Let us discuss the obtained data taking into account the growth process of layered thin-film heterostructures on a rotating substrate with ion-beam sputtering of ZnO and C targets. The $(ZnO/C)_{81}$ system manifests the island-like structure. The electrical resistivity of this two-phase ZnO/C system is much lower than that for ZnO due to the interfaces (Fig. 4a). For the $(ZnO/C)_{25}$ system with the thickness of h < 140 nm, the ZnO layers alternate with the carbon island interlayers, decreasing the electrical resistivity (Fig. 5a). When the islands grow in size in the carbon interlayer, they overlap, increasing the dangling bond concentration at the interfaces, and reducing the electrical resistivity of the film (Fig. 5a). Besides, randomly distributed charges generate a chaotic potential. Thus, in this

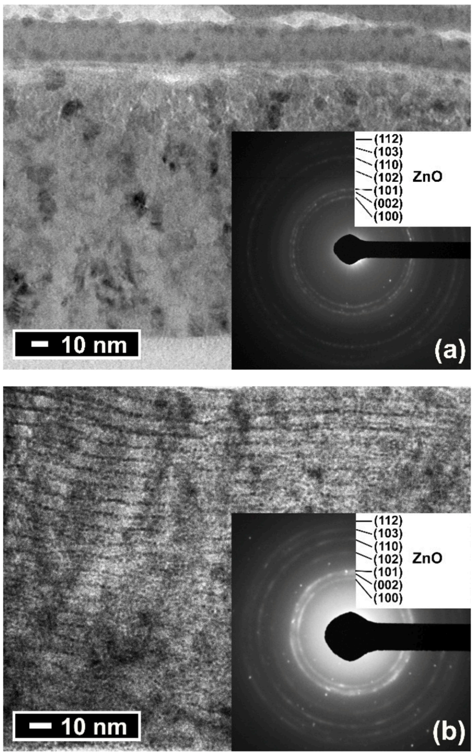

Fig. 3. TEM micrographs of the cross-section and electron diffraction patterns (shown in the insets) for the studied $(ZnO/C)_{81}$ ($h_{Bl} = 1.9$ nm) (a) and $(ZnO/C)_{25}$ ($h_{Bl} = 6.7$ nm) (b) heterostructures with the total thickness of $h = 157$ nm and $h = 135$ nm respectively.

multilayer system, the strong localization conditions take place at the interfaces with the presence of carbon islands [24].

A layered structure, consisting of ZnO and amorphous carbon layers, is formed in the $(ZnO/C)_{25}$ films more than 150 nm thick. The carbon layers and their interfaces serve as the conductive channels in this type of heterostructures. A transition from the strong to weak localization [25,26] occurs when the thickness of $(ZnO/C)_{25}$ films rises. This transition changes the conduction mechanism. A similar relationship was observed in the multilayer structure $(SnO_2/In_2O_3)_{69}$ [27].

To determine the charge transport mechanisms, we investigated the temperature dependence of resistivity in the studied samples. Figs. 10–12 show the relative resistivity of $(ZnO/C)_{81}$ and $(ZnO/C)_{25}$ films as a function of temperature in various coordinates in the temperature range of 77–170 K.

As seen from Fig. 10, the electrical resistivity is linear in the $\ln(\rho/\rho_0)$-$1/T^{1/3}$ coordinates, which is attributed to the variable range hopping mechanism over the localized states in a narrow energy band near the Fermi level [28]. In the framework of this mechanism, the electrical resistivity is described as follows:

$$\rho = \rho_0 \exp\left(B / T^{1/3}\right) \tag{2}$$

where

$$B = \left[\frac{3}{a^2 k_B g(E_F)}\right]^{1/3} \tag{3}$$

here T is the absolute temperature, $g(E_F)$ is the density of states at the Fermi level, a is the localization radius, and k_B is the Boltzmann constant.

The B magnitudes in (2), obtained from the slope of $\ln(\rho/\rho_0)$-$1/T^{1/3}$ linear graphs (see Fig. 10) are given in Table 1. Accepting $a \sim 0.8$ Å [29] as the ionic radius of Zn, we estimated the density of states $g(E_F)$ through equation (3) (see Table 1). The obtained results show a high density of localized states at the Fermi level.

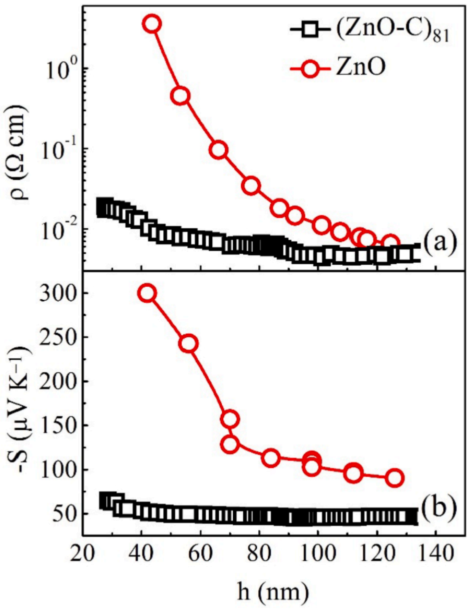

Fig. 4. The electrical resistivity (a) and thermopower (b) as a function of the thickness of thin ZnO and $(ZnO/C)_{81}$ films, measured at room temperature.

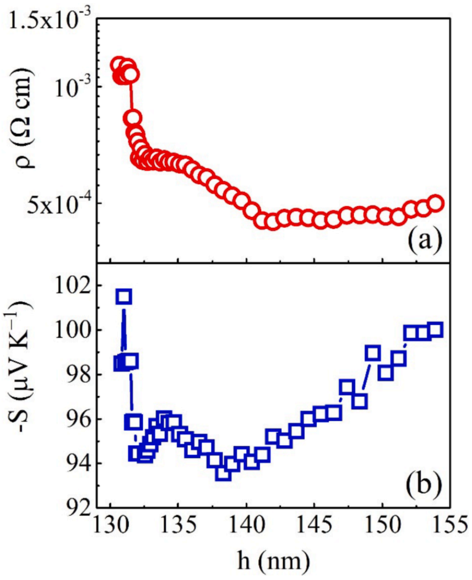

Fig. 5. The electrical resistivity (a) and thermopower (b) as a function of the thickness of thin $(ZnO/C)_{25}$ films, measured at room temperature.

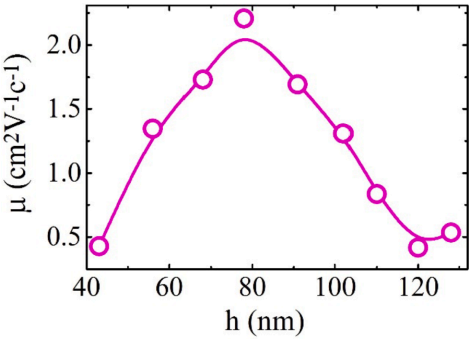

Fig. 6. The carrier mobility as a function of $(ZnO/C)_{81}$ film thickness.

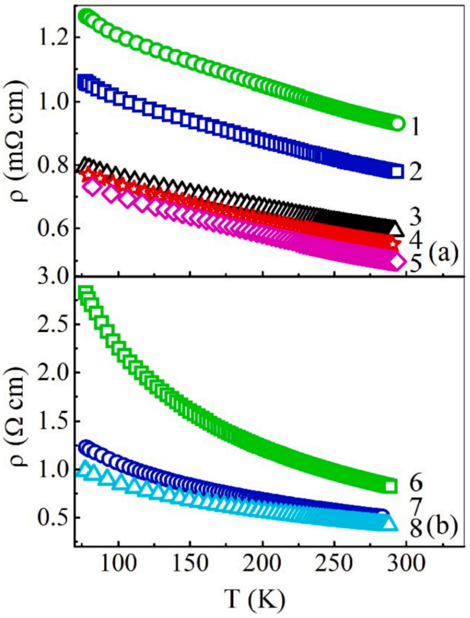

Fig. 7. Temperature dependences of resistivity for thin $(ZnO/C)_{81}$ films (a) and $(ZnO/C)_{25}$ films (b) for various film thicknesses: 1–35 nm, 2–45 nm, 3–70 nm, 4–98 nm, 5–129 nm, 6–150 nm, 7–157 nm, 8–169 nm.

In the temperature range of 200–300 K, the hopping conductivity to the nearest neighbors takes place for the studied samples. According to this mechanism, the temperature dependence of resistivity is given by the following expression [28]:

$$\rho = \rho_0 \cdot \exp\left(- \frac{W_{NNH}}{kT} \right) \tag{4}$$

here W_{NNH} is the hoping activation energy.

The Arrhenius-like temperature dependence of resistivity for the studied $(ZnO/C)_{81}$ films is linear in the $\ln(\rho/\rho_0)$-$1/T$ coordinates in a total agreement with (4) (see Fig. 11). The activation hopping energy estimated from the slope of $\ln(\rho/\rho_0)$-$1/T$ graphs is given in Table 2.

For the $(ZnO/C)_{25}$ multilayer samples with the thickness of $h > 150$ nm (when a continuous carbon layer is formed), the temperature dependence of resistivity is linear in the ρ-$\ln T$ coordinates (see Fig. 12). This dependence is typical when the weak electron

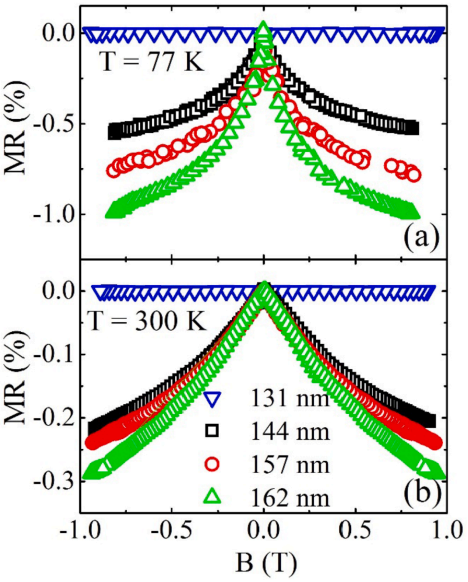

Fig. 8. The electrical resistivity as a function of the magnetic field strength for the $(ZnO/C)_{25}$ and $(ZnO/C)_{81}$ multilayer structures with different bilayer thickness measured at $T = 77$ K (a) and $T = 300$ K (b). (The thickness of $(ZnO/C)_{81}$ multilayer structure is $h = 131$ nm).

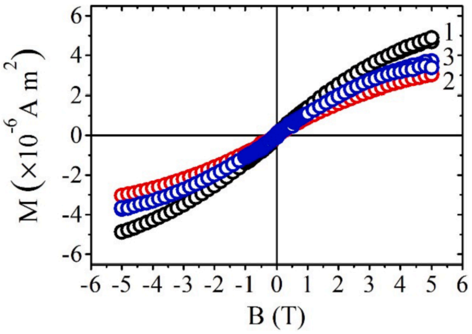

Fig. 9. The magnetization as a function of the magnetic field for multilayer $(ZnO/C)_{25}$ structures with various bilayer thickness: 1–132 nm, 2–136 nm, 3–145 nm and measured at T = 10 K.

localization occurs in 2D and 3D systems [26].

The temperature dependence of resistivity for ZnO:Ga films with a thickness of 100–400 nm, fabricated by the radio-frequency magnetron sputtering process, was studied in the work [30] in the temperature range of 300–80 K. The film resistivity with a thickness of 200 nm declined, whereas for the films 400 nm thick the temperature dependence of resistivity peaked at 160 K.

The observed temperature dependence was explained by the weak charge localization. Besides, the weak localization effects in “thick” films (400 nm) were observed for the temperatures below 160 K. This phenomenon was explained by the low lattice distortions in thick films. Consequently, at the temperature of 160 K, the diffusion length becomes comparable with the free path length within the relaxation time. Also, it was revealed that in ZnO:Ga films, synthesized by the pulsed laser deposition technique, the interference effects in the temperature dependence of resistivity occur at the higher temperatures when the Ga concentration rises. This effect was explained in the work [31] by a defect concentration increase. Taking into account these results the temperature dependence of resistivity observed in our $(ZnO/C)_{25}$ multilayered structures with a thickness of 150 nm at low temperatures can be associated with the weak charge localization.

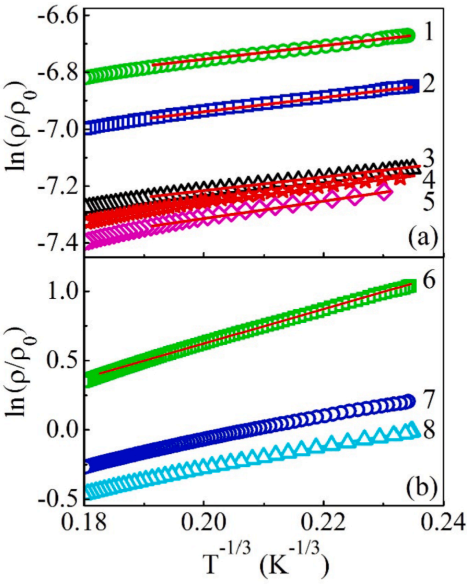

Fig. 10. Temperature dependence of resistivity in the ln$\rho\sim 1/T^{1/3}$ coordinates for thin $(ZnO/C)_{81}$ (a) and $(ZnO/C)_{25}$ (b) films with various thickness: 1–35 nm, 2–45 nm, 3–70 nm, 4–98 nm, 5–129 nm, 6–150 nm, 7–157 nm, 8–169 nm.

Table 1
The *B*-parameter and density of states $g(E_F)$ at the Fermi level in eqs. (2) and (3) determined for $(ZnO–C)_{81}$ thin films.

h (nm)	$B(K^{1/3})$	$g(E_F)_{2D}$ ($eV^{-1}cm^{-2}$)
35	2.56	$3.2\cdot10^{17}$
45	2.52	$3.4\cdot10^{17}$
70	2.28	$4.6\cdot10^{17}$
98	2.75	$2.6\cdot10^{17}$
129	3.13	$1.8\cdot10^{17}$

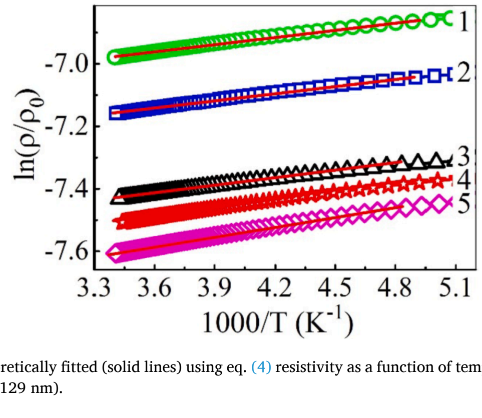

Fig. 11. Experimental (dots) and theoretically fitted (solid lines) using eq. (4) resistivity as a function of temperature for thin $(ZnO/C)_{81}$ films (1–35 nm, 2–45 nm, 3–70 nm, 4–98 nm, 5–129 nm).

Table 2
The hopping activation energy W_{NNH} (see eq. (4)) for thin $(ZnO/C)_{81}$ films in the temperature range of 200–300 K.

h (nm)	W_{NNH} (eV)
31	0.0068
45	0.0068
70	0.0066
98	0.0076
129	0.0089

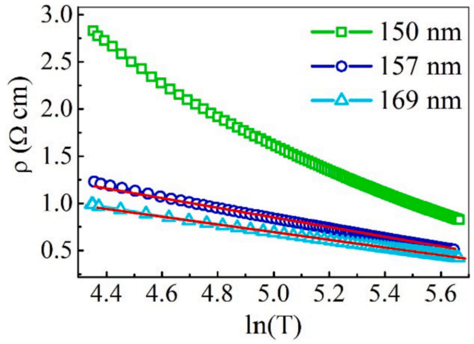

Fig. 12. Temperature dependence of resistivity for multilayer $(ZnO/C)_{25}$ heterostructures in the temperature range of 77–300 K in the ρ-ln(T) coordinates.

Fig. 9 shows the magnetization of the studied samples of various thicknesses as a function of the magnetic field. As seen in Fig. 9, ferromagnetism is not observed in the fabricated films at 10 K.

According to the literature [4,7,32], there are two scenarios for the formation of long-range magnetic ordering in ZnO-C films. In the first scenario, the carbon doping leads to a substitution of oxygen by carbon, with the formation of ZnC complexes, and generating the hole conductivity. This process initiates the ferromagnetic exchange between ZnC with the magnetic moment of 2.02 μB per C atom and affects the Curie temperature, exceeding 400 K. This scenario, was observed in Ref. [4] for the films fabricated by the pulsed laser deposition method. However, we rule out this first scenario, because our Hall and thermopower measurements demonstrate that the carbon doping does not produce the hole conductivity in the studied samples, which agrees with the work [8]. This scenario is not possible in our case because of the specific conditions of the layer-by-layer deposition method. It is worth noting, that according to the structural analysis, the ZnC phase was not detected. The second scenario is associated with the defect-induced magnetism(when the exchanging magnetic moments are formed on the dangling bonds [8]). Taking into account the electron concentration, contributing the conductivity, the presence of a large number of interfaces and the island structure produce a high defect concentration in our multilayer samples. However, we did not detect the ferromagnetism in the studied heterostructures. It does not rule out the possible formation of the magnetic moments on defects, but it seems that the exchange interaction is weak, making it lower the measurement equipment sensitivity.

The negative MR is usually considered as a consequence of the ferromagnetic ordering, but in our samples, there is no long-range magnetic order and it is necessary to conduct some extra investigations of samples with higher thickness. It is possible to explain the negative MR through quantum interference and non-interference mechanisms. The interference mechanisms are possible both in the case of variable-range hopping conductivity [33,34] and in the weak localization case (see, for example [35]). The logarithmic temperature dependence of resistivity attributed to weak localization in 2D systems (see Fig. 12) confirms the interference nature of negative MC. The charge transport occurs along the interfaces between ZnO and C. It is important to emphasize, that for the $(ZnO–C)_{81}$ films (h = 137 nm), having not continuous ZnO and C layers and demonstrating the hopping conductivity, resistivity does not depend on the magnetic field in the studied range. A specific noninterference mechanism, related to the non-spherical wave functions of electrons in the quantum wells, was proposed in Ref. [33]. This mechanism is characterized by a large value of MR (estimated to be MR = 15% [36]), a weak temperature dependence, and a linear dependence on the magnetic field. Since the field dependence is nonlinear at the temperature of 77 K, it is unlikely if the mentioned above mechanism takes place in our case. Besides, the formation of any well-defined quantum wells in the multilayer system $(ZnO/C)_{25}$ is highly doubtful. It is worth noting that in the $(ZnO/C)_{81}$ system, where the formation of quantum wells is potentially possible due to the island structure, a negative MR was found neither at room temperature nor at 77 K. Another non-interference mechanism is originated from the partial suppression of electron scattering on the magnetic moments of defects by an external magnetic field. This effect is similar to the magnetoresistance in the spin glasses or the paramagnetic ferromagnetic alloys. In our samples, this mechanism is supported by the fact that MR takes place at room temperature. Besides, the observed field dependence of the negative MR is similar to the field dependence of squared magnetization at low and room temperature. However, based on this mechanism, the value of MR at room temperature has to be more than one order of magnitude less than that at 77 K, which is not observed in our samples. Also, the relatively large magnitude of MR makes this mechanism to be scarcely realized. Thus, the observed negative magnetoresistance in the multilayer $(ZnO/C)_{25}$ system can be attributed to weak localization and 2D charge transport along the interfaces between ZnO and C layers. More detailed further studies can clarify the possible mechanisms associated with this effect.

4. Conclusions

The thin $(ZnO/C)_{81}$ and $(ZnO/C)_{25}$ films were fabricated through the layer-by-layer deposition of ZnO and C by the ion-beam sputtering method at various deposition rates. The results of XRD analysis revealed that the $(ZnO/C)_{81}$ samples are not multilayers, rather the zinc oxide nanocrystallites are randomly embedded in an amorphous carbon matrix. Thin $(ZnO/C)_{25}$ films are multilayered, consisting of ZnO crystalline and amorphous C layers. It was revealed that $(ZnO/C)_{81}$ and $(ZnO/C)_{25}$ thin-film samples manifest the n-type conductivity, with the electrical resistivity of 1–2 orders of magnitude lower than that in ZnO films without C.

The conduction mechanism changes from the variable-range hopping in a narrow energy band near the Fermi level to the hopping to the nearest neighbor mechanism in thin $(ZnO/C)_{81}$ films with an island structure. The transition from an island to a continuous structure of ZnO layers with the multilayer thickness of about 150 nm is accompanied by the transition from the strong to weak localization of charge carriers, along with the conduction mechanism changes in the studied temperature range. The fabricated films do not exhibit ferromagnetism at the temperature range from 10 K to room temperature. In the multilayer $(ZnO/C)_{25}$ thin-film structures with various bilayer thicknesses the negative magnetoresistive effect was detected at $T = 77$ K and at $T = 300$ K. The magnitude and temperature dependence of MR cannot be explained in the framework of interference and non-interference mechanisms of negative magnetoresistance. The magnitude and temperature dependence of MR can be explained by weak localization and 2D charge transport along the interfaces between ZnO and C layers.

Declaration of competing interest

No conflict of interest exists.

Acknowledgments

The work was supported by the Ministry of Education and Science of Russia (project No. 3.1867.2017/4.6) and the RFBR (project No. 19-07-00471). The work was partially funded by the Academy of Finland.

References

[1] T. Dietl, A ten-year perspective on dilute magnetic semiconductors and oxides, Nat. Mater. 9 (2010) 965–974, https://doi.org/10.1038/nmat2898.

[2] O. Volnianska, P. Boguslawski, Magnetism of solids resulting from spin polarization of p orbitals, J. Phys. Condens. Matter 22 (2010), https://doi.org/10.1088/0953-8984/22/7/073202.

[3] M. Venkatesan, C.B. Fitzgerald, J.M.D. Coey, Unexpected magnetism in a dielectric oxide, Nature 430 (2004) 630, https://doi.org/10.1038/430630a.

[4] H. Pan, J.B. Yi, L. Shen, R.Q. Wu, J.H. Yang, J.Y. Lin, Y.P. Feng, J. Ding, L.H. Van, J.H. Yin, Room-temperature ferromagnetism in carbon-doped ZnO, Phys. Rev. Lett. 99 (2007) 127201, https://doi.org/10.1103/PhysRevLett.99.127201.

[5] X.J. Ye, H.A. Song, W. Zhong, M.H. Xu, X.S. Qi, C.Q. Jin, Z.X. Yang, C.T. Au, Y.W. Du, The effect of nitrogen incorporation on the magnetic properties of carbon-doped ZnO, J. Phys. D Appl. Phys. 41 (2008), https://doi.org/10.1088/0022-3727/41/15/155005.

[6] K. Tang, S. Gu, S. Zhu, W. Liu, J. Ye, J. Zhu, R. Zhang, Y. Zheng, X. Sun, Carbon clusters in N-doped ZnO by metal-organic chemical vapor deposition, Appl. Phys. Lett. 93 (2008), https://doi.org/10.1063/1.2992197.

[7] X. Wang, X. Chen, R. Dong, Y. Huang, W. Lu, Ferromagnetism in carbon-doped ZnO films from first-principle study, Phys. Lett. Sect. A Gen. At. Solid State Phys. 373 (2009) 3091–3096, https://doi.org/10.1016/j.physleta.2009.06.049.

[8] S.-H. Choi, D. Lim, J.W. Park, D.H. Kim, M. Lee, The role of carbon doping in ZnO, J. Kor. Phys. Soc. 57 (2010) 1482–1485, https://doi.org/10.3938/jkps.57.1482.

[9] M. Venkatesan, C.B. Fitzgerald, J.M.D. Coey, Unexpected magnetism in a dielectric oxide, Nature 430 (2004) 630, https://doi.org/10.1038/430630a.

[10] N.H. Hong, N. Poirot, J. Sakai, Ferromagnetism observed in pristine Sn O2 thin films, Phys. Rev. B Condens. Matter 77 (2008), https://doi.org/10.1103/PhysRevB.77.033205.

[11] G.Z. Xing, J.B. Yi, D.D. Wang, L. Liao, T. Yu, Z.X. Shen, C.H.A. Huan, T.C. Sum, J. Ding, T. Wu, Strong correlation between ferromagnetism and oxygen deficiency in Cr-doped In2 O3-δ nanostructures, Phys. Rev. B Condens. Matter 79 (2009), https://doi.org/10.1103/PhysRevB.79.174406.

[12] C.M. Araujo, M. Kapilashrami, X. Jun, O.D. Jayakumar, S. Nagar, Y. Wu, C. Århammar, B. Johansson, L. Belova, R. Ahuja, G.A. Gehring, K.V. Rao, Room temperature ferromagnetism in pristine MgO thin films, Appl. Phys. Lett. 96 (2010), https://doi.org/10.1063/1.3447376.

[13] L. Liao, B. Yan, Y.F. Hao, G.Z. Xing, J.P. Liu, B.C. Zhao, Z.X. Shen, T. Wu, L. Wang, J.T.L. Thong, C.M. Li, W. Huang, T. Yu, P -type electrical, photoconductive, and anomalous ferromagnetic properties of Cu2 O nanowires, Appl. Phys. Lett. 94 (2009), https://doi.org/10.1063/1.3097029.

[14] H. Peng, H.J. Xiang, S.H. Wei, S.S. Li, J.B. Xia, J. Li, Origin and enhancement of hole-induced ferromagnetism in first-row d0 semiconductors, Phys. Rev. Lett. 102 (2009), https://doi.org/10.1103/PhysRevLett.102.017201.

[15] H.K. Chandra, P. Mahadevan, Defect induced local moment in ZnO as a consequence of Stoner mechanism, Solid State Commun. 152 (2012) 762–766, https://doi.org/10.1016/j.ssc.2012.01.050.

[16] E. Stoner, Collective electron ferronmagnetism, Proc. R. Soc. London. Ser. A. Math. Phys. Sci. 165 (1938) 372–414, https://doi.org/10.1098/rspa.1938.0066.

[17] T.L. Phan, Y.D. Zhang, D.S. Yang, N.X. Nghia, T.D. Thanh, S.C. Yu, Defect-induced ferromagnetism in ZnO nanoparticles prepared by mechanical milling, Appl. Phys. Lett. 102 (2013), https://doi.org/10.1063/1.4793428.

[18] C.S. Ong, T.S. Herng, X.L. Huang, Y.P. Feng, J. Ding, Strain-induced ZnO spinterfaces, J. Phys. Chem. C 116 (2012) 610–617, https://doi.org/10.1021/jp205251z.

[19] D. Wang, Z.Q. Chen, D.D. Wang, N. Qi, J. Gong, C.Y. Cao, Z. Tang, Positron annihilation study of the interfacial defects in ZnO nanocrystals: correlation with ferromagnetism, J. Appl. Phys. 107 (2010), https://doi.org/10.1063/1.3291134.

[20] V.A. Coleman, C. Jagadish, Basic properties and applications of ZnO, in: Zinc Oxide Bulk, Thin Film, Nanostructures, Elsevier Ltd, 2006, pp. 1–20, https://doi.org/10.1016/B978-008044722-3/50001-4.

[21] V.V. Rylkov, S.N. Nikolaev, V.A. Demin, A.V. Emelyanov, A.V. Sitnikov, K.E. Nikiruy, V.A. Levanov, M.Y. Presnyakov, A.N. Taldenkov, A.L. Vasiliev, K. Y. Chernoglazov, A.S. Vedeneev, Y.E. Kalinin, A.B. Granovsky, V.V. Tugushev, A.S. Bugaev, Transport, magnetic, and memristive properties of a nanogranular (CoFeB) x (LiNbO y)100–x composite material, J. Exp. Theor. Phys. 126 (2018) 353–367, https://doi.org/10.1134/S1063776118020152.

[22] Y.E. Kalinin, M.A. Kashirin, V.A. Makagonov, S.Y. Pankov, A.V. Sitnikov, Properties of amorphous carbon thin films grown by ion beam sputtering, Tech. Phys. 62 (2017) 1724–1730, https://doi.org/10.1134/S1063784217110123.

[23] O.V. Zhilova, S.Y. Pankov, A.V. Sitnikov, Y.E. Kalinin, I.V. Babkina, The structure and the gas sensitive properties of the thin films of zinc oxide, in: AIP Conf. Proc., AIP Publishing LLC, 2017, 020054, https://doi.org/10.1063/1.5002951.

[24] N.A. Lashkova, A.I. Maximov, A.A. Ryabko, A.A. Bobkov, V.A. Moshnikov, E.I. Terukov, Synthesis of ZnO-based nanostructures for heterostructure photovoltaic cells, Semiconductors 50 (2016) 1254–1260, https://doi.org/10.1134/S106378261609013X.

[25] T.A. Polyanskaya, Y.V. Shmartsev, Quantum corrections to the conductivity OF semiconductors with a two-dimensional and a 3-DIMENSIONAL electron-gas-experiments, Sov. Phys. Semiconduct. 23 (1989) 1–19.

[26] M. Nistor, F. Gherendi, J. Perrière, Degenerate and non-degenerate In2O3 thin films by pulsed electron beam deposition, Mater. Sci. Semicond. Process. 88 (2018) 45–50, https://doi.org/10.1016/J.MSSP.2018.07.024.

[27] O. V Zhilova, S.Y. Pankov, A.V. Sitnikov, Y.E. Kalinin, M.N. Volochaev, V.A. Makagonov, Structure and electrophysical properties of thin-film SnO2-In2O3 heterostructures, J. Mater. Sci. Electron. 30 (2019) 11859–11867.

[28] E.A.D.N.F. Mott, Electronic Processes in Non-crystalline Materials, Clarendon-Press, Oxford, 1971, https://doi.org/10.1002/crat.19720070420.

[29] G.V. Samsonov (Ed.), Handbook of the Physicochemical Properties of the Elements, Springer US, Boston, MA, 1968, https://doi.org/10.1007/978-1-4684-6066-7.

[30] Y. Li, Q. Huang, X. Bi, The change of electrical transport characterizations in Ga doped ZnO films with various thicknesses, J. Appl. Phys. 113 (2013), 053702, https://doi.org/10.1063/1.4789985.

[31] V. Bhosle, A. Tiwari, J. Narayan, Electrical properties of transparent and conducting Ga doped ZnO, J. Appl. Phys. 100 (2006), 033713, https://doi.org/10.1063/1.2218466.

[32] D.K. Mishra, J. Mohapatra, M.K. Sharma, R. Chattarjee, S.K. Singh, S. Varma, S.N. Behera, S.K. Nayak, P. Entel, Carbon doped ZnO: synthesis, characterization and interpretation, J. Magn. Magn Mater. 329 (2013) 146–152, https://doi.org/10.1016/J.JMMM.2012.09.058.

[33] B.L. Altshuler, A.G. Aronov, D.E. Khmelnitskii, Negative magnetoresistance in semiconductors in the hopping conduction region, JETP Lett. (Engl. Transl.) 36 (1982) 195–198.

[34] V.L. Nguyen, B.Z. Spivak, B.I. Shklovskii, Tunnel hopping in disordered systems, Sov. Phys. JETP 62 (1985) 1021–1029.

[35] T. Ohyama, M. Okamoto, E. Otsuka, Weak localization and correlation effects of two dimensional electrons in indium-tin-oxide films, J. Phys. Soc. Japan. 52 (1983) 3571–3578, https://doi.org/10.1143/JPSJ.52.3571.

[36] A.V. Shumilin, Negative magnetoresistance in the regime of hopping conduction through p states at quantum dots, JETP Lett. (Engl. Transl.) 95 (2012) 416–419, https://doi.org/10.1134/S0021364012080115.

Publication II

Fadeev, E.A., Lähderanta, E., Aronzon, B.A., Mekhiya, A.B., Kalinin, Yu.E.,
Makagonov, V.A., Pankov, S.Yu., Foshin, V.A., and Granovsky, A.B.
Unconventional magnetoresistance in ZnO/C multilayers at low temperatures

Reprinted with permission from
Journal of Magnetism and Magnetic Materials
Vol. 535, p. 167963, 2021.

Journal of Magnetism and Magnetic Materials 535 (2021) 167963

Contents lists available at ScienceDirect

Journal of Magnetism and Magnetic Materials

journal homepage: www.elsevier.com/locate/jmmm

Unconventional magnetoresistance in ZnO/C multilayers at low temperatures

E.A. Fadeev [a,*], E. Lähderanta [a], B.A. Aronzon [b], A.B. Mekhiya [b], Yu.E. Kalinin [c], V. A. Makagonov [c], S.Yu. Pankov [c], V.A. Foshin [c], A.B. Granovsky [d,e]

[a] Department of Physics, Lappeenranta-Lahti University of Technology LUT, Lappeenranta 53851, Finland
[b] Lebedev Physical Institute RAS, Moscow 119991, Russia
[c] Voronezh State Technical University, Voronezh 394026, Russia
[d] Faculty of Physics, Lomonosov Moscow State University, Moscow 119991, Russia
[e] Institute of Applied and Theoretical Electrodynamics RAS, Moscow 127412, Russia

ARTICLE INFO

Keywords:
Magnetoresistance
Zinc oxide
Amorphous carbon
Hopping conductivity

ABSTRACT

A layer-by-layer sputtering method was used to fabricate nanostructures $(ZnO/C)_{25}$ composed of zinc oxide and carbon alternating layers, with a total multilayer thickness of 146 nm and 153 nm. At low temperatures, the multilayers show signatures of local ferromagnetic order: magnetic hysteresis, weak magnetization and the characteristic shape of the thermomagnetic curve. In-plane and out-of-plane magnetoresistance (MR) was measured in a pulsed magnetic field up to 20 T in the temperature range of 15–300 K. At $T \leqslant 20$ K, MR changed its sign from negative in low magnetic fields to positive in moderate fields, and then back to negative in high magnetic fields. At $T \geqslant 80$ K, MR was negative in the full range of magnetic fields studied. The unusual MR behavior can be associated with the influence of the Zeeman effect on the Fermi level position in the case of 2D variable hopping conduction along the interfaces, scattering on magnetic heterogeneities and the effect of magnetic blockade.

1. Introduction

Recently, a lot of effort has been devoted to the development and fabrication of magnetic semiconductors with a high Curie temperature (T_C) and at the same time with sufficient for practical applications value of magnetization. Attempts to dope semiconductors (e.g. GaAs, InSb, Si) or oxides (e.g. ZnO, TiO_2, SiO_2) with transition metals, mostly Mn or Co, have not led to success, although several papers have demonstrated semiconductors with T_C higher than room temperature (RT) [1,2]. An important step was the discovery of ferromagnetic ordering in magnetic semiconductors without doping with transition metals, so-called d^0 magnetism [3]. This finding triggered study of the magnetic properties of semiconductors and oxides doped with paramagnetic and diamagnetic materials. In the latter class of materials, the ZnO-C compound plays an important role, since undoped ZnO and C exhibit ferromagnetic properties when in the form of nanoparticles or thin films [4]. In particular, thin films of ZnO-C fabricated by a pulsed laser deposition method have shown the presence of ferromagnetic order at temperatures above 400 K with a magnetic moment of about $3\mu_B$ per carbon atom with hole-type conductivity [5]. Moreover, ferromagnetism above room temperature with electron-type conductivity has been observed in the same compound grown by metal–organic chemical vapor deposition (MOCVD) technique in a nitrogen or oxygen atmosphere [6]. Our earlier attempts to discover RT ferromagnetism in thin films of ZnO-C and multilayers of ZnO/C fabricated using a layer-by-layer ion-beam sputtering method failed [7]. Information in the literature indicates that the magnetic properties of ZnO-C depend significantly on the fabrication method, structural defects, grain boundaries and type of conductivity. The nature of the ferromagnetic ordering and the role of the ZnO and C in the formation of magnetic properties are still unclear (See discussion in [7]).

The present work contains results of low-temperature magnetic and magnetotransport measurements of nanostructures fabricated by layer-by-layer sputtering of ZnO and C. The multilayers possess local ferromagnetism at low temperatures and demonstrate peculiar behavior of magnetoresistance being negative in low magnetic fields, positive in moderate fields, and again negative in high magnetic fields. In the previous paper, structural, magnetotransport and magnetic

---

[*] Corresponding author.
E-mail address: egor.fadeev@lut.fi (E.A. Fadeev).

https://doi.org/10.1016/j.jmmm.2021.167963
Received 11 December 2020; Received in revised form 22 March 2021; Accepted 23 March 2021

measurements of the same nanostructures were carried out at $T > 70$ K, but we did not observe either positive magnetoresistance or ferromagnetic behavior [7].

2. Experiment

Nanostructures $(ZnO/C)_{25}$ were fabricated by layer-by-layer ion beam sputtering of alternating ZnO and C targets onto (100) Si substrate in an argon atmosphere and at a pressure of 7×10^{-4} torr. The subscript “25” means the number of equivalent bilayers deposited onto the substrate. The targets with a purity of 99.998% were kept at room temperature during the entire sputtering process (3 h 12 min). A special setup was used to change the targets during the sputtering process at a speed of 0.13 rpm. A V-shaped screen was installed between the target and substrate holder to vary the thickness of the C- interlayer. Two obtained $(ZnO/C)_{25}$ multilayer structures with a total thickness (h) of 146 and 153 nm were used to investigate magnetotransport and magnetic properties. The only difference between the two presented samples is their thickness. The thickness of the ZnO/C bilayer is $146/25 = 5.84$ nm and $153/25 = 6.12$ nm, correspondingly. The thickness of carbon sublayer does not exceed 1 nm that follows from the TEM micrograph of the sample cross-section presented in [7]. A detailed description of the fabrication method and structural properties can be found in [7]. The heterostructures consist of nanocrystal ZnO and amorphous C layers [7]. Analysis of the temperature dependence of resistivity, and thermoelectric and Hall effects in the range of 80–300 K revealed n-type conductivity and 2D charge transport along the interfaces between ZnO and C [7].

The temperature dependence of resistivity in the temperature range of 15–300 K was recorded with a standard DC four-probe method. Pulsed magnetic fields (B) up to 20 T were applied to measure the MR with the field oriented parallel to the multilayers (in-plane) and perpendicular (out-of-plane). Applied current in the pulsed measurements was ranging, depending on the temperature, from 4 μA to 100 μA for $h = 146$ nm and from 100 μA to 1 mA for $h = 153$ nm. The symmetric (“half-sine shaped”) pulse was used with a duration of 11 ms. Special hardware and software were used to exclude parasitic signals induced by dB/dt. The magnetic field and temperature dependencies of magnetization in the in-plane orientation were measured using a SQUID magnetometer (”Cryogenic S700X”). In the present work, extraction of the magnetic moment was realized with a so-called linear motor instead of stepper motor as in [7]. This allowed us to increase measurement accuracy and to detect apparent magnetic hysteresis loops at $T \leqslant 120$ K.

3. Results and discussion

Fig. 1a presents the temperature dependence of resistivity at $T =$ 15–300 K in zero magnetic field. The resistivity rises with temperature decrease and as can be seen from Fig. 1b, behavior at $T < 80$ K is well described by the 2D Mott’s variable range hopping (VRH) mechanism [8]:

$$\rho = \rho_0 exp\left[\left(\frac{T_M}{T}\right)^{\frac{1}{3}}\right];\ T_M = \frac{\beta}{k_B g(\mu) a^2}, \tag{1}$$

where k_B is the Boltzmann constant, $g(\mu)$ is density of states at the Fermi level and a is localization radius. Different temperature dependencies of resistivity can be observed, but only the above-mentioned dependence fits well, which indicates 2D Mott’s VRH along the interfaces in the heterostructures $(ZnO/C)_{25}$. This finding agrees with the results in [7]. Additionally, it implies weak conductivity of C at low temperatures and a high concentration of interface defects, which leads to elevated charge carrier concentration in comparison to individual C or ZnO. Since thickness of the carbon layers is less than 1 nm (See the TEM micrograph in [7]), by interfaces we mean both interfaces themselves and adjacent carbon layers. The localization radius, a, can be estimated as the Bohr radius $a \approx a_B = \frac{\hbar^2 \varepsilon}{me^2}$, where ε is dielectric permeability and m is electron effective mass. For ZnO, $\varepsilon = 7.8$ and $m = 0.24$ [9], therefore $a = 1.73$ nm. For a rectangular shape of the density of states, $\beta = 13.8$ [10]. Then from Fig. 1b and Eq. (1) we obtain $T_M = 1405$ and 779 K, $g(\mu) = 3.7 \times 10^{15}$ eV^{-1} cm^{-2} and 6.9×10^{15} eV^{-1} cm^{-2} for the samples with $h = 153$ and 146 nm, respectively. The estimated value of the density of states for the $[ZnO/C]_{25}$ multilayers is about two orders of magnitude smaller than for the previously studied $[ZnO\text{-}C]_{81}$ samples, which are rather composites with randomly distributed ZnO and C than multilayers [7]. Therefore, the discrepancy in $g(\mu)$ is mostly due to the different microstructure and thickness of the samples $[ZnO/C]_{25}$ and $[ZnO\text{-}C]_{81}$. In addition, we have calculated the localization radius as $a = 1.73$ nm for the ZnO, whereas in [7] the Zn ion radius was taken as the localization radius.

Out-of-plane MR (See Fig. 2a) at $T =$ 15–20 K demonstrates surprising behavior: it is negative in low magnetic fields, positive in moderate fields and again negative in high fields. At the 50 K $\leqslant T \leqslant$ 65 K range, change of the MR sign happens only once, from negative to

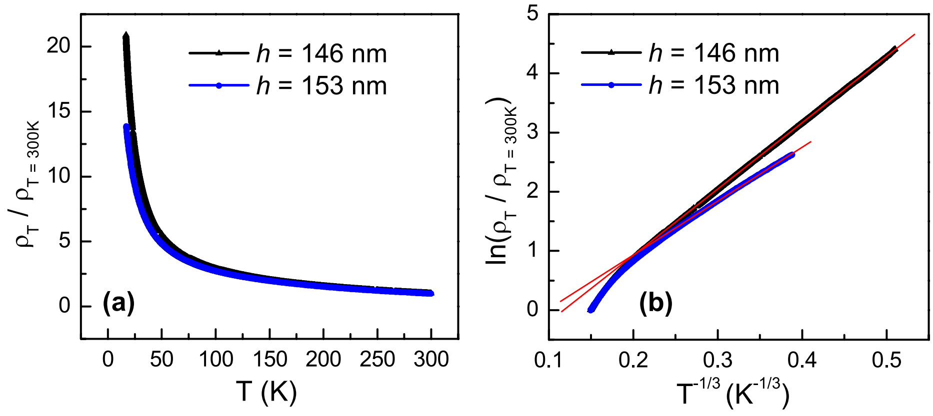

Fig. 1. Normalized resistivity versus temperature dependence of the samples with $h = 146$ nm (black) and $h = 153$ nm (blue) in the coordinates of $\rho_T/\rho_{T=300K}$ vs. T (a) and $\ln(\rho_T/\rho_{T=300K})$ vs. $T^{-\frac{1}{3}}$ (b). The red lines are linear fits.

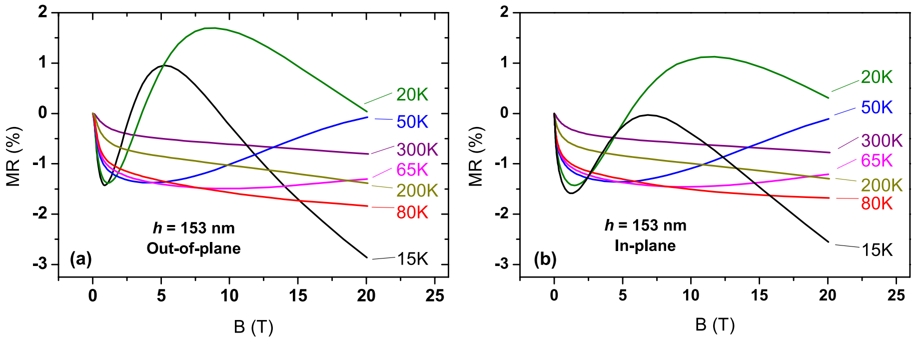

Fig. 2. Magnetic field dependence of MR of the sample with $h = 153$ nm with the field oriented: (a) out-of-plane and (b) in-plane. The magnitude of MR was determined as $MR = (R_B - R_0)/R_0 * 100$ %, where R_B and R_0 are the resistances, measured with and without magnetic field, respectively.

positive in high magnetic fields. At $T \geqslant 80$ K, negative MR grows steadily with the field increase. MR is positive in the case of shrinkage of electron wave functions in magnetic field (Efros-Shklovskii mechanism) and rises according to the exponential law $\rho(H) = \rho_0 exp\{const^*H^n\}$, where n depends on the sample dimensionality and magnetic field strength [10]. The dependence is associated with stretching of s-like states in the magnetic field, which leads to a decrease of overlap of the wavefunction tails, hindering hopping of charge carriers between sites. Obviously, this mechanism alone cannot describe the whole MR behavior of the present data. In the case of in-plane MR (See Fig. 2b), the behavior described above changes only quantitatively.

Magnetoresistance curves of the sample with $h = 146$ nm are

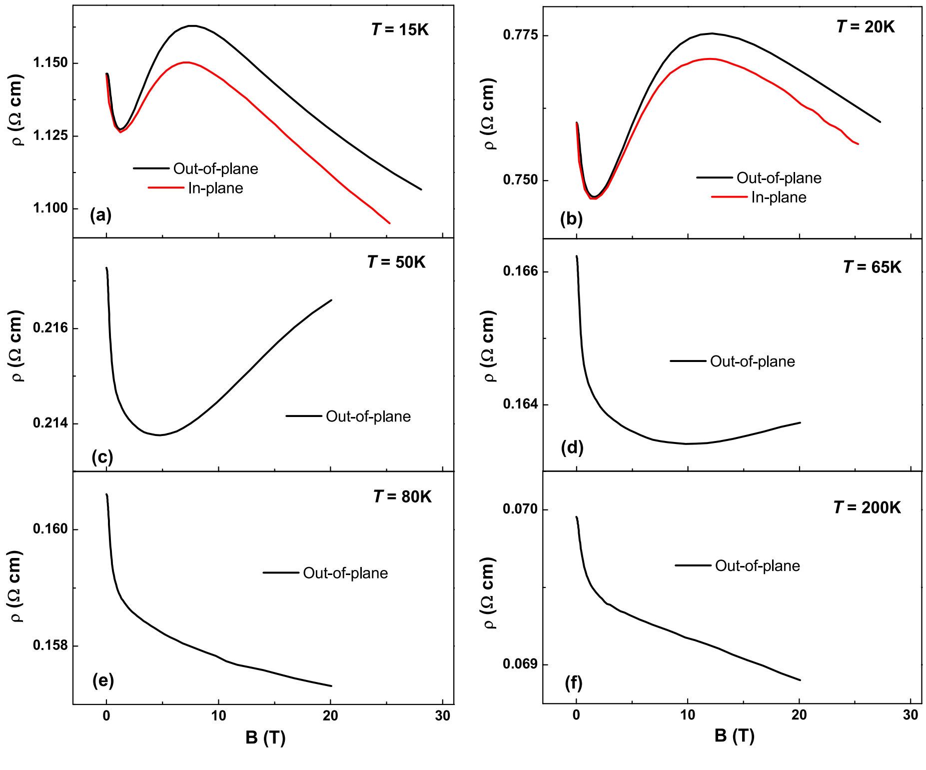

Fig. 3. Magnetic field dependence of resistivity of the sample with $h = 146$ nm at different temperatures: (a) 15 K; (b) 20 K; (c) 50 K; (d) 65 K; (e) 80 K; (f) 200 K.

separately presented for all the temperatures in Fig. 3. The following features should be noted:

1. Negative MR at $B \lesssim 1.5$ T does not depend on the field orientation, whereas at higher fields, out-of-plane MR is stronger than in-plane MR (See Fig. 3a,b),
2. At $T \geqslant 80$ K, MR is negative throughout the magnetic field range and does not show signatures of saturation (See Fig. 3e,f),
3. The value of the magnetic field H_{min}, corresponding to the minimum of MR, increases with the rise in temperature (See Fig. 3a-d),
4. The value of the magnetic field H_{max}, corresponding to the maximum of MR, is higher at 20 K than at 15 K and does not depend on the field orientation (See Fig. 3a,b).

The data above suggests the existence of at least two mechanisms responsible for negative MR and one mechanism for positive MR. Moreover, the positive contribution does not increase exponentially, as in the case of the Efros-Shklovskii mechanism, but either saturates with the field increase at low temperatures or monotonically decreases.

First, we discuss low magnetic field negative MR. Four possible mechanisms at low temperatures can be responsible for it: 1) quantum interference, which is basically a consequence of weak localization [11]; 2) increase of the density of states (DOS) due to Fermi level shift under the applied magnetic field [11]; 3) hopping of nonzero orbital momentum states [12]; and 4) scattering on the magnetic disorder. It is not reasonable to exclude the possibility that all the mechanisms are involved to some extent, however, the dependence of the results on the field orientation may suggest that the second mechanism is dominant. Indeed, the 2D interference mechanism is characterized by in-plane MR being significantly greater than out-of-plane MR [11], which does not correspond with the data in Fig. 3 in neither low nor high magnetic fields. For the hopping of nonzero orbital momentum states, MR is negative and depends linearly on the field at low fields [12]; however, the experimental curves are not linear. Scattering on the magnetic disorder certainly takes place, but it is unlikely to be the major mechanism due to the following arguments. Indeed, apparent magnetic hysteresis loops are observed at $T \leqslant 120$ K (Fig. 4a). Zero field cooled (ZFC) magnetization initially drops with the temperature increase, starts to rise at $T \approx 20$ K, reaching its maximum value at $T \approx 50$ K, and again decreases with temperature up to RT (Fig. 4b). The results of magnetic measurements indicate ferrimagnetic ordering that involves the existence of ferromagnetic sublattices, whose magnetic moments are mostly antiparallel to each other. Therefore, the application of a magnetic field reduces the magnetic moment disorientation, which should lead to a corresponding magnetic contribution in negative MR. In the case of significant magnetization, H_{max} should depend on the field orientation due to demagnetization fields. However, as can be seen from Fig. 4a, magnetization is relatively weak and $H_{\max}$ is the same for both orientations (Fig. 3a,b). The weak magnetization and absence of a tendency to MR saturation even in fields higher than the saturation field ($B_{\text{sat}} \approx 0.1$ T, not shown on the graph) indicate that the contribution of this mechanism is insubstantial. To summarize, the low magnetic field and low temperature MR is determined by a shift of the Fermi level under the applied magnetic field, inducing a rise in the DOS at the Fermi level. Other mechanisms compensate positive contribution that is associated with a reduction of the wavefunction overlap.

The magnetic field reduces the distance between the energy levels, thus narrowing the impurity band (caused by defects at the interfaces) and reducing the tail of the DOS [11]. According to the Mott's VRH, the Fermi level is located in the tail of the DOS. From the conservation law of the total number of electrons in a magnetic field, the Fermi level will be shifted towards the center of the impurity band, i.e., DOS, $g(\mu)$, will be increased by Δg. According to Eq. (1):

$$\Delta\rho \Big/ \rho = -\frac{1}{3}\Delta g \Big/ g, \tag{2}$$

i.e., MR is negative and not weak and does not correlate with temperature. Fig. 5a shows that all the MR curves (except for $T = 200$ K) are temperature-independent in $B \lesssim 0.3$ T. However, further increase of the magnetic field causes the curves to diverge, which indicates that the considered mechanisms (in particular, positive magnetoresistance) are being activated.

Next, we analyze the positive MR that takes place at low temperatures and in moderate fields, and leads to the change of MR sign and appearance of the MR maximum and minimum (Figs. 2 and 3). In low magnetic fields, the Efros-Shklovskii mechanism giving quadratic dependence of MR on the temperature is compensated by negative contribution, whereas in higher fields MR grows exponentially with field following $\rho(H) = \rho_0 exp\left\{const^{*}H^{\frac{1}{3}}\right\}$ and induces positive MR. Firstly, the described dependence actually takes place in a narrow field range (Fig. 5b). Secondly, out-of-plane MR is greater than in-plane MR, which agrees with the mechanism presented in [11]. Further increase of the magnetic field does not show exponential growth of MR, as is predicted by the Efros-Shklovskii mechanism. This behavior may be caused by the effect of magnetic blockade. The nature of the effect is that the magnetic field polarizes the spin of the charge carrier, which makes it energetically unfavorable for the charge carrier to hop to another spin-polarized state. This process is rather general since it is based on the Pauli principle. The process has been utilized to explain a bipolaron mechanism for organic MR [13]; and it has been discussed within the framework of

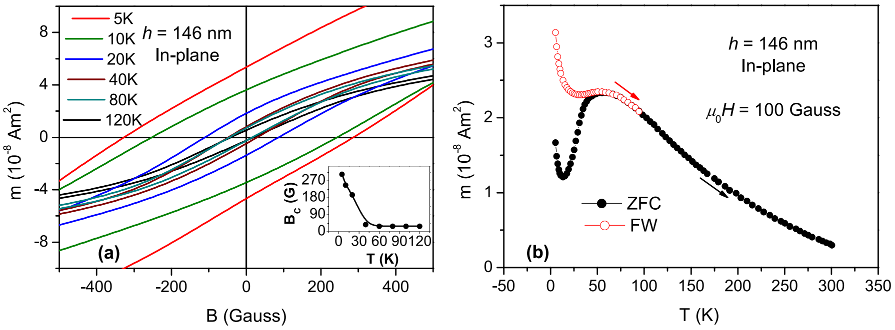

Fig. 4. In-plane magnetic properties of the sample with $h = 146$ nm. (a) Hysteresis loops. The insert shows temperature dependence of intrinsic coercivity. (b) Zero-field cooled (ZFC) and field warming (FW) thermomagnetic curves at $B = 10$ mT. Note the absence of a field cooling (FC) curve.

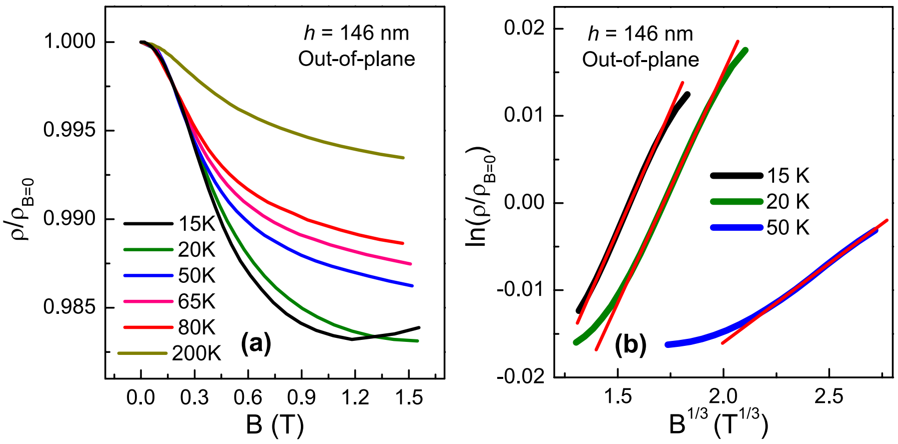

Fig. 5. Magnetic field dependence of normalized resistivity of the sample with $h = 146$ nm at different temperatures in the coordinates of $\rho/\rho_{B=0}$ vs. B (a) and $\ln(\rho/\rho_{B=0})$ vs. $B^{1/3}$ (b). The red lines are linear fits.

MR in granular magnetic films [14] and in amorphous semiconductors, considering processes of spin-flip [15] and interatomic electron–electron interaction [16]. It is worth noting that the effect of magnetic blockade should be observed not only in magnetically ordered systems, even though the presence of magnetic moment definitely enhances the effect. In our case, both the magnetic moment and charge carriers are developed due to dangling bonds at interfaces. Usually, a covalent bond involves two electrons with opposite spin index, whereas a dangling bond contains only one electron. Hopping of electrons occurs only from occupied to empty states and the Pauli principle prohibits some of the transitions, which was not taken into account in the Efros-Shklovskii mechanism and thus leads to a reduction of the positive contribution. Calculated MR demonstrates that the positive contribution, indeed, weakens in high magnetic fields after reaching a maximum peak [16]. In our case, ferromagnetic order at low temperatures, justified by hysteresis loops in Fig. 4a, strengthens the effect of the magnetic blockade, since spin polarization significantly reduces the number of sites between which hopping is possible.

4. Conclusion

Magnetotransport measurements of multilayer nanostructures $(ZnO/C)_{25}$ in high magnetic fields and at low temperatures, when hopping of charge carriers along the interfaces takes place, revealed unusual behavior of magnetoresistance (MR). At $T \leqslant 20$ K, MR changes from negative in low magnetic fields to positive in moderate fields, and again to negative in high magnetic fields. This behavior is associated with three acting mechanisms: the influence of the magnetic field on the Fermi level, scattering on magnetic disorder and wave function shrinkage due to the effect of magnetic blockade. The presence of weak local magnetism, presumably associated with the formation of defects at the interfaces, enhances the magnetic blockade effect, which leads to suppression of the positive contribution of MR.

CRediT authorship contribution statement

E.A. Fadeev: Methodology, Investigation, Data curation, Visualization, Writing - review & editing. **E. Lähderanta:** Resources, Supervision, Project administration, Funding acquisition. **B.A. Aronzon:** Validation, Formal analysis, Writing - original draft. **A.B. Mekhiya:** Validation, Formal analysis, Writing - original draft. **Yu.E. Kalinin:** Resources, Validation, Conceptualization. **V.A. Makagonov:** Resources, Validation. **S.Yu. Pankov:** Resources, Validation. **V.A. Foshin:** Resources, Validation. **A.B. Granovsky:** Conceptualization, Validation, Formal analysis, Writing - original draft, Writing - review & editing, Supervision.

Declaration of Competing Interest

The authors declare that they have no known competing financial interests or personal relationships that could have appeared to influence the work reported in this paper.

Acknowledgements

This work was partially supported by the Russian Ministry of Education and Science within the framework of state assignment No. FZGM-2020–0007 and by the Academy of Finland (Grant No. 333805).

References

[1] T. Dietl, A ten-year perspective on dilute magnetic semiconductors and oxides, Nat. Mater. 9 (12) (2010) 965–974.
[2] A.S. Semisalova, A. Orlov, A. Smekhova, E. Gan'shina, N. Perov, W. Anwand, K. Potzger, E. Lähderanta, A. Granovsky, Above room temperature ferromagnetism in dilute magnetic oxide semiconductors, in: A. Zhukov (Ed.), Novel Functional Magnetic Materials , Springer Series in Materials Science vol. 231, Springer, Cham, 2016.
[3] M. Venkatesan, C.B. Fitzgerald, J.M.D. Coey, Unexpected magnetism in a dielectric oxide, Nature 430 (7000) (2004) 630.
[4] H. Pan, J.B. Yi, L. Shen, R.Q. Wu, J.H. Yang, J.Y. Lin, Y.P. Feng, J. Ding, L.H. Van, J.H. Yin, Room-temperature ferromagnetism in carbon-doped ZnO, Phys. Rev. Lett. 99 (12) (2007), 127201.
[5] X.J. Ye, H.A. Song, W. Zhong, M.H. Xu, X.S. Qi, C.Q. Jin, Z.X. Yang, C.T. Au, Y. W. Du, The effect of nitrogen incorporation on the magnetic properties of carbon-doped ZnO, J. Phys. D: Appl. Phys. 41 (15) (2008), 155005.
[6] K. Tang, S. Gu, S. Zhu, W. Liu, J. Ye, J. Zhu, R. Zhang, Y. Zheng, X. Sun, Carbon clusters in N-doped ZnO by metal-organic chemical vapor deposition, Appl. Phys. Lett. 93 (13) (2008), 132107.
[7] M.N. Volochaev, A.B. Granovsky, O.V. Zhilova, Y.E. Kalinin, V.V. Ryl'kov, M. P. Sumets, V.A. Makagonov, S.Y. Pankov, A.V. Sitnikov, E. Fadeev, Transport and magnetic phenomena in ZnO- thin-film heterostructures, Superlattices Microstruct. 140 (2020), 106449.
[8] N.F. Mott, E.A. Davis, Electronic Processes in Non-Crystalline Materials, Oxford University Press, 2012.

[9] B.K. Meyer, H. Alves, D.M. Hofmann, W. Kriegseis, D. Forster, F. Bertram, J. Christen, A. Hoffmann, M. Straßburg, M. Dworzak, U. Haboeck, A.V. Rodina, Bound exciton and donor-acceptor pair recombinations in ZnO, Physica Status Solidi (b) 241 (2) (2004) 231–260.
[10] B.I. Shklovskii, A.L. Efros, Electronic properties of doped semiconductors, vol. 45, Springer Science & Business Media, 2013.
[11] M.E. Raikh, J. Czingon, Q.Y. Ye, F. Koch, W. Schoepe, K. Ploog, Mechanisms of magnetoresistance in variable-range-hopping transport for two-dimensional electron systems, Phys. Rev. B 45 (11) (1992) 6015.
[12] A.S. Alexandrov, V.A. Dediu, V.V. Kabanov, Hopping magnetotransport via nonzero orbital momentum states and organic magnetoresistance, Phys. Rev. Lett. 108 (18) (2012), 186601.
[13] P.A. Bobbert, T.D. Nguyen, F.W.A. Van Oost, V.B. Koopmans, M. Wohlgenannt, Bipolaron mechanism for organic magnetoresistance, Phys. Rev. Lett. 99 (21) (2007) 216801.
[14] J. Inoue, S. Maekawa, Theory of tunneling magnetoresistance in granular magnetic films, Phys. Rev. B 53 (18) (1996) 11927.
[15] B. Movaghar, L. Schweitzer, A model for the anomalous magnetoresistance in amorphous semiconductors, J. Phys. C: Solid State Phys. 11 (1) (1978) 125.
[16] A. Kurobe, H. Kamimura, Theory of magnetoresistance in amorphous semiconductors, J. Non-Crystalline Solids 59 (1983) 41–44.

Publication III

Rylkov, V.V., Emelyanov, A.V., Nikolaev, S.N., Nikiruy, K.E., Sitnikov, A.V., Fadeev,
E.A., Demin, V.A., and Granovsky, A.B.

Transport Properties of Magnetic Nanogranular Composites with Dispersed Ions in an Insulating Matrix

Reprinted with permission from
Journal of Experimental and Theoretical Physics
Vol. 131(1), pp. 160–176, 2020.

ISSN 1063-7761, Journal of Experimental and Theoretical Physics, 2020, Vol. 131, No. 1, pp. 160–176. © Pleiades Publishing, Inc., 2020.
Russian Text © The Author(s), 2020, published in Zhurnal Eksperimental'noi i Teoreticheskoi Fiziki, 2020, Vol. 158, No. 1, pp. 164–183.

Transport Properties of Magnetic Nanogranular Composites with Dispersed Ions in an Insulating Matrix

V. V. Rylkov[a,f,*], **A. V. Emelyanov**[a,b], **S. N. Nikolaev**[a], **K. E. Nikiruy**[a], **A. V. Sitnikov**[a,c], **E. A. Fadeev**[d], **V. A. Demin**[a], **and A. B. Granovsky**[e,**]

[a] *National Research Centre Kurchatov Institute, Moscow, 123182 Russia*
[b] *Moscow Institute of Physics and Technology, Dolgoprudny, Moscow oblast, 141700 Russia*
[c] *Voronezh State Technical University, Voronezh, 394026 Russia*
[d] *Lappeenranta University of Technology, Lappeenranta, 53851 Finland*
[e] *Faculty of Physics, Moscow State University, Moscow, 119991 Russia*
[f] *Kotelnikov Institute of Radio Engineering and Electronics, Fryazino Branch, Russian Academy of Sciences, Fryazino, Moscow oblast, 141190 Russia*
**e-mail: vvrylkov@mail.ru*
***e-mail: granov@magn.ru*

Received January 31, 2020; revised January 31, 2020; accepted February 6, 2020

Abstract—This review is devoted to an analysis of the electrical resistance, the magnetoresistance, and the anomalous Hall effect in magnetic "ferromagnetic metal–insulator" nanocomposites at a metal content near the percolation threshold and the memristive properties of the capacitor structures based on these nanocomposites. A high content (up to 10^{22} cm^{-3}) of dispersed atoms in intergranular gaps leads to a logarithmic temperature dependence of the electrical resistance, a positive contribution to the magnetoresistance, the appearance of tunneling anomalous Hall effect, and a multifilament mechanism of resistive switching (which causes an adaptive character of memristor nanocomposites with dispersed atoms).

DOI: 10.1134/S1063776120070109

1. INTRODUCTION

Nanogranular metal–insulator M_xD_{100-x} composites consist of an array of nanogranules chaotically distributed in an insulator matrix. In the case of magnetic nanocomposites (NCs), granules are in single-domain, superparamagnetic, or inhomogeneously magnetic state depending on the material, the anisotropy energy, the size, and the shape. These systems are of particular interest for many decades due to the application of magnetic NCs in magnetic data recording and to their diverse practically important magnetic, transport, optical, and magnetooptical properties. As examples, we can present giant magnetoresistance [1, 2], the anomalous Hall effect with a giant coefficient [3–5], the magnetorefractive effect [6], and the enhanced magnetooptical Kerr effect [7]. The application of NCs for radioabsorbing coatings is also promising due to their high resistance and magnetic softness at certain compositions near the percolation threshold [8, 9].

The memristive effect [10–14] has been recently detected in magnetic NCs, and it makes these systems competitive with numerous versions of memristors intended for multilevel memory and the emulation of synapses in neuromorphic networks [15–18] and stimulates a new stage in studying the linear and nonlinear electrophysical properties of these NC systems. In addition, magnetic NCs are an ideal platform for studying the percolation phenomenon, the quantum size effects, the spin-glass and mesoscopic properties, and the influence of various interactions on the behavior of random systems [19–21].

Earlier, most researchers considered that such systems have one critical concentration, namely, percolation threshold x_p, at which an infinite metallic chain of granules (percolation cluster) through which an electric current passes through a sample appears. This critical concentration also determined the metal–insulator transition (MIT) induced by a change in the concentration and the transition from ferromagnetic (FM) ordering to superparamagnetic, superferromagnetic, or single-domain behavior. However, the possibility of tunneling between granules and the presence of metallic ions, which can be dispersed into an insulating matrix during NC deposition, in the intergranular gaps leads to the fact that the critical concentration of MIT x_c and the concentration of disappearance of a long-range magnetic order x_f do not coincide with x_p [9, 21]. Therefore, it is necessary to experimentally determine these important parameters and to reveal how the presence of dispersed metallic ions affects the properties of NC far from and near the percolation threshold.

In this review, we discuss a number of examples, where the presence of metallic ions critically affects the behavior of resistance, magnetoresistance, and the anomalous Hall effect near the percolation threshold and the memristive effect [10–14] recently detected in metal/NC/metal capacitor structures based on magnetic NCs. There exists a number of excellent reviews of the behavior of electrical conductivity σ of NC on the dielectric and metallic sides of MIT in various NC systems [21–25], including a comprehensive theoretical analysis of the temperature and concentration dependences of σ [21]. Therefore, in this work, we restrict ourselves to revealing the role of dispersed ions in NC using recent experimental results.

2. EXPERIMENTAL

M_xD_{100-x} film NCs were prepared by ion-beam sputtering of composite targets made of cast plates of $Co_{40}Fe_{40}B_{20}$ and $Co_{84}Nb_{14}Ta_2$ alloys (hereafter, for brevity CoFeB and CoNbTa, respectively) 280 × 80 mm^2 in size to which rectangular pieces (14–15 pieces) of Al_2O_3, $LiNbO_3$, or SiO_2 oxides were fixed. The arrangement of oxide pieces on the metallic plate surfaces was nonuniform to prepare composites with a controlled change in the composition in the range $x = 6$–60 at % in one technological cycle. NC was deposited onto glass ceramic substrates in an argon atmosphere ($P_{Ar} \approx 8 \times 10^{-4}$ Torr) at room temperature (see [10, 11]). Some specimens were prepared at elevated deposition temperatures (80–90°C) to decrease the content of dispersed metallic atoms in an NC matrix.

The elemental composition of NC was determined by energy dispersive X-ray analysis (EDX) using an Oxford INCA Energy 250 attachment on a JEOL JSM-6380 LV scanning electron microscope.

The nanometer-resolution comprehensive studies of the structure of the M_xD_{100-x} films were carried out on $(CoFeB)_x(Al_2O_3)_{100-x}$ and $(CoFeB)_x(LiNbO_3)_{100-x}$ NCs by transmission electron microscopy (TEM), scanning transmission electron microscopy (STEM), and EDX on a TITAN 80-300 (FEI, United States) TEM/STEM microscope with a corrector of spherical probe aberration in bright- and dark-field modes using a high-angle annular dark-field detector of scattered electrons [10, 26, 27]. These studies demonstrated that the NCs in both cases consisted of an ensemble of crystalline bcc CoFe alloy nanogranules in an insulating oxide matrix with a smaller atomic number. In the case of the $(CoFeB)_x(Al_2O_3)_{100-x}$ NC, the granules were spherical and had a size $a = 2$–4 nm; in the $(CoFeB)_x(LiNbO_3)_{100-x}$ NC, the granules were elongated along the NC growth direction up to $a_z \approx 10$–15 nm and had the same in-plane sizes ($a_x = a = 2$–4 nm) as in the $(CoFeB)_x(Al_2O_3)_{100-x}$ NC.

The fact that the granules are crystalline indicates that significant part of boron during NC growth is in the oxide matrix, and its content in the granules is well below 20 at %, at which the amorphization of a CoFeB alloy is substantial. Since the part of boron in metallic granules and the part of boron in the oxide matrix during NC growth cannot be determined by the existing EDX techniques [26], the exact formula reflecting the synthesized NC composition cannot be written. Therefore, we use the approximate NC formulas that reflect the target composition and were applied to find x by EDX [10, 26, 27].

Another specific feature of the NC consisted in the fact that its magnetization at low temperatures ($T \leq 25$ K) had an FM component and a paramagnetic component, the contribution of which was threefold that of the FM component [10, 27]. The comprehensive precision SQUID magnetometry (Quantum Design MPMS-XL7) investigations [27] of the magnetization of the NC in the fields up to 7 T at $T = 2$–10 K showed that the paramagnetic contribution was determined by the dispersed magnetic Fe^{2+} and Co^{2+} ions with a concentration up to $N_d \approx 3 \times 10^{22}$ cm^{-3} in $(CoFeB)_x(LiNbO_3)_{100-x}$ and $N_d \approx 1.2 \times 10^{22}$ cm^{-3} (which was lower by a factor of 2–3) in $(CoFeB)_x(Al_2O_3)_{100-x}$. Under these conditions, the value of x found by EDX includes the metal atoms that are both in granules and in a dispersed form in the matrix.

The study of the I–V characteristics of the metal/nanocomposite/metal (M/NC/M) capacitor structures in strong electric fields (more than 10^4 V/cm) detected reversible resistive switching (RS) effects, which pointed to the memristive properties of the NCs. The RS effects were strongest and most stable in the structures based on $(CoFeB)_x(LiNbO_3)_{100-x}$ NC with a high content of dispersed ions [10, 28]. To reveal the mechanism of RS, we prepared $M/(CoFeB)_x(LiNbO_3)_{100-x}/M$ structures with various metal contents and an NC layer thickness $d = 1$–3 μm. In addition, we [10] synthesized M/NC/M structures with a developed oxide layer at the bottom electrode, which was formed in the initial stage of NC growth at a given O_2 flow rate and a high O_2 partial pressure ($P_{O_2} \approx 2.5 \times 10^{-5}$ Torr). The NC was deposited for 7–8 min under these conditions and the O_2 flow rate was then decreased. Further deposition was carried out for 90–300 min at an average pressure $P_{O_2} \approx 6 \times 10^{-6}$ Torr (P_{O_2} is given for the limiting vacuum $P \approx 6 \times 10^{-6}$ Torr in the chamber). An oxide layer was also formed by the deposition of NC onto a slowly rotating substrate (0.2 rpm). NC was deposited onto glass ceramic substrates coated with a copper film (or Cr/Cu/Cr film) 1–2 μm thick through a shadow mask with periodically arranged holes 5 mm in diameter. The top electrode consisted of a Cu film (or Cr/Cu/Cr film) with area $S = 0.5 \times 0.2$ mm^2.

The transport and magnetic properties of the NCs were studied on universal samples prepared with photolithography in the form of a double Hall cross with a conducting channel width $w = 1.2$ mm and with a distance $l = 1.4$ mm between the potential probes on the side faces.

The electrical conductivity and the Hall effect were studied using a computer-assisted setup equipped with a pumped out insert with a superconducting solenoid, which is immersed into a transportation helium Dewar vessel in a magnetic field up to 1.5 T and the temperature range 10–300 K.

The magnetoresistance (MR) was measured using a direct current mode and a pulsed magnetic field B up to 20 T; an 11-ms symmetric (half-sine) pulse was used. Special-purpose hardware and software were applied to exclude the dB/dt-induced spurious signal (see [29]).

The memristive properties of the M/NC/M structures, including their I–V characteristics, were studied with a four-channel PXIe-4140 (National Instruments) source–meter on a PM5 (Cascade Microtech) analytical probe station [10, 28]. We experimentally investigated the endurance of RS, the retention time of resistive states, and the possibility of their setting according to biosimilar STDP (spike-timing-dependent plasticity) rules [12–14, 28].

3. ELECTRICAL CONDUCTIVITY

The logarithmic temperature dependence of the electrical conductivity of nanogranular films at the metal concentration corresponding to a "metallic" transport mode [30],

$$\sigma = \sigma^* + \beta \ln T \tag{1}$$

provoked deep interest, since the films were thick enough and the temperatures were high enough for this dependence to be considered as a consequence of weak localization in two-dimensional structures. In his theoretical works (see [30] and review [21]), Efetov showed that this dependence in granular systems can be caused by renormalizing the Coulomb interaction. According to [21, 30], the electrical conductivity of NC with an ordered distribution of granules below the percolation threshold at $g \geq 1$ obeys the law

$$\begin{aligned}\sigma(T) &= \sigma_0\left(1 - \frac{1}{2\pi D g}\ln\frac{gE_c}{k_B T}\right)\\ &= \sigma_0\left(1 - \frac{1}{\pi k g}\ln\frac{gE_c}{k_B T}\right) \propto \beta \ln T,\end{aligned} \tag{2}$$

where $g = G_t/(2e^2/\hbar)$ is the average tunneling conductance between neighboring granules in units of conductance quantum, D is the dimension of the system, k is the coordination number of the periodic lattice (the number of contacts of a granule with the nearest neighbors), k_B is the Boltzmann constant, E_c is the Coulomb blockade energy, $\beta = \sigma_0/\pi k g$ is a parameter, and σ_0 is the metallic conductivity (according to Drude) at the temperatures that are high enough for the Coulomb blockade effects to be insignificant [21, p. 474].

Equation (2) is valid under the condition $g\delta \ll k_B T \ll E_c$, where δ is the average energy gap between the quantizing levels in an isolated granule. When the content of metallic granules is below certain critical value x_x, dimensionless conductance g turns out to be lower than unity and MIT takes place; below MIT, hopping conduction described by the well-known "1/2" law, i.e., $\ln\sigma \propto -(T_0/T)^{1/2}$, is observed. At $x > x_c$, the conduction of NC is metallic with a negative temperature coefficient of resistance $\alpha = d\rho/dT$, as in a dirty metal. However, the sign of α can change into positive above percolation threshold x_p, as in the case of pure-metal-based NCs Ni–SiO$_2$ [31]; this finding makes it possible to estimate percolation threshold x_p. Noticeable deviations from the logarithmic law in the temperature behavior of σ should also be observed near x_p, which can also be used to estimate this quantity.

The theory developed in [21, 30] has a general character, since its main parameter is tunneling conductance; therefore, it can be applied for a random arrangement of granules [21] and in the presence of metallic ions in intergranular gaps. Moreover, our investigations [10, 27, 32, 33] demonstrate that the presence of metallic ions promotes a strong increase in the intergranular FM interaction, enhancing the tunnel coupling between granules and shifting MIT to low critical values x_c [32]. In this situation, the concentration range $\delta x_p = x_p - x_c$ where Eq. (2) holds true should extend.

Under the conditions of Eq. (2), this conclusion was well supported for the $(\mathrm{CoFeB})_x(\mathrm{Al_2O_3})_{100-x}$ NC in [26, 27, 34] and, then, for the systems $(\mathrm{CoFeB})_x(\mathrm{LiNbO_3})_{100-x}$ [10, 27], $(\mathrm{CoNbTa})_x(\mathrm{Al_2O_3})_{100-x}$, and $(\mathrm{CoFeB})_x(\mathrm{SiO_2})_{100-x}$ [35, 36].

Figures 1 and 2 show the typical temperature dependences of the electrical conductivity of the $(\mathrm{CoFeB})_x(\mathrm{Al_2O_3})_{100-x}$ and $(\mathrm{CoFeB})_x(\mathrm{LiNbO_3})_{100-x}$ nanocomposites. In the case of $(\mathrm{CoFeB})_x(\mathrm{Al_2O_3})_{100-x}$, Eq. (2) is seen to be valid from 15 to 300 K in the range $x \approx 49$–56 at %. The critical concentrations x_c and x_p estimated from the $\sigma(x)$ and $\sigma(T)$ dependences are given in the figure captions (see Figs. 1a, 1b). Note that the Ni–SiO$_2$ system, which was fabricated by electron-beam sputtering and had no such ions, exhib-

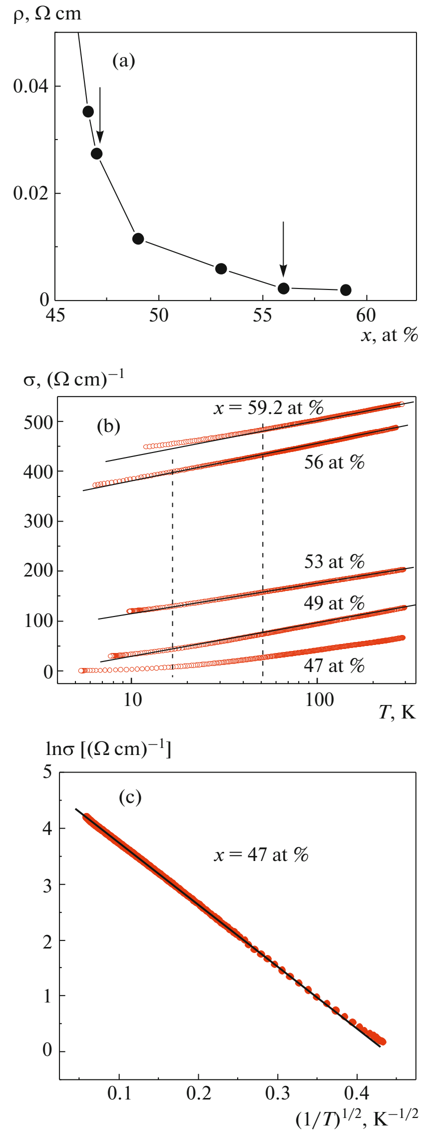

Fig. 1. (Color online) (a) Electrical resistivity of $(CoFeB)_x(Al_2O_3)_{100-x}$ samples vs. the FM alloy content near MIT ($x = 46.5$–59.2 at %) at $T = 77$ K. The arrows indicate the MIT ($x_c \approx 47$ at %) and percolation threshold ($x_p \approx 56$–59 at %) ranges. (b) Temperature dependences of the electrical conductivity of the samples with various FM alloy contents ($x = 47$–59 at %). (c) Dependence $\sigma(T)$ for the $(CoFeB)_x(Al_2O_3)_{100-x}$ sample with $x \approx 47$ at % in the coordinates $\ln\sigma$–$(1/T)^{1/2}$ (borrowed from [26]).

its $\delta x_p = x_p - x_c \approx 1$ at % [31]. In the case of $(CoFeB)_x(LiNbO_3)_{100-x}$, the temperature range of Eq. (2) is also wide, $\delta x_p \approx 8$ at %; however, it is shifted toward low temperatures $T = 10$–220 K. This finding is likely to be related to larger granules for this NC (because of their elongation); the high permittivity of amorphous $LiNbO_3$ ($\varepsilon_d \sim 10^2$–10^4 [37]); and, hence, the suppression of the Coulomb blockade effects, which shifts the range of Eq. (2) toward low temperatures [21].

According to the data in Figs. 1 and 2, the slope of the curves of the $(CoFeB)_x(LiNbO_3)_{100-x}$ NC ($\beta \approx 6\ (\Omega\ \text{cm})^{-1}$) is significantly lower than that of $(CoFeB)_x(Al_2O_3)_{100-x}$ ($\beta \approx 30\ (\Omega\ \text{cm})^{-1}$). This difference can be understood using a percolation approach, in which the conductance is $G_t \approx i\sigma(0)L$, where L is the characteristic correlation radius of the percolation network, $i \sim L/a$ is the number of tunneling gaps per this length [10, 26], and a is the average intergranule distance. Then, we can easily show that

$$\beta = \frac{\sigma_0}{\pi k g} \approx \frac{2e^2}{\hbar\pi k i L} \sim \frac{2e^2 a}{\hbar\pi k L^2}. \tag{3}$$

As follows from Eq. (3), the slope depends strongly on correlation length L. Allowing for Eq. (3), we find that the correlation length for the $(CoFeB)_x(LiNbO_3)_{100-x}$ NC ($L \approx 20$–30 nm) should be severalfold that in the $(CoFeB)_x(Al_2O_3)_{100-x}$ NC, where $L \approx 9$–13 nm [10, 26].

Another manifestation of the role of dispersed ions was revealed when the Coulomb blockade energy E_c in $(CoFeB)_x(Al_2O_3)_{100-x}$ was analyzed [34]. This energy during the transition of an electron from a granule to the nearest granule is described by the following expression if only these two granules are taken into account [24]:

$$E_c = \frac{e^2 b}{\varepsilon_d a^2 (1/2 + b/a)}, \tag{4}$$

where b is the tunneling gap width. Substituting $\varepsilon_d \approx 10$ for the Al_2O_3 matrix in NC, $a \approx 3$ nm, and $b \approx 1$ nm, we find $E_c \approx 19$ meV. On the other hand, using Eqs. (1) and (2) and experimental values $\sigma^* = 328\ (\Omega\ \text{cm})^{-1}$ and $\beta = 33\ (\Omega\ \text{cm})^{-1}$, we obtain the lower estimate of $gE_c \approx 16$ meV at $\sigma_0 \approx 500\ (\Omega\ \text{cm})^{-1}$ (we took $\sigma_0 = \sigma$ at 300 K; see Fig. 1). Since the theory is valid at $g \geq 1$, this means that dispersed ions can significantly increase the electric polarization of the tunneling gap and the entire system. Note that the difference between the permittivity in Eq. (4) and the permittivity in a stoichiometric matrix was noted earlier (see review [23]). In addition, tunneling takes an ultrashort time; therefore, we have to take into account that dynamic permittivity can differ substantially from static permittivity. These factors explain the discrepancy between the experimental results and the data calculated by Eq. (4).

Note that the presence of a significant concentration of localized states at the Fermi level in tunneling intergranular gaps (on the order of 10^{22} eV^{-1} cm^{-3}) causes deviations from the 1/2 law and the manifestation of the Mott 1/4 law in the temperature dependence of the resistance of NC below MIT ($x < x_c$) [25, 38]. Such deviations were not detected in our case despite a large number of dispersed ions (see Figs. 1, 2 and [10, 26, 27, 34–36]). Therefore, such centers should be primarily considered as scattering centers [39].

4. MAGNETORESISTANCE

The MR of homogeneous FM metals is usually negative, since the application of a magnetic field decreases the magnetic disorder in a system. The exception is longitudinal MR due to the anisotropic MR induced by spin–orbit interaction (SOI). However, the anisotropic MR in nanosystems is suppressed because of the size effect and is not observed in NCs near the percolation threshold. The absence of anisotropic MR can serve as a criterion to determine the threshold of failure x_f of a long-range magnetic order. Spin-dependent tunneling also brings about negative MR, which is observed in many NCs and reaches about 10% in strong fields. Therefore, the positive field-linear MR detected in the Ni–SiO_2 NC up to 200 K, which was not saturated in fields as high as 60 T, was attributed to the influence of a magnetic field on the suppression of the quantum corrections to electrical conductivity that appear due to electron–electron interaction in the presence of the exchange splitting of spin subbands rather than on the magnetic subsystem or tunneling [40]. However, neither the magnitude of the effect (10^{-1}% T^{-1}, which differs from the estimate by two orders of magnitude) nor the presence of quantum corrections at relatively high temperatures corresponded to this concept. It should be noted that a positive linear MR in strong fields was detected in both NC and ultrathin high-resistance Ni, Fe, Co, and NiPb films [40]. It is still unclear to what extent this phenomenon is universal and whether it has the same nature in different systems.

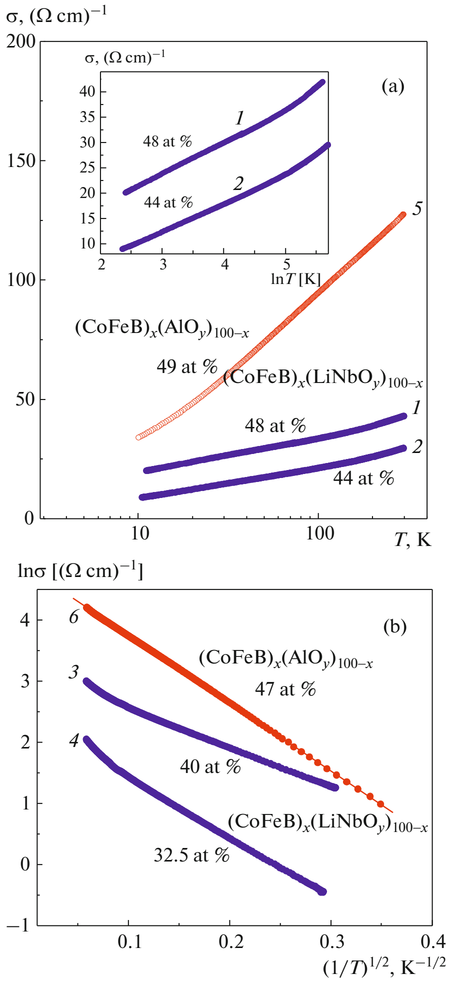

Fig. 2. (Color online) Temperature dependences of $(CoFeB)_x(Al_2O_3)_{100-x}$ NC in the coordinates (a) σ – ln*T* and (b) lnσ – $(1/T)^{1/2}$. The dependences were obtained for samples (*1*–*4*) $(CoFeB)_x(LiNbO_3)_{100-x}$ and (*5*, *6*) $(CoFeB)_x(Al_2O_3)_{100-x}$ with an FM alloy content of (*1*) 48, (*2*) 44, (*3*) 40, (*4*) 32.5, (*5*) 49, and (*6*) 47 at % (borrowed from [10]).

The main conduction mechanism in NC near the percolation threshold is spin-dependent tunneling. This brings up the question: Can spin-dependent tunneling give rise to negative MR and also generate a positive contribution in strong fields? A simple calculation in terms of the Inoue–Maekawa model of tunneling MR in granular alloys [41] with allowance for the influence of a strong magnetic field on the tunnel barrier leads to the following additional contribution to MR in the fields that are higher the saturation field [36]:

$$\frac{\Delta\rho(H)}{\rho(0)} = \xi\frac{\mu_B H}{U - E_F(0)}\left[\lambda b + \sqrt{\frac{\lambda C}{k_B T}}\right]. \qquad (5)$$

Here, parameter ξ characterizes the shift in the Fermi level in the magnetic field of exchange-split subbands with spins along and opposite to magnetization due to the Zeeman effect,

$$E_F(H) = E_F(0) - \xi\mu_B H. \tag{6}$$

The parameter is $\xi > 0$ for the subband with a spin along magnetization and is $\xi = 1$ if the subband with spin opposite to magnetization is filled. In the general case, ξ is on the order of spin polarization since $\xi \approx 0$ in the absence of spin splitting. Parameter λ characterizes the decay of the wavefunction of an electron in a tunnel barrier of height U,

$$\lambda = \sqrt{\frac{2m}{\hbar^2}(U - E_F)},$$

and C is a theory constant ($\lambda C \approx 0.015$ eV [42]).

As follows from Eq. (5), the positive contribution is field linear, exists up to room temperature or above, and is determined by the tunnel barrier height. At low temperatures, the second term in the square brackets is predominant; that is, positive MR increases as $T^{-1/2}$ when temperature decreases. Figure 3 shows the behavior of MR in two NCs systems, namely, $(\mathrm{CoFeB})_x(\mathrm{SiO}_2)_{100-x}$ and $(\mathrm{CoNbTa})_x(\mathrm{Al}_2\mathrm{O}_3)_{100-x}$, which confirms Eq. (5). Specifically, MR is negative up to the saturation field, and a linear and positive contribution with a slope of $10^{-2}\%\ \mathrm{T}^{-1}$ appears in stronger fields and increases with decreasing temperature. This effect is most pronounced in the $(\mathrm{CoNbTa})_x(\mathrm{Al}_2\mathrm{O}_3)_{100-x}$ system, which has a lower potential barrier. Therefore, it should be reliably observed in alloys below the percolation threshold at a high concentration of dispersed ions in intergranular gaps. To check this hypothesis, we prepared $(\mathrm{Co})_x(\mathrm{SiO}_2)_{100-x}$ and $(\mathrm{CoNbTa})_x(\mathrm{SiO}_{2c})_{100-x}$ samples at an elevated substrate temperature (about 80°C) and a relatively low content of dispersed ions (about $10^{21}\ \mathrm{cm}^{-3}$). In this case, we did not reveal a positive contribution at temperatures down to 4 K and fields up to 20 T.

However, the positive contribution under study is obviously small, since it is related to the influence of a magnetic field on the Fermi level. Therefore, it cannot generate the effect ($10^{-1}\%\ \mathrm{T}^{-1}$) detected in thin (10-nm-thick) Ni, Fe, and NiSiO_2 metallic films [40]. Moreover, this contribution is not universal and always positive, since the sign of parameter ξ depends on the filling of the subbands. Therefore, the problem of linear positive MR in thin metallic systems is still an open question.

5. TUNNELING ANOMALOUS HALL EFFECT

The anomalous Hall effect (AHE) is a complex quantum phenomenon, which was revealed in 1880 and explained by Karplus and Luttinger (in 1954), Luttinger (1956), and Smith and Berger (see review [43] and Refs. therein). This effect is associated with the action of SOI on spin-polarized current carriers and includes the following three main mechanisms: intrinsic mechanism (interpreted through Berry phase), skew scattering, and side jump. Which of these mechanisms is predominant in certain cases is still a subject of controversy. It should be noted that, as the first experimentally detected effect related to spin-dependent scattering, AHE is the precursor of spintronics. It is also the grandparent of the family of Hall effects, namely, direct and inverse spin, quantum anomalous, topological, tunneling, and magnetooptical Hall effects. Therefore, the investigation of the behavior of AHE in various systems is of particular interest.

AHE is most pronounced in magnetic film materials (FM metals, semiconductors, granular metal—insulator systems, etc.) with strong SOI. Their Hall resistivity is described by the sum of two terms,

$$\rho_H = R_0 B + 4\pi R_s M, \tag{7}$$

where the first term describes the ordinary Hall effect (OHE) induced by the Lorentz force, the second term characterizes the SOI-induced AHE, M is the magnetization component normal to the film plane, B is the magnetic induction component in the same direction, and R_0 and R_s are the so-called OHE and AHE coefficients, respectively. The last coefficient is expressed through the anomalous component of Hall conductivity σ_{AHE} as

$$R_s \approx (\sigma_{AHE}/4\pi M)\rho^2, \tag{8}$$

where $\rho = \rho_{xx}$ is the longitudinal electrical resistivity, which is usually much higher than the anomalous Hall resistivity $\rho_{AHE} = 4\pi R_s M$. In most cases, where MR is low, ρ_{AHE} is a linear function of magnetization and coefficient R_s is independent of both external field and spontaneous magnetization.

One of the most interesting trends in studying the AHE is to investigate ρ_{AHE} as a function of ρ, i.e., the so-called scaling behavior of AHE $\rho_{AHE} \propto \rho^n$, where n is the exponent determined by the AHE mechanism [31, 43–51]. The scaling relation in this form (or in terms of electrical conductivity, $\sigma_{AHE} = \rho_{AHE}/\rho^2 = \rho_{AHE}\sigma^2 \propto \sigma^\gamma$, where $\gamma \approx 2 - n$) is widely used to study the mechanism of AHE when the electrical resistance changes because of a change in the impurity (defect, material composition) concentration or temperature [43]. In the last case, the inelastic electron scattering by phonons and/or magnons can play a substantial role and cause a radical scaling modification [44, 46, 47, 51, 52].

In homogeneous metallic systems during elastic carrier scattering (low temperatures), we have $n = 1$ for the skew scattering mechanism and $n = 2$ for the side jump mechanism and the intrinsic AHE mechanism [43]. Exponent n decreases to $n \approx 0.4$ when the impurity scattering potential increases in high-resistance

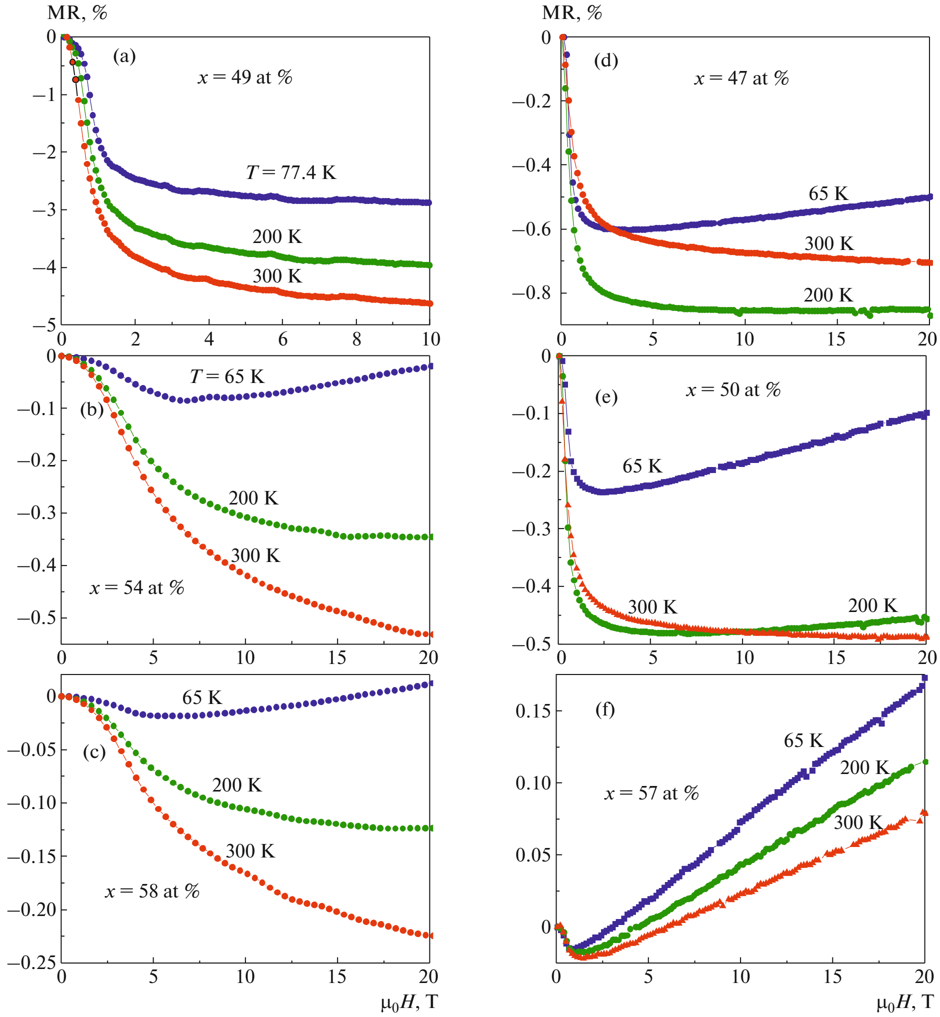

Fig. 3. (Color online) MR of samples (left column) $(CoFeB)_x(SiO_2)_{100-x}$ and (right column) $(CoNbTa)_x(Al_2O_3)_{100-x}$ in the temperature range 65–300 K (borrowed from [36]).

($\rho > 10^{-4}$ Ω cm) magnetic metallic materials (so-called dirty materials) [43, 53]. However, there exist numerous cases where the scaling relations given above are not fulfilled, and significant deviations were detected in some heterogeneous systems (see [44, 51, 54, 55] and Refs. therein). For example, we have $n \approx 0.6$ at 300 K and $n \approx 0.7$ at 77 K in magnetic granular NCs with metallic conduction (above percolation threshold), where AHE with a giant coefficient was observed when x was varied [3, 31].

The experimental studies of AHE in NCs in the dielectric composition range, especially in the range of activation hopping conduction $\ln\sigma \propto -(T_0/T)^{1/2}$, are extremely scarce because of the difficulties of measuring a weak AHE signal. The first experimental investigations of the parametric dependence $\rho_{AHE}(\rho)$ in the vicinity of MIT were carried out on $Fe{-}SiO_2$ NCs [4, 5]. When temperature was changed, the $\rho_{AHE}(\rho)$ dependence turned out to obey the power law $\rho_{AHE} \propto$

$\rho(T)^n$, where $n = 0.44$–0.59 [4]. When the Fe content was changed, the $\rho_{AHE}(\rho)$ function demonstrated strong nonmonotonic behavior: the AHE resistance in the vicinity of MIT was saturated and tended to reach a new plateau when T_0 increased [5].

The first AHE theory for the hopping mode in dilute systems with magnetic impurities was developed in [56], where a scaling law with $n = 0.5$ was obtained when the impurity concentration was changed. The main conclusion of this theory was that AHE appears due to the influence of SOI on correlated jumps between impurity triads in a percolation network (similarly to OHE in the hopping mode, which appears in impurity triads during the action of a magnetic field on the amplitude interference for the direct and indirect (second-order) transitions [57]). The further development of this approach for dilute magnetic systems was related to averaging correlated jumps in impurity centers triads using the percolation theory and let to scaling between anomalous (σ_{AHE}) and longitudinal (σ) conductivity of the form $\sigma_{AHE} \propto \sigma^\gamma$, where $1.33 < \gamma < 1.76$ (i.e., $0.67 > n > 0.24$) [58].

The authors of [59] created a microscopic AHE theory in the tunneling mode for the case of an array of close-packed FM granules coupled by contacts with a tunnel conductance $G_t \geq 2e^2/\hbar$. Recall that this condition corresponds to metallic conduction in NC at $x_c < x < x_p$ under the logarithmic law $\sigma \propto \ln T$ for conduction (see Section 3). In terms of the model [59], AHE appears only inside granules and scaling in the $\rho_{AHE}(\rho)$ dependence is absent ($n \approx 0$). Such unusual scaling with $n \approx 0$ provided $\sigma \propto \ln T$ was demonstrated in Ni–SiO_2 NC by varying the nickel content [31]. In particular, it was shown that $\rho_{AHE}(\rho) \approx$ const when ρ changes below the percolation threshold over the wide range from 2×10^{-2} to 2×10^{-1} Ω cm. It should be noted that the results of our AHE investigations in Fe–SiO_2 in the insulator composition range also indicates the manifestation of scaling with $n \approx 0$ when the Fe content changes [5].

However, later the authors of [39] showed that AHE can appear inside tunnel barrier because of the scattering of spin-polarized electrons by impurities with a high SOI constant (3*d* elements or Pt- and Ta-type heavy metals), which are located in the tunneling gaps between granules. Tunneling AHE can also appear inside a tunnel barrier layer due to the Rashba SOI induced by the potential gradient due to an applied voltage [60].

Other tunneling AHE mechanisms, which are caused by interface SOI (which brings about "skew" electron tunneling even in the absence of impurities), have recently been considered [61, 62]. As for the last two mechanisms, they require a specific crystal structure for tunnel junctions, which can hardly be formed in strongly disordered systems (including NCs). It is better to study the mechanism described in [60] in individual tunnel junctions, where the strong electric fields that are necessary for the induced Rashba SOI (more than 10^5 V/cm) can easily be reached. The typical fields in transport measurements in planar NC samples do not exceed 10^2 V/cm.

The theoretical predictions of tunneling AHE [39] and the logarithmic dependence $\sigma(T)$ detected in NC with a high dispersed ion concentration N_d [34] initiated our studies of this effect, the manifestations of which were detected in $(CoFeB)_x(Al_2O_3)_{100-x}$ NC [26]. This tunneling AHE is characterized by the fact that it is reliably observed in the range where electrical resistance depends logarithmically on temperature. The coefficient n of correlation between the AHE resistance and the conventional electrical resistance differs from this coefficient in the metallic range above the percolation threshold ($n = 0.6$–0.7 when x is varied [3, 31]) and depends strongly on the parameter to be variable (temperature or concentration). For example, for NC samples with $x = 49$–56 at %, we have $\sigma_{AHE}(T) \propto \sigma^\gamma(T)$ at $\gamma = 1.41$–1.61 when temperature is varied, which is equivalent to a decrease in n from 0.6 to 0.4 (Fig. 4). However, when the composition is varied, allowing for the magnetization is proportional to x we have $\rho_{AHE}(x)/x \propto \rho^n(x)$, where $n \approx 0.24$ at $T = 10$ K and decreases monotonically to $n \approx 0.2$ when the temperature increases to 160 K (Fig. 5). Note that this tendency in decreasing n from 0.7 to 0.6 is observed in NC with $x > x_p$ in the range $T = 77$–300 K [3, 31].

The experimental investigation of tunneling AHE is hindered by shunting this effect in granules (see Fig. 6). The authors of [26] proposed an AHE model in granular alloys, which takes into account both contributions of granules and tunneling gaps,

$$\rho_{AHE}(x,T) \approx 0.37\frac{b}{a}\rho_{Hd}(x,T) + \rho_{Hg}(T), \qquad (9)$$

where $\rho_{Hd}(x, T)$ and $\rho_{Hg}(x, T)$ are the electrical resistivities of the tunneling AHE and the AHE in granules, respectively, and b is the tunneling gap thickness. Recall that the last term in Eq. (9) is independent of x. The factor $0.37(b/a)$, which decreases the contribution tunneling AHE in Eq. (9), reflects the shunting of the local sources of tunneling AHE in our percolation system, which was noted above.

An analysis of the experimental data with Eq. (9) confirms the presence of tunneling AHE and makes it possible to qualitatively explain both the temperature and concentration dependences of AHE [26].

According to Eq. (9), a strong (by an order of magnitude) weakening of tunneling AHE is expected in the $(CoFeB)_x(LiNbO_3)_{100-x}$ system with strongly elongated granules as compared to the $(CoFeB)_x(Al_2O_3)_{100-x}$ NC with spherical granules. In addition, tunneling AHE is weakened because of impossible "head-on" tunneling between granules (Fig 6a, inset; [10]). Therefore, we failed to observe

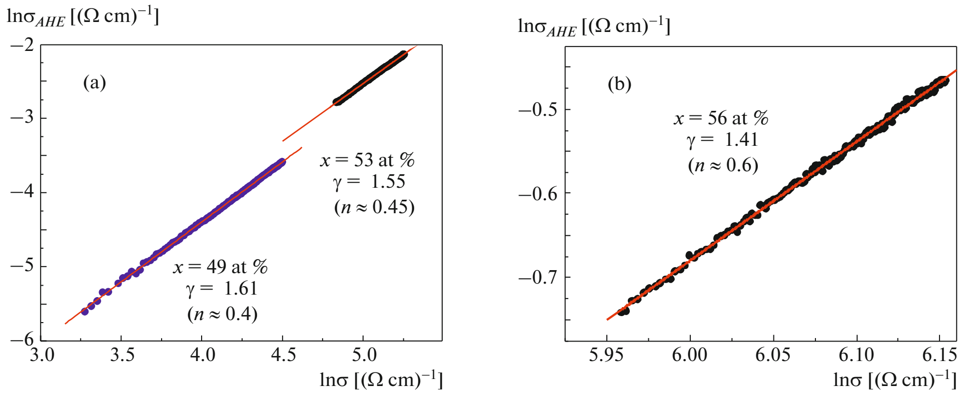

Fig. 4. (Color online) Logarithmic dependences of the electrical conductivity of AHE σ_{AHE} on σ ($\ln\sigma_{AHE} \propto \gamma\ln\sigma$) for $(CoFeB)_x(Al_2O_3)_{100-x}$ samples with x = (a) 49 and 53 at % and (b) 56 at % (borrowed from [36]).

scaling in the $\rho_{AHE}(\rho)$ dependence during the variation of x despite the fact that scaling with $n \approx 0.4$ was observed when temperature was changed [10]. In other words, the scaling was identical to that in the case of $(CoFeB)_x(Al_2O_3)_{100-x}$ samples near MIT [26].

In conclusion of this section, we note that, for tunneling AHE to be detected under the SOI scattering of tunneling electrons, it is desirable to use NCs with dispersed heavy metal (Pt, Ta, Hf) atoms [39], since the SOI constant of these atoms is an order of magnitude higher than that of the 3*d* elements. Therefore, the question of the magnitude of tunneling AHE in NC systems is still open.

6. MEMRISTIVE EFFECT

The memristive effect is associated with a change in the resistive state of an object (memristor) under an applied electric field and the charge passing through it and with the retention of this state after the removing of a voltage pulse. Memristors (memory resistors) are promising elements for designing a new type of energy-independent RRAM memory and neuromorphic computing networks (NCNs), since they consume low energy for data recording/reading, have a multilevel character of RS, and hence can emulate key NCN elements (synapses) [15–18].

The RS effect is usually observed in metal/oxide/metal (MOM) structures, where they are caused by the electromigration of oxygen (anion) vacancies or metal cations [15–18]. As a result, conducting channels (filaments) form (or rupture) in the oxide insulating layer, and the structure is switched into a low-resistance (LRS) or high-resistance (HRS) state, respectively. The formation of filaments is substantially random, which is one of the main causes of degradation of the properties of memristors during cyclic RS [15, 16]. Another disadvantage of anion or cation memristive MOM structures is related to the fact that their stable operation usually requires electroforming, which consists in the application of a relatively high voltage to a structure to form filaments (bridges).

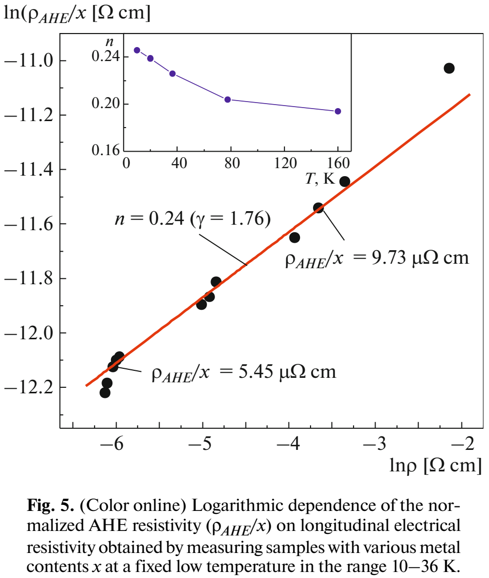

Fig. 5. (Color online) Logarithmic dependence of the normalized AHE resistivity (ρ_{AHE}/x) on longitudinal electrical resistivity obtained by measuring samples with various metal contents x at a fixed low temperature in the range 10–36 K. (inset) Temperature dependence of exponent n in the scaling relation $\rho_{AHE}/x \propto \rho^n(x)$ (borrowed from [26]).

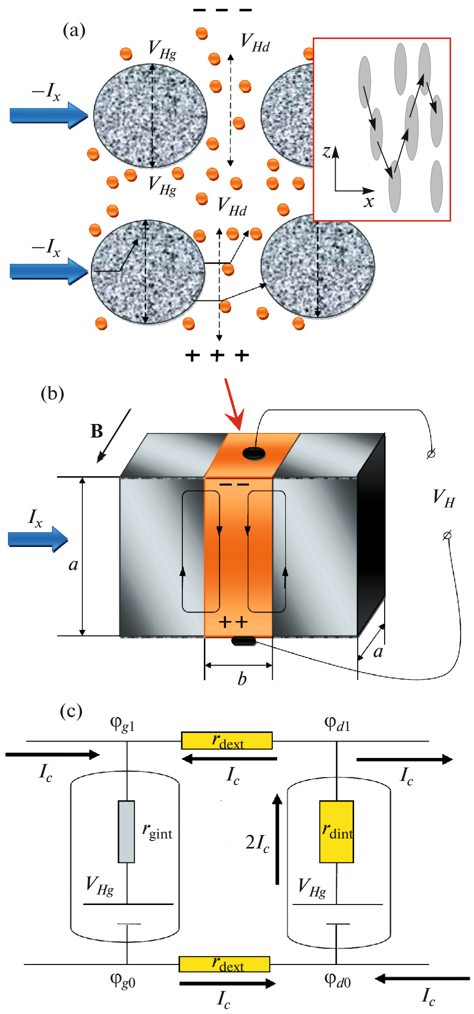

Fig. 6. (Color online) (a) Granular system with SOI scattering by defects in an oxide matrix during electron tunneling between granules. Two emf sources of AHE connected in parallel are shown: the first source is caused by SOI in granules ($V_{Hg} = R_{Hg}I_x$), and the second appears inside a tunnel barrier ($V_{Hd} = R_{Hd}I_x$). Current I_x passes through neighboring granules, and R_{Hg} and R_{Hd} are the Hall resistances of granules and an intergranular dielectric layer, respectively. (inset) Scheme of electron tunneling between granules extended along the NC growth direction [63]. (b) Schematic diagram of the tunnel junction between granules, which illustrates the appearance of eddy currents during the Hall effect in the dielectric layer. (c) Equivalent circuit of a periodic chain of tunnel junctions (resistances) with two local Hall emf sources, $r_{\text{dint}} \gg r_{\text{dext}} \gg r_{\text{gint}}$, $V_{\text{Heff}} = (1/2)[(\varphi_{g1} - \varphi_{g0}) + (\varphi_{d1} - \varphi_{d0})$ (borrowed from [26]).

Other RS mechanisms are also possible. They do not require forming and are associated with, e.g., the recharging of localized electronic states at a Schottky barrier and/or in the oxide bulk (see [64, 65] and Refs. therein), the electric repolarization of a ferroelectric oxide [66, 67], redox reactions in organic materials [68], the electromigration effect [69], and finally the temperature-induced metal–insulator transition in Mott materials (NbO_2, VO_2, V_2O_3). This transition has recently been detected and is being discussed and studied [70]. Nevertheless, oxide memristive structures are of particular interest as the systems that can have a multilevel RS character at a long retention time of resistive states, have good manufacturability, and can easily be integrated into the modern microelectronic technology [15, 17].

Despite the significant accumulated experimental data, a microscopic theory of the reversible RS effects has not been developed to date. In particular, this is caused by the difficulties in describing the mutually related nonequilibrium processes of heat, electron, and ion transport on a nanoscale and by the following additional effects: the presence of a few RS channels related to, e.g., simultaneous manifestation of cation and anion transport [71], the synergetic contributions of electric polarization of a ferroelectric and ion transport to RS [67], and the conductance quantization phenomena [72, 73].

In the case of metal/nanocomposite/metal (M/NC/M) structures based on metal–oxide NCs, the transition into a low-resistance state should be determined by percolation chains, which are specified by the spatial arrangement and concentration of metal nanogranules in NC; therefore, the endurance to the cyclic RS should be high [10]. We [10, 28] were the first to demonstrate the importance of the percolation effects in M/NC/M structures. Note that significant results were obtained for M/Pt–SiO_2/M structures, where the active layer was created by magnetron sputtering of a Pt/SiO_2 composite target and consisted of an SiO_2 matrix with dispersed Pt atom nanoclusters [74]. In this case, the maximum number of stable RS was shown to exceed $N_{\max} = 3 \times 10^7$ at a retention time of resistive states $t_r > 6$ months.

The mechanism responsible for RS in M/Pt–SiO_2/M structures was not revealed. It is likely to be related to the motion of oxygen vacancies, the formation of conducting channels (filaments) during RS, and local heating and coarsening of Pt nanoparticles in them (from 2–3 to 3–4 nm). The authors of [75] recently studied M/W–SiO_2/n-Si structures with the bottom contact made of high-doped n-Si ($\rho < 0.05\ \Omega$ cm), where the active layer was created by the implantation of SiO_2 by W ions. Such structures were shown not to require forming. Even in the presence of W metal particles, the active switching W–SiO_2 layer exhibits a rather high ratio of the HRS (off) and LRS (on) resistances,

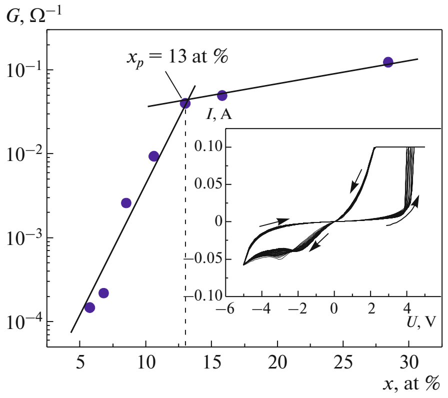

Fig. 7. (Color online) Conductance $G(x) = I/U$ of the M/(CoFeB)$_x$(LiNbO$_3$)$_{100-x}$/M structure vs. metal content x measured at a voltage $U = 0.2$ V. (inset) I–V characteristic of the structure with the optimum content $x_{\text{opt}} \approx$ 8 at %, which was obtained by 30 cyclic measurements (arrows indicate the voltage scanning direction).

$R_{\text{off}}/R_{\text{on}} > 10^4$ at $N_{\max} \approx 4 \times 10^2$ and $t_r \approx 10^4$ s [75]. Note that the plasticity of the memristor structures developed in [74, 75] was not studied, and the possible relation between the RS of the structures and the effects of their percolation conductance was not investigated.

In our recent studies of M/NC/M structures based on (CoFeB)$_x$(LiNbO$_3$)$_{100-x}$ NC [10, 28], we detected the memristive effect with $R_{\text{off}}/R_{\text{on}} > 100$ at the optimum content $x = x_{\text{opt}} \approx 8$–15 at % below the percolation threshold of the NC. This effect was well reproduced at 10^5 RS cycles or more and was almost independent of the type of contact [10, 13, 28]. Moreover, the synthesized M/NC/M structures had a high degree of plasticity (i.e., a smooth change in the resistive state in the $R_{\text{off}} - R_{\text{on}}$ window), which allowed the important properties of biological synapses to be emulated [13, 14].

These results are illustrated by the data presented in Figs. 7 and 8 and obtained for M/(CoFeB)$_x$(LiNbO$_3$)$_{100-x}$/M structures with an NC layer thickness $d \approx 2.5$ μm and strongly elongated (up to 10 nm) granules [10, 28]. Figure 7 shows the conductance of the structure $G(x) = I/U$ as a function of the metal content measured at the DC mode and a voltage $U = 0.2$ V, which is an order of magnitude lower than the RS voltage of the structure to the LRS ($U_{LRS} \approx 4$ V; see inset to Fig. 7). The form of the $G(x)$ dependence is characteristic of percolation granular systems [1]: the $G(x)$ function is exponential below a certain threshold $x < x_p$ (percolation threshold, $x_p \approx$ 13 at % in our case) at $x > x_p$, G weakly depends on x [76].

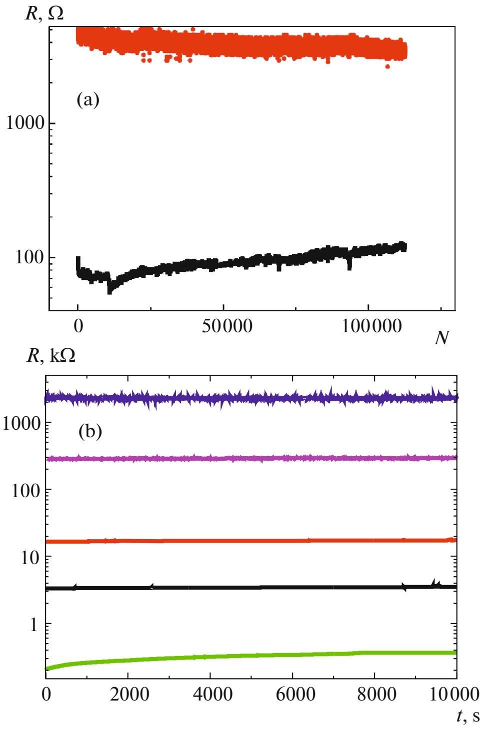

Fig. 8. (Color online) (a) Stability of the M/NC/M structure based on (CoFeB)$_x$(LiNbO$_3$)$_{100-x}$ NC at $x \approx 8$ at % to cyclic RS. (b) Time dependences of five resistive states for the M/NC/M structure grown at a high initial oxygen pressure (see text).

Note that the I–V characteristic of the M/NC/M structure is well reproduced during cyclic measurements in the range from −5 to +4 V (Fig. 7, inset). The electroforming effect is very weak: the voltages U_{LRS} of switching from HRS to LRS in the first and next switchings are close, in contrast to MOM structures based on homogeneous oxides [15, 16]. The high stability of the structures is confirmed by direct measurements of the endurance of the M/NC/M structures to degradation during cyclic switching, i.e., the maximum number of set/reset cycles ($N_{\max}$), which is certainly larger than 10^5 (see Fig. 8a and [13]).

A multilevel character of RS in combination with a long retention time of resistive states is achieved in structures with a developed oxide layer at the bottom electrode, which forms at the initial stage of NC growth at a relatively high oxygen partial pressure

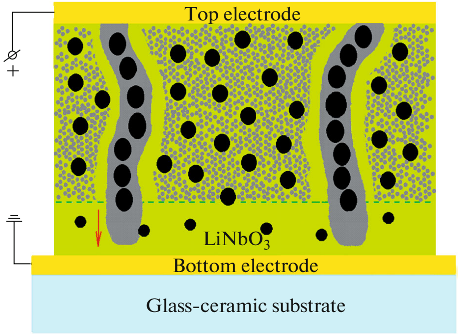

Fig. 9. (Color online) M/NC/M structure in HRS after cyclic RS and the application of a positive potential to the top electrode. The gray regions surrounding granule chains consist of a metallic condensate, which appears during the nucleation of Co and Fe atoms and oxygen vacancies when an electric current passes through the percolation chains formed by granules.

($P_{O_2} \approx 2.5 \times 10^{-5}$ Torr) and a given oxygen flow rate (see Section 2). In this case, the optimum metal content for RS is shifted toward high values $x = x_{opt} \approx$ 15 at % [76]. Figure 8b shows the retention times of resistive states in such a structure. Five weakly fluctuating and well-resolved resistive states are clearly visible within the time longer than 10^4 s.

The presence of an oxide layer was recently shown not to ensure stable RS in M/NC/M structures. Another important parameter of NC for the existence of stable RS is the presence of dispersed magnetic atoms in an insulating NC matrix at a sufficiently high concentration ($N_d \sim 10^{22}$ cm^{-3}); at a low concentration ($N_d \sim 10^{21}$ cm^{-3}), RS become unstable and ceases to be observed [32]. This fact, the high limiting currents during RS (up to 0.1 A; see inset to Fig. 7), and the recently detected strong enhancement of capacitance (by a factor of 8) during HRS–LRS switching in an M/NC/M structure allowed us to develop the qualitative multifilament model for RS (see Fig. 9) [76].

In the initial state after the preparation of an M/NC/M structure, the dispersed atoms are uniformly distributed in the insulating NC matrix. However, after the application of voltage and the passage of current, the dispersed atoms can nucleate around granule chains forming percolation paths; as a consequence, conducting "metallized" chains (MCs) can form (see Fig. 9). Obviously, the nucleation effects manifest themselves in our case due to the strong supersaturation of the system by the atomic phase and the presence of metallic nucleation centers (nanoparticles) in it. Similar effects were observed in, e.g., SiO$_2$-based memristive structures with dispersed Pt or W atoms [74, 75].

When a sufficiently high positive voltage is applied to the top electrode, the structure tends to pass to LRS via the motion of oxygen vacancies and cations to the bottom electrode along MCs and a decrease in the effective gap l_g between MCs and the bottom electrode (Fig. 9). On the other hand, the capacitance of the structure in this situation should increase, since the capacitance in a first approximation is $C \propto 1/l_g$. Obviously, the reverse situation takes place when a sufficiently high negative voltage is applied to the structure [76].

The multifilament character of RS is thought to ensure stable RS of M/NC/M structures and a smooth change in their resistance in the $R_{off} - R_{on}$ window, which in turn determines the possibilities of their use in adaptive electronics to be described in the next section.

7. ADAPTIVE PROPERTIES OF NANOCOMPOSITE STRUCTURES

Adaptive electronics is considered to be a system with the parameters of its elements that are self-adjusted during operation [77]. Interest in the development of this electronics is caused by the hope of reproducing extremely low energy consumption at a high computing efficiency of biological systems in solving so-called antromorphic problems (pattern, text, and speech recognition; decision making; generalization; forecasting) [78]. The development of NCN-based adaptive electronics is of particular interest [17, 18]: the layers of artificial neurons in NCNs are connected through synapses, integrate input signals, and generate output signals (spikes). Several successful prototypes of pulsed NCNs based on a complementary metal–oxide–semiconductor (CMOS) technology, such as True North [79], SpiNNaker [80], and Loihi [81, 82], have been created to date. However, digital CMOS elements were not optimized for neuromorphic calculations from the very beginning; therefore, they cannot completely emulate the main property of synapses, namely, their plasticity. Therefore, memristors can emulate synapses and, in part, neurons more exactly, since the principle of their operation is based on ion drift and diffusion and is fundamentally similar to the principle of functioning of these biological elements [17]. In addition, the NCNs based on crossbar arrays of memristors can be used to perform parallel and energy-effective calculations in memory (computing-in-memory) according to Kirchhoff's rules [83].

Memristor-based NCNs are being developed in the following two main directions: (i) the transfer of the algorithms of learning program neuron networks to a hardware basis (perceptron-type networks [84–86], reprogrammable memristor crossbar array in the composition of a complete hardware system on chip [87]

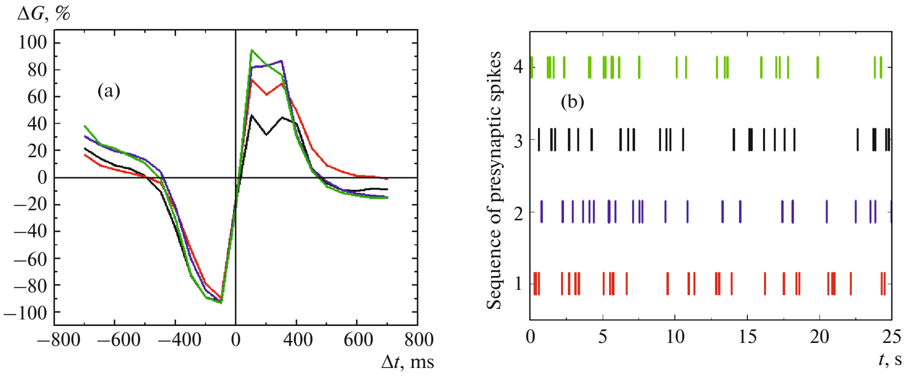

Fig. 10. (Color online) (a) STDP window for four different M/NC/M memristors based on $(\mathrm{CoFeB})_x(\mathrm{LiNbO}_3)_{100-x}$. The initial states of the memristors are 1 mS. (b) Poisson sequences of the times of presynaptic spikes used for four NCN inputs.

and long short-term memory [88]) and (ii) the use of so-called biosimilar network learning algorithms [89].

The disadvantage of the first approach is related to the complexity of its hardware implementation, since it is necessary to know the current state of each synaptic weight of a memristor at each learning step and to be able to change it by a strictly determined value [85]. Therefore, this approach of learning NCNs is likely to be suitable for solving certain (log) problems with the use of supervised learning.

The second approach, which is based on biosimilar learning principles, is poorly understood from a practical standpoint. Nevertheless, it is considered to have good prospects for constructing self-learning NCNs. Biological neuron networks learn due to the ability of synapses to change their weight, and this ability is called synaptic plasticity [90].

STDP is one of the promising mechanisms of evolution of the synaptic weight [90]. According to STDP, the synaptic weight increases if a postsynaptic neuron generates a spike right after a presynaptic neuron, indicating the presence of a cause-and-effect relation, and vice versa. The mechanism of changing the memristive weight according to the STDP rule was demonstrated on some memristors [90–92] and was used in pulsed NCNs [12, 14, 93–95]. One of the most important characteristics of memristors was found to be the possibility of their switching into numerous different states [96]. Therefore, the memristors based on magnetic nanogranular composites with dispersed ions in an insulating matrix can be ideal candidates for the role of synapses in pulsed NCNs.

To create a pulsed NCN, it is necessary to check the possibility of learning individual NC memristors according to the STDP rules. To this end, we used identical pre- and postsynaptic sawtooth spikes applied to the bottom and top electrodes of the structure, respectively. The spike amplitude (3 V) and duration (400 ms) were chosen so that a single spike did not change the resistance of a memristor. However, if two spikes with short time delay Δt between them are supplied to a memristor, the voltage drop across it can be large enough to change its conductance. The conductance G of a memristor can be related to the synaptic weight; then, the change in the conductance ΔG is equivalent to the change in the synaptic weight. The measurements were carried out before and after the supply of a sequence of pre- and postsynaptic spikes. The initial state of memristors was always the same (corresponded to a conductance of 1 mS) and specified with the algorithm from [97]. Figure 10a shows the relative weight change versus time Δt (STDP window) for four different memristors. Synaptic potentiation ($\Delta G > 0$) is seen to occur at $\Delta t > 0$ and depression ($\Delta G < 0$) at $\Delta t < 0$. A similar dependence was also revealed in biological systems [98].

To study the specific features of learning with STDP, we developed NCN consisting of four presynaptic neurons connected to a postsynaptic neuron via NC memristive synapses. All neurons were programmable: the presynaptic neurons were programmed to generate various Poisson sequences of spikes at the same average frequency of 1 Hz (Fig 10b). The postsynaptic neuron had a threshold type: it generated a spike if the total current exceeded a threshold value I_{th}. The optimum value of I_{th} (1 mA) was determined in [12]. Initially, all NCN memristors were brought to a given state R_0 using the algorithm from [97]. R_0 was taken to be 0.1, 1, and 10 kΩ. A stored sequence of spikes, which was the same for different R_0, was then supplied from the presynaptic neurons. The resistances of the memristors were measured after each postsynaptic spike. Figure 11 shows the evolution of the resistances of the memristors. After several post-

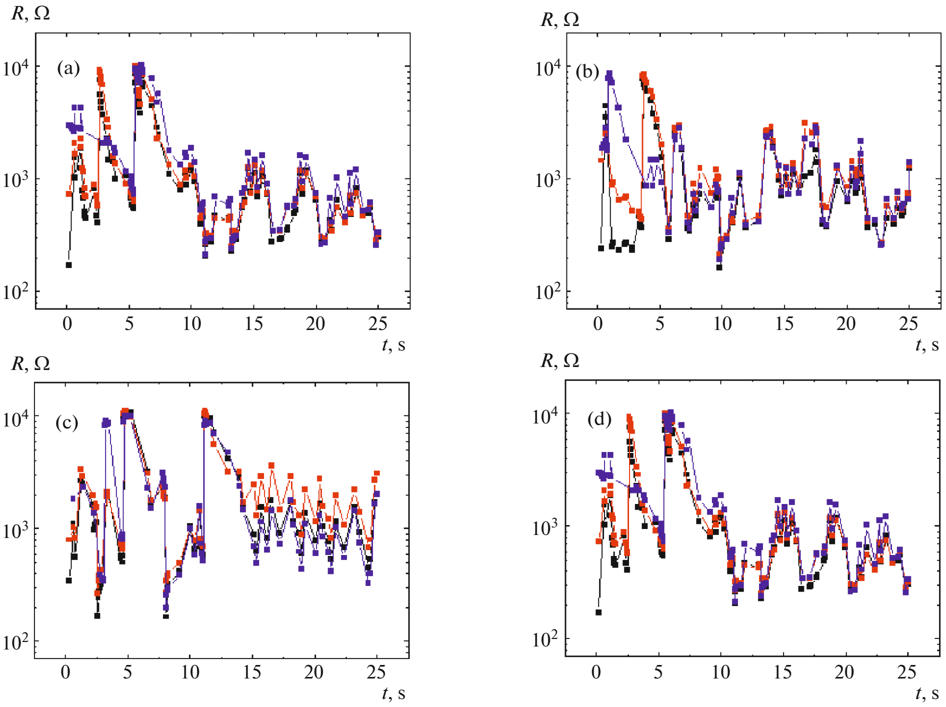

Fig. 11. (Color online) Time dependences of the current resistances of M/NC/M memristors at an initial resistance of (black squares) 0.1, (red squares) 1, and (blue squares) 10 kΩ for the (a) first, (b) second, (c) third, and (d) fourth sequence of presynaptic spikes.

synaptic spikes, the resistive state of the system elements is seen to begin to depend only on the learning conditions (in our case, a sequence of supplied spikes) and to cease to depend on the initial values of R_0. Thus, the learning of NCN according to the STDP rules demonstrates adaptive properties, which can be used to create unsupervised-learning NCN. Note also that, if given sequences of presynaptic spikes are supplied to other memristors, the final resistance of the memristor does not change [14], which indicates the stability of NCN learning according to the STDP rules to the scatter of the characteristics of memristors.

8. CONCLUSIONS

We studied the transport properties of granular metal–insulator M_xD_{100-x} NCs, which have nanogranules chaotically distributed in a dielectric matrix and a significant content (up to $N_d \sim 10^{22}$ cm^{-3}) of the atomic phase of metal atoms (which play the role of magnetic ions). The presence of a large number of dispersed ions in intergranular gaps was shown to cause a logarithmic temperature dependence of the electrical resistance, a positive contribution to MR, the appearance of tunneling AHE, and a multifilament mechanism of RS (memristive effect). This effect brings about an adaptive character of memristors based on NC with the maximum dispersed ion content (up to $N_d \sim 3 \times 10^{22}$ cm^{-3}). Resistive states were shown to be set according to biosimilar STDP rules in such memristors (possibility of local "learning"). The final state of memristors was found to be independent of their initial state and to depend only on the irradiation conditions (sequence of spikes). The results obtained open up fresh opportunities for creating autonomous neuromorphic systems to be learned to solve complex cognitive problems.

FUNDING

This work was supported by the Russian Science Foundation (project no. 16-19-10233) and was performed on the equipment of the Resource centers of the National Research Centre Kurchatov Institute.

ADDITIONAL INFORMATION

This article was prepared for the special issue dedicated to the centenary of A.S. Borovik-Romanov.

REFERENCES

1. A. Milner, A. Gerber, B. Groisman, M. Karpovsky, and A. Gladkikh, Phys. Rev. Lett. **76**, 475 (1996).
2. N. Kobayashi, S. Ohnuma, T. Masumoto, and H. Fujimori, J. Appl. Phys. **90**, 4159 (2001).
3. A. Pakhomov, X. Yan, and B. Zhao, Appl. Phys. Lett. **67**, 3497 (1995).
4. B. A. Aronzon, D. Yu. Kovalev, A. N. Lagar'kov, E. Z. Meilikhov, V. V. Ryl'kov, M. V. Sedova, N. Negre, M. Goiran, and J. Leotin, JETP Lett. **70**, 90 (1999).
5. B. A. Aronzon, A. B. Granovski, D. Yu. Kovalev, E. Z. Meilikhov, V. V. Ryl'kov, and M. A. Sedova, JETP Lett. **71**, 469 (2000).
6. A. B. Granovskii, I. V. Bykov, E. A. Gan'shina, V. S. Gushchin, M. Inue, Yu. E. Kalinin, A. A. Kozlov, and A. N. Yurasov, J. Exp. Theor. Phys. **96**, 1104 (2003).
7. E. A. Gan'shina, M. V. Vashuk, A. N. Vinogradov, A. B. Granovsky, V. S. Gushchin, P. N. Shcherbak, Yu. E. Kalinin, A. V. Sitnikov, Ch. O. Kim, and Ch. G. Kim, J. Exp. Theor. Phys. **98**, 1027 (2004).
8. S. Bedanta, T. Eimüller, W. Kleemann, J. Rhensius, F. Stromberg, E. Amaladass, S. Cardoso, and P. P. Freitas, Phys. Rev. Lett. **98**, 176601 (2007).
9. S. Bedanta and W. Kleemann, J. Phys. D **42**, 013001 (2009).
10. V. V. Rylkov, S. N. Nikolaev, V. A. Demin, A. V. Emelyanov, A. V. Sitnikov, K. E. Nikirui, V. A. Levanov, M. Yu. Presnyakov, A. N. Taldenkov, A. L. Vasil'ev, K. Yu. Chernoglazov, A. S. Vedeneev, Yu. E. Kalinin, A. B. Granovskii, V. V. Tugushev, and A. S. Bugaev, J. Exp. Theor. Phys. **126**, 353 (2018).
11. V. V. Rylkov, V. A. Demin, A. V. Emelyanov, A. V. Sitnikov, Yu. E. Kalinin, V. V. Tugushev, and A. B. Granovsky, *Novel Magnetic Nanostructures: Unique Properties and Applications*, Ed. by N. Domracheva, M. Caporali, and E. Rentschler (Elsevier, Amsterdam, 2018), Chap. 13, p. 427.
12. K. E. Nikiruy, A. V. Emelyanov, V. V. Rylkov, A. V. Sitnikov, and V. A. Demin, Tech. Phys. Lett. **45**, 386 (2019).
13. K. E. Nikiruy, A. V. Emelyanov, V. A. Demin, A. V. Sitnikov, A. A. Minnekhanov, V. V. Rylkov, P. K. Kashkarov, and M. V. Kovalchuk, AIP Adv. **9**, 065116 (2019).
14. A. V. Emelyanov, K. E. Nikiruy, A. V. Serenko, A. V. Sitnikov, M. Yu. Presnyakov, R. B. Rybka, A. G. Sboev, V. V. Rylkov, P. K. Kashkarov, M. V. Kovalchuk, and V. A. Demin, Nanotechnology **31**, 045201 (2020).
15. D. Ielmini, Semicond. Sci. Technol. **31**, 063002 (2016).
16. J. del Valle, J. G. Ramírez, M. J. Rozenberg, and I. K. Schuller, J. Appl. Phys. **124**, 211101 (2018).
17. Q. Xia and J. J. Yang, Nat. Mater. **18**, 309 (2019).
18. *Handbook of Memristor Networks*, Ed. by L. Chua, G. Ch. Sirakoulis, and A. Adamatzky (Springer, Cham, 2019).
19. B. Raquet, M. Goiran, N. Negre, J. Leotin, B. Aronzon, V. Rylkov, and E. Meilikhov, Phys. Rev. B **62**, 17144 (2000).
20. V. V. Rylkov, B. A. Aronzon, A. B. Davydov, D. Yu. Kovalev, and E. Z. Meilikhov, J. Exp. Theor. Phys. **94**, 779 (2002).
21. I. S. Beloborodov, A. V. Lopatin, V. M. Vinokur, and K. B. Efetov, Rev. Mod. Phys. **79**, 469 (2007).
22. C. J. Adkins, in *Metal–Insulator Transitions,* Ed. by P. P. Edwards and C. N. R. Rao (Taylor and Francis, London, 1995), p. 191.
23. J. E. Morris and T. J. Coutts, Thin Solid Films **47**, 3 (1977).
24. B. Abeles, Ping Sheng, M. D. Coutts, and Y. Arie, Adv. Phys. **24**, 407 (1975).
25. S. A. Gridnev, Yu. E. Kalinin, and A. V. Sitnikov, *Nonlinear Phenomena in Nano- and Microheterogeneous Systems* (BINOM, Moscow, 2012) [in Russian].
26. V. V. Rylkov, S. N. Nikolaev, K. Yu. Chernoglazov, V. A. Demin, A. V. Sitnikov, M. Yu. Presnyakov, A. L. Vasiliev, N. S. Perov, A. S. Vedeneev, Yu. E. Kalinin, V. V. Tugushev, and A. B. Granovsky, Phys. Rev. B **95**, 144202 (2017).
27. V. V. Rylkov, A. V. Sitnikov, S. N. Nikolaev, V. A. Demin, A. N. Taldenkov, M. Yu. Presnyakov, A. V. Emelyanov, A. L. Vasiliev, Yu. E. Kalinin, A. S. Bugaev, V. V. Tugushev, and A. B. Granovsky, J. Magn. Magn. Mater. **459**, 197 (2018).
28. V. A. Levanov, A. V. Emel'yanov, V. A. Demin, K. E. Nikirui, A. V. Sitnikov, S. N. Nikolaev, A. S. Vedeneev, Yu. E. Kalinin, and V. V. Ryl'kov, J. Commun. Technol. Electron. **63**, 491 (2018).
29. E. Lähderanta, M. Guc, M. A. Shakhov, E. Arushanov, and K. G. Lisunov, J. Appl. Phys. **120**, 035704 (2016).
30. K. B. Efetov and A. Tschersich, Phys. Rev. B **67**, 174205 (2003).
31. D. Bartov, A. Segal, M. Karpovski, and A. Gerber, Phys. Rev. B **90**, 144423 (2014).
32. V. Rylkov, A. Sitnikov, S. Nikolaev, A. Emelyanov, K. Chernohlazov, K. Nikiruy, A. Drovosekov, M. Blinov, E. Fadeev, A. Taldenkov, V. Demin, A. Vedeneev, A. Bugaev, and A. Granovsky, IEEE Magn. Lett. **10**, 2509504 (2019).
33. V. V. Rylkov, A. B. Drovosekov, A. N. Taldenkov, S. N. Nikolaev, O. G. Udalov, A. V. Emelyanov, A. V. Sitnikov, K. Yu. Chernoglazov, V. A. Demin, O. A. Novodvorskii, A. S. Vedeneev, and A. S. Bugaev, J. Exp. Theor. Phys. **128**, 115 (2019).
34. Yu. O. Mikhailovskii, V. N. Prudnikov, V. V. Ryl'kov, K. Yu. Chernoglazov, A. V. Sitnikov, Yu. E. Kalinin, and A. B. Granovskii, Phys. Solid State **58**, 444 (2016).
35. S. N. Nikolaev, K. Yu. Chernoglazov, V. A. Demin, N. K. Chumakov, V. A. Levanov, A. A. Magomedova, A. V. Sitnikov, Yu. E. Kalinin, A. B. Granovskii, and V. V. Ryl'kov, J. Surf. Invest.: X-ray, Synchrotron Neutron Tech. **11**, 549 (2017).
36. M. I. Blinov, M. A. Shakhov, V. V. Rylkov, E. Lähderanta, V. N. Prudnikov, S. N. Nikolaev, A. V. Sitnikov,

and A. B. Granovsky, J. Magn. Magn. Mater. **469**, 155 (2019).

37. T. Mitsuyu and K. Wasa, Jpn. J. Appl. Phys. **20**, L48 (1981).
38. Yu. A. Kalinin, A. N. Remizov, and A. V. Sitnikov, Phys. Solid State **46**, 2146 (2004).
39. A. V. Vedyayev, N. Ryzhanova, N. Strelkov, and B. Dieny, Phys. Rev. Lett. **110**, 247204 (2013).
40. A. Gerber, I. Kishon, I. Ya. Korenblit, O. Riss, A. Segal, and M. Karpovski, Phys. Rev. Lett. **99**, 027201 (2007).
41. J. Inoue and S. Maekawa, Phys. Rev. Lett. **53**, R11927 (1996).
42. J. S. Helman and B. Abeles, Phys. Rev. Lett. **39**, 1429 (1976).
43. N. Nagaosa, J. Sinova, S. Onoda, A. H. MacDonald, and N. P. Ong, Rev. Mod. Phys. **82**, 1539 (2010).
44. Y. Tian, L. Ye, and X. Jin, Phys. Rev. Lett. **103**, 087206 (2009).
45. D. Chiba, A. Werpachowska, M. Endo, Y. Nishitani, F. Matsukura, T. Dietl, and H. Ohno, Phys. Rev. Lett. **104**, 106601 (2010).
46. X. Liu, S. Shen, Z. Ge, W. L. Lim, M. Dobrowolska, and J. K. Furdyna, Phys. Rev. B **83**, 144421 (2011).
47. A. Shitade and N. Nagaosa, J. Phys. Soc. Jpn. **81**, 083704 (2012).
48. Yu. A. Mikhailovskii, D. E. Mettus, A. P. Kazakov, V. N. Prudnikov, Yu. E. Kalinin, A. S. Sitinikov, A. Gerber, D. Bartov, and A. B. Granovskii, JETP Lett. **97**, 473 (2013).
49. L. N. Oveshnikov, V. A. Kul'bachinskii, A. B. Davydov, and B. A. Aronzon, JETP Lett. **100**, 570 (2014).
50. S. A. Meynell, M. N. Wilson, J. C. Loudon, A. Spitzig, F. N. Rybakov, M. B. Johnson, and T. L. Monchesky, Phys. Rev. B **90**, 224419 (2014).
51. D. Hou, G. Su, Y. Tian, X. Jin, S. A. Yang, and Q. Niu, Phys. Rev. Lett. **114**, 217203 (2015).
52. J. G. Checkelsky, M. Lee, E. Morosan, R. J. Cava, and N. P. Ong, Phys. Rev. B **77**, 014433 (2008).
53. S. Onoda, N. Sugimoto, and N. Nagaosa, Phys. Rev. Lett. **97**, 126602 (2006); Phys. Rev. B **77**, 165103 (2008).
54. A. V. Vedyaev, A. B. Granovskii, and O. A. Kotel'nikova, *Kinetic Phenomena in Disordered Ferromagnetic Alloys* (Mosk. Gos. Univ., Moscow, 1992) [in Russian].
55. A. V. Vedyaev, A. B. Granovskii, A. V. Kalitsov, and F. Bauers, J. Exp. Theor. Phys. **85**, 1204 (1997).
56. A. V. Vedyaev and A. B. Granovskii, Sov. Phys. Solid State **28**, 1293 (1986).
57. T. Holstein, Phys. Rev. **124**, 1329 (1961).
58. X.-J. Liu, X. Liu, and J. Sinova, Phys. Rev. B **84**, 165304 (2011).
59. H. Meier, M. Yu. Kharitonov, and K. B. Efetov, Phys. Rev. B **80**, 045122 (2009).
60. A. V. Vedyayev, M. S. Titova, N. V. Ryzhanova, M. Ye. Zhuravlev, and E. Y. Tsymbal, Appl. Phys. Lett. **103**, 032406 (2013).
61. A. Matos-Abiague and J. Fabian, Phys. Rev. Lett. **115**, 056602 (2015).
62. T. Huong Dang, H. Jaffres, T. L. Hoai Nguyen, and H.-J. Drouhin, Phys. Rev. B **92**, 060403(R) (2015).
63. B. I. Shklovskii and A. L. Efros, *Electronic Properties of Doped Semiconductors* (Springer, New York, 1984; Moscow, Nauka, 1979).
64. Z. B. Yan and J.-M. Liu, Sci. Rep. **3**, 2482 (2013).
65. Y. Shuai, Y. Peng, X. Pan, L. Jin, C. Wu, W. Luo, H. Zeng, and W. Zhang, Jpn. J. Appl. Phys. **57**, 121502 (2018).
66. H. Y. Yoong, H. Wu, J. Zhao, H. Wang, R. Guo, J. Xiao, B. Zhang, P. Yang, S. J. Pennycook, N. Deng, X. Yan, and J. Chen, Adv. Funct. Mater. **28**, 1806037 (2018).
67. M. Qian, I. Fina, M. C. Sulzbach, F. Sánchez, and J. Fontcuberta, Adv. Electron. Mater. **5**, 1800646 (2019).
68. D. A. Lapkin, A. V. Emelyanov, V. A. Demin, V. V. Erokhin, P. K. Kashkarov, M. V. Kovalchuk, and L. A. Feigin, Appl. Phys. Lett. **112**, 043302 (2018).
69. A. S. Vedeneev, V. V. Rylkov, K. S. Napolskii, A. P. Leontiev, A. A. Klimenko, A. M. Kozlov, V. A. Luzanov, S. N. Nikolaev, M. P. Temiryazeva, and A. S. Bugaev, JETP Lett. **106**, 411 (2017).
70. Y. Kalcheim, N. Butakov, N. M. Vargas, M.-H. Lee, J. del Valle, J. Trastoy, P. Salev, J. Schuller, and I. K. Schuller, Phys. Rev. Lett. **122**, 057601 (2019).
71. H. Jiang, L. Han, P. Lin, Zh. Wang, M. J. Jang, Q. Wu, M. Barnell, J. J. Yang, H. L. Xin, and Q. Xia, Sci. Rep. **6**, 28525 (2016).
72. A. A. Minnekhanov, B. S. Shvetsov, M. M. Martyshov, K. E. Nikiruy, E. V. Kukueva, M. Yu. Presnyakov, P. A. Forsh, V. V. Rylkov, V. V. Erokhin, V. A. Demin, and A. V. Emelyanov, Org. Electron. **74**, 89 (2019).
73. W. Xue, S. Gao, J. Shang, X. Yi, G. Liu, and R.-W. Li, Adv. Electron. Mater. **5**, 1800854 (2019).
74. B. J. Choi, A. C. Torrezan, K. J. Norris, F. Miao, J. P. Strachan, M.-X. Zhang, D. A. A. Ohlberg, N. P. Kobayashi, J. J. Yang, and R. S. Williams, Nano Lett. **13**, 3213 (2013).
75. W. Li, X. Liu, Y. Wang, Z. Dai, W. Wu, L. Cheng, Y. Zhang, Q. Liu, X. Xiao, and C. Jiang, Appl. Phys. Lett. **108**, 153501 (2016).
76. M. N. Martyshov, A. V. Emelyanov, V. A. Demin, A. A. Minnekhanov, S. N. Nikolaev, K. E. Nikiruy, A. V. Ovcharov, M. Yu. Presnyakov, A. V. Sitnikov, A. L. Vasiliev, P. A. Forsh, A. B. Granovskiy, P. K. Kashkarov, M. V. Kovalchuk, and V. V. Rylkov, arxiv: 1912.03726.
77. S. D. Ha and S. Ramanathan, J. Appl. Phys. **110**, 071101 (2011).
78. W. Gerstner and W. M. Kistler, *Spiking Neuron Models* (Cambridge Univ. Press, Cambridge, 2002).
79. P. A. Merolla, J. V. Arthur, R. Alvarez-Icaza, A. S. Cassidy, J. Sawada, and F. Akopyan, Science (Washington, DC, U. S.) **345**, 668 (2014).
80. S. B. Furber, F. Galluppi, S. Temple, and L. A. Plana, Proc. IEEE **102**, 652 (2014).
81. M. Davies, N. Srinivasa, T. H. Lin, G. Chinya, Y. Cao, S. H. Choday, G. Dimou, P. Joshi, N. Imam, S. Jain, Y. Liao, C. Lin, A. Lines, R. D. Mathaikutty, S. Mc-

coy, A. Paul, J. Tse, G. Venkataramanan, Y. Weng, A. Wild, and Y. Yang, IEEE Micro **38**, 82 (2018).

82. G. K. Chen, R. Kumar, H. E. Sumbul, P. C. Knag, and R. K. Krishnamurthy, IEEE J. Solid State Circuits **54**, 992 (2019).
83. D. Ielmini and H. P. S. Wong, Nat. Electron. **1**, 333 (2018).
84. M. Prezioso, F. Merrikh-Bayat, B. D. Hoskins, G. C. Adam, K. K. Likharev, and D. B. Strukov, Nature (London, U.K.) **521**, 61 (2015).
85. A. V. Emelyanov, D. A. Lapkin, V. A. Demin, V. V. Erokhin, S. Battistoni, G. Baldi, A. Dimonte, A. N. Korovin, S. Iannotta, P. K. Kashkarov, and M. V. Kovalchuk, AIP Adv. **6**, 111301 (2016).
86. C. Li, M. Hu, Y. Li, H. Jiang, N. Ge, E. Montgomery, J. Zhang, W. Song, N. Dávila, C. E. Graves, Z. Li, J. P. Strachan, P. Lin, Z. Wang, M. Barnell, Q. Wu, R. S. Williams, J. J. Yang, and Q. Xia, Nat. Electron. **1**, 52 (2018).
87. F. Cai, J. M. Correll, S. H. Lee, Y. Lim, V. Bothra, and Z. Zhang, Nat. Electron. **2**, 290 (2019).
88. C. Li, Z. Wang, M. Rao, D. Belkin, W. Song, and H. Jiang, Nat. Mach. Intell. **1**, 49 (2019).
89. G. Pedretti, V. Milo, S. Ambrogio, R. Carboni, S. Bianchi, A. Calderoni, N. Ramaswamy, A. S. Spinelli, and D. Ielmini, Sci. Rep. **7**, 5288 (2017).
90. M. Prezioso, F. Merrikh-Bayat, B. D. Hoskins, K. Likharev, and D. B. Strukov, Sci. Rep. **6**, 21331 (2016).
91. D. A. Lapkin, A. V. Emelyanov, V. A. Demin, T. S. Berzina, and V. V. Erokhin, Microelectron. Eng. **43**, 185 (2018).
92. A. V. Emelyanov, K. E. Nikiruy, V. A. Demin, V. V. Rylkov, A. I. Belov, D. S. Korolev, E. G. Gryaznov, D. A. Pavlov, O. N. Gorshkov, A. N. Mikhaylov, and P. Dimitrakis, Microelectron. Eng. **215**, 110988 (2019).
93. Z. Wang, S. Joshi, S. Savel'ev, W. Song, R. Midya, Y. Li, M. Rao, P. Yan, S. Asapu, Y. Zhuo, H. Jiang, P. Lin, C. Li, J. H. Yoon, N. K. Upadhyay, et al., Nat. Electron. **1**, 137 (2018).
94. M. Prezioso, M. R. Mahmoodi, F. Merrikh-Bayat, H. Nili, H. Kim, A. F. Vincent, and D. B. Strukov, Nat. Commun. **9**, 5311 (2018).
95. S. Brivio, D. Conti, M. V. Nair, J. Frascaroli, E. Covi, C. Ricciardi, G. Indiveri, and S. Spiga, Nanotechnology **30**, 015102 (2019).
96. E. Covi, S. Brivio, A. Serb, T. Prodromakis, M. Fanciulli, and S. Spiga, Front. Neurosci. **10**, 482 (2016).
97. K. E. Nikiruy, A. V. Emelyanov, V. A. Demin, V. V. Rylkov, A. V. Sitnikov, and P. K. Kashkarov, Tech. Phys. Lett. **44**, 416 (2018).
98. G. Hennequin, E. J. Agnes, and T. P. Vogels, Ann. Rev. Neurosci. **40**, 557 (2017).

Translated by K. Shakhlevich

Publication IV

Rylkov, V., Sitnikov, A., Nikolaev, S., Emelyanov, A., Chernohlazov, K., Nikiruy, K.,
Drovosekov, A., Blinov, M., Fadeev, E., Taldenkov, A., Demin, V., Vedeneev, A.,
Bugaev, A., and Granovsky, A.

Properties of Nanocomposites With Different Concentrations of Magnetic Ions in an Insulating Matrix

Reprinted with permission from
IEEE Magnetics Letters
Vol. 10, pp. 1–4, 2019.

IEEE MAGNETICS LETTERS, Volume 10 (2019) 2509504

Magnetism in Solids

Properties of Nanocomposites With Different Concentrations of Magnetic Ions in an Insulating Matrix

Vladimir Rylkov[1,7], Alexander Sitnikov[1,2], Sergey Nikolaev[1], Andrey Emelyanov[1,3], Konstantin Chernohlazov[1], Kristina Nikiruy[1], Alexey Drovosekov[4], Mikhail Blinov[5], Egor Fadeev[6], Alexander Taldenkov[1], Vyacheslav Demin[1,3], Alexander Vedeneev[7], Alexander Bugaev[3,7], and Alexander Granovsky[5]

[1]*National Research Centre “Kurchatov Institute,” Moscow 123182, Russia*
[2]*Voronezh State Technical University, Voronezh 394026, Russia*
[3]*Moscow Institute of Physics and Technology, Dolgoprudny 141700, Russia*
[4]*Kapitza Institute for Physical Problems, Russian Academy of Sciences, Moscow 119334, Russia*
[5]*Faculty of Physics, Lomonosov Moscow State University, Moscow 119991, Russia*
[6]*Lappeenranta University of Technology, 53851 Lappeenranta, Finland*
[7]*Kotel’nikov Institute of Radio Engineering and Electronics, Russian Academy of Sciences, Fryazino 141190, Russia*

Received 4 Oct 2019, revised 26 Oct 2019, accepted 31 Oct 2019, published 22 Nov 2019, current version 23 Dec 2019.

Abstract—Using $(Co_{40}Fe_{40}B_{20})_x(LiNbO_3)_{100-x}$ (x = 6–55 at.%) nanocomposite films as an example, we have performed comparative investigations of granular systems properties with a high ($\sim 10^{22}$ cm^{-3}) and low ($\leq 10^{21}$ cm^{-3}) content of dispersed atoms (Fe and Co) in an insulating nonstoichiometric matrix. The nanocomposite films were produced using ion-beam sputtering of the composite targets onto glass-ceramic substrates at different growth temperatures (~40 and ~80 °C). We show that magnetic ions dispersed in a matrix play a crucial role both in the ferromagnetic exchange between granules and in magnetic, transport, and memristive properties below the percolation threshold $x_p \approx$ 50–55 at.%. The presence of a high content of dispersed magnetic ions induces intergranular interaction, shifts the critical concentration of the metal–insulator transition x_c from 48 to 43 at.%, leads to high-field positive magnetoresistance near x_p and superferromagnetic ordering and magnetic hysteresis below x_c (down to 33 at.%), and makes the stable resistive switching for capacitorlike structures with resistance ratio R_{OFF}/R_{ON} more than 10^2 at $x \approx 10$ at.%.

Index Terms—Magnetism in solids, granular nanocomposites, dispersed atoms, intergranular exchange, magnetic and electrophysical properties.

I. INTRODUCTION

Metal–dielectric nanocomposite (**NC**) systems with a high content of magnetic atoms dispersed in the insulating matrix are a class of granular systems as yet poorly studied [Bedanta 2007, 2009, Rylkov 2018a, 2018b, 2019].

From a fundamental point of view, these systems are interesting in the manifestation of the intergranular exchange interaction of the ferromagnetic (**FM**) type, which determines the effects of superferromagnetic (**SFM**) ordering in the ensemble of magnetic moments of the granules and, as a result, the shift to the superparamagnetic (**SPM**) behavior of the granular system in the region of markedly lower contents of metal x than the percolation threshold x_p [Bedanta 2007, 2009, Rylkov 2019]. Currently, there are quite a lot of experimental data (see Bedanta [2009], Timopheev [2012], and Udalov [2017] and references therein), indicating the manifestation of SFM ordering in granular systems. However, at present, there is no theoretical description of the SFM ordering, which takes into account, in addition to the dipole–dipole, other possible channels of intergranular interaction, associated, for example, with the competition between the hopping and Coulomb exchange mechanisms [Udalov 2017] or with the manifestation of the tunneling superexchange mechanism through atomic clusters dispersed in the insulating matrix [Kondratyev 1998, Bedanta 2009].

The high magnetic softness of granular SPM systems in combination with high values of resistivity and magnetic susceptibility makes them attractive for creating various kinds of high-frequency magnetoelectronic devices [Fujimori 2006, Sullivan 2009].

Recently, we discovered the effects of resistive switching (**RS**) in metal-NC-metal (**M/NC/M**) capacitor structures based on $(CoFeB)_x(LiNbO_3)_{100-x}$ NC with a high content of dispersed atoms $N_d \sim 10^{22}$ cm^{-3} (NC with **HCDA**) [Rylkov 2018a, 2018b]. The multilevel nature of RS makes M/NC/M structures very promising for creating memristors that emulate synapses in neuromorphic computing systems [Nikiruy 2019].

However, the role of dispersed atoms in the SFM ordering and RS has not yet been studied in detail. The purpose of this letter is to compare the magnetic, transport, and memristive properties of NCs with HCDA ($\sim 10^{22}$ cm^{-3}) and low content of dispersed atoms (**LCDA**s), $N_d \leq 10^{21}$ cm^{-3}, using $(CoFeB)_x(LiNbO_3)_{100-x}$ NC as an example.

II. SAMPLES AND EXPERIMENTAL DETAILS

The film NCs with HCDA ($N_d \sim 10^{22}$ cm^{-3}) and LCDA ($N_d \leq 10^{21}$ cm^{-3}) were fabricated by ion-beam sputtering of the composite

---

Corresponding author: Vladimir Rylkov (e-mail: vvrylkov@mail.ru). International Baltic Conference on Magnetism, Svetlogorsk, Kaliningrad, Russia, 18-22 August 2019.

Digital Object Identifier 10.1109/LMAG.2019.2955060

targets onto glass-ceramic substrates at different growth temperature $T_g \leq 40$ °C and $T_g = 70$–90 °C, respectively. The composite targets consisted of a plate of $Co_{40}Fe_{40}B_{20}$ metallic alloy and 14–15 oxide stripes ($LiNbO_3$, SiO_2, or Al_2O_3) placed onto the plate. The special target design makes it possible to obtain composite systems with the content of the metallic phase continuously varying ($\delta x = 0.5$–0.7 at.%) in a wide range $x \approx 6$–60 at.% in a single technological cycle. The thickness of the produced NC layers in planar and capacitor structures was about $d \approx 1$–2 μm.

The investigations of transport and magnetic properties, including FM resonance (**FMR**), were performed on the same samples fabricated in the shape of the Hall bar with the conduction channel width $w = 1.2$ mm and the distance between potential probes $l_p = 1.4$ mm.

As contacts in capacitor M/NC/M structures, three-layer Cr/Cu/Cr films or films from Cu 1 μm thick were used (Cu films were used for subsequent magnetization measurements). It was previously shown that the type of contact (Cr/Cu/Cr or Cu films) does not affect memristive properties of M/NC/M structures [Levanov 2018]. Details of planar film samples and capacitorlike M/NC/M structures, as well as their structural characterization, are given in Rylkov [2018a, 2018b, 2019].

The magnetic properties of the NCs were studied with a Quantum Design MPMS-XL7 superconducting quantum interference device magnetometer in the temperature range 1.9–350 K and a field up to 7 T oriented in the sample plane. The resistivity was measured with a standard dc method. The pulsed magnetic field up to 20 T was applied to measure the magnetoresistance.

FMR was studied at room temperature using a laboratory-developed cavity-based spectrometer at frequency 7.65 GHz. The field-sweep absorption spectra were obtained in magnetic fields up to 17 kOe applied at different angles with respect to the film plane.

The *I*–*V* characteristics and the memristive properties of the M/NC/M structures based on $(CoFeB)_x(LiNbOy)_{100-x}$ NCs were studied in strong electric fields (>10^4 V/cm) at room temperature using a multifunctional NI PXI-4140 (National Instruments, Austin, TX, USA) source meter and an analytical PM5 (Cascade Microtech, Beaverton, OR, USA) probe station equipped with a PSM-100 (Motic) system, which provides micrometer-scale probe motion.

III. RESULTS AND DISCUSSION

A. Magnetization

We found that the use of metal alloys with additives promoting amorphizing as targets, such as $Co_{40}Fe_{40}B_{20}$, for the synthesis of NCs by ion-beam sputtering leads to a sharp increase in the content of dispersed paramagnetic metal atoms (up to $N_d \sim 10^{22}$ cm^{-3}) in all the insulating matrices we studied ($LiNbO_3$, SiO_2, or Al_2O_3) if the growth temperature of NC is small enough ($T_g \leq 40$ °C) [Rylkov 2017, 2018a, 2018b, Blinov 2019]. However, at growth temperatures of about 80 °C, the grain size increases by 1 nm from $a \approx 2.5$ nm up to $a \approx 3.5$ nm and the N_d value decreases significantly to $N_d \leq 10^{21}$ cm^{-3}, which is accompanied by a sharp drop in the paramagnetic contribution of M_{PM} to the magnetization (see Fig. 1).

Fig. 1 demonstrates the difference in high-field magnetization for NCs with LCDA and HCDA in the case of compositions below the percolation threshold x_p. FM granules are easily magnetized, but it is not the case for isolated dispersed magnetic atoms. The paramagnetic contribution of dispersed atoms and FM contribution of granules denoted as M_{PM} and M_{FM}, correspondingly, as well as the content of paramagnetic atoms N_d and the average magnetic moment m per dispersed atom, were determined by analyzing the temperature dependence of magnetization M at low temperatures ($T < 10$ K). The change $\Delta M(M,T_1,T_2) = M(M,T_1) - M(M,T_2)$ was fitted by the difference of Brillouin's functions, $\Delta B_J(H) = B_J(H, T_1) - B_J(H, T_2)$ [Rylkov 2018a, 2018b]. The accuracy of fitting was better than 1%; the magnet moment of paramagnetic center was in the range $m = (5.1$–$5.8) \cdot \mu_B$ that approximately coincides with the average moment of magnetic ions Fe^{3+}, Fe^{2+}, and Co^{2+} with $m = 5.9$, 5.4, and 4.8 μ_B, respectively.

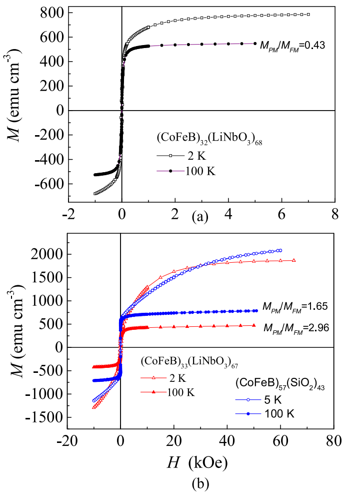

Fig. 1. Magnetization as a function of applied field. (a) For $(CoFeB)_{32}(LiNbO_3)_{68}$ LCDA NC grown at ≈75 °C ($N_d \approx 3.2 \times 10^{21}$ cm^{-3}). (b) For $(CoFeB)_{33}(LiNbO_3)_{67}$ and $(CoFeB)_{57}(SiO_2)_{43}$ HCDA NCs grown at ≈40 °C with $N_d \approx 3.1 \times 10^{22}$ and 3.2×10^{22} cm^{-3}, respectively.

B. Electrical Conductivity and Magnetoresistance

For both types of NCs with LCDA and HCDA with compositions $x_c < x < x_p$, where x_c corresponds to the metal–insulator transition (**MIT**), the temperature dependence of conductivity in the range $T \approx 10$–200 K is well described by the logarithmic law $\sigma(T) \propto \cdot \ln T$ under strong intergranular tunnel coupling, which is replaced by the law "1/2" below x_c (see Fig. 2) [Beloborodov 2007]. However, in the case of NCs with LCDA, the value of $x_c \approx 48$ at.% is larger by 5 at.% than for NCs with HCDA ($x_c \approx 43$ at.%). Apparently, the atoms located between metallic granules increase intergranular coupling that shifts the MIT. These dispersed atoms also diminish the tunnel barrier height that is important for hopping electron transport in the vicinity of the percolation threshold. As a result, we observed positive high-field magnetoresistance in NCs with HCDA [Blinov 2019] but only conventional negative magnetoresistance in NCs with LCDA.

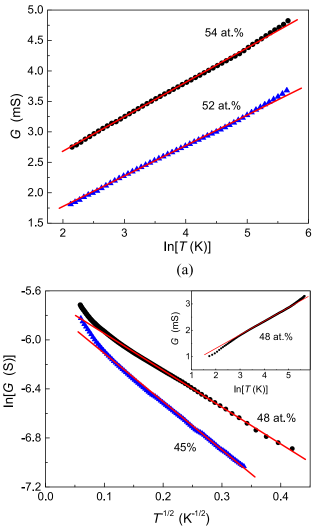

(a)

(b)

Fig. 2. Temperature dependences of conductance $G(T)$ in coordinates (a) G versus ln$T$ and (b) ln$G$ versus $(1/T)^{1/2}$ for (CoFeB)$_x$(LiNbO3)$_{100-x}$ NCs with LCDA ($T_g \approx 75$ °C) with various FM alloy content $x = 45$–54 at.%. Inset shows $G(T)$ dependence for sample with $x \approx 48$ at.% in coordinates G versus ln$T$.

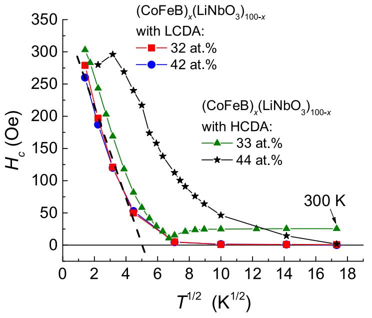

Fig. 3. Temperature dependences of the coercive field $H_c(T)$ for LCDA ($T_g \approx 75$ °C) and HCDA ($T_g \approx 40$ °C) NC films with various FM alloy content below percolation threshold.

C. Coercive Field and FMR

The presence of dispersed magnetic ions in the insulating matrix favors SFM ordering [Bedanta 2007, Timopheev 2012, Rylkov 2018a, 2018b]. We observed magnetic hysteresis in NCs with HCDA far below the percolation threshold (down to 33 at.%), that is a signature of SFM ordering, and also found some anomaly in the temperature behavior of coercive field $H_c(T)$ (minimum at $T \approx 50$ K) probably due to the influence of surface magnetic anisotropy of granules (see Fig. 3) [Rylkov 2019]. By contrast, in the case of NCs with LCDA at $x \le 42$ at.%, the temperature dependence of the coercive force is well described by the Néel–Brown law for noninteracting granules with a blocking temperature about 25 K (see Fig. 3). The absence of intergranular interaction in NCs with LCDA is also confirmed by studies of angular dependencies of the FMR linewidth $\Delta H(\theta_H)$ (see Fig. 4).

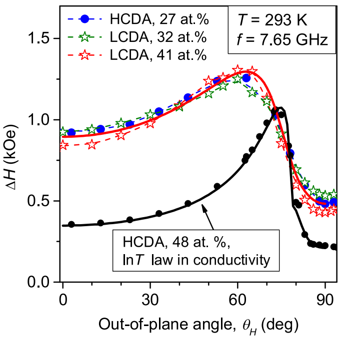

Fig. 4. Angular dependencies of FMR linewidth $\Delta H(\theta_H)$ for (CoFeB)$_x$(LiNbO3)$_{100-x}$ LCDA ($T_g \approx 75$ °C) and HCDA ($T_g \approx 40$ °C) NCs with various FM alloy content below percolation threshold. Points are the experimental data, and thick solid lines are their theoretical approximation. The red line is obtained taking into account the inhomogeneous FMR line broadening mechanism. For the black line, the two magnon scattering mechanism prevails.

The FMR linewidth far below MIT is mainly determined by the inhomogeneous distribution of the local anisotropy axes in the film plane. On the other hand, above MIT under strong tunnel coupling between granules, the contribution of this inhomogeneity to the $\Delta H(\theta_H)$ sharply decreases (see Fig. 4). Using theoretical simulation, we have shown that two-magnon magnetic relaxation processes begin to play a significant role in the formation of the linewidth as for homogeneous FM films [Drovosekov 2020].

D. Resistive Switching

The RS is observed in (CoFeB)$_x$(LiNbO$_3$)$_{100-x}$ NCs with LCDA at optimal value of $x \approx 15$ at.% with small resistance ratio $R_{\mathrm{OFF}}/R_{\mathrm{ON}} \approx 5$; this effect completely disappears at $x \le 12$ at.%. On the other hand in NCs with $N_d \sim 10^{22}$ cm^{-3}, the ratio $R_{\mathrm{OFF}}/R_{\mathrm{ON}}$ exceeds 10^2 and the number of stable RS is more than 10^5 at $x \approx 10$ at.% (see Fig. 5) [Rylkov 2018a, 2018b, Nikiruy 2019].

Recently, based on the obtained experimental data, we argued that the multifilament structure is the origin of the memristive properties of the M/NC/M samples with (CoFeB)$_x$(LiNbO$_3$)$_{100-x}$ NC. Multifilament structure is caused by a nucleation of the dispersed atoms around chains of the granules forming percolation paths. When a sufficiently large negative voltage is applied to the top electrode, the structure switches in a high-resistance OFF-state due to moving of cations and oxygen vacancies to the top electrode. The reverse situation arises when sufficiently large positive voltage is applied to the structure [Martyshov 2019]. The multifilamentary character of RS, apparently, entirely determines the high level of plasticity of the memristive M/NC/M structures. It is a great advantage of NCs-based

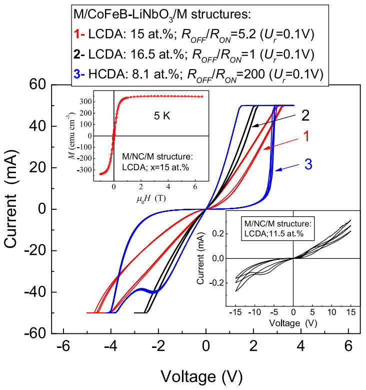

Fig. 5. I–V characteristic of the M/(CoFeB)$_x$(LiNbO3)$_{100-x}$/M structure with LCDA ($N_d \sim 10^{20}$ cm^{-3} and $T_g \approx 90$ °C) and various FM alloy content $x = 15$ and 16.5 at.%. For comparison, the I–V curve for M/(CoFeB)$_x$(LiNbO3)$_{100-x}$/M structure with HCDA ($N_d \sim 10^{22}$ cm^{-3} and $T_g \approx 40$ °C) is shown. Upper inset presents $M(H)$ dependence of M/NC/M structure with LCDA ($N_d \sim 10^{20}$ cm^{-3} and $x \approx 15$ at.%) and lower inset shows I–V curve for M/NC/M structure with LCDA ($N_d \sim 10^{20}$ cm^{-3} and $x \approx 11.5$ at.%).

memristors that allow emulating the unique properties of biological synapses [Emelyanov 2020].

IV. CONCLUSION

The presented results of comparative investigations of (CoFeB)$_x$(LiNbO$_3$)$_{100\text{-}x}$ NCs with high ($\sim 10^{22}$ cm^{-3}) versus low ($\leq 10^{21}$ cm^{-3}) content of dispersed atoms (Fe and Co) in the insulating matrix clearly show strong influence of magnetic ions on magnetic and electrophysical properties of these systems below percolation threshold $x_p \approx (50–55)$ at.%. In particular, the presence of HCDA shifts the critical concentration of the MIT x_c from 48 to 43 at.% and leads to magnetic hysteresis below x_c down to 33 at.%. Under this condition, we also observed in capacitorlike structures strong RS effect with the resistance ratio $R_{\text{OFF}}/R_{\text{ON}} \sim 10^2$ and more than 10^5 stable RS at $x \approx 10$ at.%. These features of NCs with HCDA are due to the participation of dispersed atoms in intergranular interaction and also to their tendency to nucleate under charge carriers flow in a strong electric field. It makes such systems promising for applications in high-frequency magnetoelectronic devices as well as in memristors for emulation of synapses in neuromorphic networks.

ACKNOWLEDGMENT

This work was supported by the Russian Science Foundation under Grant 16-19-10233 for the synthesis and investigation of memristive properties of capacitorlike NC structures. The investigations of magnetic properties, ferromagnetic resonance, magnetoresistance, and conductivity of planar samples were supported by the Russian Foundation for Basic Research under Grant 18-52-50021, Grant 18-07-00772, Grant 18-29-19047, Grant 18-07-00729, Grant 19-07-00471, Grant 19-07-00738, and Grant 19-29-03022.

REFERENCES

Bedanta S, Eimüller T, Kleemann W, Rhensius J, Stromberg F, Amaladass E, Cardoso S, Freitas P P (2007), “Overcoming the dipolar disorder in dense CoFe nanoparticle ensembles: Superferromagnetism,” *Phys. Rev. Lett.*, vol. 98, 176601, doi: 10.1103/PhysRevLett.98.176601.

Bedanta S, Kleemann W (2009), “Supermagnetism,” *J. Phys. D.: Appl. Phys.*, vol. 42, 013001, doi: 10.1088/0022-3727/42/1/013001.

Beloborodov I S, Lopatin A V, Vinokur V M, Efetov K B (2007), “Granular electronic systems,” *Rev. Mod. Phys.*, vol. 79, pp. 469–518, doi: 10.1103/RevModPhys.79.469.

Blinov M I, Shakhov M A, Rylkov V V, Lähderanta E, Prudnikov V N, Nikolaev S N, Sitnikov A V, Granovsky A B (2019), “Magnetoresistance of $(\text{Co}_{40}\text{Fe}_{40}\text{B}_{20})_x$ $(\text{SiO}_2)_{100\text{-}x}$ and $(\text{Co}_{84}\text{Nb}_{14}\text{Ta}_2)_x(\text{Al}_2\text{O}_3)_{100\text{-}x}$ nanocomposites below the percolation threshold in pulsed magnetic fields,” *J. Magn. Magn. Mater.*, vol. 469, pp. 155–160, doi: 10.1016/j.jmmm.2018.08.023.

Drovosekov A B, Kreines N M, Barkalova A S, Nikolaev S N, Rylkov V V, Sitnikov A V (2020), “Mechanisms of FMR line broadening in CoFeB−LiNbO$_3$ granular films in the vicinity of metal-insulator transition,” *J. Magn. Magn. Mater.*, vol. 495, 165875, doi: 10.1016/j.jmmm.2019.165875.

Emelyanov A V, Nikiruy K E, Serenko A V, Sitnikov A V, Presnyakov M Y, Rybka R B, Sboev A G, Rylkov V V, Kashkarov P K, Kovalchuk M V, Demin V A (2020), “Self-adaptive STDP-based learning of a spiking neuron with nanocomposite memristive weights,” *Nanotechnology*, vol. 31, 045201, doi: 10.1088/1361-6528/ab4a6d.

Fujimori H, Ohnuma S, Kobayashi N, Masumoto T (2006), “Spintronics in metal–insulator nanogranular magnetic thin films,” *J. Magn. Magn. Mater.*, vol. 304, pp. 32–35, doi: 10.1016/j.jmmm.2006.02.005.

Kondratyev V N, Lutz H O (1998), “Shell effect in exchange coupling of transition metal dots and their arrays,” *Phys. Rev. Lett.*, vol. 81, pp. 4508–4511, 10.1103/PhysRevLett.81.4508.

Levanov V A, Emel’yanov A V, Demin V A, Nikirui K E, Sitnikov A V, Nikolaev S N, Vedeneev A S, Kalinin Y E, Ryl’kov V V (2018), “Memristive properties of structures based on $(\text{Co}_{41}\text{Fe}_{39}\text{B}_{20})_\text{x}(\text{LiNbO}_3)_{100-x}$ nanocomposites,” *J. Commun. Technol. Electron.*, vol. 63, pp. 491–496, doi: 10.1134/S1064226918050078.

Martyshov M N, Emelyanov A V, Demin V A, Minnekhanov A A, Nikolaev S N, Nikiruy K E, Presnyakov M Y, Sitnikov A V, Vasiliev A L, Forsh P A, Granovskiy A B, Kashkarov P K, Kovalchuk M V, Rylkov V V (2019), “Multifilamentary character of anticorrelated capacitive and resistive switching in memristive structures based on $(\text{CoFeB})_\text{x}(\text{LiNbO}_3)_{100-\text{x}}$ nanocomposite,” [Online]. Available: https://arxiv.org/abs/1912.03726

Nikiruy K E, Emelyanov A V, Demin V A, Sitnikov A V, Minnekhanov A A, Rylkov V V, Kashkarov P K, Kovalchuk M V (2019), “Dopamine-like STDP modulation in nanocomposite memristors,” *AIP Adv.*, vol. 9, 065116, doi: 10.1063/1.5111083.

Rylkov V V, Nikolaev S N, Chernoglazov K Y, Demin V A, Sitnikov A V, Presnyakov M Y, Vasiliev A L, Perov N S, Vedeneev A S, Kalinin Y E, Tugushev V V, Granovsky A B (2017), “Tunneling anomalous Hall effect in the nanogranular CoFe-B-Al-O films near metal-insulator transition,” *Phys. Rev. B*, vol. 95, 144402, doi: 10.1103/PhysRevB.95.144202.

Rylkov V V, Sitnikov A V, Nikolaev S N, Demin V A, Taldenkov A N, Presnyakov M Y, Emelyanov A V, Vasiliev A L, Kalinin Y E, Bugaev A S, Tugushev V V, Granovsky A B (2018a), “Properties of granular $(\text{CoFeB})_x(\text{Al}_2\text{O}_3)_{100\text{-}x}$ and $(\text{CoFeB})_x(\text{LiNbO}_3)_{100\text{-}x}$ nanocomposites: Manifestation of superferromagnetic ordering effects,” *J. Magn. Magn. Mater.*, vol. 459, pp. 197–201, doi: 10.1016/j.jmmm.2017.11.022.

Rylkov V V, Nikolaev S N, Demin V A, Emelyanov A V, Sitnikov A V, Nikiruy K E, Levanov V A, Presnyakov M Y, Taldenkov A N, Vasiliev A L, Chernoglazov K Y, Vedeneev A S, Kalinin Y E, Granovskii A B, Tugushev V V, Bugaev A S (2018b), “Transport, magnetic, and memristive properties of a nanogranular $(\text{CoFeB})_x(\text{LiNbO}y)_{100-x}$ composite material,” *J. Exp. Theor. Phys.*, vol. 126, pp. 353–367, doi: 10.1134/S1063776118020152.

Rylkov V V, Drovosekov A B, Taldenkov A N, Nikolaev S N, Udalov O G, Emelyanov A V, Sitnikov A V, Chernoglazov K Y, Demin V A, Novodvorski O A, Vedeneev A S, Bugaev A S (2019), “Unusual behavior of the coercive field in a $(\text{CoFeB})_x(\text{LiNbO}_y)_{100-x}$ nanocomposite with a high content of magnetic ions in an insulating matrix,” *J. Exp. Theor. Phys.*, vol. 128, pp. 115–124, doi: 10.1134/S1063776119010163.

Sullivan C R (2009), “Integrating magnetics for on-chip power: Challenges and opportunities,” in *Proc. IEEE Custom Integr. Circuits Conf.*, pp. 291–298, doi: 10.1109/CICC.2009.5280823.

Timofeev A A, Bdkin I, Lozenko A F, Stognei O V, Sitnikov A V, Los A V, Sobolev N A (2012), “Superferromagnetism and coercivity in Co-Al$_2$O$_3$ granular films with perpendicular anisotropy,” *J. Appl. Phys.*, vol. 111, 123915, doi: 10.1063/1.4730397.

Udalov O G, Beloborodov I S (2017), “Competition of the Coulomb and hopping-based exchange interactions in granular magnets,” *Phys. Rev. B*, vol. 95, 045427, doi: 10.1103/PhysRevB.95.045427.

Publication V

Fadeev, E.A., Shakhov, M.A., Lähderanta, E., Taldenkov, A.N., Vasiliev, A.L., Sitnikov, A.V., Rylkov, V.V., and Granovsky, A.B.

High-Field Magnetoresistance of Magnetic Nanocomposites near the Percolation Threshold

Reprinted with permission from
Journal of Experimental and Theoretical Physics
Vol. 133(6), pp. 771–778, 2021.

ISSN 1063-7761, Journal of Experimental and Theoretical Physics, 2021, Vol. 133, No. 6, pp. 771–778. © Pleiades Publishing, Inc., 2021.
Russian Text © The Author(s), 2021, published in Zhurnal Eksperimental'noi i Teoreticheskoi Fiziki, 2021, Vol. 160, No. 6, pp. 903–911.

High-Field Magnetoresistance of Magnetic Nanocomposites near the Percolation Threshold

E. A. Fadeev[a,*], **M. A. Shakhov**[b], **E. Lähderanta**[a,**], **A. N. Taldenkov**[c],
A. L. Vasiliev[c,d], **A. V. Sitnikov**[e], **V. V. Rylkov**[c,f], **and A. B. Granovsky**[f,g]
[a] *Lappeenranta-Lahti University of Technology LUT, Lappeenranta, 53850 Finland*
[b] *Ioffe Institute, St. Petersburg, 194021 Russia*
[c] *National Research Center "Kurchatov Institute," Moscow, 123098 Russia*
[d] *Moscow Institute of Physics and Technology (MIPT), Dolgoprudny, Moscow oblast, 141701 Russia*
[e] *Voronezh State Technical University, Voronezh, 394026 Russia*
[f] *Institute of Applied and Theoretical Electrodynamics RAS, Moscow, 127412 Russia*
[g] *Faculty of Physics, Moscow State University, Moscow, 119991 Russia*
** e-mail: egor.fadeev@lut.fi*
*** e-mail: erkki.lahderanta@lut.fi*

Received July 15, 2021; revised July 15, 2021; accepted August 23, 2021

Abstract—We present results of experimental studies of high-field magnetoresistance of Co–SiO_2, Co–$LiNbO_3$, CoNbTa–SiO_2 nanocomposites with metal volume fraction close to the percolation threshold. The nanocomposite films were deposited onto a glass-ceramic substrate by ion-beam sputtering at the growth temperature not exceeding 80°C. Magnetization was measured using a superconducting quantum interference device (SQUID) magnetometer in the temperature range of 4.2–300 K. Out-of-plane magnetoresistance was measured in a pulsed magnetic field up to 20 T in the temperature range of 4.2–300 K with the pulse duration of 11–12 ms. In addition to negative magnetoresistance, a linear positive contribution to magnetoresistance was observed in high magnetic fields for nanocomposites with the composition close to the percolation threshold. This effect was explained by the influence of the Zeeman effect on the tunnel barrier height. It is shown that the unconventional anisotropy of magnetoresistance of Co–$LiNbO_3$ is associated with the peculiarities of its microstructure.

DOI: 10.1134/S1063776121120049

1. INTRODUCTION

The discovery of linear positive magnetoresistance (LPMR) in high magnetic fields in a variety of ferromagnetic materials, composites and manganites ([1, 2] and references therein) has induced significant interest. This is mainly because LPMR could not be explained by known mechanisms of magnetoresistance (MR) in magnetic materials [1, 2], in which MR is commonly negative and anisotropic in the magnetic fields lower than a saturation field. LPMR is isotropic and it does not show signatures of saturation even in magnetic fields up to 60 T. Potentially it can be used as a basis for the development of high magnetic field sensors. LPMR was not observed in chemically homogeneous bulk magnetic materials nor in paramagnetic thin films [1]; only inhomogeneous magnetic materials such as deposited polycrystalline thin films of ferromagnetic materials (Ni, Fe, Co) or magnetic nanocomposites demonstrate the effect [1, 2]. Commonly, LPMR value does not exceed 0.001–0.01% T^{-1}, however, in weakly conductive Ni films mixed with insulating SiO_2 LPMR reaches a value of 0.1% T^{-1} [1].

It is still unclear, whether LPMR is a result of only one mechanism or not. In [1], the LPMR is explained by the influence of the Zeeman effect on the quantum corrections to resistivity, which are caused by electron–electron interaction. However, as the authors themselves mentioned, the proposed mechanism can not explain the magnitude of the effect. Moreover, LPMR takes place in systems without any indication of the contribution of the quantum corrections to resistivity. In [2], the LPMR is associated with the influence of the Zeeman effect on the tunnel barrier height in the case of spin-polarized tunneling. This mechanism is universal since tunneling takes place in a variety of materials such as island and polycrystalline films, nanocomposites with concentrations close to the percolation threshold, binary structures, etc. To explain the LPMR behavior, authors of [2] derived a simple expression based on the Inoue–Maekawa model of tunneling MR in granular films [3]. This expression allowed them to explain qualitatively the LPMR results of $(Co_{40}Fe_{40}B_{20})_x(SiO_2)_{100-x}$ and $(Co_{84}Nb_{14}Ta_2)_x(Al_2O_3)_{100-x}$ nanocomposites [2]. However, the Inoue-Maekawa model is valid only for nanocomposites with a composition below a metal-insulator transition (MIT), whose temperature dependence of resistivity follows "$T^{1/2}$" law ($\ln\rho \propto T^{-1/2}$), whereas the temperature dependence of resistivity of the studied nanocomposites follows "ln$T$" law ($\rho \propto \ln T$) [2]. Commonly, such behavior is observed for metal concentrations above the MIT (x_c), but below the percolation threshold (x_p), and corresponds to conductivity of "dirty metal" with strong tunnel coupling between granules. Moreover, in [2], the MR curves of the studied samples were measured only at $T > 65$ K.

In the present paper, we continue search for and investigation of LPMR in nanocomposite materials. New compounds were fabricated with material variation of both magnetic granules and dielectric matrices. MR was measured in pulsed magnetic fields at the temperatures down to 4.2 K. The expression from [2] was modified for "metallic" side from the MIT with the "ln$T$" law.

2. EXPERIMENTAL

Nanocomposite Co–SiO_2, Co–$LiNbO_3$, CoNbTa–SiO_2 films with a thickness of 1.7 μm were fabricated by ion-beam sputtering of components' targets onto a glass-ceramic substrate at the temperature not exceeding 80°C. Details of fabrication, elemental composition investigation, and structural characterization are the same as in [3, 4]. Concentration of the metallic granules varied from the "metallic" region to the concentrations corresponding to the MIT. Magnetization was measured using a SQUID magnetometer (Quantum Design MPMS-XL7). The temperature dependences of resistivity in the range of 50–300 K were recorded with a standard DC four-probe method. Pulsed magnetic fields up to 20 T were applied to measure MR. A symmetric ("half-sine shaped") pulse was used with a duration of 11–12 ms. Special hardware and software were used to exclude parasitic signals induced by dB/dt (see details in [5]).

To study structural properties of the fabricated samples, cross-sectional lamellae of the nanocomposite films were prepared using a focused ion beam (FIB) Ga^+ system in a scanning electron microscope (SEM)/FIB "Helios NanoLab^{TM} 600i" (Thermo Fisher Scientific, USA). High-resolution images were obtained using a scanning/transmission electron microscope (S/TEM) "Tecnai Osiris" (Thermo Fisher Scientific, USA) operating at 200 kV equipped with energy dispersive X-ray spectrometer (EDXS) "Super-X" (Bruker, USA) and high-angle annular dark-field detector (HAADF) (Fischione, USA).

3. RESULTS AND DISCUSSION

The magnetic hysteresis loops of the studied samples are typical for magnetic nanocomposites and are presented in Fig. 1. The hysteresis loops converge in $H \approx 2$–3 kOe, but at low temperatures and in high magnetic fields, magnetization continues to grow due to the presence of superparamagnetic granules and magnetic ions, dispersed in the dielectric matrix [3, 6]. In magnetic fields lower than the saturation ones ($H_{sat} \approx 2$–4 kOe), the MR is negative and its magnitude rises sharply with magnetic field (Figs. 2–4). Nonetheless, in $H > H_{sat}$, the negative MR continues to grow, which is typical for tunneling MR with the presence of superparamagnetic granules (Figs. 2–4). The LPMR is observed only at low temperatures (Figs. 2–4).

At $T = 4.2$ K, the LPMR of Co–SiO_2 and CoNbTa–SiO_2 is 0.03 and 0.06% T^{-1}, respectively. The order of magnitude agrees with the results of the papers [1, 2]. In the Co–$LiNbO_3$ film, at $T = 50$ K, the LPMR is less by the order of magnitude. We were not able to measure MR of the Co–$LiNbO_3$ nanocomposite at $T < 50$ K due to the sharp rise of resistance at the lower temperatures. To discuss and analyze the obtained data we modify the theory developed in [2] and we take into account the differences in structure, magnetic properties, and conductivity of the studied magnetic nanocomposites.

As mentioned above, there are two possible conductivity regimes for nanogranular films with concentrations near the MIT ($x \approx x_c$). The first regime ($x \le x_c$) takes place when average tunneling conductance between adjacent granules (G_t) is less than the conductance quantum ($G_q = 2e^2/h$), meaning $g = G_t/G_q < 1$, then conductivity σ is described by the "$T^{1/2}$" law,

$$\ln\sigma \propto \left(\frac{T_0}{T}\right)^{1/2}. \qquad (1)$$

The second regime ($x_c \le x \le x_p$) is observed when $g = G_t/G_q \gg 1$ with strong tunnel coupling between granules at the slightly elevated metal concentration in comparison to the first regime. The second regime is described by the "ln$T$" law [5, 7],

$$\sigma(T) = \sigma_0\left(1 - \frac{1}{2\pi Dg}\ln\frac{gE_c}{k_BT}\right), \qquad (2)$$

where σ_0 is nanocomposite conductivity at relatively high temperature when it is possible to neglect the effect of Coulomb interaction, and D is dimensionality of the system. The Coulomb blockade energy can be written as

$$E_c = \frac{e^2 s}{\epsilon_d a^2(1/2 + s/a)}, \qquad (3)$$

where a is diameter of a granule, s is tunnel gap width and ϵ_d is permittivity of the matrix [8].

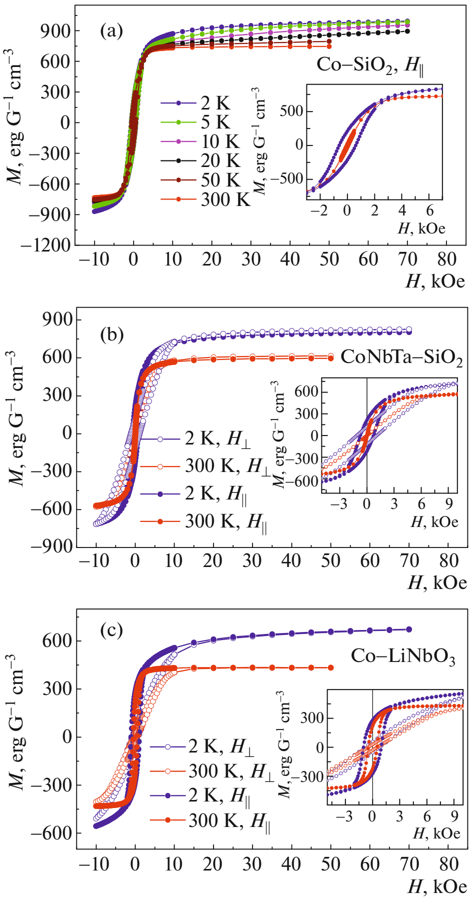

Fig. 1. Magnetic hysteresis loops of the studied nanocomposites at different temperatures and orientations. The inserts show different scales of the same curves.

For the first regime, in the framework of the Inoue–Maekawa model, authors of [2] have derived the expression for LPMR based on the influence of the Zeeman effect on the tunnel barrier height. At low temperatures, this expression takes form

$$\begin{aligned}\frac{\Delta\rho(H)}{\rho(0)} &= \frac{\rho(H)-\rho(H=0)}{\rho(H=0)}\\ &= \xi\frac{\mu_B H}{U-E_F(0)}\sqrt{\frac{\lambda C}{k_B T}},\end{aligned} \tag{4}$$

where $C = sE_c$, k_B is the Boltzmann constant, and the Fermi energy depends on the applied magnetic field as

$$E_F(H) = E_F(0) - \xi\mu_B H. \tag{5}$$

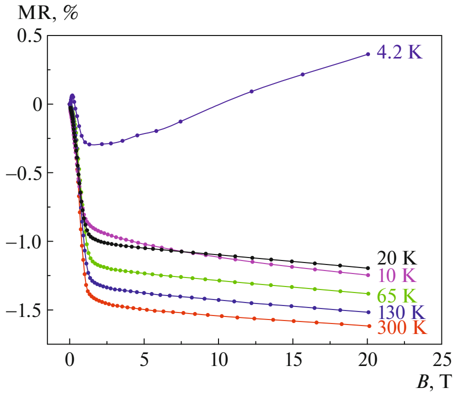

Fig. 2. Out-of-plane MR of $(\mathrm{Co})_x(\mathrm{SiO_2})_{100-x}$ with x = 65 at %.

Here ξ is a parameter that characterizes a shift of the Fermi level and is equal in the magnitude to spin polarization P, and μ_B is the Bohr magneton. The parameter

$$\begin{aligned}\lambda &= \sqrt{\frac{2m}{\hbar^2}(U-E_F(0))},\\ \lambda(H) &= \sqrt{\frac{2m}{\hbar}(U-E_F(0)+\xi\mu_B H)}\end{aligned} \tag{6}$$

characterizes a wave function decay of a tunneling electron in a barrier with the height of $U - E_F(0)$.

For the second regime, conductance can be written as follows

$$g(H) \propto (1+P^2m^2)e^{-2\lambda(H)s}, \tag{7}$$

where m is relative magnetization, which in saturation equals to 1 [9]. Then, the Fermi level shifts under the influence of the Zeeman effect (5), and using (2), (5)–(7) we derive the expression for LPMR in $H > H_{sat}$:

$$\frac{\Delta\rho(H)}{\rho(H)} = \xi\frac{\mu_B H}{U-E_F(0)}\frac{\lambda s}{2\pi Dg}\left[\ln\left(\frac{gE_c}{k_B T}\right)-1\right]. \tag{8}$$

Both (4) and (8) give the same order of magnitude but different temperature dependences of LPMR. For $a \approx$ 3 nm, $s \approx 1$ nm, $D = 3$ and $d \approx 3.75$ (for SiO$_2$) one has $E_c \approx 51.5$ meV, and then for $U - E_F = 1.0$ eV and $g =$ 1.0, at $T = 4.2$ K, the LPMR $\frac{\Delta\rho(H)}{\rho(0)} \approx 0.01\%\ \mathrm{T}^{-1}$. We emphasize that in the second regime it is the maximum value of LPMR at $U - E_F = 1.0$ eV and $g = 1.0$, since we assumed that $\xi = 1$, which implies 100% spin polarization. At $U - E_F = 0.1$ eV and with the rest parameters being the same, the LPMR is increased by

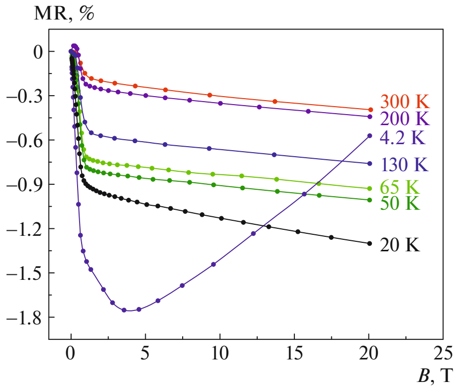

Fig. 3. Out-of-plane MR of $(CoNbTa)_x(SiO_2)_{100-x}$ with $x = 58.5$ at %.

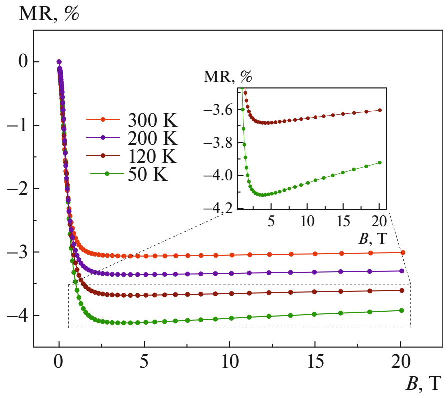

Fig. 4. Out-of-plane MR of $(Co)_x(LiNbO_3)_{100-x}$ with $x =$ 49 at %.

3.3 times, whereas at $U - E_F = 0.1$ eV and $g = 10$, $\frac{\Delta\rho(H)}{\rho(0)} \approx 0.1\%\ T^{-1}$.

Presented in [2] the LPMR results at $T = 65$ K of the nanocomposites CoFeB–SiO_2 and CoNbTa–Al_2O_3 are characterized by the "ln$T$" law and lie within the range of $\frac{\Delta\rho(H)}{\rho(0)} \approx 10^{-3}$–$10^{-4}\%\ T^{-1}$. These values correspond to the calculation results using the obtained expression (8). Note that signatures of quantum corrections for the nanocomposites in [2] were not observed, which excludes the mechanism of LPMR proposed in [1].

3.1. $(Co)_x(SiO_2)_{100-x}$

The LPMR is observed only for the composition with $x = 65$ at % and its magnitude is 0.03% T^{-1} (Fig. 2). Temperature dependences of resistivity of the studied nanocomposites are presented in Figs. 5–7. For the $(Co)_x(SiO_2)_{100-x}$ with $x = 65$ at %, the "ln$T$" law describes the data better than the "$T^{1/2}$" law (Fig. 5). As can be seen from the slope of the curves $1/2\pi Dg$ in Fig. 5, for this composition, $g \approx 1$ at $D = 3$. However, as noted in [3], for the considered model $2D$ is equal to the number of the nearest granules (Z) between which tunneling is possible, that is, for the disordered case $D < 3$. Therefore, for the composition with $x = 65$ at %, $g > 1$, and we can use the expression (8), which correctly describes the obtained data.

As can be seen from Fig. 2, the negative MR is higher at $T = 300$ K than at low temperatures. To explain this anomaly we should take into account possibility of formation of granules and aggregates at the concentrations close to the MIT. This may induce not only tunneling MR, but also negative MR due to suppression of magnetic disorder in the granules. The latter contribution can be of the same magnitude as negative tunneling MR and it rises with temperature due to an increase of spin fluctuations. The data from electron microscopy of the studied nanocomposites confirms the presence of such aggregates. Moreover, the metal concentration in the vicinity of the percolation threshold of the nanocomposite in Fig. 2 is higher than the concentration of the other studied nanocomposites. This indirectly confirms the presence of the aggregates. In addition, in $H > H_{sat}$ and at low temperatures, positive contribution to MR, due to the effect of magnetic blockade, is possible [9], which diminishes the negative MR at low temperatures.

3.2. $(CoNbTa)_x(SiO_2)_{100-x}$

For the nanocomposite $(CoNbTa)_x(SiO_2)_{100-x}$ with $x = 58.5$ at %, metal concentration is lower than in the previous sample, and resistivity is well described by the "ln$T$" law (Fig. 6). Concentration change of ions dispersed in dielectric matrix and composition variation of ferromagnetic granules can change the tunnel barrier height and spin polarization, leading to the increase of the LPMR up to $\frac{\Delta\rho(H)}{\rho(0)} \approx 0.06\%\ T^{-1}$. This magnitude is the highest among all the nanocomposites studied.

It should be noted that LPMR, according to the proposed mechanism, is extremely sensitive to the concentration of dispersed magnetic and nonmagnetic ions in the tunnel gap. On the one hand, such ions can decrease the tunnel barrier height, but on the other hand, by changing the permittivity of the matrix, their presence can reduce the Coulomb blockade

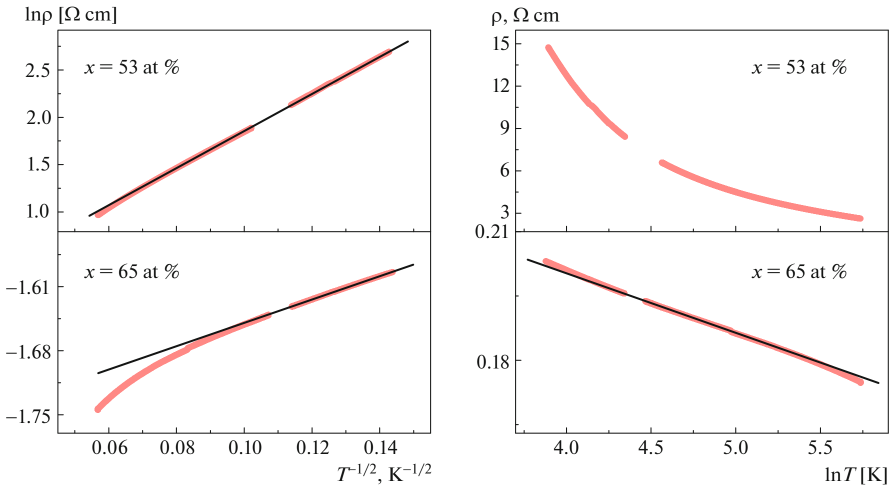

Fig. 5. Temperature dependences of resistivity of the $(Co)_x(SiO_2)_{100-x}$ nanocomposite. The left column represents $\ln\rho \propto T^{-1/2}$ behavior, the right column represents $\rho \propto \ln T$ behavior. The black solid lines are linear fits.

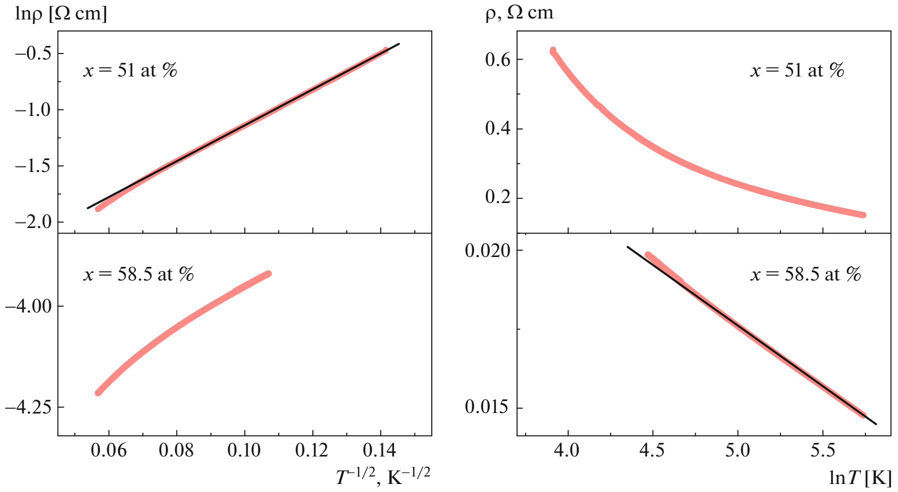

Fig. 6. Temperature dependences of resistivity of the $(CoNbTa)_x(SiO_2)_{100-x}$ nanocomposite. The left column represents $\ln\rho \propto T^{-1/2}$ behavior, the right column represents $\rho \propto \ln T$ behavior. The black solid lines are linear fits.

energy and also lead to the absence of magnetic and MR saturation in high magnetic fields. Presumably, that is the reason why the LPMR of the $(Co)_x(SiO_2)_{100-x}$ and $(CoNbTa)_x(SiO_2)_{100-x}$ nanocomposites takes place at $T = 4.2$ K, but is not observed already at $T = 10$ K even though (3) and (8) do not predict strong temperature dependence. Indeed, the studied nanocomposites are fabricated at the elevated temperature of the substrate (80°C), which makes their microstructure, and hence magnetic properties, to be different from the ones studied in [2]. For example, the magnetization of the $(Co)_x(SiO_2)_{100-x}$ nanocomposite saturates at $T = 2$ K

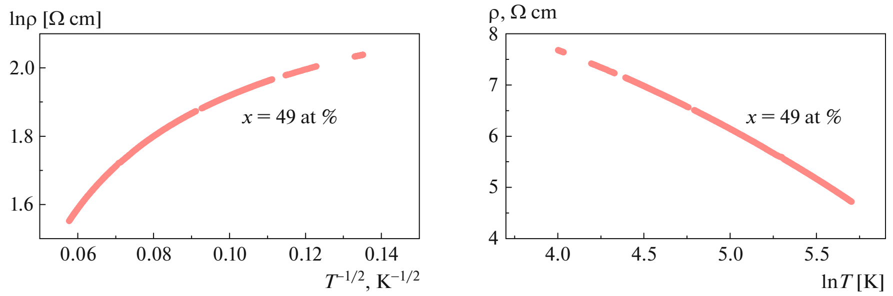

Fig. 7. Temperature dependences of resistivity of the $(\mathrm{Co})_x(\mathrm{LiNbO_3})_{100-x}$ nanocomposite. The left column represents $\ln\rho \propto T^{-1/2}$ behavior, the right column represents $\rho \propto \ln T$ behavior.

in $H \approx 4$ kOe, but at higher magnetic fields, the magnetization continues to grow (Fig. 1), which means a rise of the negative tunneling contribution to the MR. With the increased negative tunneling contribution, the positive contribution to the MR becomes indistinguishable. Therefore, the major reason why LPMR is not visible at $T > 4.2$ K is the strong competitive negative contribution to MR in high magnetic fields due to the presence of superparamagnetic granules and dispersed ions.

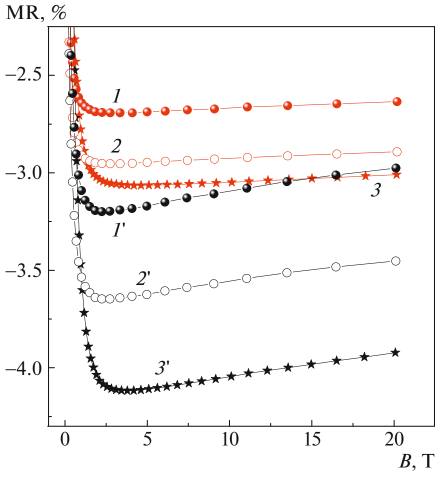

Fig. 8. Magnetoresistance of the $(\mathrm{Co})_x(\mathrm{LiNbO_3})_{100-x}$ nanocomposite with $x = 49$ at % at different orientations of the magnetic field to the sample plane and current direction: *1*, *1'*—magnetic field is parallel to both sample plane and current direction; *2*, *2'*—magnetic field is parallel to sample plane and perpendicular to current direction; *3*, *3'*—magnetic field is perpendicular to both sample plane and current direction. Curves with and without prime are measured at $T = 50$ and 300 K, respectively.

3.3. $(Co)_x(LiNbO_3)_{100-x}$

The conductivity of the nanocomposite Co–$\mathrm{LiNbO_3}$ does not follow either “ln$T$” or “$T^{1/2}$” laws (Fig. 7), nevertheless, in Fig. 4 one can see the signatures of positive MR in high magnetic fields for the composition with $x = 49$ at %. The LPMR is of the order of 10^{-3}% $\mathrm{T^{-1}}$, which is similar value to the composites CoFeB–$\mathrm{SiO_2}$ and CoNbTa–$\mathrm{Al_2O_3}$, however, the MR of Co–$\mathrm{LiNbO_3}$, in contrast to other studied samples, is anisotropic. The in-plane MR (magnetic field oriented parallel to the sample plane) is higher when magnetic field is oriented perpendicular to the current direction rather than parallel. Additionally, when magnetic field is perpendicular to the current direction, the in-plane MR differs from the out-of-plane MR (Fig. 8). Neither of these features were observed in the previous two samples nor in the samples of [1]. It would be natural to connect these features with microstructure properties of the Co–$\mathrm{LiNbO_3}$ nanocomposite, which is discussed below.

The results of STEM/TEM study of the Co–$\mathrm{LiNbO_3}$ nanocomposite are presented in Fig. 9, where one can see a columnar structure near the interface between $(\mathrm{Co})_x(\mathrm{LiNbO_3})_{100-x}$ and the glass-ceramic substrate. The structure consists of cobalt granules, elongated mainly in the direction of nanocomposite growth with a lateral size in the film plane of 5–8 nm (Fig. 9, image B). Vertical growth continues up to ~20 nm, where the columnar granules start to bend (Fig. 9). Above the columnar structure layer (~100 nm thick), an amorphous-crystalline nanocomposite is formed, consisting of spherical crystalline nanoparticles with a size of 5–30 nm, separated by an amorphous interlayer. The high-resolution TEM results together with EDXS mapping (not shown here) demonstrated that the crystalline particles and the interlayer consist of

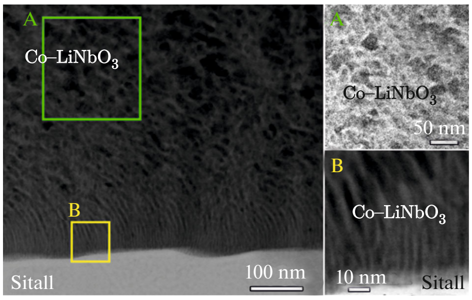

Fig. 9. Bright-field STEM image of a cross-section of $(Co)_x(LiNbO_3)_{100-x}$ film ($x = 49$ at %) on the glass-ceramic substrate (left side). Top right image (A) shows a dark-field TEM image obtained using hollow cone illumination mode with the objective aperture set in the diffuse background area. Such mode leads to bright contrast of amorphous layer in between the crystalline Co particles. Bottom right image (B) shows a bright-field STEM image of the interface area. The elongated grains up to 20–25 nm forming from the interface are clearly visible.

Co and amorphous $LiNbO_3$, respectively. The high defectiveness of Co nanoparticles should be noted, consisting of stacking faults and twins, which is typical for Co nanoparticles. A similar columnar structure was observed earlier in the $(CoFeB)_x(LiNbO_3)_{100-x}$ nanocomposite with the CoFe granules, elongated in the direction of nanocomposite growth up to 10–15 nm and with a lateral size of 2–4 nm [10, 11]. However, the $(CoFeB)_x(LiNbO_3)_{100-x}$ nanocomposite films have uniform thickness and follow the logarithmic law of thermal resistivity [10, 11]. The growth anisotropy of the Co–$LiNbO_3$ nanocomposite is apparently associated with the possibility of formation of an additional equilibrium phase of $LiCoO_2$ and, as a consequence, with the manifestation of unusual nucleation effects. High-resolution images with following Fast Fourier Transform analysis indicated that Co grains in the bottom part of the film do not correspond to cubic Co.

The presence of tightly packed granules in the lower part of the $(Co)_x(LiNbO_3)_{100-x}$ film and large particles in the upper part determines the ferromagnetic properties of the structure and its MR anisotropy. As can be seen from Fig. 9, intergranular gaps in the upper part of the film are considerably large (~5 nm), hence strong tunnel coupling between granules is excluded. Under these conditions, conductivity will be mainly determined by a hopping transfer along localized defects of amorphous matrix, which is commonly determined by the Mott's "$T^{1/4}$" law. For the lower part of the nanocomposite with the elongated granules, the so-called "oblique tunneling" with the subsequent transport of electrons along the chains of elongated granules appears to be crucial [7]. Conductivity of the relatively small part with elongated granules can be comparable or even higher than conductivity of the isotropic part of the nanocomposite. Therefore, the total conductivity is described neither by "$T^{1/2}$" nor "$\ln T$" laws. The high value of permittivity (ϵ_d ~ 50 [12]) of amorphous $LiNbO_3$ decreases the energy of the Coulomb blockade, and hence decreases possible value of LPMR during tunneling between granules in the lower part of the nanocomposite. Besides, shunting effect of the upper part is also important. Thus, the observed MR behavior of the given nanocomposite is mainly determined by the properties of its structure.

4. CONCLUSIONS

Along with the negative magnetoresistance (MR), associated with the spin-dependent tunneling, a linear positive MR (LPMR) is observed in the nanocomposites near the percolation threshold at low temperatures and in magnetic fields above the saturation field. In the nanocomposites $(Co)_x(SiO_2)_{100-x}$ ($x = 65$ at %) and $(CoNbTa)_x(SiO_2)_{100-x}$ ($x = 58.5$ at %) with a strong tunnel coupling between granules, characterized by a logarithmic temperature dependence of resistivity, the LPMR at $T = 4.2$ K is 0.03% and 0.06% T^{-1}, respectively. The developed simple theory of the LPMR for these nanocomposites, based on the influence of the Zeeman effect on the tunneling barrier height in the spin-dependent tunneling, makes it possible to qualitatively explain the results. The MR of $(Co)_x(LiNbO_3)_{100-x}$ ($x = 49$ at %) nanocomposite is anisotropic, and the LPMR at $T = 50$ K is about 10^{-3}% T^{-1} that is associated with the formation of the columnar structure at the initial stage of growth of this film.

FUNDING

This work was partially supported by the Russian Foundation for Basic Research (grant no. 19-07-00471) and by the Academy of Finland (grants nos. 333805 and 318405).

CONFLICT OF INTEREST

The authors declare that they have no conflicts of interest.

REFERENCES

1. A. Gerber, I. Kishon, I. Y. Korenblit, O. Riss, A. Segal, M. Karpovski, and B. Raquet, Phys. Rev. Lett. **99**, 027201 (2007).
2. M. Blinov, M. Shakhov, V. Rylkov, E. Lähderanta, V. Prudnikov, S. Nikolaev, A. Sitnikov, and A. Granovsky, J. Magn. Magn. Mater. **469**, 155 (2019).
3. V. Rylkov, S. Nikolaev, K. Y. Chernoglazov, V. Demin, A. Sitnikov, M. Y. Presnyakov, A. Vasiliev, N. Perov, A. Vedeneev, Y. E. Kalinin, et al., Phys. Rev. B **95**, 144202 (2017).

4. V. V. Rylkov, V. A. Demin, A. V. Emelyanov, A. V. Sitnikov, Y. E. Kalinin, V. V. Tugushev, and A. B. Granovsky, in *Novel Magnetic Nanostructures* (Elsevier, Amsterdam, 2018), p. 427.
5. E. Lähderanta, M. Guc, M. Shakhov, E. Arushanov, and K. Lisunov, J. Appl. Phys. **120**, 035704 (2016).
6. V. Rylkov, A. Emelyanov, S. Nikolaev, K. Nikiruy, A. Sitnikov, E. Fadeev, V. Demin, and A. Granovsky, J. Exp. Theor. Phys. **131**, 160 (2020).
7. I. Beloborodov, A. Lopatin, V. Vinokur, and K. Efetov, Rev. Mod. Phys. **79**, 469 (2007).
8. B. Abeles, P. Sheng, M. Coutts, and Y. Arie, Adv. Phys. **24**, 407 (1975).
9. J. Inoue and S. Maekawa, Phys. Rev. B **53**, R11927 (1996).
10. V. Rylkov, A. Sitnikov, S. Nikolaev, V. Demin, A. Taldenkov, M. Y. Presnyakov, A. Emelyanov, A.Vasiliev, Y. E. Kalinin, A. Bugaev, et al., J. Magn. Magn. Mater. **459**, 197 (2018).
11. V. Rylkov, S. Nikolaev, V. Demin, A. Emelyanov, A. Sitnikov, K. Nikiruy, V. Levanov, M. Y. Presnyakov, A. Taldenkov, A. Vasiliev, et al., J. Exp. Theor. Phys. **126**, 353 (2018).
12. T. Mitsuyu and K. Wasa, Jpn. J. Appl. Phys. **20**, L48 (1981).

ACTA UNIVERSITATIS LAPPEENRANTAENSIS

988. CAMPOSANO, JOSÉ CARLOS. Integrating information systems across organizations in the construction industry. 2021. Diss.

989. LAUKALA, TEIJA. Controlling particle morphology in the in-situ formation of precipitated calcium carbonate-fiber composites. 2021. Diss.

990. SILLMAN, JANI. Decoupling protein production from agricultural land use. 2021. Diss.

991. KHADIM, QASIM. Multibody system dynamics driven product processes. 2021. Diss.

992. ABDULKAREEM, MARIAM. Environmental sustainability of geopolymer composites. 2021. Diss.

993. FAROQUE, ANISUR. Prior experience, entrepreneurial outcomes and decision making in internationalization. 2021. Diss.

994. URBANI, MICHELE. Maintenance policies optimization in the Industry 4.0 paradigm. 2021. Diss.

995. LAITINEN, VILLE. Laser powder bed fusion for the manufacture of Ni-Mn-Ga magnetic shape memory alloy actuators. 2021. Diss.

996. PITKÄOJA, ANTTI. Analysis of sorption-enhanced gasification for production of synthetic biofuels from solid biomass. 2021. Diss.

997. MASHLAKOV, ALEKSEI. Flexibility aggregation of local energy systems—interconnecting, forecasting, and scheduling. 2021. Diss.

998. NIKITIN, ALEKSEI. Microwave processes in thin-film multiferroic heterostructures and magnonic crystals. 2021. Diss.

999. VIITALA, MIRKA. The heterogeneous nature of microplastics and the subsequent impacts on reported microplastic concentrations. 2021. Diss.

1000. ASEMOKHA, AGNES. Understanding business model change in international entrepreneurial firms. 2021. Diss.

1001. MUSTO, JIRI. Improving the quality of user-generated content. 2021. Diss.

1002. INKERI, EERO. Modelling of component dynamics and system integration in power-to-gas process. 2021. Diss.

1003. GARIFULLIN, AZAT. Deep Bayesian approach to eye fundus image segmentation. 2021. Diss.

1004. ELFVING, JERE. Direct capture of CO2 from air using amine-functionalized resin - Effect of humidity in modelling and evaluation of process concepts. 2021. Diss.

1005. KOMLEV, ANTON. Magnetism of metal-free graphene-based materials. 2021. Diss.

1006. RISSANEN, MATTI. EcoGame and Ecosystem Profiler: solutions for business ecosystem management. 2021. Diss.

1007. VANHAMÄKI, SUSANNA. Implementation of circular economy in regional strategies. 2021. Diss.

1008. LEHTINEN, VESA. Organisaation emergentti itseohjautuvuus, case sinfoniaorkesteri: ”Miksi orkesteri soittaa hyvin, vaikka sitä johdettaisiin huonosti?”. 2022. Diss.

1009. KÄHKÖNEN, TIINA. Employee trust repair in the context of organizational change – identification and measurement of active trust repair practices. 2022. Diss.

1010. AHONEN, AILA. Challenges in sport entrepreneurship: cases in team sport business. 2022. Diss.

1011. LEVIKARI, SAKU. Acoustic emission testing of multilayer ceramic capacitors. 2022. Diss.

1012. ZAHEER, MINHAJ. Evaluation of open-source FEM software performance in analysing converter-fed induction machine losses. 2022. Diss.

1013. HAAPANIEMI, JOUNI. Power-based electricity distribution tariffs providing an incentive to enhance the capacity effectiveness of electricity distribution grids. 2022. Diss.

1014. BUAH, ERIC. Artificial intelligence technology acceptance framework for energy systems analysis. 2022. Diss.

1015. GIVIROVSKIY, GEORGY. In situ hydrogen production in power-to-food applications. 2022. Diss.

1016. SOMMARSTRÖM, KAARINA. Teachers’ practices of entrepreneurship education in cooperation with companies. 2022. Diss.

1017. KAN, YELENA. Coherent anti-stokes raman scattering spectromicroscopy in biomedical and climate research. 2022. Diss.

1018. MÄNDMAA, SIRLI. Financial literacy in perspective – evidence from Estonian and Finnish students. 2022. Diss.

1019. QORRI, ARDIAN. Measuring and managing sustainable development in supply chains. 2022. Diss.

1020. MARTIKAINEN, SUVI-JONNA. Meaningful work and eudaimonia: contributing to social sustainability in the workplace. 2022. Diss.

1021. MANNINEN, KAISA. Conducting sustainability target-driven business. 2022. Diss.

1022. LI, CHANGYAN. Design, development, and multi-objective optimization of robotic systems in a fusion reactor. 2022. Diss.

1023. CHOUDHURY, TUHIN. Simulation-based methods for fault estimation and parameter identification of rotating machines. 2022. Diss.

1024. DUKEOV, IGOR. On antecedents of organizational innovation: How the organizational learning, age and size of a firm impact its organizational innovation. 2022. Diss.

1025. BREIER, MATTHIAS. Business model innovation as crisis response strategy. 2022. Diss.

LUT University

ISBN 978-952-335-817-1
ISBN 978-952-335-818-8 (PDF)
ISSN-L 1456-4491
ISSN 1456-4491
Lappeenranta 2022